Electronic and thermoelectric properties of graphene/boron nitride in-plane heterostructures

van Truong Tran

NNT : 2015SACLS133

THESE DE DOCTORAT
DE L'UNIVERSITE PARIS-SACLAY,
préparée à l'Université Paris-Sud

ÉCOLE DOCTORALE N° 575
Electrical, Optical, Bio – physics and Engineering (EOBE)

IEF - Institut d'Electronique Fondamentale

Spécialité de doctorat : Electronique et Optoélectronique, Nano et Microtechnologies

Par

Van-Truong Tran

Propriétés électroniques et thermoélectriques des hétérostructures planaires de graphène et de nitrure de bore

Thèse présentée et soutenue à Orsay, le 26 Novembre 2015 :

Composition du Jury :

M. VOLZ Sebastian	EM2C, CNRS	Président
M. GOUPIL Christophe	LIED, Université Paris Diderot	Rapporteur
M. PALA Marco	IMEP-LAHC, CNRS	Rapporteur
M. SAINT-MARTIN Jérôme	IEF, Université Paris-Sud	Examinateur
M. DOLLFUS Philippe	IEF, CNRS	Directeur de thèse

Contents

List of figures

Acknowledgements

I would like to send my heartfelt thanks and gratitude to my two supervisors Philippe Dollfus and Jérôme Saint-Martin for their kindness and the whole-hearted guidance during my PhD. I greatly appreciate their concern not only on my work but also on my life. I believe that without these helps my projects would never completed.

On this occasion, I would like to thank all my colleagues in COMICS group (Prof. Arnaud Bournel, Dr. Damien Querlioz, Dr. Michele Amato, Mr. Salim Berrada, Mr. Adrien Vincent, Mr. Jérôme Larroque, Dr. Viet-Hung Nguyen, Ms. Thu-Trang Nghiem-Thi, Ms. Mai Chung Nguyen and others) for a friendly atmosphere and also their help in life and works. Especially, Mr. Christophe Chassat for his helps in setting up my desktop and debugging computer problems.

It is also an opportunity for me to acknowledge Université Paris-Sud 11, Université Paris-Saclay and CNRS (Centre National de la Recherche Scientifique) for the financial supports.

Finally, I would like to express my thanks and gratefulness to my parents, my brothers, my sister, my wife and my little daughter for their love, share and encouragement.

This work is dedicated for all people I love.

Orsay, 01 September, 2015

Van-Truong Tran

Abstract

Graphene is a fascinating 2-dimensional material exhibiting outstanding electronic, thermal and mechanical properties. It is expected to have a huge potential for a wide range of applications, in particular in electronics. However, this material also suffers from a strong drawback for most electronic devices due to the gapless character of its band structure, which makes it difficult to switch off the current. For thermoelectric applications, the high thermal conductance of this material is also a strong limitation. Hence, many challenges have to be taken up to make it useful for actual applications.

This thesis work focuses on the theoretical investigation of a new strategy to modulate and control the properties of graphene that consists in assembling in-plane heterostructures of graphene and Boron Nitride (BN). It allows us to tune on a wide range the bandgap, the thermal conductance and the Seebeck coefficient of the resulting hybrid nanomaterial. The work is performed using atomistic simulations based on Tight Binding (TB), Force Constant (FC) models for electrons and phonons, respectively, coupled with the Green's function formalism for transport calculation.

The results show that thanks to the tunable bandgap, it is possible to design graphene/BN based transistors exhibiting high on/off current ratio in the range 10^4-10^5. We also predict the existence hybrid quantum states at the zigzag interface between graphene and BN with appealing electron transport. Finally this work shows that by designing properly a graphene ribbon decorated with BN nanoflakes, the phonon conductance is strongly reduced while the bandgap opening leads to significant enhancement of Seebeck coefficient. It results in a thermoelectric figure of merit *ZT* larger than one at room temperature.

Résumé

Le graphène, matériau bidimensionnel constitué d'une monocouche d'atomes de carbone formant un réseau en nid d'abeille, est bien connu pour ses exceptionnelles propriétés électroniques.[1] Sa structure de bandes d'énergie ne présente pas de bande interdite, avec une dispersion quasi-linéaire autour du point de neutralité. Enfin la mobilité électronique y est extrêmement élevée.[2] Parmi ses nombreux autres avantages, ce matériau présente également des propriétés thermiques et mécaniques exceptionnelles, dont une très forte conductivité thermique [3] et une aptitude à supporter de grandes déformations.[4] On espère donc qu'il puisse donner lieu à un grand nombre d'applications.[5] La structure de bande et les propriétés du graphène ont d'abord été étudiées théoriquement par Wallace dès 1947.[6] Cependant, la limitation des techniques expérimentales à cette époque n'a pas permis aux scientifiques de confirmer les fascinantes propriétés prédites théoriquement. Il a fallu attendre 2004 pour que Geim et son étudiant Novoselov réussissent à isoler une forme stable de graphène en exfoliant une seule couche de carbone à partir de graphite.[7] Cet avancée scientifique a démontré l'existence d'un matériau bidimensionnel à base de carbone, qui a alors été nommé graphène. Ensuite, le graphène est rapidement devenu pour les physiciens un sujet de recherche très en vogue, aussi bien d'un point de vue fondamental qu'au niveau des applications.

En dépit de ses excellentes propriétés électroniques, le graphène présente des inconvénients qui en limitent certaines applications, notamment en électronique. Tout d'abord, il est impossible de bloquer complètement le courant dans des dispositifs en graphène du fait de l'absence de bande interdite dans la structure électronique. Un autre problème est la croissance du graphène et son dépôt sur des substrats isolants. Comme le graphène est très mince, la surface assez rugueuse du SiO_2, souvent utilisé comme substrat, peut piéger les charges et modifier la forme plane du graphène,[8,9] ce qui affecte fortement le transport électronique. En effet, bien que la mobilité des électrons dans le graphène doit théoriquement pouvoir atteindre environ 200 000 $cm^2 \cdot V^{-1} \cdot s^{-1}$ à température ambiante,[5] une telle valeur n'a été obtenue que dans du graphène suspendu (sans substrat). [2] Pour le graphène sur SiO_2, la meilleure mobilité expérimentale mesurée est d'environ 40 000 $cm^2 \cdot V^{-1} \cdot s^{-1}$,[10] mais elle est généralement beaucoup plus basse, ce qui est loin des attentes initiales. Ainsi, le choix du substrat est d'une grande importance en vue de parvenir à des applications électroniques hautes performances.

Le graphène est également prévu pour être appliqué dans le contexte de la spintronique. Même si le couplage spin-orbite dans le graphène est très faible et incapable de séparer les électrons à spin "up" et les électrons à spin "down",[11] dans des rubans de graphène avec des bords zigzag, il est possible de fabriquer des filtres de spin grâce à la séparation de spin dans des états de bord de faible énergie.[12,13] Toutefois, seuls des rubans de graphène extrêmement étroits de type zigzag sont pertinents pour exploiter cet effet.

En ce qui concerne les propriétés thermoélectriques, le graphène souffre de limitations intrinsèques malgré son excellente mobilité électronique. L'absence de bande d'énergie interdite fait qu'il est difficile de séparer les contributions opposées d'électrons et de trous pour l'effet Seebeck qui y est donc faible.[14] En outre, comme mentionné ci-dessus, la propagation des phonons est également très bonne dans le graphène ce qui est une autre limitation pour les applications thermoélectriques.[3] En effet, la capacité thermoélectrique d'un matériau est évaluée par la figure de mérite thermoélectrique $ZT = G_e S^2 T / \left(K_e + K_p \right)$ qui est définie par l'intermédiaire de la conductance électrique G_e, le coefficient Seebeck S et la conductance thermique des électrons et des phonons (K_e et K_p). Ainsi, avec un très faible coefficient Seebeck et une très haute conductance thermique, le ZT du graphène est faible, inférieur à 0.01, alors qu'un matériau thermoélectrique efficace doit avoir ZT ~ 1. Pour rendre le graphène plus propice à la thermoélectricité, certaines stratégies de conception et nanostructuration doivent être appliquées pour à la fois améliorer le coefficient Seebeck et aussi réduire la conductance thermique.

En fait, en raison de l'énorme potentiel du graphène, les scientifiques ont cherché continuellement des solutions pour en surmonter ses limites. Fondamentalement, la recherche sur le graphène a connu différentes périodes. Avant 2004, seulement quelques travaux théoriques prédisaient des propriétés intéressantes du graphène. Après la découverte expérimentale de graphène, de 2004 à 2010 la plupart des travaux ont été axés sur le graphène pur, visant essentiellement à ouvrir une bande interdite dans sa structure de bandes en exploitant les structures 1D de graphène (rubans de graphène) [15-18] ou en appliquant des champs électriques perpendiculaires aux bicouches de graphène.[19] D'autres propriétés physiques ont été également étudiées comme l'effet Hall quantique et les interactions de spin.[20-22] Au cours des dernières années, les activités de recherche sur le graphène ont été élargies vers de nombreuses orientations visant à trouver de nouvelles propriétés pour de

nouvelles applications. Ces recherches peuvent être classérs en quatre grandes tendances de recherche :

(i) L'étude de nouveaux effets sur le graphène tels que (1) le dopage avec des atomes substitutionnels tels que le bore ou de l'azote pour ouvrir une bande iterdite [23]; (2) la découpe d'un réseau périodique de trous dans les feuilles de graphène [24]; (3) la fonctionnalisation avec l'hydrogène, nommée graphone [25,26]; (4) la construction d'une logique ultra-faible puissance à mémoire non volatile à l'aide de la grande longueur de diffusion du spin dans le graphène 2D [27,28]; (5) l'étude des effet géométrique comme la rugosité de bord, les défauts ou les torsions [29]; (6) l'amélioration de la performance thermoélectrique en utilisant des géométries sophistiquées.[30-33]

(ii) L'étude d'hétérostructures entre le graphène et d'autres matériaux: (1) l'ouverture de bande interdite avec des structures hybrides de graphène/BN,[34-37] (2) l'utilisation de substrat de haute qualité en nitrure de bore hexagonal qui est en accord de maille quasi parfait avec le graphène et qui est lisse.[38]

(iii) L'étude de nouvelles propriétés des matériaux 2D comme le graphène tels que MoS_2, SiC, phosphorène et silicène. De plus ils ont l'avantage de présenter une bande interdite intrinsèque et un fort couplage spin-orbite.[39]

(iv) L'étude de nouveaux allotropes de carbone: ce sont des matériaux à base de carbone mais qui ont une structure légèrement différente du graphène comme le pentagraphène (structures pentagonales) [40] ou le Graphyne et le graphdiyne avec des structures circulaires.[41,42]

En ce qui concerne la tendance de la recherche sur les hétérostructures graphène/BN, récemment des expérimentateurs ont démontré avec succès la synthèse de structures de graphène/BN sur une seule couche, [43-45] ce qui a motivé certaines études théoriques sur les structures de bandes électroniques [34,35,46,47] et aussi sur le transport [46,48-51] dans ce nouveau matériau hybride.

Dans ce contexte, ce projet de thèse a été consacré aux propriétés des hétérostructures planaires de graphène/BN dans le but de comprendre et d'améliorer leurs propriétés électroniques et thermoélectriques par rapport au graphène 2D. Il se concentre particulièrement sur l'ouverture d'une bande interdite et sur les propriétés de transport qui peuvent être utilisées pour réaliser de bons transistors ou de bons convertisseurs d'énergie.

L'étude est basée sur des méthodes semi-empiriques comme celles des liaisons fortes pour les électrons et celles des constantes de force pour les phonons. Ces méthodes ont été largement utilisées en physique de la matière condensée en raison de leur efficacité de calcul. Nous utilisons aussi les fonctions de Green hors équilibre (NEGF) combinées avec les approches atomistiques mentionnées plus haut pour étudier le transport quantique.

Une visite guidée de la thèse

Ce manuscrit de thèse est organisé en cinq chapitres et quatre annexes.

Chapitre 1 : Contexte théorique

Dans ce chapitre, je présente le contexte théorique de mon étude. Tout d'abord, les méthodes empiriques, y compris les modèles « liaisons fortes » et « constantes de forces », sont examinées. L'équation de Schrödinger pour les électrons et l'équation de mouvement de Newton pour les phonons peuvent être formulées dans un problème aux valeurs propres, à savoir, respectivement

$$H.C = E.C \tag{1}$$

et

$$\omega^2 U = DU \tag{2}$$

Dans l'équation (1), H est le Hamiltonien électronique, E est l'énergie et C les fonctions d'ondes locales. Dans l'équation (2), ω fait référence à la fréquence de vibration des phonons, U est le vecteur de déplacement dans l'espace et D est la matrice décrivant la dynamique de couplages entre les atomes.

Dans le cas où le système est périodique, ces problèmes de valeur propre peuvent être réduits à l'équation pour une cellule élémentaire

$$\left[H_{\alpha\alpha} + \sum_{\beta \neq \alpha} H_{\alpha\beta} . \mathrm{e}^{i\vec{k}.\left(\vec{R}_\beta - \vec{R}_\alpha\right)} \right] \phi_0 = E\phi_0 \tag{3}$$

où $H_{\alpha\alpha}$ est le Hamiltonien des électrons (ou la matrice dynamique des phonons) pour une cellule unitaire α et $H_{\alpha\beta}$ est la matrice de couplage entre les cellules unitaires α et β.

Connaissant les bandes d'énergie (ou la dispersion des phonons) et la fonction d'onde, certaines grandeurs physiques telles que la bande interdite, la densité d'états (DOS), la densité locale d'états (LDO), la densité de charge, la vitesse de groupe, la masse effective peuvent être calculées.

Pour étudier le transport dans les systèmes hors-équilibre, les fonctions de Green d'un système ouvert qui est connecté à des contacts (gauche et droite) sont introduites. Elles sont calculées par

$$G_D = \left(E - H_D - \Sigma_L - \Sigma_R\right)^{-1} \tag{4}$$

où H_D est le Hamiltonien de la région active ("Device") et $\Sigma_{L(R)} = \tau_{DL(R)} g_{L(R)} \tau_{L(R)D}$ est la self-energy du contact gauche (droite). Ensuite, la transmission peut être calculée par l'intermédiaire de la fonction de Green par la formule de Meir-Wingreen

$$T = trace\left[\Gamma_L G_D \Gamma_R G^{\dagger}{}_D\right] \tag{5}$$

où

$$\Gamma_{L(R)} = i\left[\Sigma_{L(R)} - \Sigma_{L(R)}{}^{\dagger}\right] \tag{6}$$

sont appelés les taux d'injection au niveau des contacts.

Avec la transmission obtenue par expression (5), d'autres quantités de transport, par exemple, le courant, la conductance, le coefficient Seebeck, le facteur de mérite *ZT* peuvent être calculés.

Les principales étapes de calcul et les différentes techniques utilisées pour calculer les propriétés de transport sont indiquées dans le chapitre.

Dans la dernière partie de ce chapitre, la modélisation et les méthodes ci-dessus sont appliquées pour examiner les propriétés électroniques et thermiques de certains systèmes simples comme la chaîne linéaire d'atomes ainsi que des structures 2D et 1D de graphène et de Nitrure de Bore hexagonal.

Chapitre 2 : Hétérostructures graphène/BN avec une bande interdite accordable et des électrons à haute vitesse

Dans ce chapitre, je présente les mécanismes d'ouverture de la bande interdite et sa modulation dans des hétérostructures de graphène/BN. Les bandes interdites de différentes configurations de rubans « armchair » et « zigzag » sont étudiées en utilisant un calcul de liaisons fortes fondé sur un modèle simple d'interaction au premier voisin. L'étude permet de comprendre quelles configurations présentent une bande interdite intéressante. Elle démontre que les structures hybrides avec des interfaces parallèles à la direction du transport conservent de bonnes propriétés de transport (vitesse de groupe élevée), meilleures que dans les structures avec des interfaces perpendiculaires à la direction de transport comme on le voit dans la Figure 1. Il est également montré que toutes les hétérostructures « armchair » sont semi-conductrice avec une bande interdite. Les structures « zigzag » sont soit métalliques soit semi-conductrices, selon le type de couplage à l'interface entre le graphène et le BN.

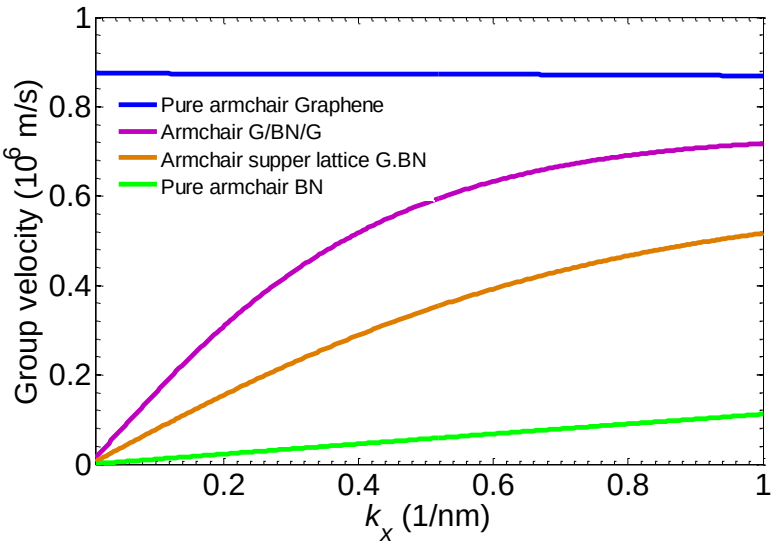

Figure 1: Comparaison de la vitesse de groupe dans quatre structures « armchair » de même largeur $M = 59$.

Chapitre 3 : Modulation de largeur de bande interdite et du courant dans des nanorubans de graphène/BN sous champ électrique transverse

Dans ce chapitre, j'étudie l'effet d'un champ électrique dans le plan sur les bandes d'énergie d'une structure « armchair » G/BN à deux rubans de graphène séparés par un ruban BN comme esquissé dans la Figure 2 (a). Tout d'abord, une première approche simple est appliquée pour étudier l'effet d'un champ électrique externe dans différentes structures, y compris le G/BN armchair et des rubans armchair de pur graphène avec l'hypothèse que le potentiel électrostatique est linéaire (donc sans auto cohérence avec l'équation de Poisson). Cette approche simple nous montre que la structure G/BN/G présente un net avantage par rapport à de simples rubans de graphène : l'application d'un champ électrique externe permet de moduler efficacement la largeur de la bande interdite.

Ensuite, j'étudie cet effet dans la structure G/BN armchair en prenant en compte l'effet de redistribution de charge en résolvant les équations de Schrödinger-Poisson couplées:

$$\begin{cases} \nabla\left(\varepsilon\nabla V\right) = -\dfrac{\rho}{\varepsilon_0} \\ \left[H_0 + U\right]\phi_0 = E\phi_0 \end{cases} \tag{7}$$

L'évolution de la bande interdite avec l'étude d'auto-cohérente montre que la bande interdite est fortement réduite sous l'effet d'un champ électrique de moins de 20 mV/Å. En outre, l'effet de redistribution de charge reste faible pour un champ électrique inférieur à 6 mV/Å. Avec la modulation de la forte largeur de bande interdite sous l'effet du champ électrique, le courant est commandé avec succès dans un dispositif hybride constitué d'un ruban de graphène/BN comme montré sur la Figure 2 (b). Le rapport des courants ON et OFF à la polarisation V_{bias} = 0.2 V est défini comme le rapport des courants à F_0 = 20 mV/Å et au F_0 = 0 mV/Å. Il est de 3830 pour une longueur de la région active de 10.5 nm et atteint même jusqu'à 14200 si cette longueur est de 17 nm.

(a) (b)

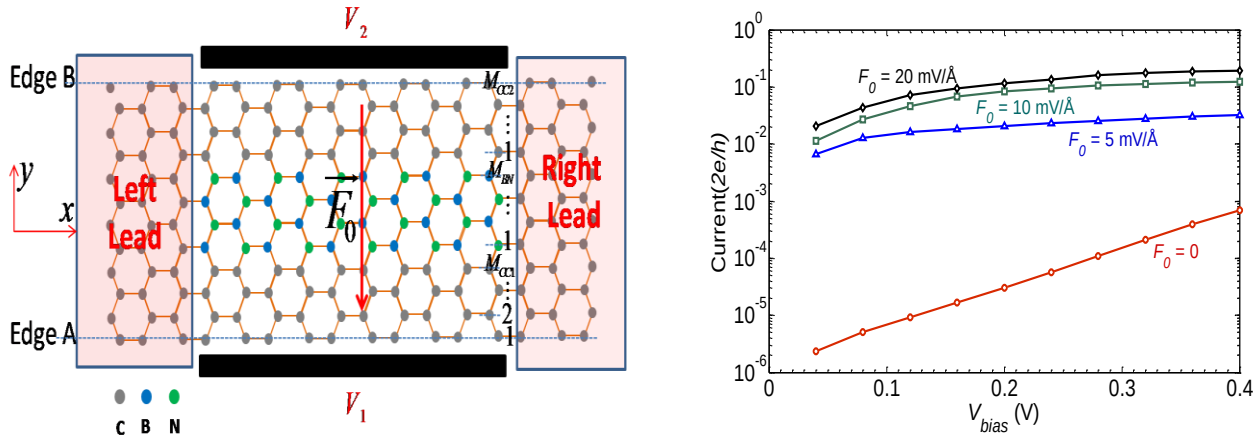

Figure 2: (a) Vue schématique de la structure graphène/BN/graphène armchair étudiée. Le système est placé entre deux grilles latérales qui génèrent un champ électrique transversal. La région active est connectée à deux contacts de graphène. (b) Courant en fonction de la tension de polarisation pour des champs électriques transversaux F_0 = 0, 5, 10 et 20 mV/Å. La simulation a été effectuée à température ambiante T = 300 K, avec E_F = 0.2 eV. La longueur de la région active est L_A = 10,5 nm.

Chapitre 4 : Etats hybrides dispersifs et transport quantique dans des hétérostructures graphène/BN

Dans ce chapitre, j'étudie l'émergence d'Etats qui sont localisés à l'interface des hétérostructures zigzag de graphène/BN. Pour des résultats précis, les interactions juqu'au deuxième voisin sont prises en compte

$$H = \sum_i \varepsilon_i |i\rangle\langle i| - \sum_{\langle i,j\rangle} t_{ij} |i\rangle\langle j| - \sum_{\langle\langle i,j\rangle\rangle} t'_{ij} |i\rangle\langle j| + \sum_i V_i^{dec} |i\rangle\langle i| \qquad (8)$$

Un potentiel V_i^{dec} est également ajouté pour reproduire les calculs ab initio.

L'étude est reprise pour différentes configurations d'hétérostructure G/BN zigzag. L'analyse de la structure de bandes indique que les états de bords au niveau des interfaces de G/BN (Figure 3 (a)) sont robustes par rapport aux états de bords dans des rubans zigzag de pure graphène. Ces états ont (courbes rouges dans la Figure 3 (b)) des vitesses de groupe très

élevées jusqu'à 7.4×10^5 m/s. La transmission due à l'émergence de ces états, subit une amélioration significative, qui se répercute sur la conductance électrique à basse énergie. Les états d'interface robustes survive aussi dans des structures en G/BN zigzag avec des interfaces imparfaites. En outre, on étudie l'effet de la parité pour comprendre les propriétés de transport dans des structures graphène/BN zigzag.

(a) (b)

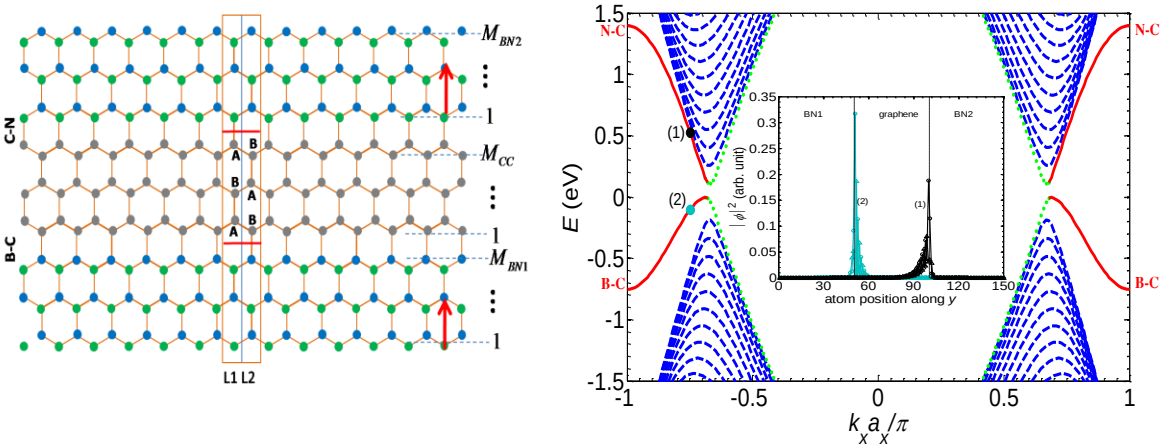

Figure 3: (a) vue schématique d'un zigzag BN/G/BN avec interfaces B-C--C-N (b) la structure de bande pour $M_{BN1} = M_{CC} = M_{BN2}$ **= 50** et le profil de la densité de probabilité pour les deux états (1) et (2). Une largeur de bande peut être clairement observée dans la figure (b).

Chapitre 5 : Amélioration de la performance thermoélectrique dans des hétérostructures graphène/BN

Dans le chapitre 5, j'étudie les propriétés thermoélectriques d'hétérostructures de graphène/BN constituées d'un ruban de graphène décorés par des nano-flocons de BN régulièrement espacés (Figure 4 (a)). Cette géométrie efficace engendre une forte réduction de la conductance des phonons par rapport à celle des rubans de graphène. De plus, une bonne conductivité électrique est conservée car la présence du BN, qui est un isolant, sur les côtés du graphène n'affecte pas la cionduction électrique. Il en résulte une valeur élevée de *ZT* de 0,81 pour un ruban hybride avec M_{CC} = 5 (Figure 4 (b)). Le pic de *ZT* peut être observé à basse énergie μ = 0,41 eV, ce qui est beaucoup plus faible que dans le cas de structures en super-réseau transverse. Les effets de la température et des lacunes sur les propriétés thermoélectriques sont également étudiées. Remarquablement, les lacunes au centre du ruban

de graphène peuvent conduire à une amélioration supplémentaire du facteur de mérite *ZT*. Avec trois lacunes introduites dans le canal, un *ZT* de 1,48 est obtenu (Figure 4 (b)).

(a) (b)

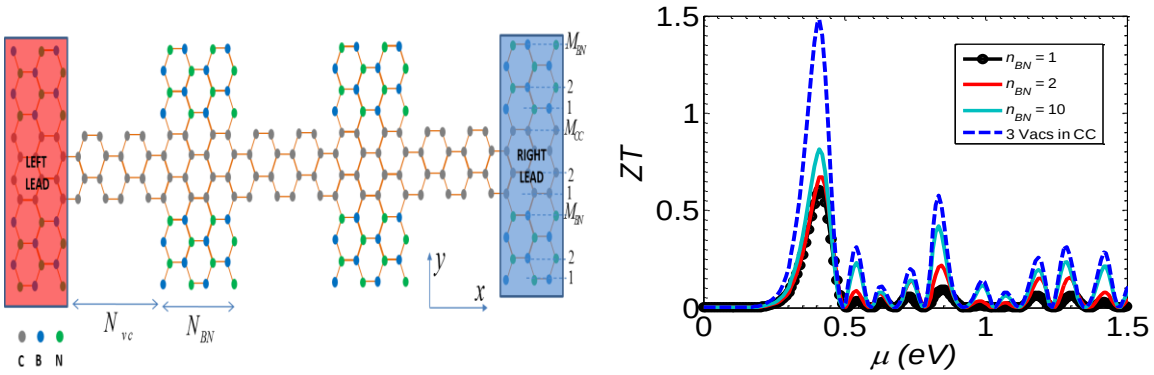

Figure 4: (a) Vue schématique de l'hétérostructure de graphène/BN avec des flocons BN. (b) La figure de mérite thermoélectrique *ZT* en fonction du potentiel chimique μ pour le M_{CC} = 5 et *T* = 300K.

Enfin, une partie de l'étude est consacrée aux conclusions et perspectives. Les principales contributions de ce travail de thèse sont mises en évidence et les futurs travaux possibles sont discutés. Enfin, quatre annexes présentent la méthode numérique de résolution de l'équation de Poisson, les bases du formalisme NEGF pour un système ouvert arbitraire, et le calcul de la formule de transmission. La bibliographie et la liste des publications de l'auteur sont données à la fin du manuscrit.

Introduction

Graphene, a monolayer (two-dimensional) material made of carbon atoms arranged in a honeycomb lattice, is now well-known for its exceptional electronic properties,[1] with gapless and quasi-linear dispersion around the neutrality point and extremely high intrinsic electron mobility.[2] Among many other features, this material also offer outstanding thermal and mechanical properties with very high thermal conductivity[3] and ability to sustain large strain.[4] It is thus expected to give rise to a large number of various applications.[5] The band structure and related properties of Graphene were first studied theoretically by P. R. Wallace since 1947.[6] However, the limitation of experimental techniques at that time did not allow scientists to confirm these fascinating predicted properties. In 2004, Geim and his student Novoselov isolated successfully a stable form of Graphene by exfoliating a single layer of carbon from graphite.[7] This event demonstrated the existence of a two dimensional carbon-based material, which was later named Graphene. Then, Graphene rapidly become a hot research topic in physics from fundamental up to application viewpoints.

Besides its excellent electronic properties, Graphene has some drawbacks which makes it not directly suitable for applications. First, it is impossible to switch off completely the current in devices made of Graphene as Graphene is lacking of a bandgap. Another problem is the growth of Graphene and its deposit on insulating substrates. As an insulator stable at high temperature and easy to process, silicon dioxide (SiO_2) has been frequently used as a substrate for Graphene in experiments and devices. However, as Graphene is very thin, the rough SiO_2 surface causes charge trapping on the surfaces and modifies the planar shape of Graphene,[8,9] which strongly affect the electronic transport in Graphene. Indeed, although the electron mobility in Graphene has theoretically predicted to reach around 200 000 $cm^2 \cdot V^{-1} \cdot s^{-1}$ at room temperature,[5] such a high value has been obtained only for suspended (substrate-free) Graphene.[2] For Graphene on SiO_2, the very best experimental mobility achieved is about 40 000 $cm^2 \cdot V^{-1} \cdot s^{-1}$,[10] but it is usually much below, which is far from the initial expectations. Thus, the choice of substrate is of high importance with a view to reach high performance electronic applications.

Graphene is also expected to be applied in the context of spintronics. Even if the spin orbit coupling in Graphene is very weak and unable to separate spin up and down,[11] in Graphene

ribbons with zigzag edges, it is possible to make spin filters thanks to the separation of spin at low energy edge states.[12,13] However, only extremely narrow zigzag Graphene ribbons are relevant, i.e. ribbons wherein edge states at two sides are close enough to be able to interact.

Regarding thermoelectric properties, Graphene suffers from intrinsic limitations though it has an excellent electron mobility. This is due in particular to the lack of energy gap in 2D Graphene that makes it difficult to separate the opposite contributions of electrons and holes to the Seebeck effect and leads to a very small Seebeck coefficient.[14] Additionally, as mentioned above, the phonon propagation is also confirmed to be very good in Graphene, which is another limitation for thermoelectrics.[3] Indeed, the thermoelectric ability of a material is assessed by the thermoelectric figure of merit *ZT* which is defined via the electrical conductance G_e, the Seebeck coefficient S and the thermal conductance of electron and phonon (K_e and K_p) as $ZT = G_e S^2 T / \left(K_e + K_p\right)$. Hence, with extremely small Seebeck coefficient and very high thermal conductance, 2D Graphene has very small *ZT* which in fact is less than 0.01, while an efficient thermoelectric material needs *ZT*~1. To make Graphene more suitable for thermoelectrics, some strategies of nanostructuring design need to be applied to enhance the Seebeck coefficient and reduce the thermal conductance.

Actually, due to the huge potential of Graphene, scientists have been continually seeking solutions to overcome its limitations. Basically, research on Graphene underwent different periods. Before 2004, just few theoretical works predicted interesting properties of Graphene. After the experimental discovery of Graphene, from 2004 to 2010 most of works were focused on pure Graphene, essentially aiming at opening a band gap by exploiting 1D structures of Graphene (Graphene ribbons),[15–18] on applying perpendicular electric fields in bilayer Graphene.[19] Other physical properties were also investigated such as the quantum Hall effect and the spin interactions.[20–22] In recent years, research activities on Graphene were broadened towards many new directions aiming at finding novel properties for new applications. These researches can be classified into four main research trends:

(i) The study of new effects on Graphene such as (1) doping with atoms such as Boron or Nitrogen into Graphene sheet to open a mini gap[23]; (2) cutting Graphene into Graphene nanomesh with periodic holes in the sheets[24]; (3) Graphene with Hydrogen functionality named as Graphene and graphone[25,26]; (4) using the large spin diffusion length in 2D Graphene to build up ultra-low power non-volatile logic and memory through spin current

processing[27,28]; (5) effect of geometrical shape such as edge roughness, defects, strain or twisted Graphene[29]; (6) enhancement of thermoelectric performance by reducing phonon conductance using sophisticated designs.[30–33]

(ii) The study of heterostructures of Graphene and other materials: (1) opening wider band gap of Graphene with hybrid structures of Graphene/BN[34–37], (2) high quality substrate for Graphene using hexagonal Boron Nitride thank to the perfect match in crystal structures of these two materials and the flatness of h-BN surface [38].

(iii) The study of new properties of Graphene-like materials: some 2D materials have similar structures than Graphene such as MoS_2, SiC, Phosphorene and Silicene but they exhibit intrinsic bandgap and strong spin-orbit coupling.[39]

(iv) The study of new allotropes of carbon structures: these are carbon-based materials which have a slightly different structure like Graphene-like penta-Graphene (pentagonal structures)[40] or Graphyne and graphdiyne with circle structures.[41,42]

Regarding the research trend on Graphene/BN heterostructures, recently experimentalists have successfully demonstrated the synthesis of Graphene/BN structures in a single sheet [43–45], which has motivated some theoretical studies on electronic band structures [34,35,46,47] and also on transport[46,48–51] in this new hybrid material.

In such context, this PhD project has been devoted to the properties of in-plane heterostructures of Graphene/BN with the aim at understanding and improving their electronic and thermoelectric properties with respect to pristine Graphene. It particularly focuses on bandgap opening and transport properties that can be applied in transistors or energy converters. The study is based on semi-empirical methods like Tight Binding (TB) model for electrons and Force Constant (FC) model for phonons. These methods have been widely used in condensed mater physics because of their efficiency in calculation and reasonable computation time. We also use the atomistic non-equilibrium Green's function (NEGF) approach for studying quantum transport as it can be easily combined with the semi-empirical methods mentioned above.

A guiding tour to the thesis:

This thesis manuscript is organized in five chapters and four appendices.

In Chapter 1, I present the theoretical background of my study. First, the empirical methods including Tight Binding and Force Constant models are reviewed. Then, some physical quantities which can be obtained from band structures are introduced. The following section presents atomistic Green's function method and some transport properties that can be computed using this formalism. Next, the electronic and thermal properties of some textbook cases such as the linear chain of atoms, 2D and 1D structures of pristine Graphene and hexagonal Boron Nitride are presented.

In Chapter 2, I present the bandgap opening and its modulation in in-plane Graphene/BN heterostructures. The energy band diagram and bandgap for different configurations of armchair and zigzag Graphene/BN ribbons are investigated using simple Tight Binding calculation based on a first nearest neighbor interaction model. The investigation will help us to understand which configurations of Graphene/BN with a finite bandgap could be interesting for applications.

In chapter 3, I study the effect of an in-plane electric field to energy band of an armchair G/BN structure with two Graphene ribbons separated by a BN ribbon. First, a first simple approach is applied to investigate the effect of an external electric field in different structures including the armchair G/BN and pure armchair Graphene ribbons with the assumption that electrostatic potential in each homogeneous region is linear. Next, I study this effect in the armchair G/BN structure including the effect of charge redistribution by solving self-consistently of the coupled Schrödinger-Poisson equations. The evolution of bandgap with the applied electric field is then applied to control the current in a device made of a hybrid Graphene/BN ribbon.

In chapter 4, I investigate the emergence of states which are localized at the interface of zigzag Graphene/BN heterostructures. These states have peculiar properties which contribute to enhance significantly the electron transport in zigzag Graphene structures. Besides, the parity effect is also investigated to understand transport properties of zigzag Graphene/BN structures.

In chapter 5, I show our proposal of a Graphene/BN heterostructures that exhibit appealing thermoelectric performance. By using an efficient design, in this structure the phonon conductance is strongly reduced with respect to pure Graphene ribbons and a good electrical conductance is kept. The effects of temperature and vacancies on thermoelectric properties are also investigated.

Finally, a section is dedicated to the conclusions and perspectives. The main contributions of this thesis work are emphasized and the related possible future works are discussed. Four appendices (presenting derivations of some important formulas), the bibliography and the list of author's publications can be found at the end of the manuscript.

Chapter 1:

Theoretical Background

In this chapter we intend to review the main theoretical concepts and numerical methods that directly relate to this PhD work. The chapter covers the review of (i) semi-empirical methods including Tight Binding and Force Constant models, (ii) the physical quantities that can be deduced from band structure, (iii) the Green's function formalism of quantum transport for investigating nanostructures. These models and methods are finally applied to investigate some basic electronic and thermal properties of several systems such as linear chain, graphene and Boron Nitride as illustrative examples.

1.1 The semi-empirical methods

Before reviewing the main features of Tight Binding (TB) and Force Constant (FC) models widely used in this work, we would like to discuss the reasons why we chose these semi-empirical methods for our study.

It is well known that ab initio methods are powerful tools to investigate material properties in condensed matter physics because they directly derive from first principles of quantum mechanics, with the highest possible level of accuracy. They usually give very good agreements with experimental results.[52] In spite of their advantage in providing reliable results, the use of these techniques is rapidly limited when dealing with devices of reasonable size as computational costs could easily exceeds the capacity of current computers. In fact, current ab initio methods can only be applied for small systems with limited number of atoms (about a few tens of atoms), while computation of larger systems still faces with many challenges. It is thus required to consider other efficient methods to be able to deal with larger systems of a few hundreds or thousands of atoms.

Tight Binding and Force Constant models are semi-empirical methods that do not require a fully self-consistent process for the computation of electron and phonon dispersions, and thus are much faster compared to ab initio calculations. However, they require the prior knowledge of some given empirical parameters which are called onsite and hopping energies in electron study and force constant parameters in phonon study. These parameters are usually adjusted so that dispersion results from Tight Binding (or Force Constant) simulation fit well with that

of ab initio calculation or experiments.[52–54] With good selected parameters it has been demonstrated that the semi-empirical methods may give good agreements with ab initio and experimental results, especially at low energy [55] or low frequency ranges [54]. Thus Tight Binding and Force Constant models are considered to be useful tools for investigation of large systems, especially in devices, with reasonable computational efforts and time. They are now widely used.

Recently, the combination of ab initio and semi-empirical calculations has led to powerful approaches to study structures and devices at a multi scale level. Within such multi scale methodology, ab initio techniques are first applied to investigate small systems and then to generate parameters for the semi-empirical models such as Tight Binding. The obtained parameters are then used for semi-empirical simulations to study energy bands for larger systems, and can be combined with other quantum methods such as Green's functions or scattering matrix for the study of transport.[56]

1.1.1 Tight Binding model for electron study

The Tight Binding method is widely used by many physicists because it can not only reproduce well results from more complex and accurate methods such as ab initio, but also quickly allows scientists to predict quantitative results on the basis of a simple and physically meaningful model. Great success were evidenced from many works on many materials and devices, including graphene.[6,37,57–61]

The Tight Binding (TB) method is based on the theory of atomic orbitals. The term “tight binding” means that in solids electrons are tightly bound to the atom that they belong to and thus the electrons have limited interactions with surrounding atoms in the solid. Thus the overlap of wave functions between two adjacent atoms is very limited, which makes orbitals in solids close to that in atomic orbitals of free atoms.

Though Tight Binding technique was applied very soon for the study of graphene in 1947 by Wallace,[6] the complete parametrized Tight Binding method was actually generalized by John Clarke Slater in 1954.[62] It is also sometimes known as Linear Combination of Atomistic Orbital (LCAO) method, in particular in chemistry.

Mathematically, Tight Binding calculations can start with a basis consisting of the atomic orbitals of all atoms. In general, a system can contain N atoms and each atom has M orbitals

that conduction electrons can occupy (**Figure 1-1**). To avoid possible confusion due to many indices notations later, we assume for simplicity that each atom contributes one orbital only.

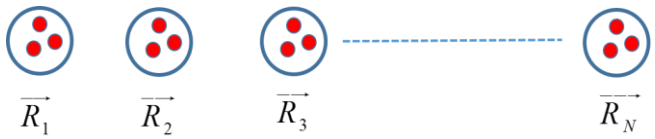

Figure 1-1: A system consists of *N* atoms and in each atom *M* orbitals (sketched by red regions) contribute to conduction.

We denote $\varphi\left(\vec{r}-\vec{R}_i\right)$ the wave function at a given position $\vec{r}$ due to the orbital of *i-th* atom $\left(i=\overline{1,N}\right)$. Quantum mechanics suggests that the general wave function at $\vec{r}$ is a superposition of individual wave functions $\varphi\left(\vec{r}-\vec{R}_i\right)$ and it can be expressed as a linear combination of the atomic orbitals as follows:

$$\Psi\left(\vec{r}\right)=\sum_i c\left(\vec{R}_i\right).\varphi\left(\vec{r}-\vec{R}_i\right) \tag{1-1}$$

The time-independent Schrödinger's equation for the system is:

$$H\Psi\left(\vec{r}\right)=E\Psi\left(\vec{r}\right) \tag{1-2}$$

where

$$H=\sum_i H_{at}\left(\vec{r}-\vec{R}_i\right)+U\left(\vec{r}\right) \tag{1-3}$$

is the Hamiltonian of the system which is assumed to be equal to the total Hamiltonian of isolated atoms plus the interaction potentials between atoms when they are put together within the crystal. Plugging (1-1) into (1-2) we have

$$H\sum_i c\left(\vec{R}_i\right).\varphi\left(\vec{r}-\vec{R}_i\right)=E\sum_i c\left(\vec{R}_i\right).\varphi\left(\vec{r}-\vec{R}_i\right) \tag{1-4}$$

The equation (1-4) can be solved by multiplying both sides of (1-4) by $\varphi^*\left(\vec{r}-\vec{R}_j\right)$ $\left(j=\overline{1,N}\right)$ and then integrating the whole equation in the real space, leading to:

$$\int d\vec{r}.\varphi^*\left(\vec{r}-\vec{R}_j\right)H\sum_i c\left(\vec{R}_i\right).\varphi\left(\vec{r}-\vec{R}_i\right)=\int d\vec{r}.\varphi^*\left(\vec{r}-\vec{R}_j\right)E\sum_i c\left(\vec{R}_i\right).\varphi\left(\vec{r}-\vec{R}_i\right)$$

$$\Leftrightarrow \sum_i\left[\int d\vec{r}.\varphi^*\left(\vec{r}-\vec{R}_j\right)H\varphi\left(\vec{r}-\vec{R}_i\right)\right].c\left(\vec{R}_i\right)=E\sum_i\left[\int d\vec{r}.\varphi^*\left(\vec{r}-\vec{R}_j\right)\varphi\left(\vec{r}-\vec{R}_i\right)\right].c\left(\vec{R}_i\right)$$

$$\Leftrightarrow \sum_i h_{ji}.c\left(\vec{R}_i\right)=E\sum_i s_{ji}.c\left(\vec{R}_i\right) \qquad (1\text{-}5)$$

where $h_{ji}=\int d\vec{r}.\varphi^*\left(\vec{r}-\vec{R}_j\right)H\varphi\left(\vec{r}-\vec{R}_i\right)$ stands for an element of the Hamiltonian and $s_{ji}=\int d\vec{r}.\varphi^*\left(\vec{r}-\vec{R}_j\right)\varphi\left(\vec{r}-\vec{R}_i\right)$ refers to the overlap between two atomic orbitals.

The equation (1-5) is the general equation for the energy bands of the system (no matter the system is finite or infinite). Solving it requires to know the terms h_{ji} and s_{ji}. In principle, for a specific kind of atom the isolated Hamiltonian H_{at} in (1-3) can be determined and thus the atomic orbitals $\varphi\left(\vec{r}-\vec{R}_j\right)$ can also be found from equation: $H_{at}\left(\vec{R}_i\right)\varphi\left(\vec{R}_i\right)=\varepsilon_i\varphi\left(\vec{R}_i\right)$. If the profile of potential between atoms $U\left(\vec{r}\right)$ is known, one has sufficient information to calculate h_{ji} and s_{ji}.

Now we are going to discuss more about the terms h_{ji} which constitute the important terms in the concept of tight binding calculations and will be used frequently later on. Using the form of Hamiltonian (1-3) we have

$$h_{ji}=\int d\vec{r}.\varphi^*\left(\vec{r}-\vec{R}_j\right)H\varphi\left(\vec{r}-\vec{R}_i\right)=\int d\vec{r}.\varphi^*\left(\vec{r}-\vec{R}_j\right)\left[\sum_p H_{at}\left(\vec{r}-\vec{R}_p\right)+U\left(\vec{r}\right)\right]\varphi\left(\vec{r}-\vec{R}_i\right)$$

$$\begin{aligned}\Leftrightarrow h_{ji}&=\sum_p\int d\vec{r}.\varphi^*\left(\vec{r}-\vec{R}_j\right)H_{at}\left(\vec{r}-\vec{R}_p\right)\varphi\left(\vec{r}-\vec{R}_i\right)+\int d\vec{r}.\varphi^*\left(\vec{r}-\vec{R}_j\right)U\left(\vec{r}\right)\varphi\left(\vec{r}-\vec{R}_i\right)\\&=\sum_p\int d\vec{r}.\varphi^*\left(\vec{r}-\vec{R}_j\right)\varepsilon_p.\delta_{pi}.\varphi\left(\vec{r}-\vec{R}_i\right)+\int d\vec{r}.\varphi^*\left(\vec{r}-\vec{R}_j\right)U\left(\vec{r}\right)\varphi\left(\vec{r}-\vec{R}_i\right) \qquad (1\text{-}6)\\&=\varepsilon_i.s_{ji}+t_{ji}\end{aligned}$$

Here $t_{ji}=\int d\vec{r}.\varphi^*\left(\vec{r}-\vec{R}_j\right)U\left(\vec{r}\right)\varphi\left(\vec{r}-\vec{R}_i\right)$ is called bond energy between the orbital of the $j-th$ atom and the orbital of the $i-th$ atom. It is also often called hopping energy in

common Tight Binding models, while ε_i is called on-site energy at the $i-th$ atom. These two parameters are the most important terms in tight binding calculations. Though ε_i and t_{ji} can be found in principle if atomic orbital $\varphi\left(\vec{r}-\vec{R}_j\right)$ and potential $U\left(\vec{r}\right)$ are known, however, in fact the analytical solution for $\varphi\left(\vec{r}-\vec{R}_j\right)$ can be found only for simple atomic configurations such as Hydrogen. In general, it is really difficult to know exactly the form of atomic orbitals and in most of cases, the onsite and hopping energy are parametrized to fit with experimental or ab initio results. For example, in the case of graphene it was found that $\varepsilon_i \approx 0,\ t_{\mathrm{i,i\pm1}} \approx -2.7\left(eV\right)$.[53]

1.1.2 Force Constant model for phonon study

Unlike electrons, phonons are not real particles, but pseudo-particles. They are used formally as quantum elements involved in lattice thermal conduction in solid as we describe electrical conductance by electron transport. The concept of phonon is thus directly related to the vibration modes of atoms in the solid and the thermal conduction results in fact from the transfer of internal energy due to collisions between atoms leading to changes in the vibration modes of atoms.

The vibration of atoms at lattice sites can be described by a Force Constant model in which each pair of atoms is assumed to be linked by a spring (**Figure 1-2**) and interactive force between atoms are dominated by Hooke's law. The theory of Force Constant model was presented in the book "Dynamical theory of crystal lattices" of Born and Huan in 1956, [63] and later developed by Kaplan.[64]

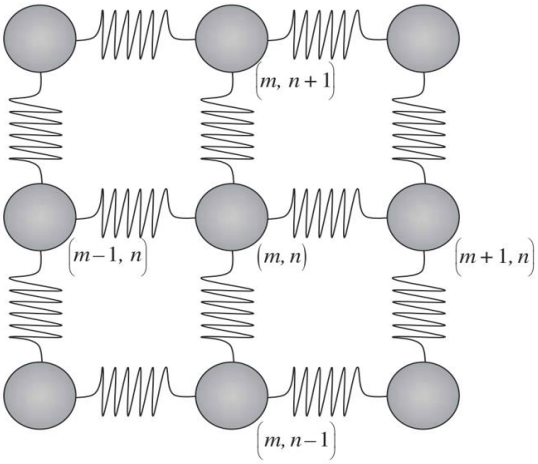

Figure 1-2: Force Constant model with springs connect between atoms. [65]

In general, we can write the motion equation for any atom in the lattice as follows:[66]

$$M_i \frac{d^2 \bar{u}_i}{dt^2} = \sum_{j \neq i} K_{ij} \left(\bar{u}_j - \bar{u}_i \right) \tag{1-7}$$

where M_i and $\bar{u}_i$ are the mass and the time-dependent displacement of the *i*-th atom, respectively, and K_{ij} is the characteristic of the spring connecting the *i*-th and *j*-th atoms. In general, an atom can be subjected to 3D vibrations so K_{ij} are 3×3 tensors and $\bar{u}_i$ are 3×1 column matrices vectors with three spacing components *x, y, z* of displacements.

Vibrations are assumed to be periodic in time, so the Fourier transform can be written for a small time-dependent displacement:

$$\bar{u}_i = u_i . e^{i\omega t} \tag{1-8}$$

where u_i is time-independent part (space part) of the displacement $\bar{u}_i$ and ω is the angular frequency of the atomic vibrations. So equation (1-7) can be rewritten as

$$-\omega^2 M_i u_i = \sum_{j \neq i} K_{ij} \left(u_j - u_i \right)$$

or

$$\omega^2 M_i u_i = \sum_{j \neq i} K_{ij} \left(u_i - u_j \right) \tag{1-9}$$

This equation holds for any atom i $\left(i = \overline{1, N} \right)$. Similarly to equation (1-5), equation (1-9) allows us to find vibration modes ω for any systems. The method for solving (1-5) and (1-9) efficiently will be discussed in next section.

1.1.3 Matrix representation for Tight Binding and Force Constant calculations

It is well known that any system of equations like (1-5) and (1-9) can be transformed into a single matrix equation which is called Secular equation and the problem of solving this matrix equation is addressed as the Eigen value problem. The solutions for E or ω^2 are called Eigen values and the column matrices $c\left(\vec{R}_i\right)$ or u_i are called Eigen vectors.[67]

1.1.3.1 Eigen value problem for electron energy

If we put all terms $\left\{h_{ji}\right\}, \left\{s_{ji}\right\}, \left\{c_i = c\left(\vec{R}_i\right)\right\}$ in the matrix forms

$$H = \left\{h_{ji}\right\} = \begin{array}{c} \\ \boldsymbol{\varphi_1} \\ \boldsymbol{\varphi_2} \\ \cdot \\ \cdot \\ \cdot \\ \boldsymbol{\varphi_N} \end{array} \begin{array}{c} \begin{array}{cccccc} \boldsymbol{\varphi_1} & \boldsymbol{\varphi_2} & \boldsymbol{\varphi_3} & \cdot & \cdot & \boldsymbol{\varphi_N} \end{array} \\ \begin{bmatrix} h_{11} & h_{12} & h_{13} & . & . & . \\ h_{21} & h_{22} & h_{23} & & & \\ . & & & . & & \\ . & & & & & \\ & & & & & \\ & & & & & h_{NN} \end{bmatrix} \end{array},$$

$$S = \left\{s_{ji}\right\} = \begin{array}{c} \\ \boldsymbol{\varphi_1} \\ \boldsymbol{\varphi_2} \\ \cdot \\ \cdot \\ \cdot \\ \boldsymbol{\varphi_N} \end{array} \begin{array}{c} \begin{array}{cccccc} \boldsymbol{\varphi_1} & \boldsymbol{\varphi_2} & \boldsymbol{\varphi_3} & \cdot & \cdot & \boldsymbol{\varphi_N} \end{array} \\ \begin{bmatrix} s_{11} & s_{12} & s_{13} & . & . & . \\ s_{21} & s_{22} & s_{23} & & & \\ . & & & . & & \\ . & & & & & \\ & & & & & \\ & & & & & s_{NN} \end{bmatrix} \end{array}, \quad C = \left\{c_i\right\} = \begin{bmatrix} c_1 \\ c_2 \\ . \\ . \\ . \\ c_N \end{bmatrix} \tag{1-10}$$

The system of equations (1-5) now becomes a matrix equation: [55]

$$H.C = E.S.C \tag{1-11}$$

In most cases, the tight binding approach leads to the conclusion that the overlap matrix S is identical to unity matrix I due to very small overlap of atomic orbitals between two adjacent atoms, i.e. $s_{ji} = \int d\vec{r}.\varphi^*\left(\vec{r} - \vec{R}_j\right)\varphi\left(\vec{r} - \vec{R}_i\right) \approx 0$ for $j \neq i$ and thus only diagonal terms are nonzero $s_{jj} = \int d\vec{r}.\varphi^*\left(\vec{r} - \vec{R}_j\right)\varphi\left(\vec{r} - \vec{R}_j\right) = 1$. Then equation (1-11) is exactly in the form of a secular equation:

$$H.C = E.C \tag{1-12}$$

We can solve this Eigen value problem to find energy dispersion E and vectors C of amplitudes of each state. Even in the case where overlap of orbitals are taken into account, we can still transform (1-11) in the form of a secular equation as: $S^{-1}H.C = E.C \Leftrightarrow H'.C = E.C$.

1.1.3.2 Eigen value problem of vibrant frequency

To get a secular equation for phonons, we need a little more effort compared to the case of electrons. Since M_i in equation (1-9) maybe different for different atoms, to deal with a Hermitian matrix (leading to real Eigen values) we can set $u_i = \frac{A_i}{\sqrt{M_i}}$. This way, $\bar{u}_i$ in (1-8) can be written as $\bar{u}_i = A_i / \sqrt{M_i}.e^{i\omega t}$. Plugging u_i into (1-9) we have

$$\omega^2 M_i \frac{A_i}{\sqrt{M_i}} = \sum_{j \neq i} K_{ij}\left(\frac{A_i}{\sqrt{M_i}} - \frac{A_j}{\sqrt{M_j}}\right)$$

$$\Leftrightarrow \omega^2 A_i = \sum_{j \neq i} \frac{K_{ij}}{M_i} A_i - \sum_{j \neq i} \frac{K_{ij}}{\sqrt{M_i M_j}} A_j \tag{1-13}$$

Equation (1-13) is for the single *i-th* atom $\left(i = \overline{1, N}\right)$. By considering all atoms in the system and all equations can be gathered in a matrix equation as

$$\omega^2 U = DU \tag{1-14}$$

$$\text{Where } U=\begin{bmatrix} A_1 \\ A_2 \\ . \\ . \\ . \\ A_N \end{bmatrix},\ D=\begin{bmatrix} \sum_{j\neq 1}\frac{K_{1j}}{M_1} & -\frac{K_{12}}{\sqrt{M_1M_2}} & -\frac{K_{13}}{\sqrt{M_1M_3}} & . & . & . \\ -\frac{K_{21}}{\sqrt{M_2M_1}} & \sum_{j\neq 2}\frac{K_{2j}}{M_2} & & & & \\ -\frac{K_{31}}{\sqrt{M_3M_1}} & & . & & & \\ . & & & . & & \\ . & & & & . & \\ . & & & & & \sum_{j\neq N}\frac{K_{Nj}}{M_N} \end{bmatrix} \quad (1\text{-}15)$$

D refers to the Dynamical matrix which involves all couplings between atoms in the system. Noting that in general case (3D vibration in real space), $\bar{u}_i\left(A_i\right)$ is a 3×1 column matrix vector, K_{ij} is a 3×3 matrix, so the full size of U is $3N$×1 and D is $3N$×$3N$. Equation (1-14) is completely solved if the matrix D is known. In fact, we still need one more step to calculate D. The coupling tensor K_{ij} between the i-th and j-th atoms is defined by using a unitary rotation in the plane of the mono-layer material

$$K_{ij}=U^{-1}\left(\theta_{ij}\right)K^0{}_{ij}U\left(\theta_{ij}\right) \quad (1\text{-}16)$$

where $U\left(\theta_{ij}\right)=\begin{bmatrix} \cos\left(\theta_{ij}\right) & \sin\left(\theta_{ij}\right) & 0 \\ -\sin\left(\theta_{ij}\right) & \cos\left(\theta_{ij}\right) & 0 \\ 0 & 0 & 1 \end{bmatrix}$ is the rotation matrix [66] and θ_{ij} is the anticlockwise rotating angle formed between the positive direction of the x-axis and the vector joining the i-th to the j-th atoms. Finally, $K^0{}_{ij}$ is the force constant tensor given by

$$K^0{}_{ij}=\begin{pmatrix} \Phi_r & 0 & 0 \\ 0 & \Phi_{t_i} & 0 \\ 0 & 0 & \Phi_{t_o} \end{pmatrix} \quad (1\text{-}17)$$

where $\Phi_r, \Phi_{t_i}, \text{and}\,\Phi_{t_o}$ are the force constant coupling parameters in the radial, in-plane and out-of-plane directions, respectively (See **Figure 1-3**), depending on the level of neighboring.

In Force Constant models Φ_r, Φ_{t_i}, and Φ_{t_o} are given so we can know $K^0{}_{ij}$ and thus we are able to calculate K_{ij} from equation (1-16) and then the Dynamical matrix *D* in (1-15).

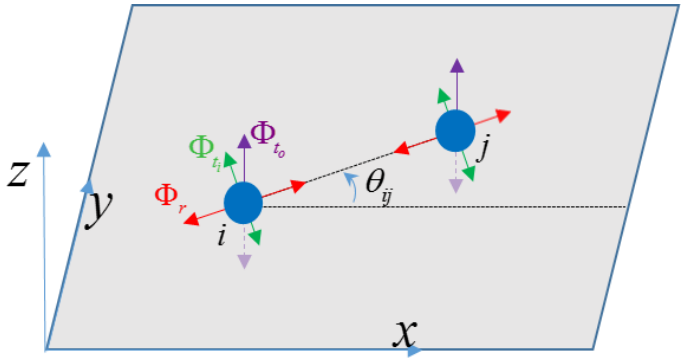

Figure 1-3: Schematic view of vibration directions of each atom in a plan *xoy* and the rotational angle from *i-th* atom to *j-th* atom.

1.1.3.3 Advantage of matrix representations:

We have derived problems of both electron energy and vibration modes into the same problem of solving eigen values and Eigen vectors. The matrix representation thus has a strong advantage for solving these different problems. First, the matrix form of the Hamiltonians *H* (1-10) and *D* (1-15) shows clearly the physics picture of interactions between atoms in the systems. Second and most important, this representation is very convenient from the numerical point of view because we deal with discrete data instead of continuous variables as in common mathematical formulas. Each matrix element is easily managed as a discrete data in numerical calculations. Because of these advantages the matrix representation will be used in most parts of the thesis.

1.1.4 Operator form of Tight Binding Hamiltonian

1.1.4.1 Tight Binding Hamiltonian in the form of Ket-Bra vectors

Since Pauli introduced the notations of Ket $|\ \rangle$ and Bra $\langle\ |$ vectors as column and row matrices in 1939,[68] they have been widely used in quantum mechanics and extended for more convenient calculations. Each state $\varphi\left(\vec{r}-\vec{R}_j\right)$ can be denoted by a Ket vector $|\varphi_j\rangle$ in

Hilbert space (space of state vectors) and a corresponding Bra $\langle\varphi_j|$. The integral of $\varphi^*\left(\vec{r}-\vec{R}_j\right)\varphi\left(\vec{r}-\vec{R}_i\right)$ over the full space can be simply noted as

$$\int d\vec{r}.\varphi^*\left(\vec{r}-\vec{R}_j\right)\varphi\left(\vec{r}-\vec{R}_i\right)=\langle\varphi_j|\varphi_i\rangle=\delta_{ji} \tag{1-18}$$

Here we assume that the overlap between orbitals is negligible. Any Ket vector of the general wave function (1-1) can be expanded as

$$|\Psi\rangle=\sum_i c_i.|\varphi_i\rangle \tag{1-19}$$

and for any operator *X* we have $\int d\vec{r}.\Psi^*\left(\vec{r}\right)X\Psi\left(\vec{r}\right)=\langle\Psi|X|\Psi\rangle$

Thus the element h_{ji} of the matrix form of the Hamiltonian *H* can be written as

$$h_{ji}=\int d\vec{r}.\varphi^*\left(\vec{r}-\vec{R}_j\right)H\varphi\left(\vec{r}-\vec{R}_i\right)=\langle\varphi_j|H|\varphi_i\rangle \tag{1-20}$$

If we define the operator form of the Hamiltonian *H* as

$$H=\sum_i \varepsilon_i.|\varphi_i\rangle\langle\varphi_i|+\sum_{j\neq i} t_{ji}|\varphi_j\rangle\langle\varphi_i| \tag{1-21}$$

we can rewrite the matrix element h_{ji} in (1-6) by just simply using (1-20) and (1-21). Indeed

$$\begin{aligned}
h_{ji}&=\langle\varphi_j|H|\varphi_i\rangle=\langle\varphi_j|\left\{\sum_p \varepsilon_p.|\varphi_p\rangle\langle\varphi_p|+\sum_{h\neq p} t_{hp}|\varphi_h\rangle\langle\varphi_p|\right\}|\varphi_i\rangle\\
&=\sum_p \varepsilon_p.\delta_{jp}.\delta_{pi}+\sum_{h\neq p} t_{hp}.\delta_{jh}.\delta_{pi}\\
&=\varepsilon_i.\delta_{ji}+t_{ji}
\end{aligned}$$

The operator form of Hamiltonian (1-21) expressed in Ket and Bra vectors is widely used by many authors. [37,58,69–72]

1.1.4.2 Tight Binding in second quantization form

In many lectures, one also uses the operator form of Tight Binding Hamiltonian within the formalism of second quantization.[1,73–76] Here we do not intend to review the detail of second quantization theory but we try to make a link between Tight Binding and second quantization. In second quantization, physics of parameters of Tight Binding becomes clearer thanks to the concept of annihilation and creation of particles. The term "hoping parameter" t_{ji} can be understood as follows: though an electron can be bounded tightly to the atom to which it belongs by potential barriers between atoms, it is still possible for the electron to tunnel through the barrier potential and hop (jump) from a lattice site to another with a none zero probability. The tunneling effect is associated with an energy changes equal to t_{ji}. This event is equivalent to the annihilation of an electron at $j-th$ site and the concomitant creation of an electron at $i-th$ site. We can thus write the Hamiltonian as:

$$H = \sum_i \varepsilon_i . a^\dagger{}_i a_i + \sum_{j \neq i} t_{ji} a^\dagger{}_i a_j \tag{1-22}$$

where $a^\dagger$, a are called creation and annihilation operators, respectively. This second quantization picture also allows us to predict that hoping energy tends to decrease when increasing the distance between two atoms (because hopping is harder).[55]

1.1.5 Eigen value problem for infinite periodic structures

It is natural to ask the question of how to deal with Eigen value problem for very large or infinite structures, because the matrix size of Hamiltonian (1-10) and (1-15) becomes so large that it is impossible to solve the full system. The answer is yes, we can do it if the structures are periodic. In the case of a structure consisting in the repetition of periodical unit cells, we can even reduce the Hamiltonian matrix to the size of one unit cell, which makes the problem much easier to solve.

Now we assume that there is *P* atoms in a unit cell, we can thus divide index *i* (*i=1, N* where *N* is the total number of atoms in the system) in (1-1) or (1-19) into two indices: small letters *n(m)=1:P* is the index of an atom in one cell and Greek symbols $\alpha(\beta)$ as the index of unit cell in the system (*P* × (number of unit cells) = *N*). Since the structure is periodic, the wave function must be a Bloch wave function, i.e.

$$\Psi\left(\vec{r}\right)=\sum_{\alpha=1}^{\infty}\sum_{n}^{P}c_n.\mathrm{e}^{i\vec{k}.\vec{R}_\alpha}.\varphi_\alpha\left(\vec{r}-\vec{R}_n\right) \tag{1-23}$$

It means $c_{n,\alpha}=c_n.\mathrm{e}^{i\vec{k}.\vec{R}_\alpha}$. So if we define $\phi_\alpha=\left\{c_{n,\alpha}\right\}=\begin{bmatrix}c_1 & c_2 & . & . & . & c_P\end{bmatrix}^T.\mathrm{e}^{i\vec{k}.\vec{R}_\alpha}=\phi_0.\mathrm{e}^{i\vec{k}.\vec{R}_\alpha}$ from the set of coefficients of the wave function in one unit cell, the Hamiltonian *H* and matrix *C* in (1-10) become:

$$H=\begin{bmatrix}H_{11} & H_{12} & H_{13} & . & . & . \\ H_{21} & H_{22} & H_{23} & & & \\ . & & & . & & \\ . & & & & & \\ & & & & & \\ & & & & & .\end{bmatrix},\ \text{and}\ C=\begin{bmatrix}\phi_1\\ \phi_2\\ \phi_3\\ .\\ .\\ .\end{bmatrix}$$

where $H_{\alpha\alpha}$ is the matrix of the $\alpha-th$ unit cell and $H_{\alpha\beta}$ is the coupling matrix of unit cells $\alpha-th$ and $\beta-th$. Taking an arbitrary row of *H* and multiplying by *C* as in equation (1-12) we have

$$\begin{aligned}&\sum_{\beta}H_{\alpha\beta}.\phi_\beta=E\phi_\alpha\\ \Leftrightarrow&\sum_{\beta}H_{\alpha\beta}.\phi_0.\mathrm{e}^{i\vec{k}.\vec{R}_\beta}=E\phi_0.\mathrm{e}^{i\vec{k}.\vec{R}_\alpha}\\ \Leftrightarrow&\sum_{\beta}H_{\alpha\beta}.\phi_0.\mathrm{e}^{i\vec{k}.\left(\vec{R}_\beta-\vec{R}_\alpha\right)}=E\phi_0\end{aligned}$$

$$\left[H_{\alpha\alpha}+\sum_{\beta\neq\alpha}H_{\alpha\beta}.\mathrm{e}^{i\vec{k}.\left(\vec{R}_\beta-\vec{R}_\alpha\right)}\right]\phi_0=E\phi_0 \tag{1-24}$$

Thus the equation (1-12) for the whole system has been reduced to the equation (1-24) for only one unit cell (hold for an arbitrary α) with the size of matrix equal to *P*×*P* that is usually easy to solve. For phonons we can obtain a similar equation by just replacing $H_{\alpha\beta}$ by $D_{\alpha\beta}$. Equation (1-24) is the general equation to be solved to calculate the dispersion as a function of momentum *k* for any periodic structures. Noting that if we do not choose the wave function of two unit cells differing by a plane wave as (1-23), but for each kind of atom as suggested in some papers [55,77,78], we can not go to the equation (1-24). However the solutions of Eigen

values are the same. The detailed discussion about the choice of wave form was reported in ref. [79].

1.2 Physical quantities that can be obtained from band structure

Solving an Eigen value problem has become a standard in condensed matter physics for understanding properties of a materials. Which physical quantities can we know from band structure (Eigen values) and wave vectors? Here, we are going to review some basic quantities that are usually deduced from solutions of an Eigen problem.

1.2.1 Bandgap

A bandgap is a forbidden energy region that no electron is allowed to occupy. It means there is no available state in the bandgap. The bandgap is a criterion for classifying a material as metallic, semiconducting or insulating (see **Figure 1-4**).

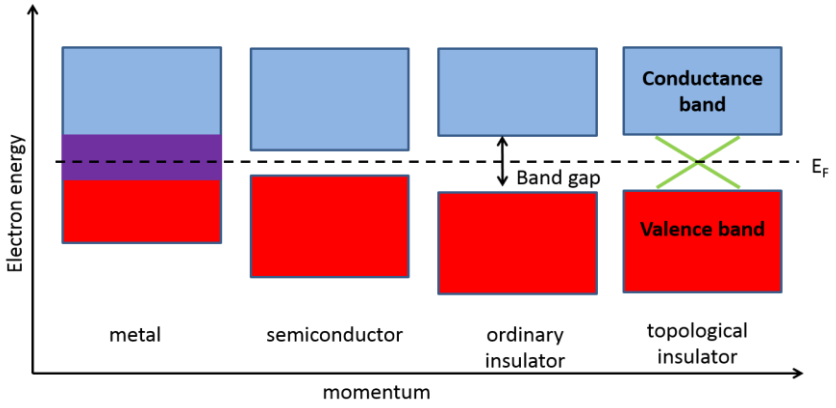

Figure 1-4: Diagram of energy bands in a solid body for different phases.

From the energy band obtained by solving equation (1-24), we can separate upper (conduction) bands and lower (valence) bands with respect to the Fermi level, and the bandgap can be determined as the difference between the lowest conduction energy and the highest valence energy.

$$E_{\text{gap}} = \min\left(E_{\text{conduction}}\right) - \max\left(E_{\text{valence}}\right) \tag{1-25}$$

1.2.2 Density of states and local density of states

The density of state (DOS) is defined as the number of states per unit of energy and per unit of volume (so unit of DOS is usually 1/eV/atom or 1/eV/unit cell or $1/eV/m^3$).[80] While local density of state (LDOS) can be understood as DOS at a specific position in the space.

DOS and LDOS are calculated as:

(i) DOS:

$$D(E) = \frac{dN(E)}{dE} = \sum_n \delta(E - E_n) \tag{1-26}$$

where $N(E)$ is the number of states between energies E and $E + dE$ in a specific volume.

(ii) LDOS:

$$D(E, \vec{r}) = \sum_n \left|\Phi_n(\vec{r})\right|^2 .\delta(E - E_n) \tag{1-27}$$

The sum is taken over all possible states in the system.

Noting that DOS and LDOS for phonons are calculated with the same formulas by taking phonon energy $E_n = \hbar\omega_n$ and $\Phi_n(\vec{r})$ is the vibration matrix vector.

1.2.3 Electron and hole distributions

If the wave function helps us to understand the distribution of each state in real space, the total number of electrons or holes distributed in real space can be calculated by[80]:

$$\mathrm{n}_h(\vec{r}) = 2. \sum_{\text{all states in valence bands}} \left[1 - f(E_v - E_F)\right].\left|\phi_v(\vec{r})\right|^2 \tag{1-28}$$

And $$\mathrm{n}_e(\vec{r}) = 2. \sum_{\text{all states in conduction band}} f(E_c - E_F).\left|\phi_c(\vec{r})\right|^2 \tag{1-29}$$

Here $E_v, \phi_v(\vec{r})$ and $E_c, \phi_c(\vec{r})$ refer to valence and conduction states, respectively.

1.2.4 Group velocity

The group velocity indicates how fast an electron can propagate in the channel. This *k*-dependent velocity contributes to drift velocity of electrons. It is fully related to the shape of each energy band and can be calculated as [80]

$$v_{x(y)} = \frac{1}{\hbar}\frac{\partial E_n}{\partial k_{x(y)}} \tag{1-30}$$

It is thus proportional to the slope of the band. We can also calculate the group velocity from the Hamiltonian and the wave functions via the group velocity operator defined by:

$$\hat{v}_x = \frac{1}{\hbar}\frac{\partial H}{\partial k_x} \tag{1-31}$$

For example, if we only have couplings between nearest neighbor unit cells, we have from (1-24)

$$H = H_{nn} + H_{n,n-1}e^{-ik_x a_x} + H_{n,n+1}e^{ik_x a_x}$$

Where a_x is the periodic lattice constant along x direction. So

$$\hat{v}_x = \frac{1}{\hbar}\frac{\partial}{\partial k_x}\left\{H_{nn} + H_{n,n-1}e^{-ik_x a_x} + H_{n,n+1}e^{ik_x a_x}\right\} = \frac{ia_x}{\hbar}.\left[H_{n,n+1}e^{ik_x a_x} - H_{n,n-1}e^{-ik_x a_x}\right]$$

When we solve the equation (1-24) we obtain E and ϕ_0, then the group velocity can be computed as

$$v_x = \langle \phi_0 | \hat{v}_x | \phi_0 \rangle = \phi_0^{\dagger}\hat{v}_x\phi_0 \tag{1-32}$$

1.2.5 Effective mass

In many cases, we are only interested in low energy region and we can use an effective mass model to simplify the Hamiltonian and energy dispersion. The effective mass along x direction is calculated from the band structure as follows [80]

$$m_x = \hbar^2 / \left(\frac{\partial^2 E}{\partial k_x{}^2} \right) \tag{1-33}$$

Since an energy band is usually not exactly parabolic, effective mass is only evaluated around the bottom of valleys energy, for instant around the Gamma point k = 0. Effective mass and group velocity are in an inverse ratio relationship, which means that electrons have small group velocity if the effective mass is heavy and vice versa. From energy obtained by from (1-24), we can apply a discrete form of the second derivative to calculate the effective mass as

$$\left. \frac{\partial^2 E}{\partial k_x{}^2} \right|_{k_{x,i}} = \frac{\dfrac{E_{i+1} - E_i}{\Delta k_x} - \dfrac{E_i - E_{i-1}}{\Delta k_x}}{\Delta k_x} = \frac{E_{i+1} - 2E_i + E_{i-1}}{\left(\Delta k_x\right)^2}, \tag{1-34}$$

where E_i (or we can use notation $E(i)$) is the energy data corresponds to the momentum $k_x(i)$.

1.3 Coupled Schrödinger -Poisson's equations

Though Tight Binding equation (1-24) does not require a self-consistent numerical scheme, however, if the system is under the effect of electric field, a charge redistribution may be generated (screening effect) and the potential energy in the system must be reconsidered. This requires to solve the coupled Poisson's and Schrödinger's equations to know exactly the potential profile and energy bands in the system, i.e.

$$\begin{cases} \nabla\left(\varepsilon \nabla V\right) = -\dfrac{\rho}{\varepsilon_0} \\ \left[H_0 + U\right]\phi_0 = E\phi_0 \end{cases} \tag{1-35}$$

The first equation linking charge and potential (Voltage) is the Poisson's equation in which ε is the relative permittivity of the material. This parameter may be space-dependent. The quantity $\rho = \rho_e + \rho_h$ is the total charge in the system, with here $\rho_e\left(\vec{r}\right) = -e.n_e\left(\vec{r}\right)$, $\rho_h\left(\vec{r}\right) = e.n_h\left(\vec{r}\right)$ are charge density of electron (negative carriers) and hole (positive carriers), respectively. The resulting potential V will be used to calculate the potential energy $U = -eV$ for Schrödinger's equation. The solution of wave functions is used

to calculate charge density using formulas (1-28), (1-29) and put back into the Poisson's equation to solve a new potential. The process is repeated until the convergence of potential is reached.

For simple case of 1D problems, the Poisson's equation can be written as

$$\frac{d}{dx}\left(\varepsilon(x).\frac{d}{dx}V\right)=-\frac{\rho(x)}{\varepsilon_0}$$

$$\frac{d\varepsilon(x)}{dx}.\frac{dV(x)}{dx}+\varepsilon(x).\frac{d^2V(x)}{dx^2}=-\frac{\rho(x)}{\varepsilon_0} \tag{1-36}$$

Equation (1-36) can be solved numerically for any form of $\varepsilon(x)$ and $\rho(x)$. See the details in Appendix A.

1.4 Green's function method

1.4.1 General definition of a Green's function

If we have a linear differential equation

$$Ly(x)=f(x) \tag{1-37}$$

where L is an operator, the Green's function corresponding to this operator is defined as

$$LG(x,x')=\delta(x-x') \tag{1-38}$$

It is easy to transform (1-37) into

$$y(x)=\int_a^b G(x,x').f(x').dx' \tag{1-39}$$

Hence, to solve the differential equation (1-37), we just need to solve equation (1-38) and to use the Green's function $G(x,x')$ to calculate the solution $y(x)$. There are two advantages in using the Green's function via (1-38) and (1-39) compared to equation (1-37): (i) solving the differential equation (1-38) is in principle easier compared to the equation (1-37) because it

does not include $y(x)$ and $f(x)$ but only depends on the form of the operator L; additionally, the same solution $G(x,x')$ of (1-38) can be used to solve different equations (1-37) with different $y(x)$ and $f(x)$; (ii) for all different equations (1-37) it is possible to use a standard method for calculating $y(x)$ by equation (1-39).

1.4.2 Green's function in Physics. Atomistic Green's function

The Green's functions have been widely used in physics, for instance to solve Poisson's equation or Schrödinger's equation, and it has different physical meanings depending on the context. In electrostatics, the Green's function is defined as the electrostatic potential caused by a point charge. In this present work, we will consider mainly the Green's function which relates to the Hamiltonian of Schrödinger's equation.

Starting from Schrödinger's equation, we have

$$\left(E-H\right)\left|\Psi\right\rangle = 0$$

According to the definition of Green's function, the operator $\left(E-H\right)$ can be associated with a Green's function defined by

$$\left(E-H\right)G\left(\vec{r},\vec{r}';E\right)=\delta\left(\vec{r}-\vec{r}'\right) \tag{1-40}$$

Taking advantage of the matrix representation in which the Hamiltonian is already constructed as in (1-10) and (1-15), we can definite a matrix form for the Green's function as

$$\left(E-H\right)G\left(E\right)=I \text{ Or } G\left(E\right)=\left(E-H\right)^{-1} \tag{1-41}$$

Since *H* is the matrix formed from the interactions between atoms in the system, it can be called atomistic Hamiltonian and the Green's function defined by (1-41) is then called atomistic Green's function.

1.4.3 Green's functions for an open system

In most transport problems, we have a region called active region (device or scattering region) connected with two leads, i.e. left and right leads. The active region can be considered as an open system that exchanges energy with the two leads. To calculate exactly the amount of the energy exchanged between the active region and the other parts, let us consider a general case where we have initially an isolated system denoted X, and then a part A attached to the system X as in **Figure 1-5**.

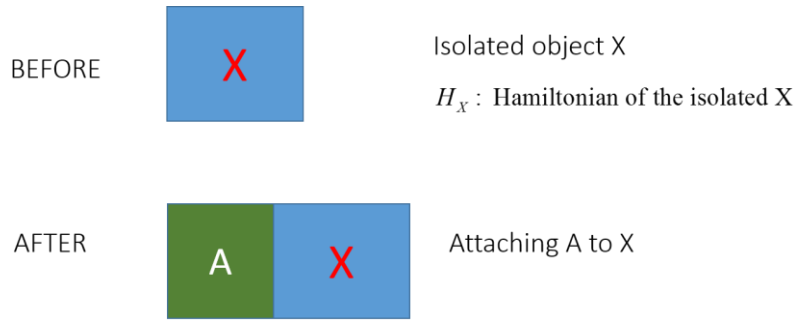

Figure 1-5: Exchanged energy in an open system X when it is connected to another system A.

The Hamiltonian of the whole system can be written in the matrix form $H = \begin{pmatrix} H_A & \tau_{AX} \\ \tau_{XA} & H_X \end{pmatrix}$.

Starting with Schrödinger's equation for the whole system, we can get the Green's function of the part X as: (see Appendix B)

$$G_X = \left(E - H_X - \tau_{XA} g_A \tau_{AX}\right)^{-1} = \left(E - H_X - \Sigma_A\right)^{-1} \tag{1-42}$$

Where

$$g_A = \left(E - H_A\right)^{-1} \tag{1-43}$$

is the isolated Green's function of part A, and

$$\Sigma_A = \tau_{XA} g_A \tau_{AX} \tag{1-44}$$

Compared to the Green's function $g_X = (E - H_X)^{-1}$ of the isolated Hamiltonian of X we can see that there is an extra part Σ_A added into the Hamiltonian H_X in (1-42). This part is called self-energy of X due to coupling with the part A. The result can be extended for the case with *N* external parts connected to the system X with the assumption that these attached parts do not interact together but only interact with the open system X. For example, in the case of an active region (open system X) connected with two leads, the Green's function of the active region is now

$$G_D = (E - H_D - \Sigma_L - \Sigma_R)^{-1} \tag{1-45}$$

where H_D is the Hamiltonian of the active region (Device) and $\Sigma_{L(R)} = \tau_{DL(R)} g_{L(R)} \tau_{L(R)D}$ is the self-energy due to the left (right) contact.

The equation (1-45) is very important and general for any open system. It can be also applied to calculate the surface Green's function $G^0{}_{L(R)}$ and to reduce the size of the Device Green's function G_D by the so-called recursive technique.

1.4.4 Calculation of DOS by Green function

The DOS calculated by (1-26) can be calculated via the Green's function thank to the Lorentz form of delta function as

$$D(E) = \sum_n \delta(E - E_n) = \lim_{\eta \to 0} \sum_n \frac{1}{\pi} . \frac{\eta}{(E - E_n)^2 + \eta^2} \tag{1-46}$$

where η is a very small number (some time it is noted as 0^+) and it has physical meaning of a broadening energy to avoid divergence when $E = E_n$.

If we use the Eigen vectors of the Hamiltonian *H* as basis, the Green's function defined by $G(E) = (E + i\eta - H)^{-1}$ contains the diagonal terms

$$G(E)=\begin{pmatrix} \dfrac{1}{E+i\eta-\varepsilon_1} & & & \\ & \dfrac{1}{E+i\eta-\varepsilon_2} & & \\ & & . & \\ & & & \dfrac{1}{E+i\eta-\varepsilon_N} \end{pmatrix} \tag{1-47}$$

Noting that $G_{nn}-G^{\dagger}{}_{nn}=\dfrac{1}{E+i\eta-\varepsilon_n}-\dfrac{1}{E-i\eta-\varepsilon_n}=\dfrac{-2i\eta}{(E-\varepsilon_n)^2+\eta^2}$ is close to the Lorentz form of delta function, the DOS can be thus calculated from the diagonal elements G_{nn} of the Green's function as follows:

If we define

$$A=i\left[G-G^{\dagger}\right] \tag{1-48}$$

Which is called spectral function, we have

$$trace(A)=i.trace\left[G-G^{\dagger}\right]=\sum_n \frac{2\eta}{(E-\varepsilon_n)^2+\eta^2}$$

Comparing with (1-46) we have finally

$$D(E)=\frac{trace(A)}{2\pi} \tag{1-49}$$

1.5 Physical quantities obtained from transport study

In this section we will consider the most important quantities/formulas in a quantum transport problem using Green's function formalism.

1.5.1 Calculation of the Transmission from Green's function

In ballistic regime, the transmission of the system can be calculated via the Green's function by Meir-Wingreen's formula [80–82]

$$T = trace\left[\Gamma_L G_D \Gamma_R G^{\dagger}{}_D\right] \tag{1-50}$$

where $$\Gamma_{L(R)} = i\left[\Sigma_{L(R)} - \Sigma_{L(R)}{}^{\dagger}\right] \tag{1-51}$$

are the injection rates at the contacts.[80]

Though formula (1-50) is the standard one for calculation of transmission, but the use of it is not very useful in practice because the size of the matrix H_D is very large and thus it is very difficult to make the inversion (1-42). The transmission can be calculated efficiently when different techniques are applied to reduce the size the left(right) Green's function and of the device Green's function to the size of the Green's function of single layers at interface of the device and of the contacts.[83] Then the transmission can be calculated as (see Appendix C)

$$T = \mathrm{Tr}\left\{\Gamma_L^s\left[i\left(G_{11} - G_{11}{}^{\dagger}\right) - G_{11}\Gamma_L^s G_{11}{}^{\dagger}\right]\right\} \tag{1-52}$$

Here $\Gamma_{L(R)}^s = i\left(\Sigma_{L(R)}^s - \Sigma_{L(R)}^s{}^{\dagger}\right)$ is the surface injection rate at the left (right) contact, and $\Sigma_{L(R)}^s = \tau_{DL(R)} G^0{}_{L(R)} \tau_{L(R)D}$ where G^0 is the surface Green's function of contacts.

1.5.2 Local density of states

LDOS is very important in transport because it is associated with energy levels localized in the scattering region and especially important in resonance effects where each peak of transmission is corresponding to a confined state in the scattering region that can be observed clearly via LDOS spectrum. The LDOS at the position of *i-th* layer in the device can also be calculated via Green's function as in (1-49), but now the Green function is the device Green's function G_D (for convenience, we just simply note it as G) and the corresponding spectral function of *i*-th layer is $A_{ii} = i\left[G_{ii} - G_{ii}{}^{\dagger}\right]$. It is thus

$$D_{ii}(E) = \frac{trace(A_{ii})}{2\pi} \tag{1-53}$$

By noting that $A_{ii} = i\left[G_{ii} - G_{ii}{}^{\dagger}\right] = -2\,\mathrm{Im}\left(G_{ii}\right)$ with $\mathrm{Im}\left(G_{ii}\right)$ is the imaginary part of G_{ii} we can also make a direct relation between LDOS and Green's functions as below

$$D_{ii}(E) = -trace\left[\frac{\mathrm{Im}(G_{ii})}{\pi}\right] \tag{1-54}$$

1.5.3 Electron current

When a bias is applied at source and drain, an electric field is generated along the transport direction and drives carriers in the channel. A flow of current in the device can be measured. The total current in ballistic regime can be calculated by Landauer's formula [80]

$$I = \frac{2e}{h}\int_{-\infty}^{+\infty} dE.T(E)\left[f_L(E-\mu_L) - f_R(E-\mu_R)\right], \tag{1-55}$$

where $f(E,\mu,T) = 1/\left(1+e^{\frac{E-\mu}{K_bT}}\right)$ is the Fermi function giving the distribution of electrons around the chemical energy μ. And $\mu_R = E_{F_R} + U_R$, $\mu_L = E_{F_L} + U_L$, $U_L - U_R = qV_b$ where E_{F_L} and E_{F_R} are the Fermi energies in Source (left) and Drain (right). Usually, we choose $U_L = 0$ and $U_R = -eV_b$ or $U_L = eV_b/2$ and $U_R = -eV_b/2$

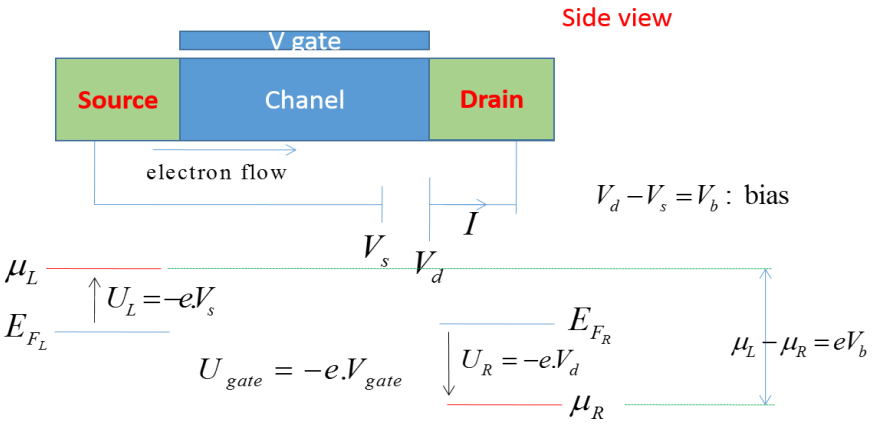

Figure 1-6: Electron current in the device under a bias.

At zero Kelvin we can simplify (1-55) thank to the convergence of Fermi's function

$$f\left(E-\mu\right)=\frac{1}{1+e^{\frac{E-\mu}{K_bT}}}=\begin{cases}0 \text{ if } E>\mu \text{ due to } e^{\frac{E-\mu}{K_bT}}\to\infty \text{ when } T\to 0\\ 1 \text{ if } E<\mu \text{ due to } e^{\frac{E-\mu}{K_bT}}\to 0 \text{ when } T\to 0\\ \frac{1}{2} \text{ if } E=\mu\end{cases}$$

Thus,

$$f_L\left(E-\mu_L\right)-f_R\left(E-\mu_R\right)=\begin{cases}0 \text{ if E}>\mu_L \text{ or E}<\mu_R\\ 1 \text{ if } \mu_R<\text{E}<\mu_L\end{cases} \tag{1-56}$$

And the current can be computed simply from the integral of transmission as

$$I=\frac{2e}{h}\int_{\mu_R}^{\mu_L} dE.T\left(E\right) \tag{1-57}$$

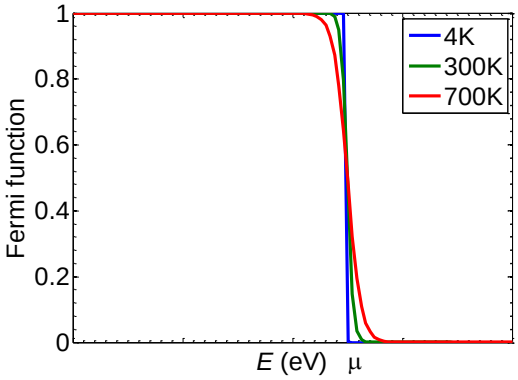

Figure 1-7: Fermi function as a function of energy for different temperatures from very low (4 K) to room temperature (300 K) and high temperature (700 K).

1.5.4 Conductance

The electronic conductance is usually defined at low bias and in ballistic regime it can be calculated by Landauer's formula [80]

$$G_e(\mu,T)=\lim_{V_b\to 0}\frac{I}{V_b}=\frac{2e^2}{h}\int_{-\infty}^{+\infty}dE.T_e(E).\frac{-\partial f(E,\mu,T)}{\partial E} \quad (1\text{-}58)$$

Where $T_e(E)$ is the transmission of electrons and $f(E,\mu,T)$ is the Fermi function.

Unlike electrons, phonons are classified as boson particles and they are governed by the Bose-Einstein's distribution function $n=1/\left(e^{\hbar\omega/K_bT}-1\right)$. The phonon conductance is calculated by [84]

$$K_p=\int_0^{\infty}\frac{d\omega}{2\pi}.\hbar\omega.\mathrm{T_p}(\omega).\frac{\partial n}{\partial T} \quad (1\text{-}59)$$

Where $\mathrm{T_p}(\omega)$ is the phonon transmission.

1.5.5 Thermoelectric effects

In an electronic system (and in any system), efficiency of energy conversion between power in and power out never reaches 100%. In fact, a large portion of energy is lost due to heating into the air. So it is natural to wonder how to convert some wasted heat energy into useful energy such as electrical energy. One of the first phenomenon of conversion between heat and electricity was observed by Seebeck in 1821 when he discovered deflection of a compass needle placed nearby a close lop of two different metals with different temperatures at the two junctions. Later on, in 1934 Peltier discovered an opposite phenomenon when a current goes through a junction of two different conductors it can generate or remove heat at the junction. Since 1950s, scientists have developed techniques to convert in practice some waste heating energy into electricity and the field of energy conversion between heat and electric energy is named as thermoelectrics.

The thermoelectric efficiency of a material is assessed by a coefficient called figure of merit *ZT* which is defined as

$$ZT=\frac{G_eS^2}{K_e+K_p}T \quad (1\text{-}60)$$

where T is the absolute temperature, G_e, S, K_e and K_p are the electrical conductance, the Seebeck coefficient, the electron thermal conductance and the phonon thermal conductance, respectively. It should be noted that K_e includes the contribution of electrons to the two types of thermal transfer, i.e. convection and conduction process, while phonons carry heat only by conduction process, fully included in K_p. The figure of merit ZT determines the maximum efficiency of energy conversion in a thermoelectric device[84]

$$\eta_{\max} = \eta_0 . \frac{\sqrt{1+ZT}-1}{\sqrt{1+ZT}+T_c/T_h} \tag{1-61}$$

where T_h and T_c are temperatures of hot and cold sites, respectively, and $\eta_0 = (T_h - T_c)/T_h$ is the Carnol efficiency for an ideal system. Though most materials are thermoelectric but there are not much materials with high efficiency for energy conversion. The most common material used in practice is Bi_2Te_3 with figure of merit ZT is bout 0.8-1.[85] In spite of very high electrical conductivity Graphene suffers from strong limitations for thermoelectric applications because of small Seebeck's coefficient and very high thermal conductance leading to small figure of merit ZT.[3,14]

Meanwhile K_p can be calculated by formula (1-59), G_e, S and K_e can be calculated by Landauer's-Onsager's approach[86] via an intermediate function called Lorentz function:

$$L_n(\mu,T) = \frac{2}{h}\int_{-\infty}^{+\infty} dE\, T_e(E)(E-\mu)^n \frac{-\partial f_e(E,\mu,T)}{\partial E} \tag{1-62}$$

With electron transmission $T_e(E)$ obtained from Green's function method (1-50) or (1-52), $f_e(E,\mu,T)$ is the Fermi function. Then[86]

$$\begin{cases} G_e(\mu,T) = e^2 L_0(\mu,T) \\ S(\mu,T) = \dfrac{1}{eT}\dfrac{L_1(\mu,T)}{L_0(\mu,T)} \\ K_e(\mu,T) = \dfrac{1}{T}\left[L_2(\mu,T) - \dfrac{L_1(\mu,T)^2}{L_0(\mu,T)}\right] \end{cases} \tag{1-63}$$

1.6 Computational Techniques

In large systems with a big number of atoms, the matrix size of Hamiltonians is very large so it is very difficult to make inversion (1-42) and (1-43). Some special techniques were developed to make simulations possible and more effortless. If we can divide a system into layers so that a certain layer only interacts with its nearest layers, the Hamiltonian of the system will be a tri-diagonal matrix of block layers. Then the surface Green's function of a contact can be computed by an iterative technique which was introduced first by Sancho[87] and rewritten well with detail of computational steps in Ref.[88] Then the surface Green's function can be used to calculate self-energies. To calculate elements of device Green's function, recursive techniques[82] can be applied to filter useful elements G_{ij} of device Green's function such as G_{nn} of layer *n-th* for computing transmission and local density of states. In **Figure 1-8** we show the main computational steps of Green's function techniques. These steps work for both electrons and phonons.

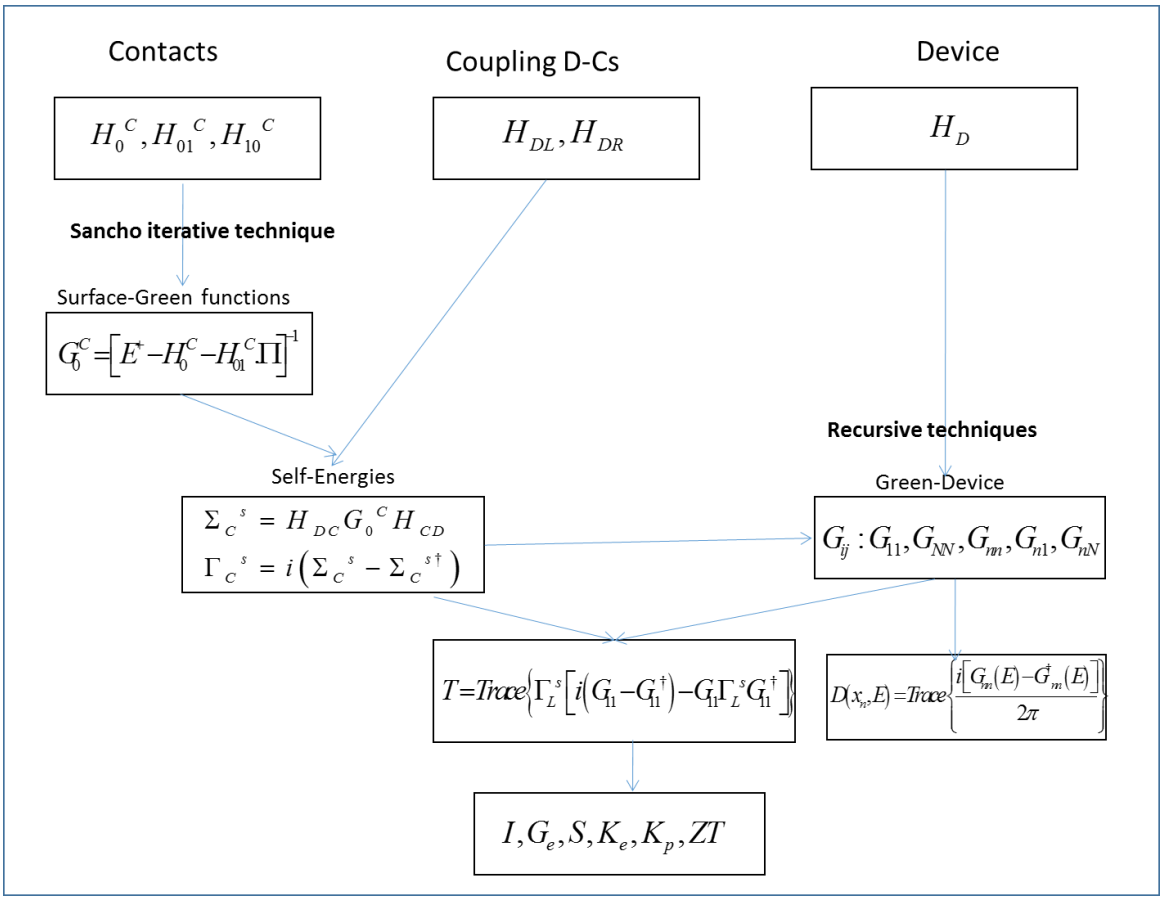

Figure 1-8: Flowchart of computational steps for Green's function techniques.

1.7 Examples: electrons and phonons in linear chain, graphene and Boron Nitride (BN).

In this section we intend to apply the above models and methodologies in order to consider and review the physical properties of some basic systems. The first one is the simplest system with atoms linked together in a linear chain, this toy system is a good example for which we can implement analytical results that can be used to validate numerical results. The second system is graphene which is considered as a standard system in our study. The third one is Boron Nitride that is an insulator which consists of Boron and Nitrogen atoms in a honeycomb lattice as graphene. Because of complexity of methods, to be objective we will make some comparisons between our results and the results of published works to check our understanding in the use and control on calculation techniques.

1.7.1 Linear chain

1.7.1.1 Electrons

1.7.1.1.1 Band structure

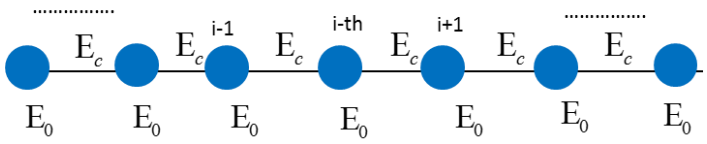

Figure 1-9: An infinite linear chain with 1 atom per unit cell. Onsite energy is E_0 and hopping parameter is E_c.

Within a first neighbor interaction model, the *i-th* atom only interacts with $i\pm1-th$ atoms, so from equation (1-24) we have $\left[H_{ii}+H_{i,i-1}.\mathrm{e}^{-i\vec{k}.\vec{a}}+H_{i,i+1}.\mathrm{e}^{i\vec{k}.\vec{a}}\right]\phi_0=E\phi_0$ with $H_{ii}=E_0,\ H_{i,i\pm1}=E_c$. This is a scalar equation so it immediately gives $E=E_0+E_c.\mathrm{e}^{-ik.a}+E_c.\mathrm{e}^{ik.a}=E_0+2E_c.\cos\left(k.a\right)$. The dispersion is plotted in **Figure 1-10** with assumption that $E_0 = 0$, E_c = -1 eV.

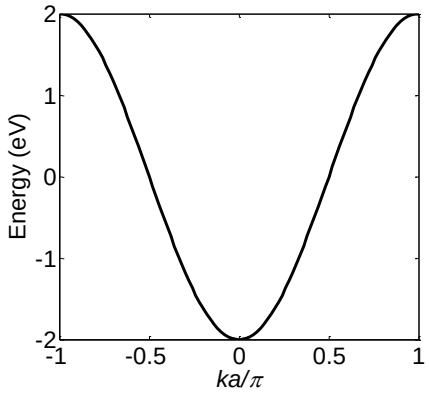

Figure 1-10: Band structure of a periodic chain line for E_0 = 0, E_c = -1 eV.

1.7.1.1.2 Electron transport

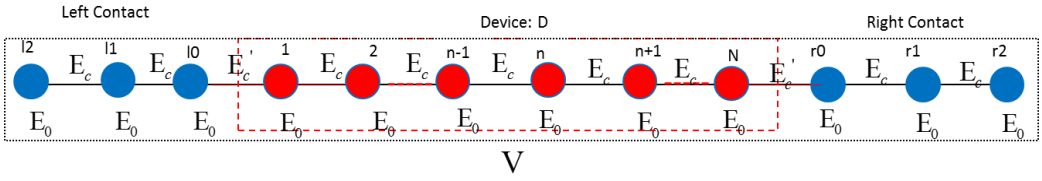

Figure 1-11: Device of N atoms. Hopping Energy between the atoms of the device and the contacts E_c' is different from that between atoms in the contacts and the device E_c. Contacts are semi-infinite.

To investigate electron transport in systems formed of a chain of atoms, we consider a system as in **Figure 1-11** with N atoms in the scattering region, two contacts are assumed to be semi-infinite. A potential V is also assumed to have an influence on the electronic properties of the device part. First we will examine transmission of the system using the Green's function method, then we will use Scattering method in order to compare the results of these two approaches. For the Green's function method, thanks to the simplicity of the system we will solve analytically the surface Green's function of the contacts and then make a comparison with the numerical results obtained by Sancho iterative technique.

1.7.1.1.2.1 Green's function method

First of all, the Hamiltonian of each part: the left contact H_L, the device H_D and the right contact can be written independently as

$$H_L = \begin{array}{c} \\ \cdot \\ \cdot \\ \langle l_2| \\ \langle l_1| \\ \langle l_0| \end{array} \begin{array}{c} \begin{array}{ccccc} \cdot & \cdot & \langle l_2| & \langle l_1| & \langle l_0| \end{array} \\ \begin{pmatrix} \cdot & \cdot & & & \\ \cdot & \cdot & \cdot & & \\ & \cdot & E_0 & E_c & \\ & & E_c & E_0 & E_c \\ & & & E_c & E_0 \end{pmatrix} \end{array} \qquad H_R = \begin{array}{c} \\ \langle r_0| \\ \langle r_1| \\ \langle r_2| \\ \cdot \\ \cdot \end{array} \begin{array}{c} \begin{array}{ccccc} \langle r_0| & \langle r_1| & \langle r_2| & \cdot & \cdot \end{array} \\ \begin{pmatrix} E_0 & E_c & & & \\ E_c & E_0 & E_c & & \\ & E_c & E_0 & \cdot & \\ & & \cdot & \cdot & \cdot \\ & & & \cdot & \cdot \end{pmatrix} \end{array}$$

$$H_D = \begin{array}{c} \\ \langle 1| \\ \langle 2| \\ \cdot \\ \cdot \\ \langle N| \end{array} \begin{array}{c} \begin{array}{ccccc} |1\rangle & |2\rangle & \cdot & \cdot & |N\rangle \end{array} \\ \begin{pmatrix} E_0+V & E_c & & & \\ E_c & E_0+V & E_c & & \\ & E_c & \cdot & \cdot & \\ & & \cdot & \cdot & E_c \\ & & & E_c & E_0+V \end{pmatrix} \end{array}$$

We assume that the two contacts only interact with the active region (device) and do not interact together. The coupling between atoms in the contacts and in the device can also bewritten individually as

$$\tau_{DL} = \begin{array}{c} \\ \langle 1| \\ \langle 2| \\ \cdot \\ \cdot \\ \langle N| \end{array} \begin{array}{c} \begin{array}{ccccc} \cdot & \cdot & \langle l_2| & \langle l_1| & \langle l_0| \end{array} \\ \begin{pmatrix} \cdot & \cdot & 0 & 0 & E_c' \\ & & & 0 & 0 \\ & & & & 0 \\ & & & & \cdot \\ & & & & \cdot \end{pmatrix} \end{array}, \quad \tau_{DR} = \begin{array}{c} \\ \langle 1| \\ \langle 2| \\ \cdot \\ \cdot \\ \langle N| \end{array} \begin{array}{c} \begin{array}{ccccc} \langle r_0| & \langle r_1| & \langle r_2| & \cdot & \cdot \end{array} \\ \begin{pmatrix} \cdot & & & & \\ \cdot & & & & \\ 0 & & & & \\ 0 & & & & \\ E_c' & 0 & 0 & \cdot & \cdot \end{pmatrix} \end{array}$$

Noting that $\tau_{RD} = \tau_{DR}^{\dagger}, \tau_{LD} = \tau_{DL}^{\dagger}$. The Green's function of the left contact is determined from the formula (1-41)

$$\left(E + i0^{+} - H_L\right).G_L = I$$

Or in details we have

$$\begin{pmatrix} \cdot & \cdot & & & & \\ \cdot & \cdot & \cdot & & & \\ & \cdot & E+i0^{+}-E_0 & -E_c & & \\ & & -E_c & E+i0^{+}-E_0 & -E_c & \\ & & & -E_c & E+i0^{+}-E_0 \end{pmatrix} \begin{pmatrix} \cdot & \cdot & & & \\ \cdot & \cdot & \cdot & & \\ & \cdot & G_2^{\,l} & G_{21}^{\,l} & G_{20}^{\,l} \\ & & G_{12}^{\,l} & G_1^{\,l} & G_{10}^{\,l} \\ & & G_{02}^{\,l} & G_{01}^{\,l} & G_0^{\,l} \end{pmatrix} = \begin{pmatrix} \cdot & & & & \\ & \cdot & & & \\ & & 1 & & \\ & & & 1 & \\ & & & & 1 \end{pmatrix}$$

Where 0^{+} is a very small number added into energy to avoid divergence, $G_0^{\,l}$ is the surface Green's function of the left contact that we need to find. It is easy to derive equations

$$\begin{cases} -E_c G_{20}^{\,l} + \left(E+i0^{+}-E_0\right) G_{10}^{\,l} - E_c G_0^{\,l} = 0 \\ -E_c G_{10}^{\,l} + \left(E+i0^{+}-E_0\right) G_0^{\,l} = 1 \end{cases}$$

The solution of these equations can be found in the form of the Bloch wave [80] $G_{n0}^{\,l} = G_0^{\,l}.e^{ik.na}$ and we can get

$$\begin{cases} E+i0^{+} = E_0 + 2E_c \cos ka \\ G_0^{\,l} = \dfrac{1}{E_c} e^{ik.a} \end{cases} \qquad (1\text{-}64)$$

The first expression is actually the energy dispersion that we obtained in section 1.7.1.1.1, the second one is thus the analytical form of the surface Green's function of the left contact. We get an exact formula for the right contact. We use this analytical result to check the numerical outcome which can be obtained from the standard Sancho's iterative scheme [87], the comparison is shown in **Figure 1-12**. It can be seen clearly that the two results are totally identical.

The surface Green's function in (1-64) can be used to compute the self-energy (1-44) and the injection rate and it is thus possible to calculate the device Green's function and then the transmission. In **Figure 1-13** we show the transmission in the system for several situations of coupling energy and potential *V*. In case where no potential is applied, $V = 0$, and $E_c' = E_c$ we have perfect junctions between the device and the contacts and the system is homogenous so there is no scattering and transmission is perfectly equal to one as we observe from the solid blue line in **Figure 1-13.** In the case $E_c' = 1.5E_c$ we observe significant transmission only in the region of energy larger than zero meanwhile electron is blocked in the lower energy

region. This is because this high energy coupling at the junctions of the device and the contacts cause a barrier potential obstructing the transmission of electrons from the contacts to the device. Only high energy electrons can pass through the barrier potential and contribute to the total transmission.

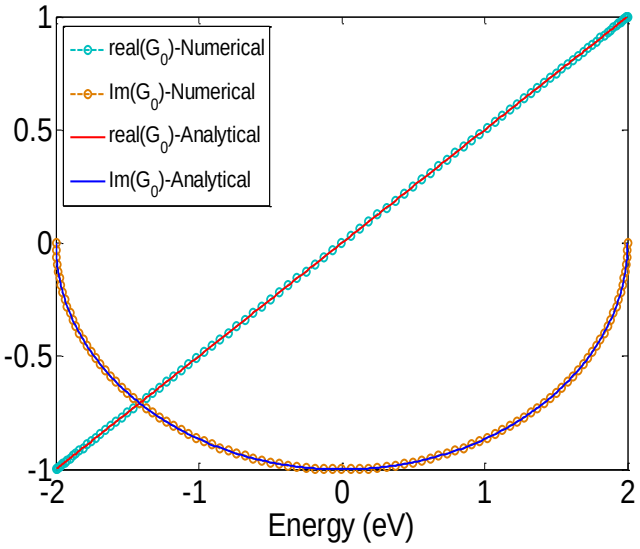

Figure 1-12: Comparison of numerical Sancho iterative technique and analytical results for Surface Green function. $E_0 = 0$, $E_c = -1$ eV.

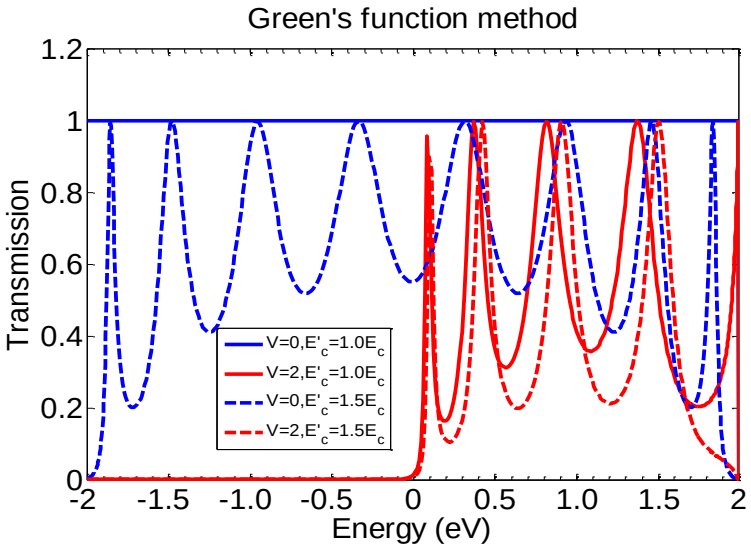

Figure 1-13: Electron Transmission for a device with $N = 10$ atoms and $E_0 = 0$, $E_c = -1$ eV.

1.7.1.1.2.2 Scattering matrix method. A comparison

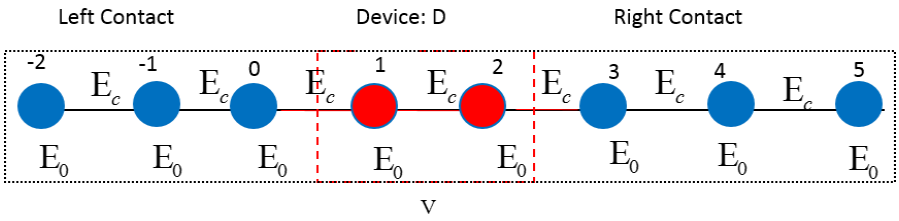

Figure 1-14: Device of two atoms with energy connection between the atom of the device and contact is the same as energy between atoms in contacts

The transmission can also be obtained by the scattering method in which the incoming, reflection and transmission waves of a scattering region are considered using continuous condition of wave functions. We illustrate this method by considering a simple system with only two atoms in the active region as schematized in **Figure 1-14**. The Scattering method requires the knowledge of wave functions, so we need to formulate an expression of momentum k from energy E. In regions of contacts we have from the energy dispersion (1-64)

$$k = \frac{1}{a} arc\cos\left(\frac{E - E_0}{2E_c}\right)$$

So the wave functions in the region of the left and the right contacts are

$$\begin{cases} \psi_L = e^{ik.na} + r.e^{-ik.na} \\ \psi_R = t.e^{ik.na} \end{cases}$$

Here $x = n.a$ is the position of *n-th* atom in the whole system and r, t are reflection and transmission coefficients, respectively.

In the region of the device, the wave function $\psi_D = \psi_1$ at the position of atom 1st and equals ψ_2 at the position of the atom 2nd.

These wave functions must satisfy the continuity conditions at the junctions:

$$\begin{cases}\psi_L(n=1)=\psi_D(n=1)=\psi_1\\ \psi_2=\psi_D(n=2)=\psi_R(n=2)\end{cases}$$

These equations lead to

$$\begin{cases}e^{ik.a}+r.e^{-ik.a}=\psi_1\\ \psi_2=te^{2ik.a}\end{cases} \tag{1-65}$$

Moreover, we have the Schrödinger equation for the whole system

$$\begin{array}{c} \\ \\ |0\rangle \\ |1\rangle \\ |2\rangle \\ |3\rangle \\ \\ \\ \end{array}\begin{array}{c}\begin{array}{cccccccc} \cdot & \cdot & |0\rangle & |1\rangle & |2\rangle & |3\rangle & \cdot & \cdot \end{array}\\ \begin{pmatrix} & & & \cdot & \cdot & & & \\ & & & \cdot & \cdot & & & \\ \cdot & \cdot & E_0 & E_c & 0 & 0 & \cdot & \cdot \\ \cdot & \cdot & E_c & E_0+V & E_c & 0 & \cdot & \cdot \\ & & 0 & E_c & E_0+V & E_c & \cdot & \cdot \\ & & & 0 & E_c & E_0 & & \\ & & & \cdot & \cdot & \cdot & & \\ & & & \cdot & \cdot & \cdot & & \end{pmatrix}\end{array}\begin{pmatrix}\\ \\ \psi_0\\ \psi_1\\ \psi_2\\ \psi_3\\ \\ \\ \end{pmatrix}=E\begin{pmatrix}\\ \\ \psi_0\\ \psi_1\\ \psi_2\\ \psi_3\\ \\ \\ \end{pmatrix}$$

$$\Rightarrow\begin{cases}E\psi_1=E_c\psi_0+(E_0+V)\psi_1+E_c\psi_2\\ E\psi_2=E_c\psi_1+(E_0+V)\psi_2+E_c\psi_3\end{cases} \tag{1-66}$$

where

$$\begin{cases}\psi_0=\psi_L(n=0)=1+r\\ \psi_3=\psi_R(n=3)=t.e^{3ika}\end{cases} \tag{1-67}$$

Plugging (1-65) and (1-67) into (1-66) we have a system equations of *t* and *r*. With few step of derivation we can get the final result for transmission as

$$T=|t|^2=\frac{4{E_c}^4.\sin^2 qa}{\left|-X^2+{E_c}^2\right|^2} \tag{1-68}$$

where $X=E_c.e^{-ika}-V$

The comparison of Green's function and the scattering method is plotted in **Figure 1-15**. One more time we see an excellent agreement between Green's function and the result obtained by another method which is the scattering method in this case.

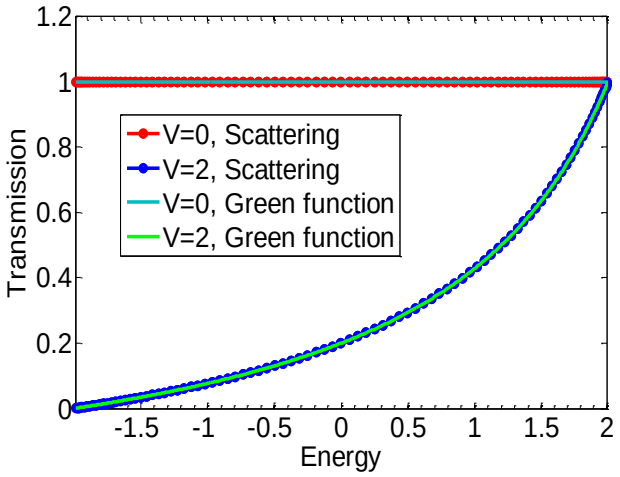

Figure 1-15: Comparison between Scattering method and Green's function method for a device with $N = 2$.

1.7.1.1.2.3 Current: comparison with Figure in Data's book

So far we have considered transport in devices made of linear chains without any bias potential between the left and right contacts. In case where a bias is applied, we will have a current through the channel that can be calculated by (1-55). Here we assume there is a bias applied for the device in **Figure 1-11** and transport in the system is ballistic. In this case we assume $E_0 = 2t_0$, $E_c = -t_0$ with $t_0 = \hbar^2/\left(2ma^2e\right)$. Here $m = 0.25m_0$ is the effective mass of an electron and $a = 3\times10^{-10}$ m is the lattice constant. The initial Fermi energy in the left and right contacts are assumed to be equal to 0.1 eV. In **Figure 1-16** we show the comparison between the result from our performance and that which is presented in Figure 9.10.5 of the famous book of Datta [80]. The results are mostly identical.

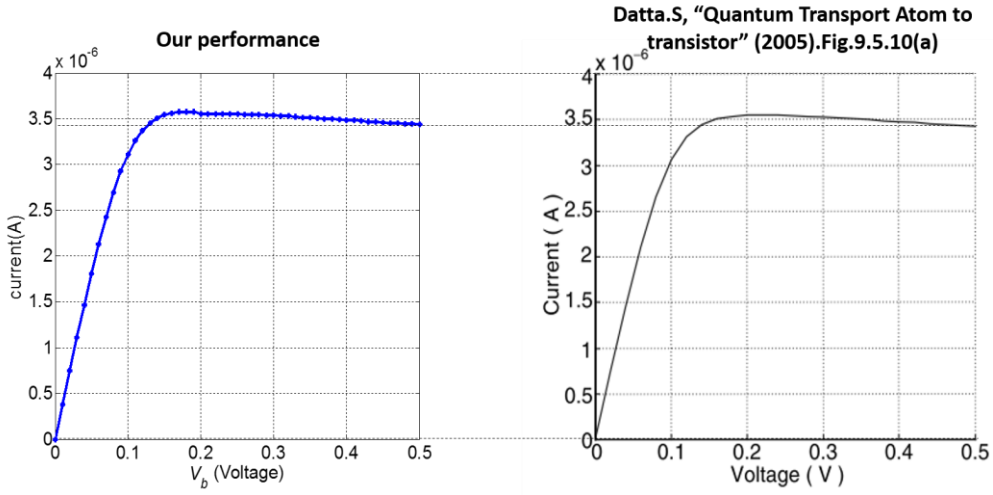

Figure 1-16: I-V characters in the device of a linear chain. Parameters are N_A = 20; Ef_L = 0.1 eV, Ef_R = 0.1 eV, E_0 = 2.t_0 , E_c = - t_0 with $t_0 = \hbar^2 / \left(2m.a^2.e\right)$, m = 0.25m_0 , a = 3×10^{-10} m.

1.7.1.2 Phonons

In this section phonon dispersion and transmission will be considered.

1.7.1.2.1 Phonon dispersion

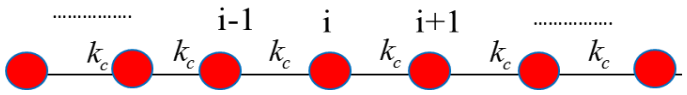

Figure 1-17: Vibration in a system of an infinite linear chain with two nearest atoms coupled by a spring with stiffness k_c.

In **Figure 1-17** we assume that two nearest neighbor atoms are coupled by a spring with the stiffness k_c. Each unit cell only covers one atom, so we have dynamical matrices of one unit cell and its couplings to the neighbor cells from (1-15) are

$$D_{nn} = 2k_c / m, D_{n,n\pm1} = -k_c / m$$

The secular equation (1-14) leading to

$$\omega^2 = 2k_c / m - (k_c / m).e^{iq.a} - (k_c / m)e^{-iq.a}$$

And thus

$$\omega = \sqrt{\frac{4k_c}{m}} \left| \sin \frac{qa}{2} \right| \tag{1-69}$$

The vibration modes ω are plotted in **Figure 1-18** for a linear chain of carbon atoms.

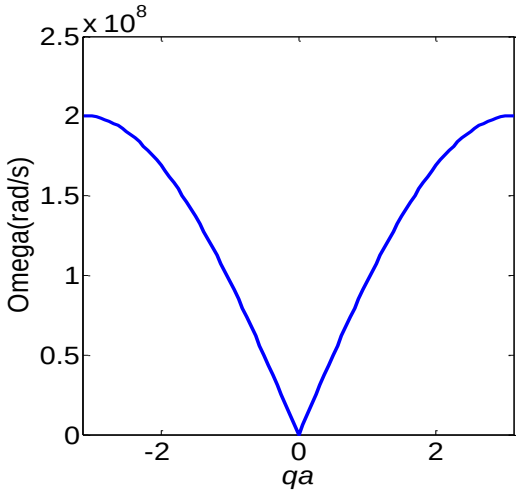

Figure 1-18: Phonon dispersion of a linear chain with one atom per cell

Figure 1-18 shows phonon dispersion for a linear chain of Carbon atoms with one atom/cell with stiffness of the spring between two atoms assumed k_c = 2×10^{-10} N/m. a carbon atom has m = 1.994×10^{-26} kg.

1.7.1.2.2 Phonon transport

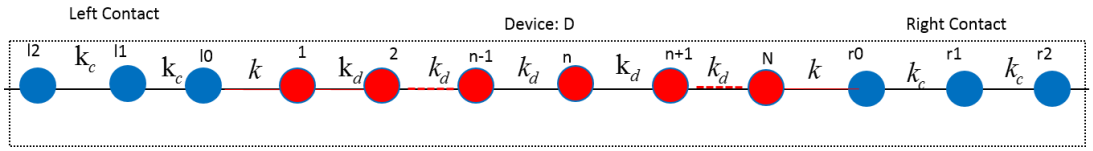

Figure 1-19: A device of chain lines for phonon study. k_c and k_d are the stiffness in the contacts and device, respectively. k is the coupling between nearest atoms in the contacts and the device.

If we denote L, D, R are left contact, device and right contact, the matrix equation (1-14) can be divided as

$$\begin{array}{c} \\ \mathrm{L} \\ \mathrm{D} \\ \mathrm{R} \end{array}\begin{array}{c} \begin{array}{ccc} \mathrm{L} & \mathrm{D} & \mathrm{R} \end{array} \\ \begin{pmatrix} K_L & \tau_{LD} & 0 \\ \tau_{DL} & K_D & \tau_{DR} \\ 0 & \tau_{RD} & K_R \end{pmatrix} \end{array}\begin{pmatrix} U_L \\ U_D \\ U_R \end{pmatrix} = m\omega^2 \begin{pmatrix} U_L \\ U_D \\ U_R \end{pmatrix}$$

where

$$K_L = \begin{array}{c} \\ . \\ . \\ |l_2\rangle \\ |l_1\rangle \\ |l_0\rangle \end{array}\begin{array}{c} \begin{array}{ccccc} . & . & |l_2\rangle & |l_1\rangle & |l_0\rangle \end{array} \\ \begin{pmatrix} . & . & & & \\ . & . & . & & \\ & . & 2k_c & -k_c & \\ & & -k_c & 2k_c & -k_c \\ & & & -k_c & k_c + k \end{pmatrix} \end{array} \qquad K_R = \begin{array}{c} \\ |r_0\rangle \\ |r_1\rangle \\ |r_2\rangle \\ . \\ . \end{array}\begin{array}{c} \begin{array}{ccccc} |r_0\rangle & |r_1\rangle & |r_2\rangle & . & . \end{array} \\ \begin{pmatrix} k_c + k & -k_c & & & \\ -k_c & 2k_c & -k_c & & \\ & -k_c & 2k_c & . & \\ & & . & . & . \\ & & & . & . \end{pmatrix} \end{array}$$

are the coupling matrix in the left and right contacts, respectively. And

$$K_D = \begin{array}{c} \\ |1\rangle \\ |2\rangle \\ . \\ . \\ |N\rangle \end{array}\begin{array}{c} \begin{array}{ccccc} |1\rangle & |2\rangle & . & . & |N\rangle \end{array} \\ \begin{pmatrix} k_d + k & -k_d & & & \\ -k_d & 2k_d & -k_d & & \\ & -k_d & . & . & \\ & & . & 2k_d & -k_d \\ & & & -k_d & k_d + k \end{pmatrix} \end{array}$$

is the coupling matrix in the device. Coupling Matrices between the contacts and the device are

$$\tau_{DL} = \begin{array}{c} \\ |1\rangle \\ |2\rangle \\ \cdot \\ \cdot \\ |N\rangle \end{array} \begin{array}{c} \begin{array}{ccccc} \cdot & \cdot & |l_2\rangle & |l_1\rangle & |l_0\rangle \end{array} \\ \begin{pmatrix} \cdot & \cdot & 0 & 0 & -k \\ & & & 0 & 0 \\ & & & & 0 \\ & & & & \cdot \\ & & & & \cdot \end{pmatrix} \end{array} \qquad \tau_{DR} = \begin{array}{c} \\ |1\rangle \\ |2\rangle \\ \cdot \\ \cdot \\ |N\rangle \end{array} \begin{array}{c} \begin{array}{ccccc} |r_0\rangle & |r_1\rangle & |r_2\rangle & \cdot & \cdot \end{array} \\ \begin{pmatrix} \cdot & & & & \\ \cdot & & & & \\ 0 & & & & \\ 0 & & & & \\ -k & 0 & 0 & \cdot & \cdot \end{pmatrix} \end{array}$$

Similarly to the case of electrons, we can define the Green's function for the contacts using

$$\left(m\omega^2 + i0^+ - K_L\right).G_L = I$$

and the surface Green's function can be obtained in the form

$$G_0^{\,l} = \frac{1}{k_c - k_c e^{-iq.a} - k} \tag{1-70}$$

This result is used to calculate the self-energies and then the phonon transmission. In **Figure 1-20** we show the transmission spectrum of phonon for different cases of coupling stiffness k. The results indicate that if the coupling between the contacts and the device is weak (for example, $k = 0.2k_c$), vibration is only transmitted at low frequencies and significantly reduced at higher frequencies (blue line). In the case this coupling is strong, transmission retains at good values in a longer range of frequency. In the both cases, some resonances can be observed when phonons vibrate at proper frequencies of the atoms in the device.

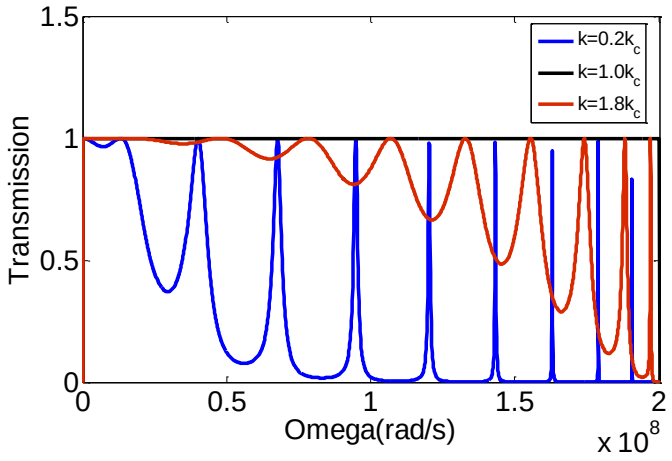

Figure 1-20: $N = 10$, $k_c = k_d = 2\times10^{-10}$ N/m, a carbon atom has $m = 1.994\times10^{-26}$ kg.

1.7.2 Graphene

It is now time to make a review of graphene. Here we summarize basic electronic and thermal properties of graphene with different configurations, from 2D structures to 1D with ribbons.

1.7.2.1 2D Graphene

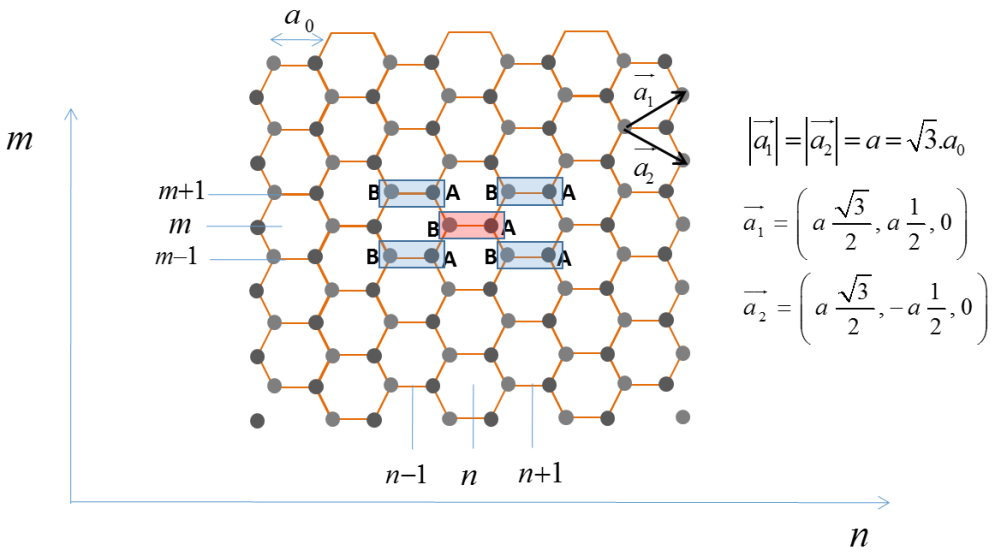

Figure 1-21: structure of 2D graphene. In nearest neighbor interaction, the unit cell (n,m) (red) only interacts with its four nearest cells.

Graphene has a honeycomb structure in which the distance between two nearest Carbon atoms is a_0 = 0.142 nm. [1] Due to the difference of geometrical positions, atoms in a graphene sheet can be sorted into two kinds of atoms: atoms sub-lattice A and sub-lattice B. In 2D graphene structure, a unit cell contains two atoms one of each sub-lattice, as we see in **Figure 1-21**. The lattice vector $\vec{a}_1$ and $\vec{a}_2$ define repetition of carbon atoms in the structure. In the momentum space, the reciprocal lattice is determined by two vector $\vec{b}_1$ and $\vec{b}_2$ which can be found from relations

$$\begin{cases} \vec{a}_i.\vec{b}_i = 2\pi \\ \vec{a}_j.\vec{b}_i = 0 \end{cases} \quad (i, j = 1 \text{ or } 2)$$

And we can get

$$\begin{cases} \vec{b_1} = \left(\frac{2\pi}{a\sqrt{3}}, \frac{2\pi}{a}, 0 \right) \\ \vec{b_2} = \left(\frac{2\pi}{a\sqrt{3}}, -\frac{2\pi}{a}, 0 \right) \end{cases} \tag{1-71}$$

For nearest TB calculation, we can solve the Eigen value equation $h\phi_0 = E\phi_0$ with

$$\begin{aligned} h = H_{nm} + H_{(n,m),(n+1,\mathrm{m}-1)}.e^{i\vec{k}\left(\vec{R}_{(n+1,\mathrm{m}-1)} - \vec{R}_{(n,m)}\right)} + H_{(n,m),(n+1,\mathrm{m}+1)}.e^{i\vec{k}\left(\vec{R}_{(n+1,\mathrm{m}+1)} - \vec{R}_{(n,m)}\right)} \\ + H_{(n,m),(n-1,\mathrm{m}-1)}.e^{i\vec{k}\left(\vec{R}_{(n-1,\mathrm{m}-1)} - \vec{R}_{(n,m)}\right)} + + H_{(n,m),(n-1,\mathrm{m}+1)}.e^{i\vec{k}\left(\vec{R}_{(n-1,\mathrm{m}+1)} - \vec{R}_{(n,m)}\right)} \end{aligned} \tag{1-72}$$

Here

$$\vec{R}_{(n+1,m+1)} - \vec{R}_{(n,m)} = \vec{a_1}, \vec{R}_{(n-1,m-1)} - \vec{R}_{(n,m)} = -\vec{a_1}, \vec{R}_{(n+1,m-1)} - \vec{R}_{(n,m)} = \vec{a_2}, \vec{R}_{(n-1,m+1)} - \vec{R}_{(n,m)} = -\vec{a_2}$$

And

$$H_{nm} = \begin{pmatrix} 0 & -t \\ -t & 0 \end{pmatrix}, H_{(n,m),(n+1,\mathrm{m}-1)} = \begin{pmatrix} 0 & 0 \\ -t & 0 \end{pmatrix}, H_{(n,m),(n+1,\mathrm{m}+1)} = \begin{pmatrix} 0 & 0 \\ -t & 0 \end{pmatrix},$$
$$H_{(n,m),(n-1,\mathrm{m}-1)} = \begin{pmatrix} 0 & -t \\ 0 & 0 \end{pmatrix}, H_{(n,m),(n-1,\mathrm{m}+1)} = \begin{pmatrix} 0 & -t \\ 0 & 0 \end{pmatrix}$$

are Hamiltonians of the center cell (*n,m*) and the couplings of this cell and its neighbors. By diagonalizing *h* we can obtain exactly the energy dispersion as

$$E = \pm t\sqrt{1 + 4\cos\left(k_x a_x\right).\cos\left(k_y.a_y\right) + 4\cos^2\left(k_y.a_y\right)} \tag{1-73}$$

where $a_x = \frac{3}{2}a_0, a_y = \frac{\sqrt{3}}{2}a_0$ are the lattice constant along *x* and *y* directions, respectively. The full bands are plotted in the top right corner of **Figure 1-22**. Underneath this figure we see a projection of the band on k_x and k_y, which shows that there are six Dirac cones (green points) in the band structure of 2D graphene. In the right column, the projections on k_x, k_y directions are shown individually, which confirms that the bandgap is equal zero. Interestingly, the zoom of energy band around a Dirac cone (the center figure) shows that energy is almost linear with momentum. Physically, it means that electrons in this region are massless and

move very fast. The energy dispersion of this region is approximately $E = \pm v_F k$ with $k = \sqrt{k_x^{\,2} + k_y^{\,2}}$ and $v_F \approx 10^6$ m/s is the Fermi velocity.[1]

Also in many cases, band structure of 2D graphene can be plotted along high symmetrical directions instead of 3D plot as in **Figure 1-22**. In **Figure 1-23** we replot the electronic band structure along directions MG, GK and KM and we also plot the computed DOS (blue lines). We compare our results with results obtained by two other works, i.e. ref.[55] and ref. [89].

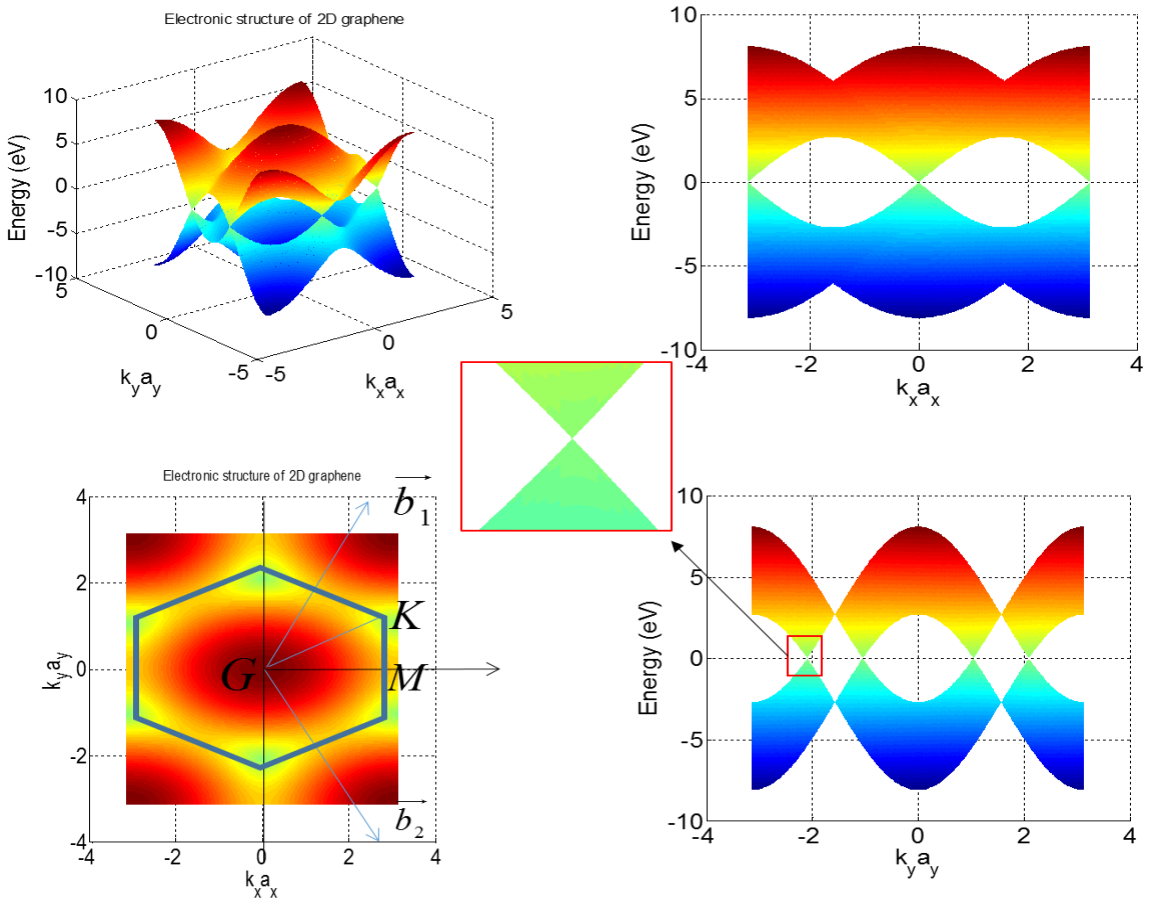

Figure 1-22: 3D plot for electronic band structure of 2D graphene. The left panels: band structure and first Brillouin zone. The right panels: projections of the band structures on k_x (upper) and k_y (lower) and the center figure is a Dirac cone around zero energy.

The phonon dispersion of 2D graphene was also calculated. Due to sophistication in calculations for phonons, the detail is not shown here but we make another comparison between our calculation and results demonstrated by Wirtz el all.[54] for phonon dispersion of 2D graphene. It can be seen clearly from both figures that our results are identical to those of the previous works, which validates again our numerical model.

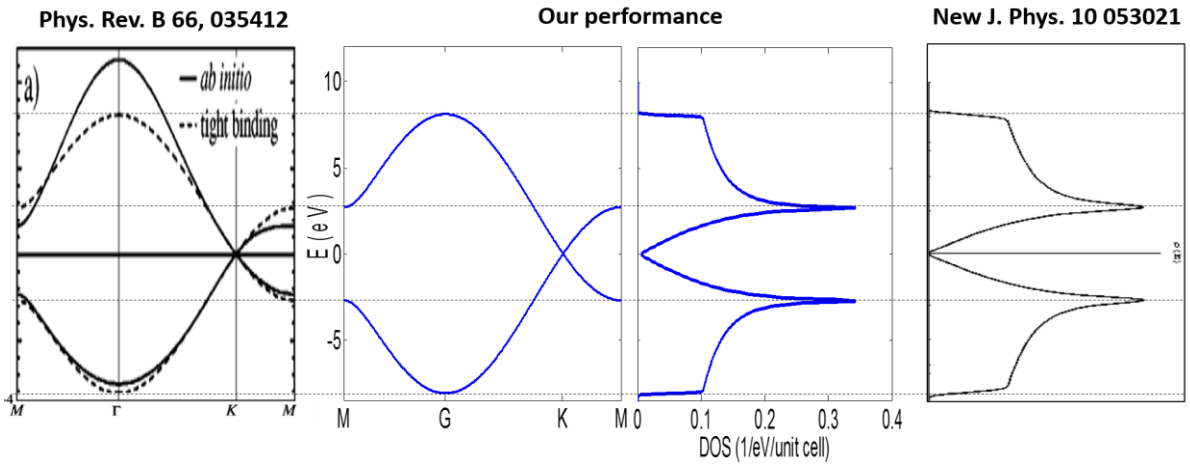

Figure 1-23: Comparison for the energy band and DOS (2D graphene) between our calculation and results obtained by Reich el all [55], Carpio el all [89]**.** All works were based on first nearest TB calculation with t = 2.7eV. Energy is plotted along high symmetrical directions MG-GK-KM.

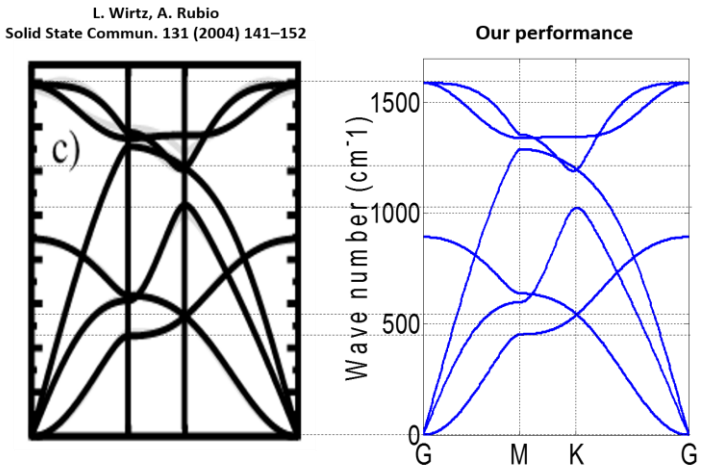

Figure 1-24: Comparison of phonon dispersion between our calculation and results obtained by Wirtz el all [54]. FC model up to 4th nearest neighbor interaction, using off-diagonal parameters of Wirtz.

1.7.2.2 Ribbons

We also validate the methodologies for the case of ribbons as shown in **Figure 1-25** and **Figure 1-26**. In **Figure 1-25** we compare our results with that of ref.[90] for energy bands and DOS in Armchair and Zigzag graphene ribbons. The agreement is clear. Here we can observe that zigzag graphene is always metallic while armchair graphene ribbons may have a finite bandgap depending on the width of ribbon.

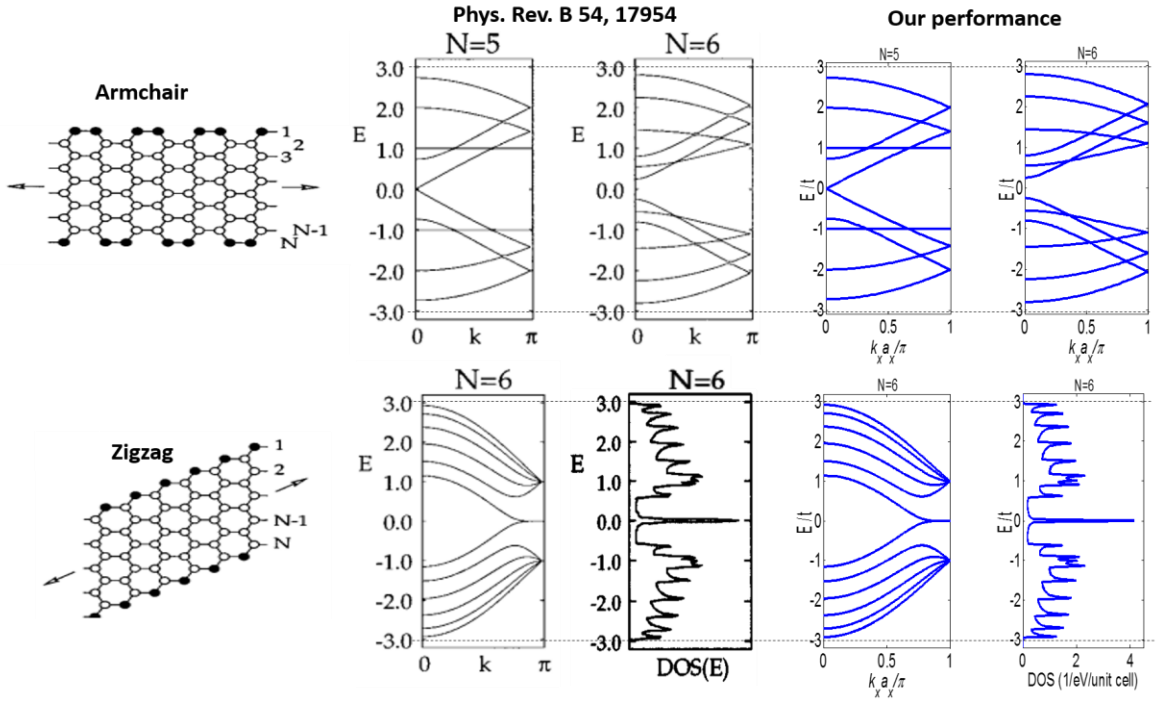

Figure 1-25: Comparison of energy dispersion for armchair and zigzag Graphene ribbons. Energy is taken in unit of hopping parameter *t*. Reference: *Nakada el al*. [90]

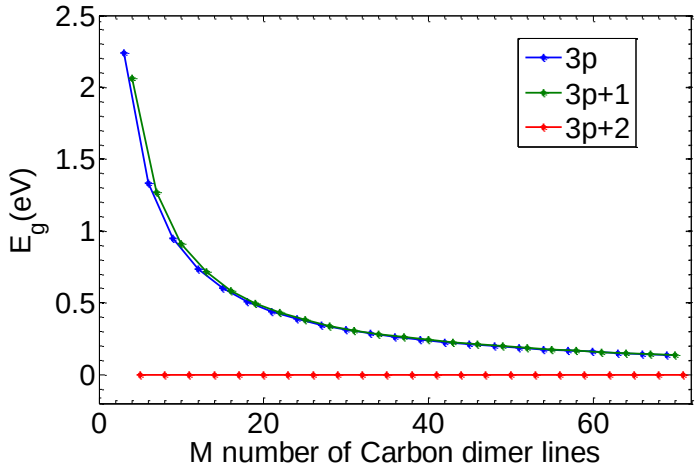

Figure 1-26: Bandgap in armchair graphene is classified in 3 groups 3*p*, 3*p* + 1 and 3*p* + 2. $E_{3p+2} < E_{3p} < E_{3p+1}$.

The dependence of bandgap on the width *M* of armchair graphene ribbons is shown in **Figure 1-26**. Bandgap varies for different groups of *M*. For *M* = 3*p* + 2 with *p* is an integer number, bandgap is always equal to zero, meanwhile bandgap is open for ribbons with *M* = 3*p* + 1 or 3*p*. The bandgap corresponds to the group 3*p* + 1 is slightly larger than that of the group 3*p*.

The relationship between the band structure and the transport properties can be seen in **Figure 1-27**. Here we plot the transmission (i.e. the electrical conductance G_e at zero Kelvin in unit of G_0) for perfect ribbons. It shows that for the case of semiconducting armchair graphene, zero conductance can be obtained thanks to bandgap opening in the structures ((a) and (b)). In contrast, metallic graphene (armchair graphene 3*p* + 2 and zigzag graphene) always have finite electrical conductance ((c) and (d)). Thus bandgap modulation in graphene ribbons is strongly dependent on the width of ribbons. Hence, a precise control is required to obtain the desired gap.

(a)

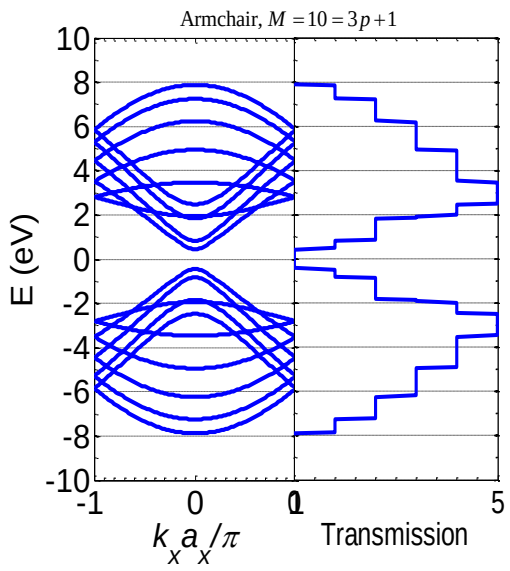

(b)

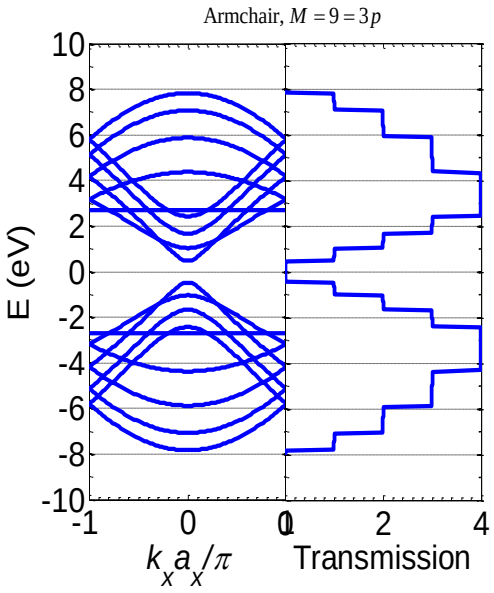

(c)

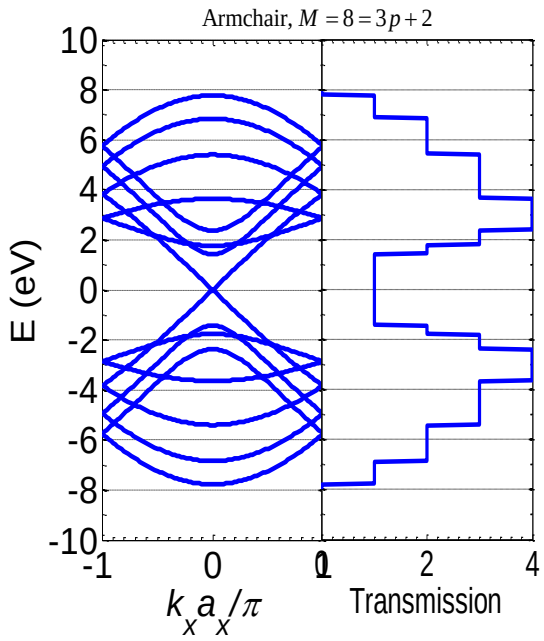

(d)

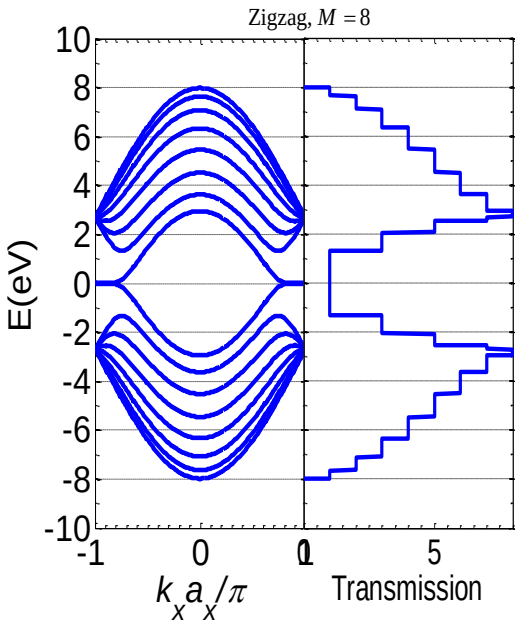

Figure 1-27: Transmission for different groups of Armchair graphene (a), (b), (c) and for zigzag graphene (d).

1.7.3 Boron Nitride

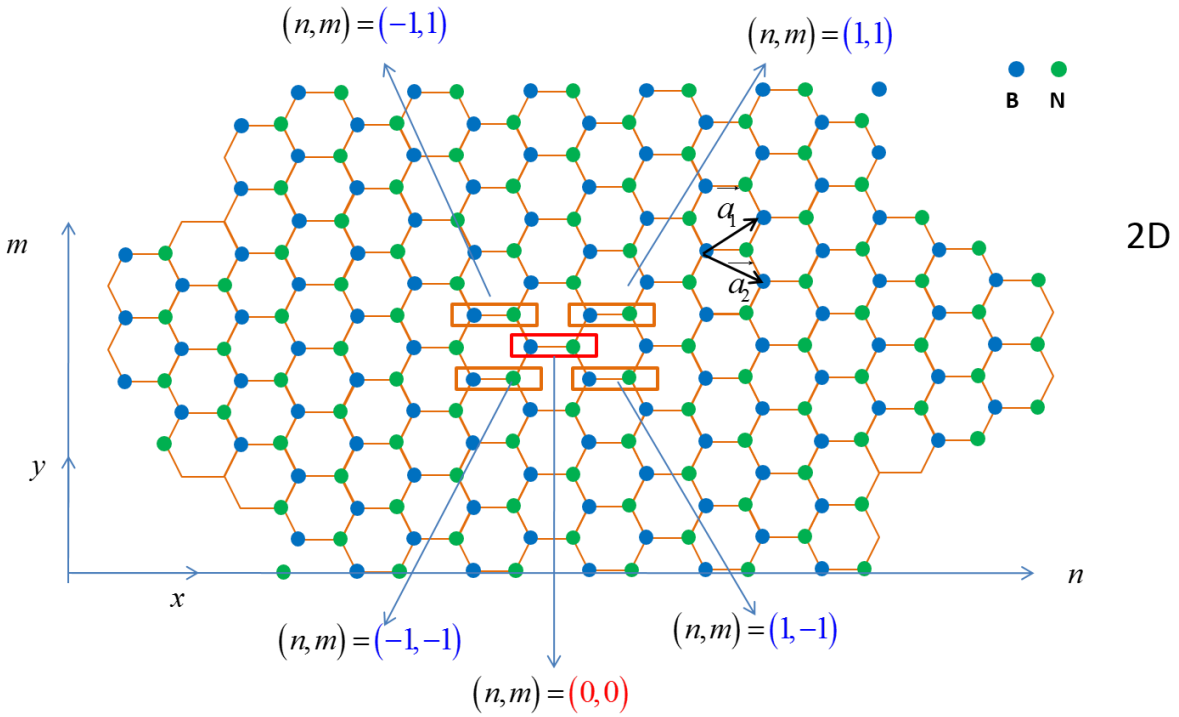

Figure 1-28: 2D structure of Boron Nitride (BN). The blue atoms are Boron and the green ones are Nitrogen atoms.

In this section we review the electronic and thermal properties of BN. In **Figure 1-28** is the illustration of the 2D structure of BN. Solving the Eigen value problem as we have made for 2D graphene we can obtain the energy dispersion for the case of 2D BN as

$$E=\frac{\left(\varepsilon_B+\varepsilon_N\right)\pm\sqrt{\left(\varepsilon_B-\varepsilon_N\right)^2+4{t_{BN}}^2\left[1+4\cos\left(k_x a_x\right)\cos\left(k_y a_y\right)+4\cos^2\left(k_y a_y\right)\right]}}{2} \quad (1\text{-}74)$$

In the case of BN, onsite energies of Boron and Nitrogen atoms are unequal and nonzero while onsite energy of carbon atoms in graphene is almost equal to zero which makes the dispersions (1-74) a bit different from (1-73). With TB parameters from ref. [91] we can plot the band structure for 2D BN as in **Figure 1-29**. The observed bandgap is about 4.57 eV which indicates that BN is a good insulator.

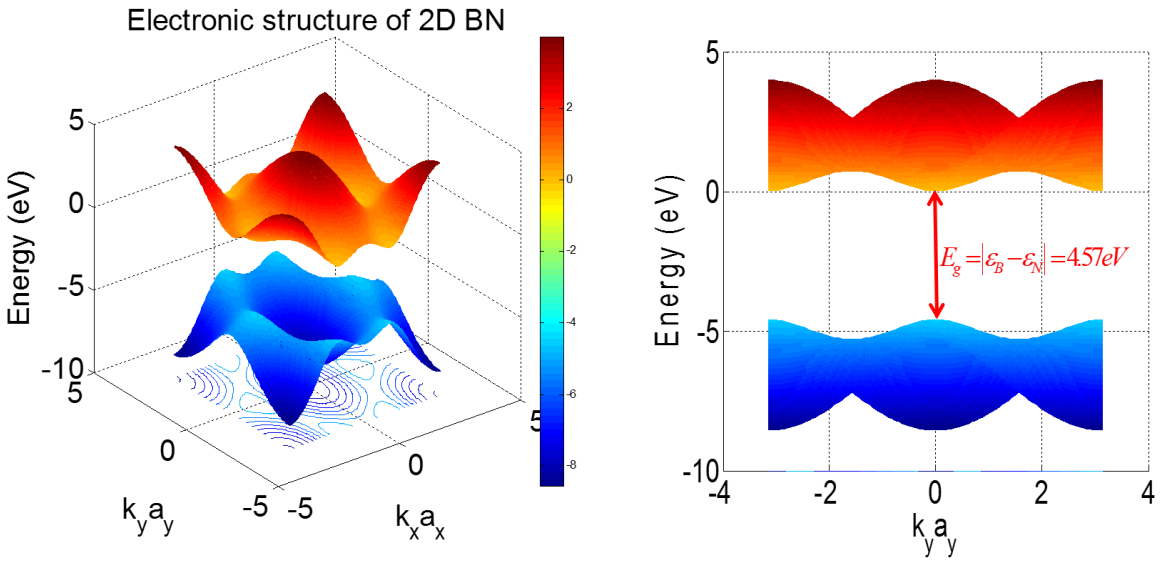

Figure 1-29: Electronic band structure of 2D BN. Here t_{BN} = 1.95 eV; E_B = 0; E_N = -4.57 eV; [91]

We also computed the phonon dispersion for 2D BN and show it in **Figure 1-30**. The parameters were taken from [92]. Unlike electronic properties in which graphene is semi-metallic and BN is insulating, frequency ranges of BN and Graphene are not so different, i.e. vibration modes of BN is in the range [0, 1420 cm^{-1}] and of Graphene is in the range [0, 1590 cm^{-1}], showing that BN is also a good thermal material as graphene. It is thus very promising to integrate graphene and BN in a heterostructure so that we can modulate strongly the phonon conductance of the system, which should make it possible to enhance thermoelectric performance in graphene.

In **Figure 1-31** we show the phonon conductance for armchair BN ribbons and we compare our results with that of ref.[93] Thus our results on thermal transport are also in excellent agreement with the results of other works. Note that we have obtained transport results by using standard procedures of Green's function formalism (Surface Green by Sancho's iterative procedure, device Green's function by recursive technique) as as shown in **Figure 1-8**. Besides these results, we also have excellent agreement on many other results such as transmission, electrical conductance, Seebeck coefficient, figure of merit *ZT* for graphene and BN. However, it is not useful to show all of them here.

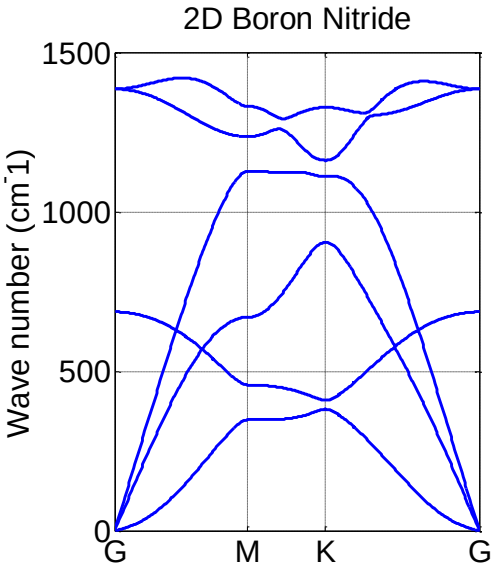

Figure 1-30: Phonon dispersion of 2D BN. Force constant parameters are from ref.[92]

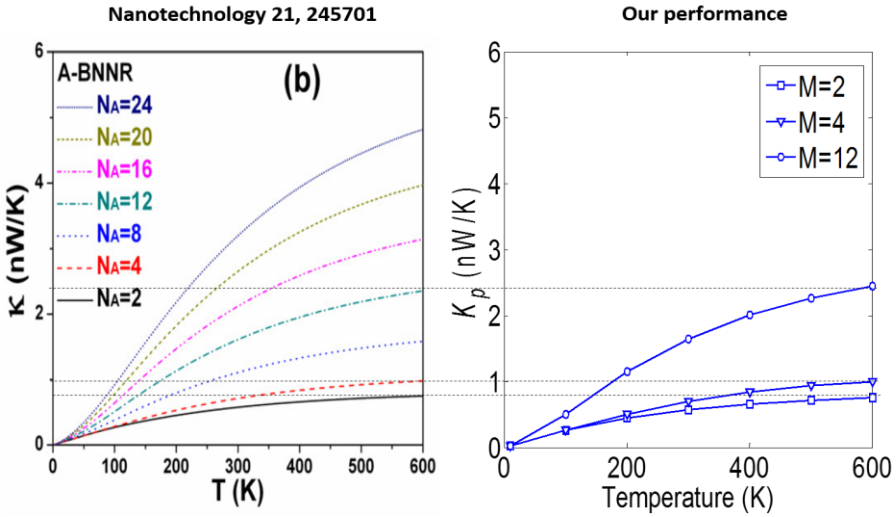

Figure 1-31: Comparison of phonon conductance for armchair BN ribbons. Reference: *Ouyang, et al*.[93]

1.8 Conclusions

In this chapter I have reviewed some basic concepts such as tight binding, force constant models and Green's formalism. Some important physical quantities in energy and transport studies were also highlighted. The modelling and methods were then applied to investigate energy band, DOS, transmission, current, conductance in some well-known systems such as linear atomic chain, graphene and Boron Nitride (BN). Many comparisons between analytical and numerical results, and between our results and others of published works were also provided to validate the reliance on methodologies used. These methods and techniques will be used to study electronic and thermoelectric properties of graphene/BN heterostructures in the next chapters.

Chapter 2:

Graphene/BN heterostructures with tunable gap and high electron velocity

In this chapter we study a wide range of possible configurations of armchair and zigzag graphene/BN hybrid nanoribbons. By using tight binding calculation, we investigate a series of different in-plane Graphene/BN ribbons and show that tunable gaps and high electron velocity can be observed in many configurations of Graphene/BN heterostructures.

2.1 Introduction

In spite of excellent transport properties, making it a material of choice for nanoelectronic applications, graphene suffers from the lack of an energy bandgap, which plays a very important role in device operation [1]. However, another 2D material called hexagonal-Boron Nitride (h-BN) with similar geometrical structure has a very large gap (~5.0 eV), as shown in Chapter 1 and in Refs. [94,95] as well.

It is thus natural that the idea of combining Graphene and BN has been recently raised and has suggested a new strategy to open and control bandgap in graphene. This new direction has been demonstrated experimentally in several works including the use of B (N) atoms as doping elements in graphene sheets [96] or the growth of in-plane structures of Graphene and BN domains [36,43–45,97]. Regarding the synthesis of in-plane Graphene/BN hybrid structures, in Ref. [45] Liu et al. reported the fabrication process with controlled domain sizes from nanometre scale to micrometre scale. The three main steps of the process are illustrated in **Figure 2-1**(i)**:** First (1) ammonia borane (NH_3-BH_3) powder was used to grow h-BN films on copper/nickel substrates using chemical vapor deposition (CVD) method. Next, (2) a defined part of the h-BN was removed by laser-cut masks. Then, (3) few layer graphene was grown on the etched region by using a carbon source such as CH_4.

Photolithography can be used to produce masks with different patterns for argon ion etching. This technique can provide graphene/BN regions with sizes of a few micrometres. To create nanoscale patterns, the focused ion beam (FIB) was used as an etching method. The fabricated patterns can be examined by different techniques such as scanning electron microscopy

(SEM), or optical imaging. **Figure 2-1**(ii) shows SEM images of patterns made of alternative strips of graphene/BN in which the panels (a) and (b) correspond to patterns formed using photolithography technique with micrometer scale size and pattern shown in (c) were obtained using FIB technique with nanoscale size.

(i)

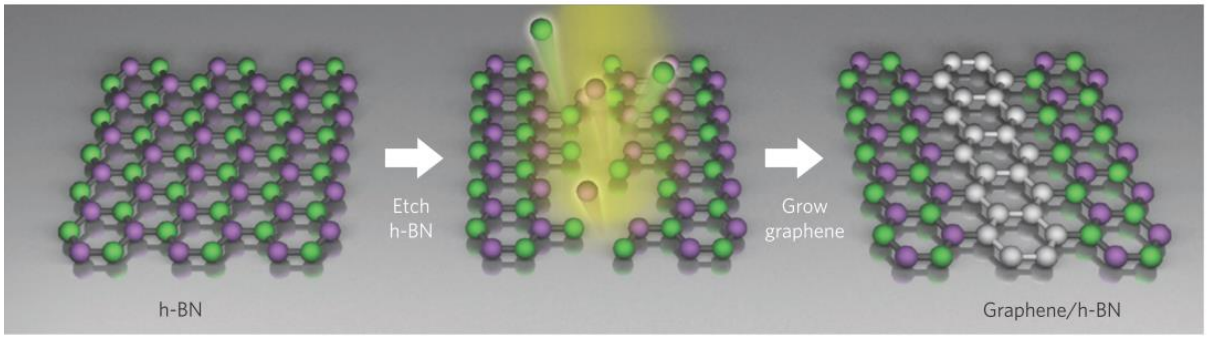

(ii)

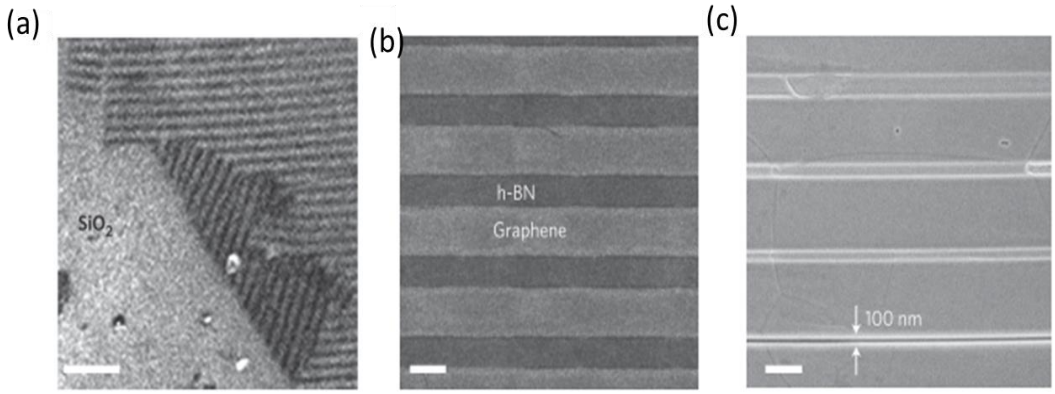

Figure 2-1: (i) Illustration of the main steps of the synthesis process for in-plane Graphene/BN heterostructures. (ii) SEM images of graphene/h-BN stripes with (a) and (b) domains controlled by Photolithography with each strip width of about 10 µm, the scale bars are 50 mm and 10 mm, respectively. In (c) domains were controlled using FIB technique, the width of strips, from top to bottom, are 1 mm, 500 nm, 200 nm and 100 nm, respectively. Scale bar, 1 mm. *Reference: Liu et al.* [45]

The interface between graphene and BN can be characterized by several techniques, as for instance Raman spectroscopy, atomic force microscopy (AFM) and scanning transmission electron microscopy (STEM).

The Raman spectra can be used to identify very well the regions of pure graphene or pure BN and also their interfaces. If the Raman spectrum obtained from the h-BN regions only shows a vibration mode with the peak around 1360 cm^{-1}, three peaks can be observed in the spectrum of the Graphene regions, including the peaks around 1350 cm^{-1}, 1590 cm^{-1} and 2700 cm^{-1}. All these intrinsic modes from both graphene and BN can be observed at the interface (see **Figure 2-2**).

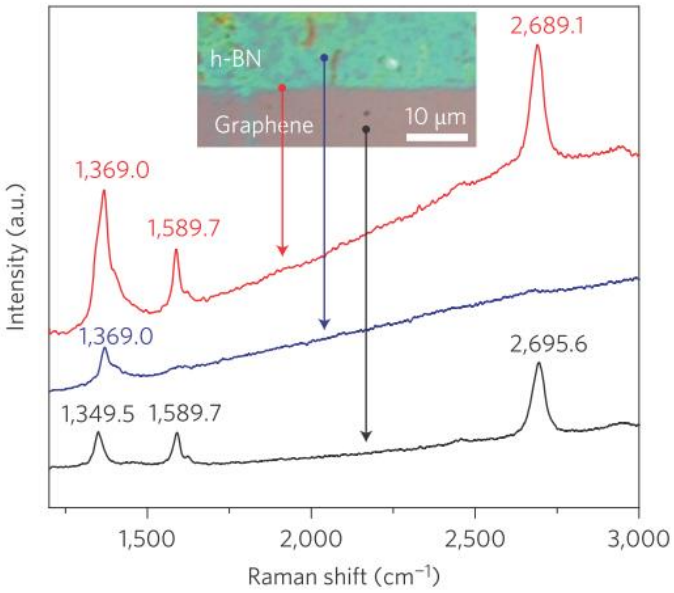

Figure 2-2: Raman spectra collected in graphene, h-BN regions and their interface in a graphene/h-BN film. *Reference: Liu et al.* [45]

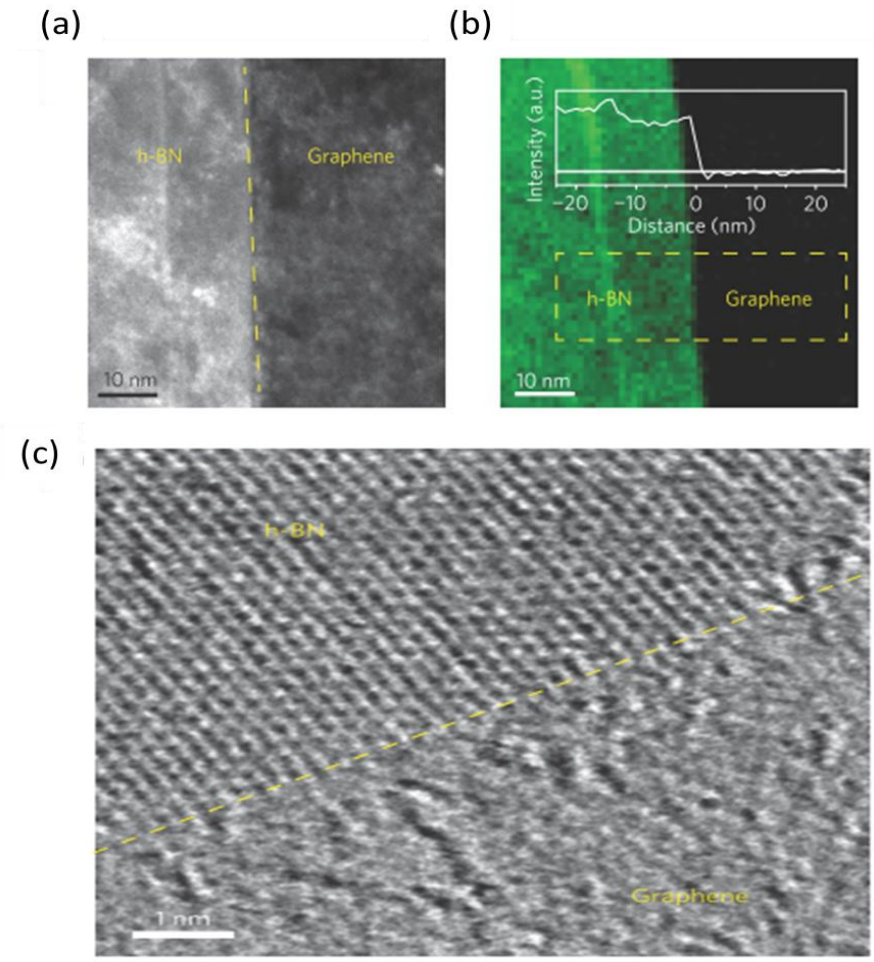

Figure 2-3: (a) STEM-ADF image shows the graphene/h-BN interface. The darker region is graphene and the other is BN. (b) EELS analysis with the inset is intensity profile along the trajectory in the dashed box, showing the sharp interface between the h-BN and graphene. (c) STEM bright field (BF) imaging of the graphene/h-BN interface. *Reference: Liu et al.* [45]

The interface can be also visible with either annular dark field (ADF) (**Figure 2-3** (a) & (b)) or bright-field STEM images (**Figure 2-3** (c)) with the interface marked as a dashed line. **Figure 2-3** (b) is the STEM image with the analysis using electron energy loss spectroscopy (EELS) showing more clearly the interface.

The fabrication method and techniques presented above were also used successfully in several works to synthesize in-plane graphene/BN with either armchair or zigzag interface.[36,43]

On theoretical side, the advancement of research is also very exciting with different works on bilayer Graphene/BN [98–101], B(N) doping in graphene [102,103] and in-plane domains of

Graphene/BN [34,35,46,47,74,104–108]. Most of these works have been focused on solving the gapless problem of graphene. In Ref.[98], by using ab initio calculation, Giovannetti et al. demonstrated that a relative large bandgap about 53 meV can be open in a structure of a Graphene sheet on top of a lattice-matched BN substrate. In the case of bilayer Graphene/BN, it was also reported that bandgap is tunable from 0 to about 130 meV by using a vertical electric field.[99,100] In the case of in-plane Graphene/BN heterostructures bandgap can be even larger thanks to confinement effect in ribbons. In Refs.[35,108] the authors showed that bandgap in a hybrid structure with an armchair graphene ribbon embedded between two BN armchair ribbons may range from few hundred meV to larger than 1eV for different sub-ribbon widths. In-plane zigzag structure of a zigzag Graphene ribbon and a zigzag BN ribbon with Hydrogenated edges was also confirmed to exhibit bandgap with narrow sub-ribbons.[34] There are thus several works that have paid attention on bandgap opening in in-plane Graphene/BN hybrid structure, but a systematic study is still missing. Additionally, we know that transport properties not only depend on bandgap but also on other electrical properties of energy band such as density of states, group velocity, Fermi energy,... Moreover, almost all theoretical works have been based on ab initio calculations which are usually limited to small ribbon widths, i.e. in the range 1-2 nm.

In this work, by using Tight Binding (TB) simulation that allows us to consider a larger range of ribbon widths, two types of structures of G/BN are investigated: (i) structures with interfaces perpendicular to the transport direction and (ii) structures with interfaces parallel to the transport direction. We demonstrate that tunable bandgaps are open in these structures and we also examine further electronic properties of band structure to determine which configuration is better for electronic transport.

This chapter is organized as follows: In section 2.2 we briefly describe the models and methodologies we have used for the chapter. In section 2.3, we present and discuss in details the results obtained for armchair (section 2.3.1) and zigzag ribbons (section 2.3.2). Finally, we make some concluding remarks in section 2.4.

2.2 The modeling and methodologies

We will consider many possible configurations of armchair and zigzag hybrid Graphene/BN ribbon. For each kind of edge orientation (armchair or zigzag), we can distinguish different kinds of hybrid structures:

(1) First kind of structures: interfaces perpendicular to the transport direction. These structures with alternating arrangement of graphene and BN sections forming a superlattice are called superlattice structures.

(2) Second kind of structures: interfaces parallel to the transport direction. There are basically two configurations of this type of heterostructures: (i) a system containing one graphene and one BN ribbon which is called armchair (zigzag) G/BN system, and (ii) a system containing two graphene (BN) ribbons separated by a BN (Graphene) ribbon which is called armchair (zigzag) BN/G/BN (G/BN/G) structure.

Electronic energy bands of these structures will be first investigated on the basis of a simple tight binding model with nearest neighbor interactions with the aim of understanding the physics with qualitative results. More sophisticated calculation will be described for specific models in each chapter later. Within this simple approach, the Tight Binding Hamiltonian can be in the form of formula (1-21) in chapter 1:

$$H = \sum_i \varepsilon_i |i\rangle\langle i| - \sum_{\langle i,j \rangle} t_{ij} |i\rangle\langle j| \tag{2-1}$$

Here we use the sign "-" before t_{ij} which implicitly assumes that t_{ij} is taken as a positive number in the calculation. Since the structures are periodic along *x* direction, the Schrodinger equation can be simplified into the equation of one unit cell as we demonstrated in chapter 1:

$$h.\phi_0 = E.\phi_0 \tag{2-2}$$

where $h = H_{n,n-1}e^{-ik_x a_x} + H_{nn} + H_{n,n+1}e^{ik_x a_x}$ contains the matrix of the *n-th* unit cell H_{nn} and the coupling of this unit cell to its neighboring unit cells (*n-1*)-th and (*n+1*)-th via $H_{n,n-1}$ and $H_{n,n+1}$. Since the lattice constant difference of Graphene and BN is less than 5% making stable the in-plane interfaces of Graphene and BN, which has been confirmed by ab initio

calculation with structure optimization[35] and also by experimental observation [45], in all calculations we take the distance between two nearest atoms equal to $a_0 = 0.142$ nm and neglect the relaxation at the interfaces. The periodic constant along *x* is $a_x = 3a_0$ for armchair structures and $a_x = \sqrt{3}a_0$ for zigzag structures. Parameters of on-site energies and hoping parameters are taken from ref. [35] (see **Table 2-1**) which were parameterized to fit to first principles calculation.

Table 2-1: Tight Binding parameters used in this chapter for the study of electron properties of in-plane Graphene/BN structures

E_{C_A} (eV)	E_{C_B} (eV)	E_B (eV)	E_N (eV)	t_{CC} (eV)	t_{BN} (eV)	t_{BC} (eV)	t_{NC} (eV)
0.015	-0.015	1.95	-1.95	2.5	2.9	2.0	2.5

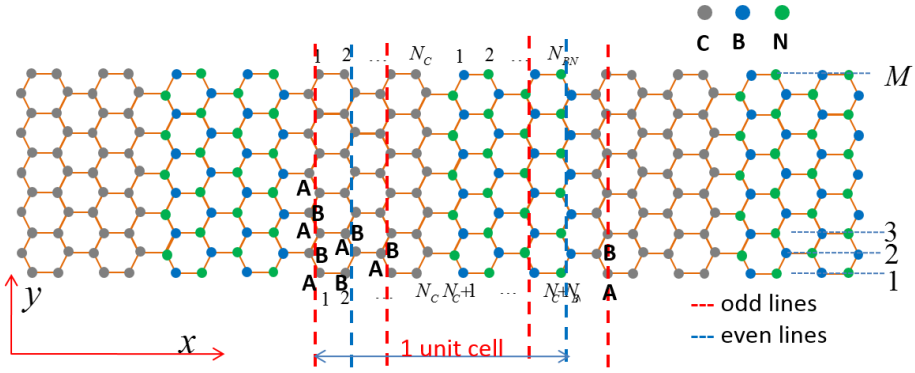

Figure 2-4: Armchair G/BN superlattice structure with graphene and BN sections arranged alternatively along transport direction *Ox*. There are N_C Carbon lines and N_{BN} Boron Nitride lines in one unit cell.

(a) Armchair G/BN nanoribbons

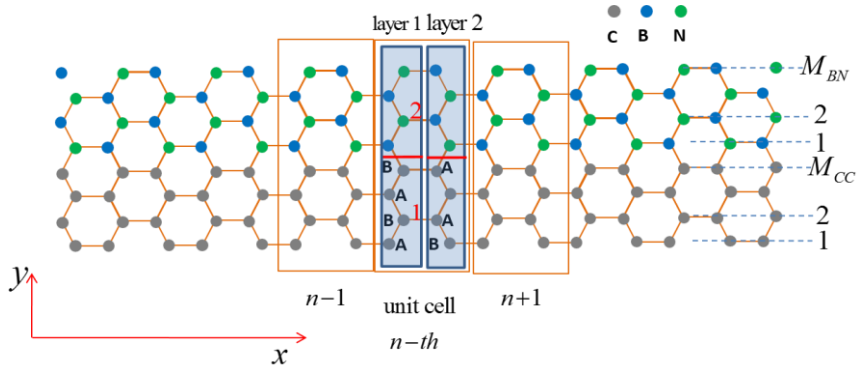

(b) Armchair G/BN/G nanoribbons

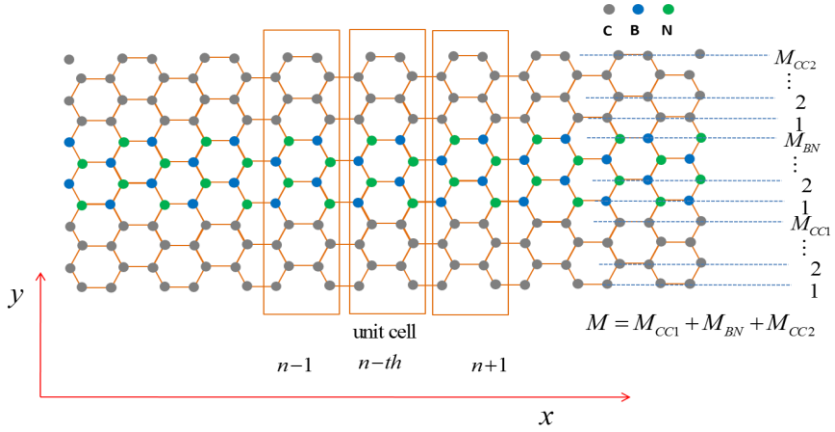

(c) Armchair BN/G/BN nanoribbons

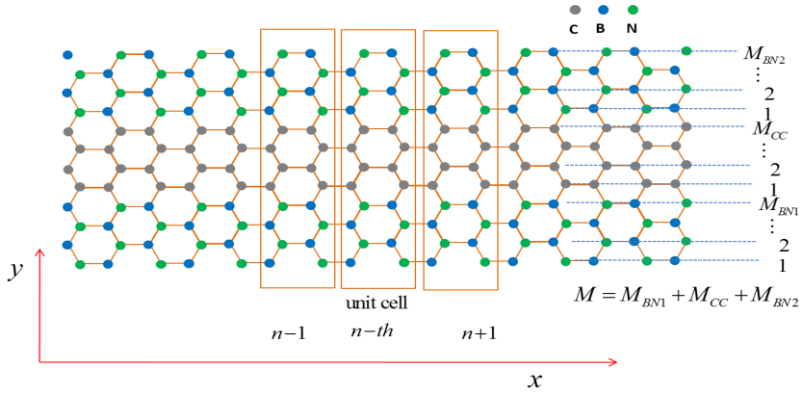

Figure 2-5: Heterostructures of Armchair G/BN ribbons with interfaces parallel to the transport direction *Ox*. (a) Armchair G/BN structures with two sub-ribbons (b) Armchair G/BN/G ribbons with a BN ribbon embedded between two other Graphene ribbons. (c) Armchair BN/G/BN ribbons with a graphene ribbon embedded between two other BN ribbons.

2.3 Results and discussion

In this section we focus on examining the electronic band structures of different armchair and zigzag ribbons of Graphene/BN heterostructures, in particular in terms of bandgap and transport properties.

2.3.1 Bandgap opening in armchair Graphene/BN ribbons

First of all, four possible configurations of armchair Graphene/BN ribbons are considered, including the armchair G/BN superlattice as sketched in **Figure 2-4**, the armchair G/BN ribbons, the armchair G/BN/G and the armchair BN/G/BN schematized in **Figure 2-5**.

In **Figure 2-6** we plot the band structure of these four heterostructures (**Figure 2-6** (b-e)) for a first look at the shape of energy bands. They are also compared to the band structure of an armchair graphene ribbon of same width $M = 8$ (**Figure 2-6** (a)). At the first glance we can see that the band structures of the armchair hybrid ribbons are quite different from that of the pure armchair graphene ribbon. In particular, these structures have a finite gap compared to the gapless nature of the armchair graphene ribbon. The electronic bands of the superlattice structure is very different from those of the parallel interface structures with larger bandgap and flatter bands. Since the electronic bands of heterostructures are strongly dependent on geometrical parameters of each sub-section/ribbons, to analyze better the electronic properties of these structures, we are going to consider them one by one.

2.3.1.1 The armchair superlattice graphene/BN ribbons

Because bandgap is the essential concern in graphene, let us first start to examine the bandgap in the armchair superlattice structure of **Figure 2-4**. Though some mini gaps can be observed in the band structure, as seen in **Figure 2-6**(b), we are only interested in the main gap around the neutrality point. So the bandgap can be determined as the difference of energy between the lowest conduction band and the highest valence band. Since the structure is defined by the parameters M, N_C, N_{BN} the electronic structure strongly depends on these geometrical parameters.

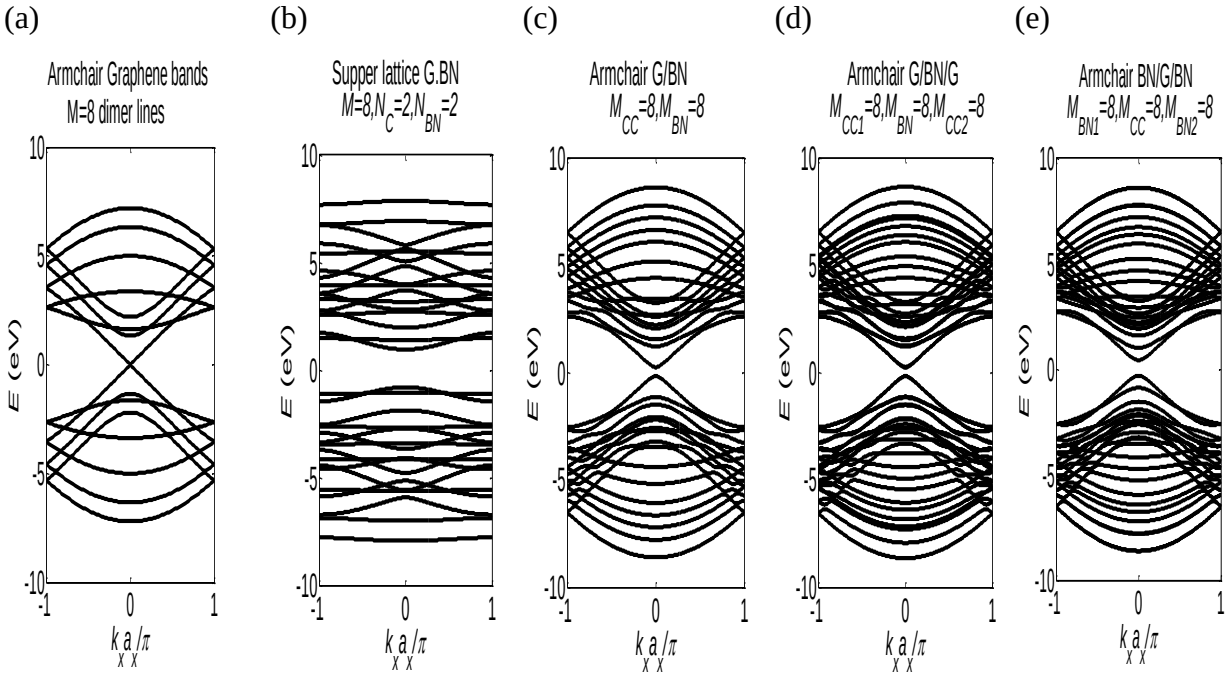

Figure 2-6: Energy bands of different armchair ribbons: (a) pure armchair graphene with M = 8, (b) superlattice G.BN with M = 8, $N_C = N_{BN}$ = 2, (c) Armchair G/BN with M_{CC} = 8, M_{BN} = 8, (d) Armchair G/BN/G with $M_{CC1} = M_{CC2}$ =8, M_{BN} = 8, (e) Armchair BN/G/BN with $M_{BN1} = M_{BN2}$ =8, M_{CC} = 8.

In chapter 1 we have seen that the energy gap in armchair graphene (also in armchair BN) ribbons are sorted into three groups according to the number of dimer lines M along the width: $M = 3p$, $3p + 1$ and $3p + 2$. It is thus needed to consider the modulation of the gap with different ribbon width M. It is also noticed that the size of a super cell ($N_C + N_{BN}$) and the ratio between graphene and BN sections in a cell will certainly affect the electronic properties of the structure because they determine the range of electron scattering.

To analyze the influence of these factors we will look at the dependence of bandgap on the ratio $r = N_{BN} / N_C$ for each group of width M. We will consider three possible cases of r: $r = 1$ for equal contributions of graphene and BN into a cell, $r > 1$ where BN dominates the structure and $r < 1$ where graphene dominates the structure.

(a) (b) (c)

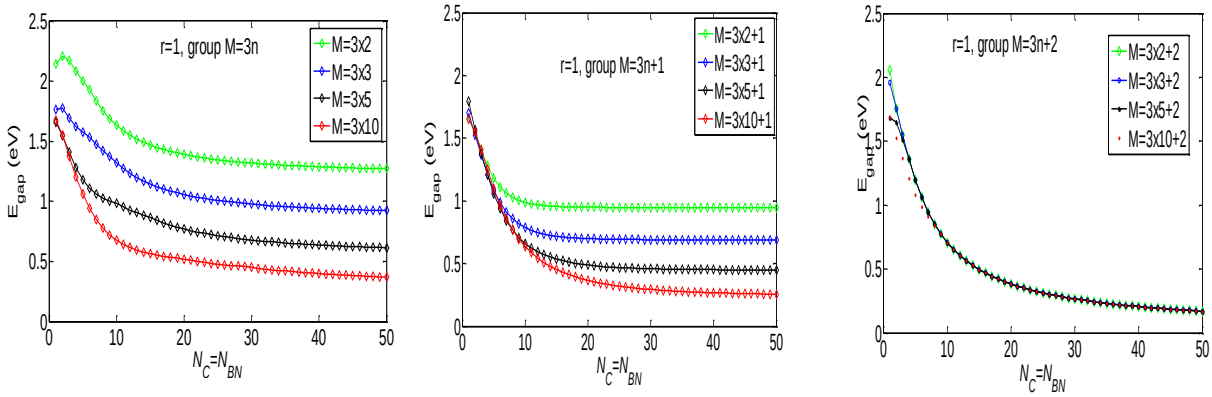

Figure 2-7: Bandgap for the case r = 1: (a) group $M = 3n$, (b) group $M = 3n + 1$, (c) group $M = 3n + 2$.

In **Figure 2-7** we can observe basically that bandgap tends to reduce with the increase of the lengths N_C and N_{BN} of each graphene/BN section in a cell. First, the gap has a sharp drop in the range $N_C = N_{BN}$ = 1:10 with values falling from about 2 eV to about 0.7 eV depending on the width M of the ribbon. Then the degradation is weaker and tends to a saturation at large size of graphene/BN sections. Interestingly, in the group $3p + 2$ the finite bandgap does not depend on the width M (exception at narrow N_C, N_{BN}) for all pairs of N_C and N_{BN}. Meanwhile the bandgap of this group was found equal to zero for the case of pure armchair graphene as we have seen in section **1.7.2.2** in Chapter 1. Thus our primary conclusion is that the bandgap is open in the group $3p + 2$ due to the presence of BN and the armchair G/BN superlattice ribbons are always semiconducting.

The results displayed in **Figure 2-8** for $N_C > N_{BN}$ ($r < 1$) and **Figure 2-9** for $N_{BN} > N_C$ ($r > 1$) show that the bandgap in this heterostructure of graphene/BN is sensitive to the size of graphene regions and less sensitive to the length of BN regions. This result can be understood because BN is an insulator so it only has significant effect to the energy band of the heterostructure at high energy. Meanwhile in the low energy region, the energy bands come mainly from electron orbitals of Carbon atoms. Moreover, the bandgap is defined from the lowest conduction band and the highest valance band which are in the low energy region. Hence, the bandgap must strongly depend on the graphene region. In principle, the bandgap decreases with the increase of the length N_C of graphene regions as we can observe in **Figure 2-8**. In contrast, it increases rapidly with the increase of N_{BN} at low values of N_{BN} ($N_{BN} < 10$).

This result is in agreement with first-principles calculation for narrow cells of the superlattice structure studied by Li et al.[109] The gap remains unchanged even for large BN areas (**Figure 2-9**). We can thus conclude that graphene dominates the bandgap size in the superlattice armchair graphene/BN structure.

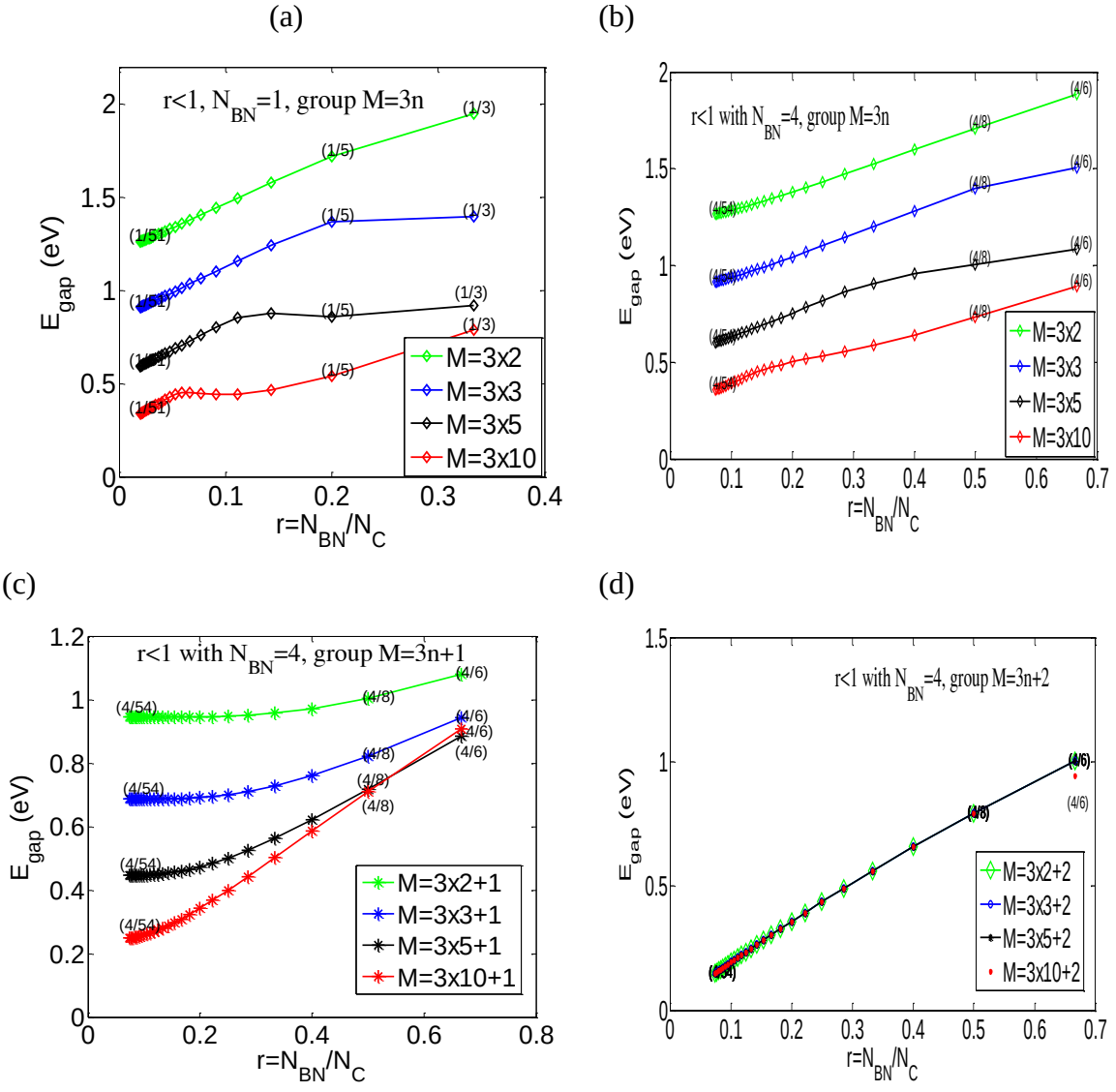

Figure 2-8: Bandgap in the superlattice armchair graphene/BN structures in the case where graphene dominates the supercell ($r < 1$).

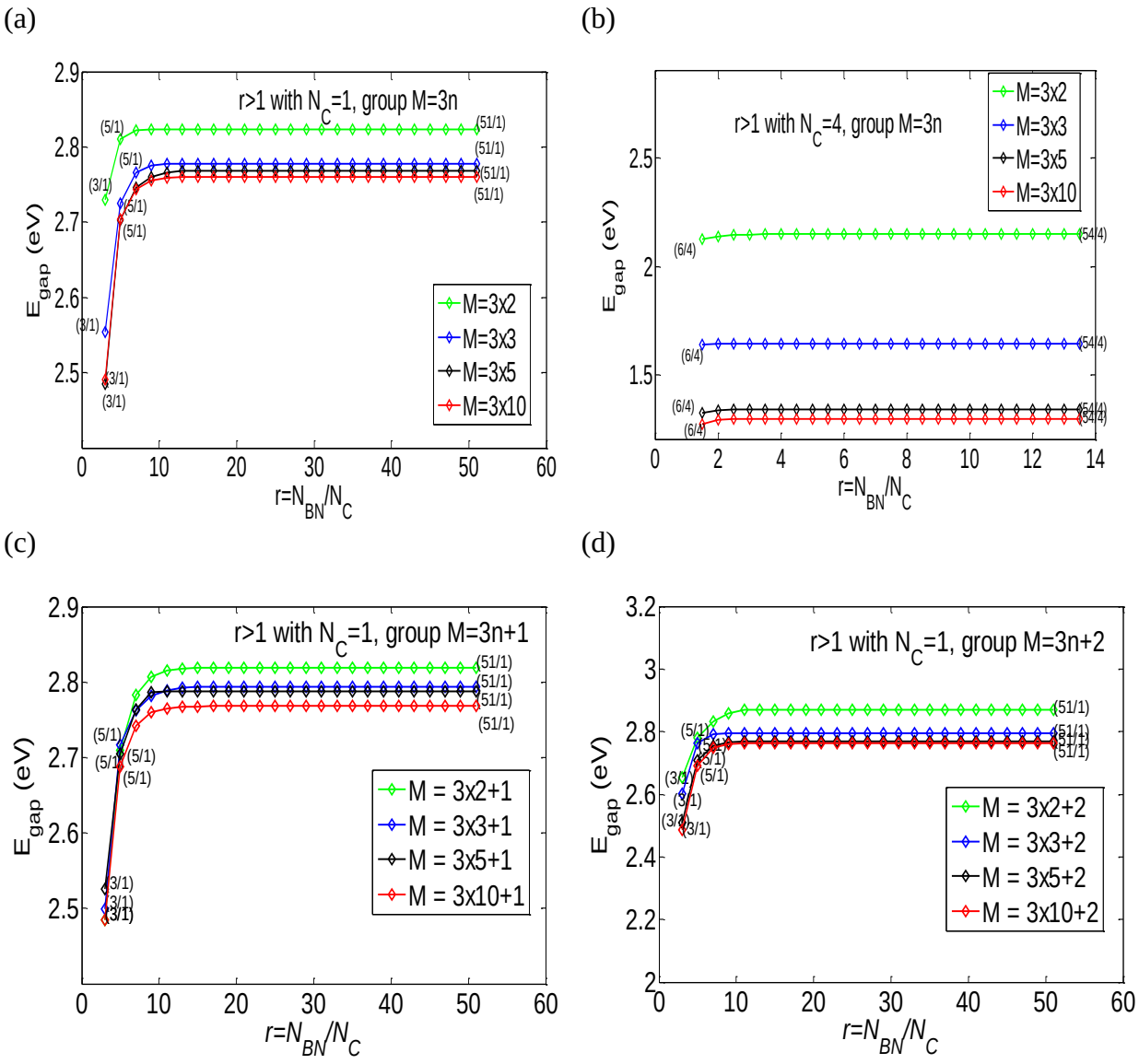

Figure 2-9: Bandgap in the superlattice armchair Graphene/BN structure in the case where BN dominates the supercell ($r > 1$).

2.3.1.2 The parallel interface structures of armchair graphene/BN ribbons

We are now going to examine the bandgap in the three parallel interface structures as sketched in **Figure 2-5**. In these structures, each unit cell only covers two chain lines so that the band structure only depends on two main parameters, i.e. M_{BN} and M_{CC}. Let us consider $M_{BN1} = M_{BN2} = M_{BN}$ for the armchair BN/G/BN structures and $M_{CC1} = M_{CC2} = M_{CC}$ for the armchair G/BN/G structures. We will later discuss for the case $M_{CC1} \neq M_{CC2}$.

In **Figure 2-10**(a) we show the bandgap in the armchair G/BN structure as a function of M_{CC} for a few values of M_{BN} ranging from 1 to 10. It first shows that the bandgap is fluctuating

with the width of graphene ribbon as previously observed in pure armchair graphene, but the bandgap always exists in this structure. The dependence of bandgap on BN ribbon width M_{BN} is strong when M_{BN} increase from 1 to 2 and become weaker for larger M_{BN}. This dependence can be seen in **Figure 2-10**(b) where bandgap is plotted as a function of M_{BN}. It can be recognized that for all cases of M_{CC}, the bandgap is only effected by BN if $M_{BN} < 8$, and remains unchanged for larger BN ribbons. The insensitivity of bandgap to BN is thus similar to what we have observed in the superlattice structures above. In **Figure 2-10**(c) and (d) we plot three groups of bandgap with respect to the graphene width $M_{CC} = 3p$, $3p + 1$ and $3p + 2$ for two cases of $M_{BN} = 1$ and 10. Interestingly, if in a pure armchair graphene ribbon we have zero gap for group $3p + 2$ and bandgap order is $3p + 1 > 3p > 3p + 2$ (see section **1.7.2.2** in chapter 1), here we observe a bandgap opening for the group $3p + 2$ and a new order of bandgap size $3p > 3p + 1 > 3p + 2$.

A similar result can also be seen in **Figure 2-11**(a) for the armchair structure G/BN/G. Among three configurations illustrated in **Figure 2-5**, it seems that this armchair G/BN/G is the structure where BN has the higher influence. Indeed if $M_{BN} = 0$ or is very small, the two graphene ribbons are very close and they certainly have a coherence. It is thus needed to discuss more about the effect of M_{BN} on the bandgap in this structure. In **Figure 2-11**(b) we plot the bandgap as a function of M_{BN} for different values of M_{CC}. Interestingly, there is a phase transition from semi-metallic to semiconducting when M_{BN} increases from 1 to larger values when $M_{CC} = 17$, that means for the group $3p + 2$. This results can be also seen from triangles ($M_{BN} = 1$) and circles ($M_{BN} = 10$) red curves in **Figure 2-11**(a). Additionally, if in the armchair superlattice (**Figure 2-9**) and the armchair G/BN structure (**Figure 2-10**(b)) the bandgap quickly saturates for $M_{BN} > 8$, here we observe from **Figure 2-11**(b) that for a given M_{CC} the bandgap is stable only for $M_{BN} > 15$.

The armchair G/BN/G structure is also a good example to examine the effect of difference in the width of the two Graphene sub-ribbons. **Figure 2-12** is dedicated to the case $M_{CC1} \neq M_{CC2}$. Here we can see that the bandgap in the case $M_{CC1} = 15$, $M_{CC2} = 25$ is very close to gap of the case $M_{CC1} = M_{CC2} = 25$ which has smaller bandgap than in the case $M_{CC1} = M_{CC2} = 15$. The gap is even identical to the gap of the case $M_{CC1} = M_{CC2} = 25$ when M_{BN} is large enough ($M_{BN} > 5$). Thus if $M_{CC1} = a$, $M_{CC2} = b$ then the gap of the system is almost equal the smaller gap of two cases $M_{CC1} = M_{CC2} = a$ and $M_{CC1} = M_{CC2} = b$. Hence, studying the case $M_{CC1} = M_{CC2} = M_{CC}$ is enough for understanding the physics of all cases.

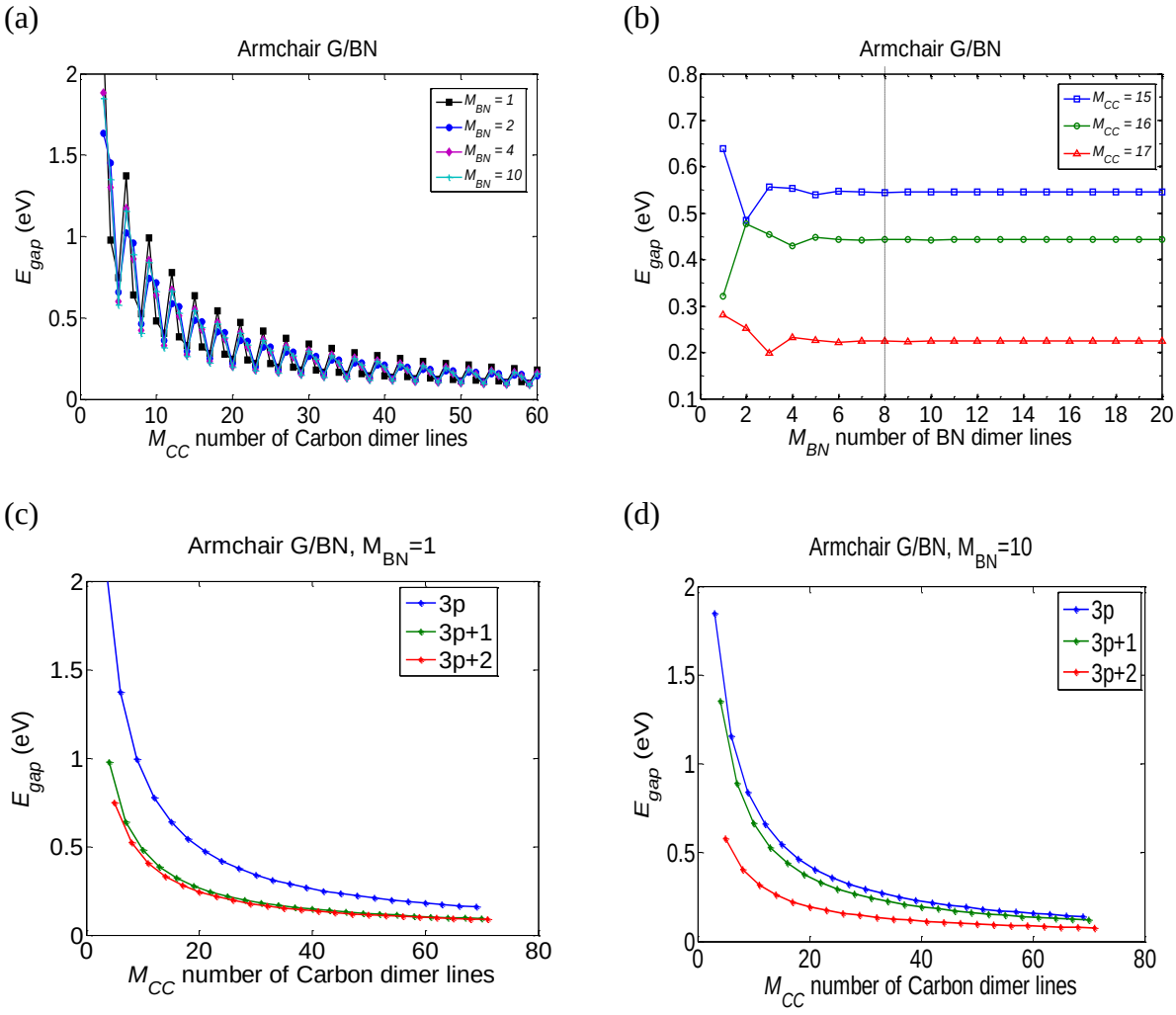

Figure 2-10: (a) Bandgap in armchair G/BN structure is plotted as function of (a) M_{CC} and (b) M_{BN}. (c) and (d) three groups of bandgap as a function of graphene ribbon width with M_{BN} = 1 and 10, respectively.

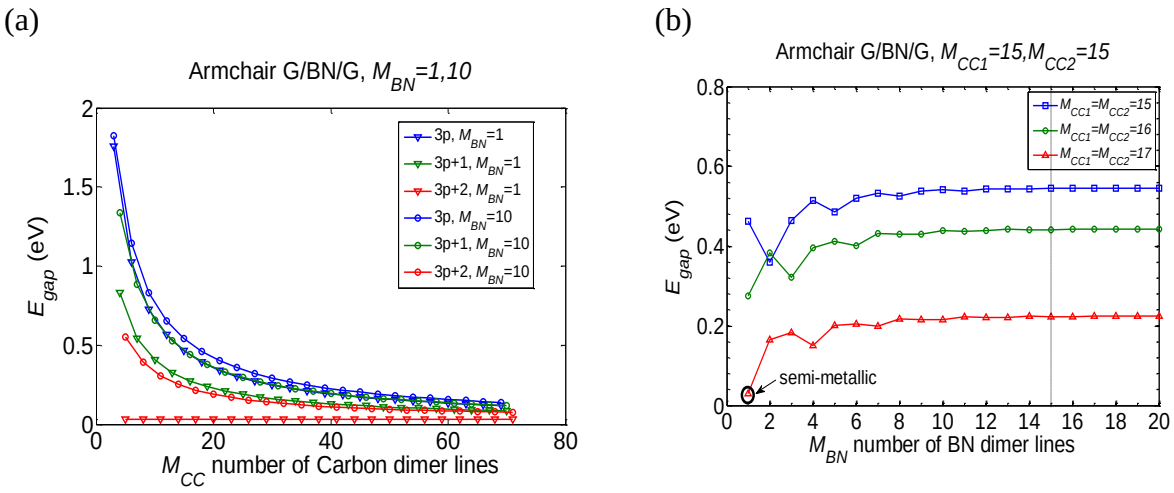

Figure 2-11: Bandgap in the armchair G/BN/G structures as a function of M_{CC} and M_{BN}.

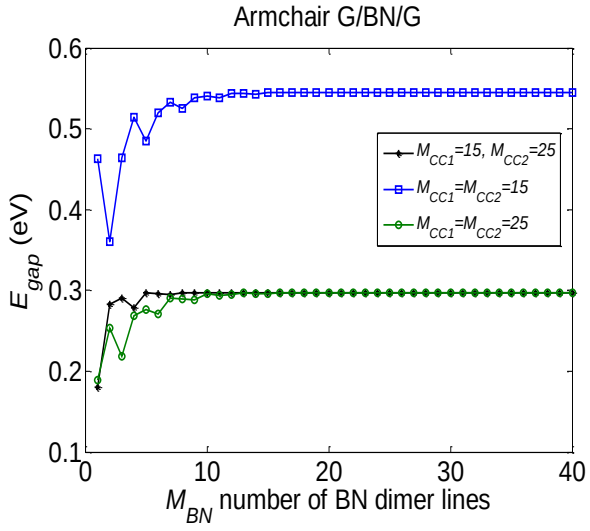

Figure 2-12: Bandgap in the armchair G/BN/G structures for the case $M_{CC1} \neq M_{CC2}$.

Unlike the cases of the armchair G/BN and G/BN/G ribbons where only one edge of a graphene ribbon is connected to BN while the other edge is free, in the armchair BN/G/BN ribbons, both edges of the graphene ribbon are modified by BN ribbons. It is thus expected that energy bands of graphene are affected more strongly in this case. Indeed, if the order of energy gaps among the different group remains $3p > 3p + 1 > 3p + 2$ for both configurations armchair G/BN and G/BN/G when we increase the width of BN region, in **Figure 2-13** we see a strong change in this order when the BN ribbon widths increase, i.e. for $M_{BN1} = M_{BN2} = 1$ we have the hierarchy $3p > 3p + 2 > 3p + 1$ (**Figure 2-13**(a)), but it is quickly upset and changed

to $3p + 1 > 3p > 3p + 2$ when $M_{BN1} = M_{BN2} = 2$ (**Figure 2-13**(b)). A new arrangement is set up for $M_{BN1} = M_{BN2} \geq 3$ with the bandgaps in the order $3p > 3p + 1 > 3p + 2$ (**Figure 2-13**(c-d)). This final arrangement is thus the same as what we have observed in the armchair G/BN and G/BN/G ribbons and in agreement with conclusions in Refs.[35,108]

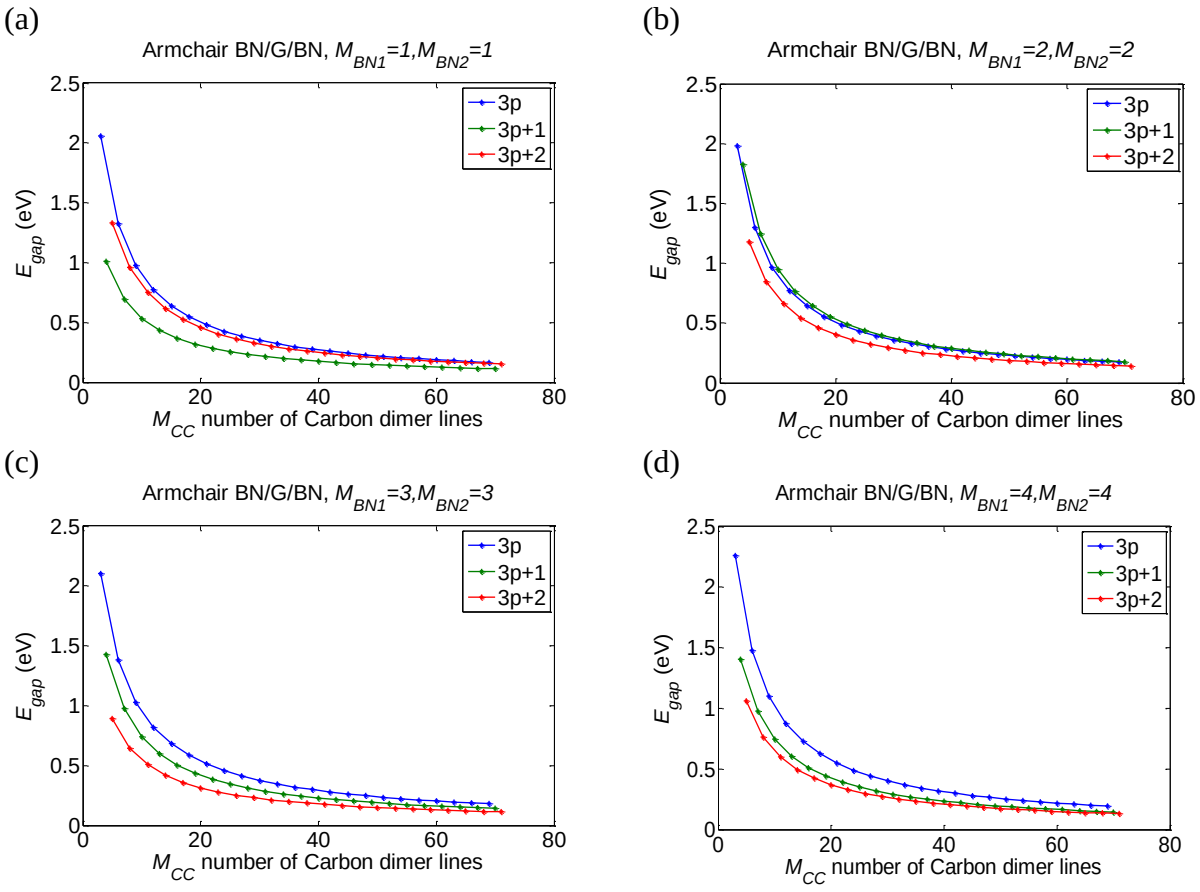

Figure 2-13: Bandgap in the armchair BN/G/BN structures as a function of M_{CC} and M_{BN}.

To compare the bandgaps between these different structures and between these structures and pure armchair graphene, in **Figure 2-14** we separate the three bandgap groups and fix M_{BN} = 10 for the G/BN structures. The circle lines are the results for the armchair G/BN structures, the triangular lines are the results for the armchair BN/G/BN structures, the square lines are corresponding to the armchair G/BN/G structures and the star lines are for pure armchair graphene. From **Figure 2-14** we can see that the bandgap of the G/BN and the G/BN/G structures are almost the same for all three groups. Their bandgaps are larger than bandgap of pure armchair graphene in the group $3p + 2$ and almost equal in the group $3p$ while it is found

slightly smaller in the group 3*p* + 1. The bandgaps of the BN/G/BN ribbons are larger than that of the others in most cases, exception for 3*p* + 1. Thus armchair BN/G/BN configuration is an efficient design in which larger bandgap can be obtained.

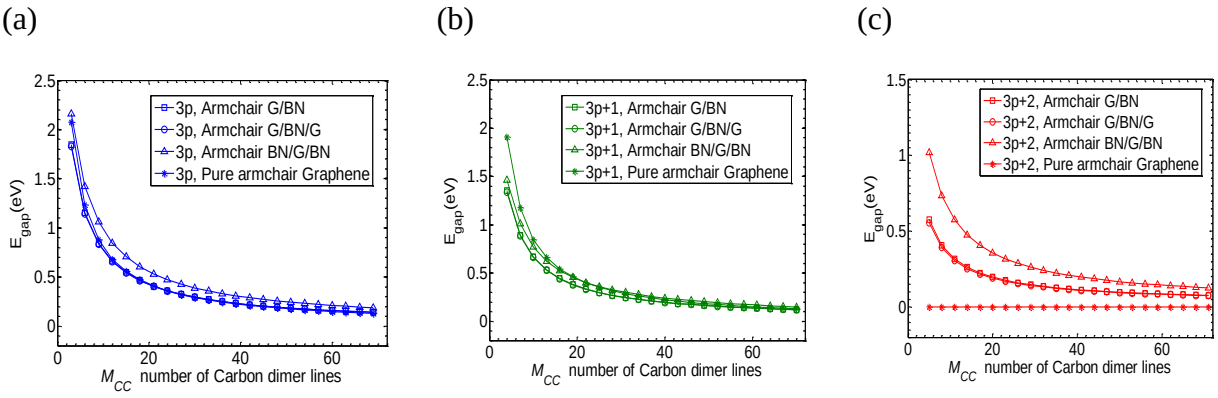

Figure 2-14: Comparison bandgap of pure armchair graphene ribbons and armchair Graphene/BN structures width different configurations. Here we fix M_{BN} = 10 for all structures of graphene/BN.

The above analysis of bandgap indicates that bandgap is open in both the perpendicular and parallel interface structures. However, to be applied for transport, other features such as DOS, Fermi energy, group velocity or effective mass should be also considered. In **Figure 2-15** we show the energy bands and DOS for two structures which have the same total width M = 59: **Figure 2-15** (a) is for the armchair superlattice structure with N_C = 3, N_{BN} = 1 and **Figure 2-15** (b) is for the armchair G/BN/G structure with M_{CC1} = M_{CC2} = 15 and M_{BN} = 29. It should be noted that the shape of band structures for the armchair G/BN and BN/G/BN structures are quite similar to that of the armchair G/BN/G structure.

(a) (b)

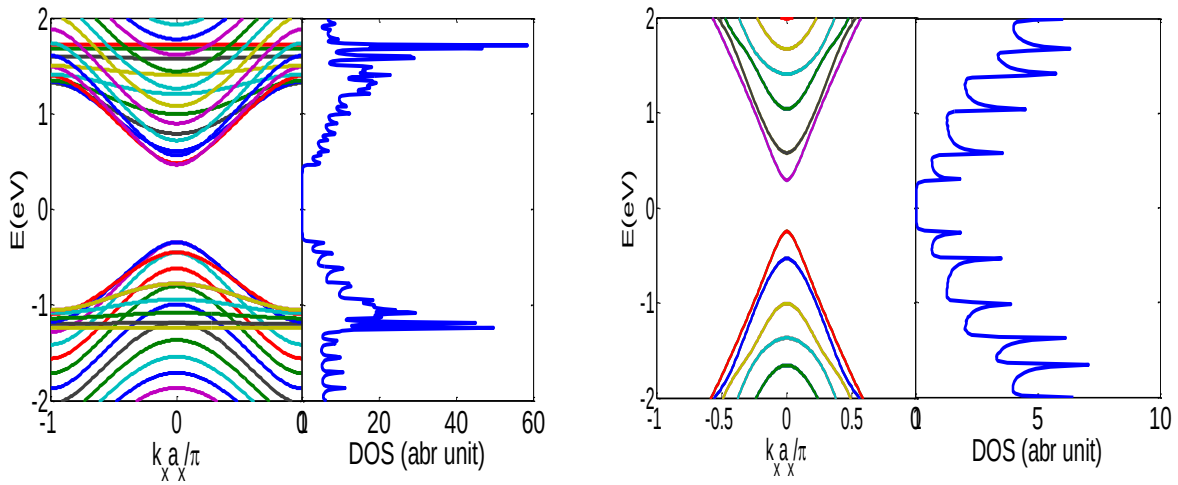

Figure 2-15: Energy bands and density of states of (a) a superlattice structure with N_C = 3, N_{BN} = 1, M = 59 dimmer lines. (b) An armchair G/BN/G structure with M_{CC1} = M_{CC2} = 15, M_{BN} = 29.

First of all, we can see that DOS in both systems are not perfectly symmetric around zero energy, which means that the neutrality points E_N in both systems are no longer localized at zero energy like in the case of pure armchair graphene. In fact, It was found out that E_N = 0.14 eV for the superlattice structure and 0.198 eV for the G/BN/G structure. The shift of the neutrality point of the band structure is due to the fact that the coupling of B and N atoms with C atoms are different, which breaks the symmetry in energy.

In **Figure 2-16** we show a comparison of group velocity in the first conduction band of these two structures with those of pure armchair graphene and BN ribbons of the same width. The embedded structure shows a good behavior for transport with high group velocity compared to very low group velocity in BN, and, to a smaller extent, in the superlattice structure. This result is not surprising because perpendicular scattering is usually stronger than that in the parallel directions. Thus the armchair G/BN/G structure and other parallel interface structures (armchair G/BN and BN/G/BN) appear as good candidates for electronic applications due to both a tunable bandgap and a high electron velocity.

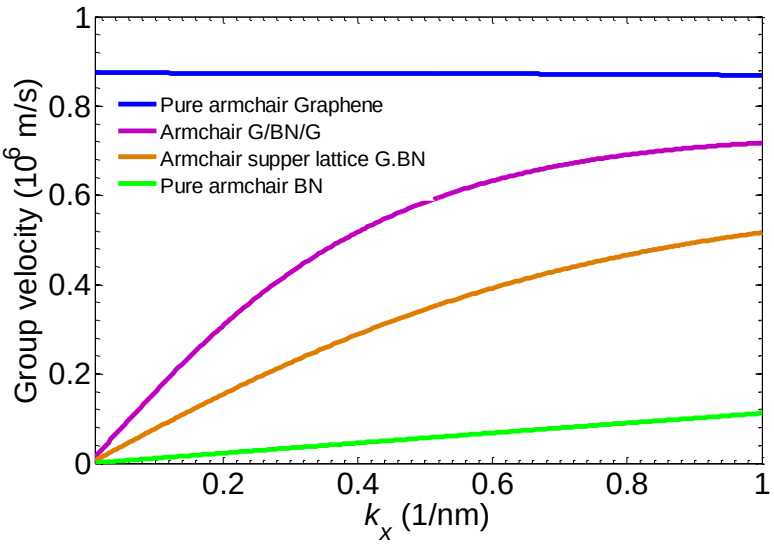

Figure 2-16: Comparison of group velocity in four armchair structures of the same width M = 59 dimmer lines.

2.3.2 Bandgap opening in zigzag Graphene ribbons

We now focus our attention on the parallel interfaces for zigzag structures of graphene/BN. Unlike the case of armchair structures, here we have more configurations because there are more possibilities of coupling between graphene and BN ribbons. We may have either B or N atoms connected to Carbon atoms at the interfaces. For the case of zigzag G/BN ribbons we have two possible configurations with either B-C or N-C connections at the interface, as shown in **Figure 2-17**. The bandgaps of these structures are plotted in **Figure 2-18** and we can see that a bandgap is open in these structures in contrast with the gapless case of zigzag graphene ribbons, as shown in chapter 1. The influence of BN width is still small, as in the case of armchair structures. Interestingly, **Figure 2-18**(a) and (b) indicate that the bandgap changes monotonically with the modulation of graphene ribbon width, which may be important to control the bandgap more easily than in the case of armchair ribbons.

(a) Nano roads zigzag G/BN with B-C bonding

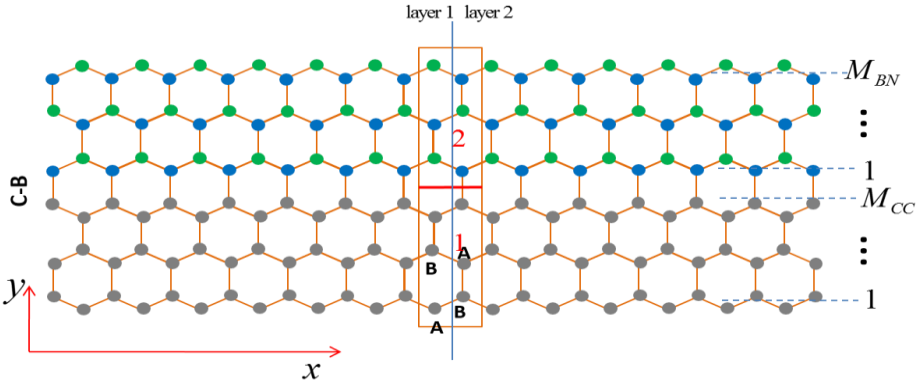

(b) Nano roads zigzag G/BN with N-C bonding

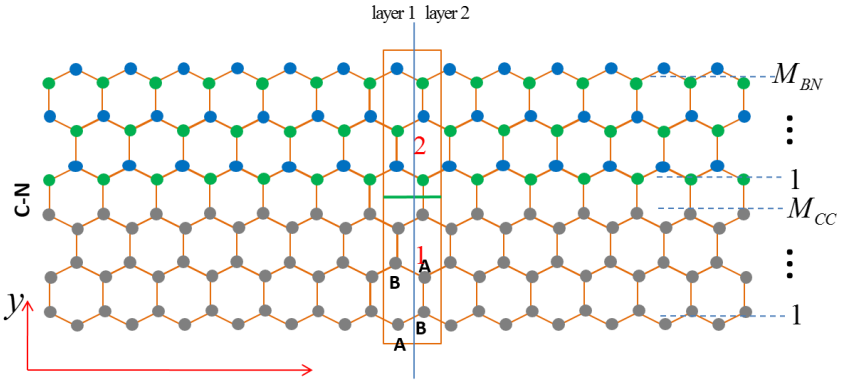

Figure 2-17: Zigzag graphene/BN with two configurations: (a) B-C and (b) N-C connections at the interface.

In the case of the embedded structures: the zigzag G/BN/G has only one configuration with one interface is B-C connections and the other with N-C connections as shown in **Figure 2-19**. Meanwhile, the zigzag BN/G/BN has three different configurations with bonding at interfaces are B-C--C-B, N-C--C-N and B-C--C-N as sketched in **Figure 2-20**. The bandgap of the G/BN/G structure is presented in **Figure 2-21**(a), it shows that bandgap of this structure stays firmly at about 30 meV for any width of each sub-ribbon. The persistency of the bandgap is due to the fact that the structure G/BN/G has edge state at the edge of graphene edges which are flat and very close to zero neutrality point (see **Figure 2-22**(a)). These states exist for any width of sub-ribbons and define bandgap of the structure at almost 0 eV. In the B-C--C-B structure we also observe zero gap in most of cases as seen in **Figure 2-21** (b). However, physics is different in this case. Here the bonding at the two edge of graphene are

the same (B-C bonding) so two states at the edges are still the same and identical in band structures (see **Figure 2-22**(b)). So there is no bandgap opening in this case. It is very easy to guess that such kind of physics/result also occurs in the N-C--C-N structure and no gap can be found in this structure.

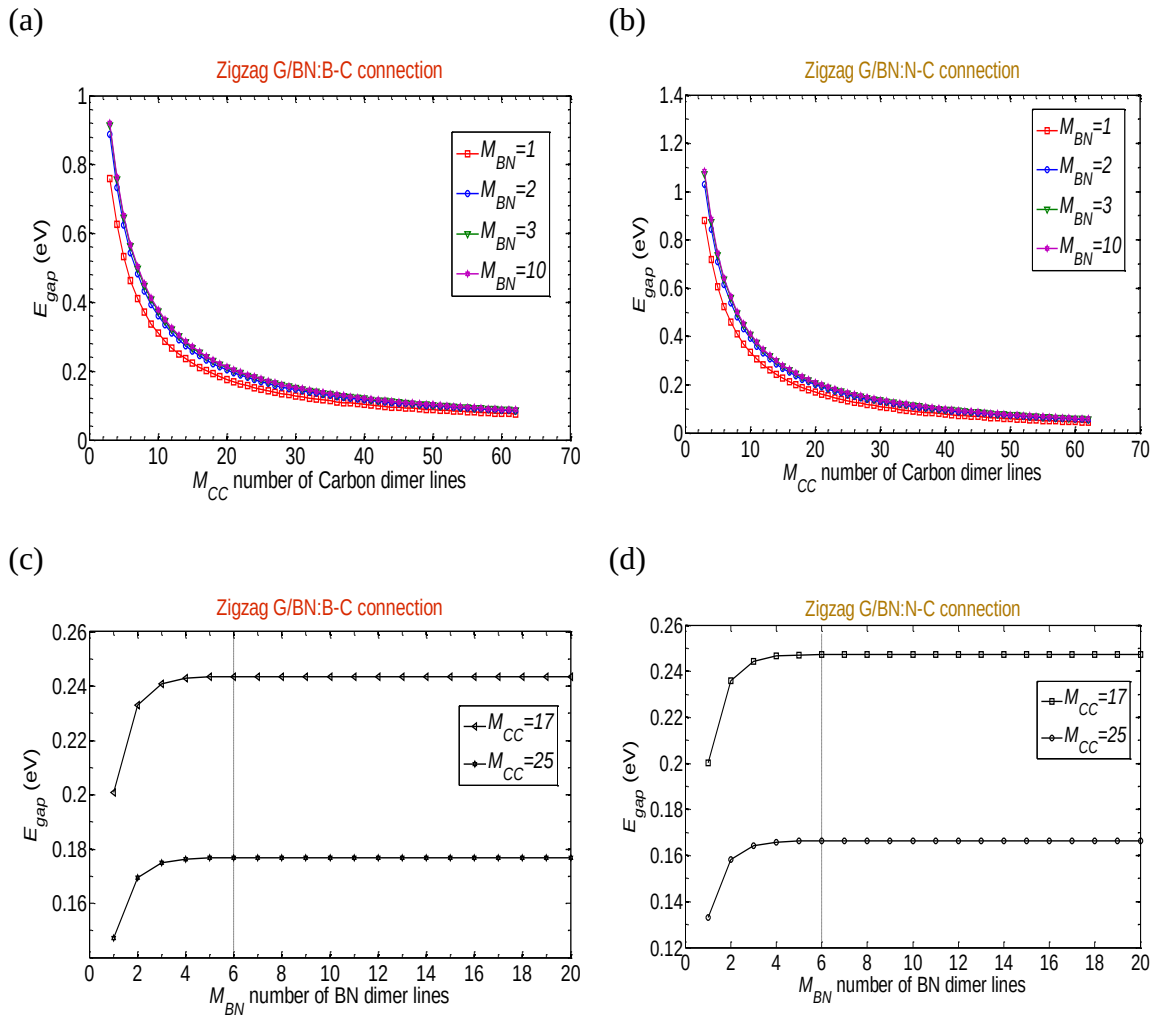

Figure 2-18: (a), (b) Bandgap in the zigzag graphene/BN with B-C connections. (c), (d) bandgap in the zigzag graphene/BN with N-C connections.

Interestingly, sizable gap can be obtained in the case of the zigzag B-C--C-N structure as presented in **Figure 2-22**(c). In this structure, the bandgap is also less sensitive to the BN ribbon widths and monotonic with the increase of graphene ribbon width as in the case zigzag B-C and N-C structures. However, like the case armchair BN/G/BN which has largest gap

among armchair configurations, this zigzag BN/G/BN with B-C--C-N interfaces seems to have a larger gap compared to two cases of zigzag B-C and N-C ribbons, i.e. for M_{CC} = 10, M_{BN} = 10 we obtain a bandgap of 0.63 eV in zigzag B-C--C-N, while it is about 0.38 eV and 0.41 eV for zigzag B-C and N-C ribbons, respectively.

It is worth to notice that edge states are peculiar states in zigzag ribbons of Graphene.[73,90,110], it is thus interesting to consider this kind of states in zigzag structures of Graphene/BN. With the aim of focusing mainly on the bandgap opening in this chapter, the study of edge states is not presented here but in another chapter (chapter 4).

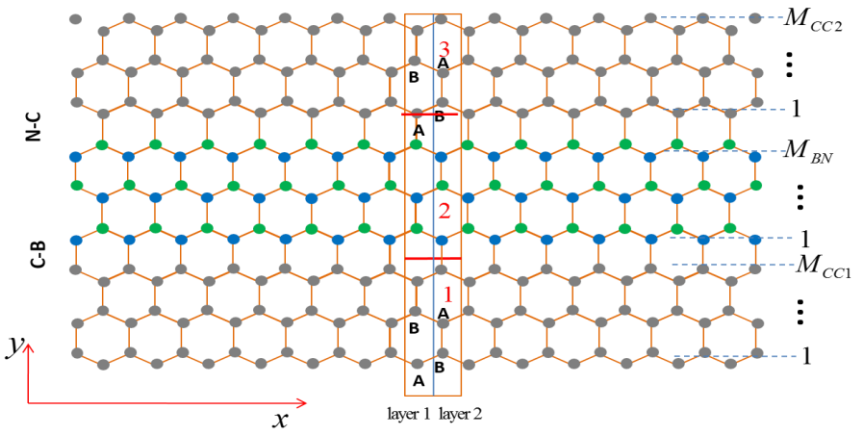

Figure 2-19: The zigzag G/BN/G ribbons have only one configuration.

(a) Zigzag BN/G/BN ribbons with B-C-C-B bonding

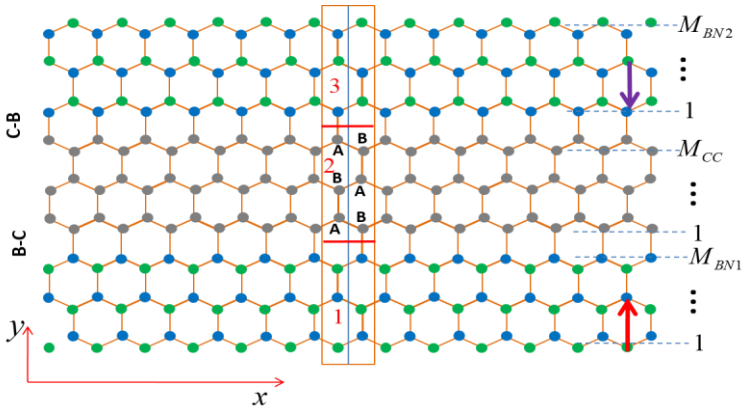

(b) Zigzag BN/G/BN ribbons with N-C-C-N bonding

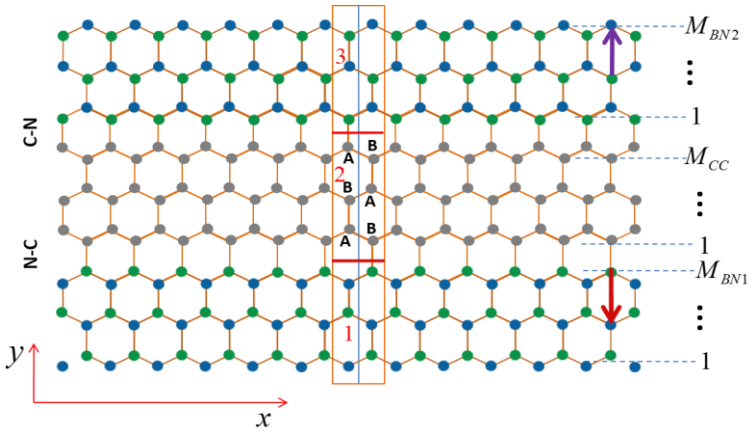

(c) Zigzag BN/G/BN ribbons with B-C-C-N bonding

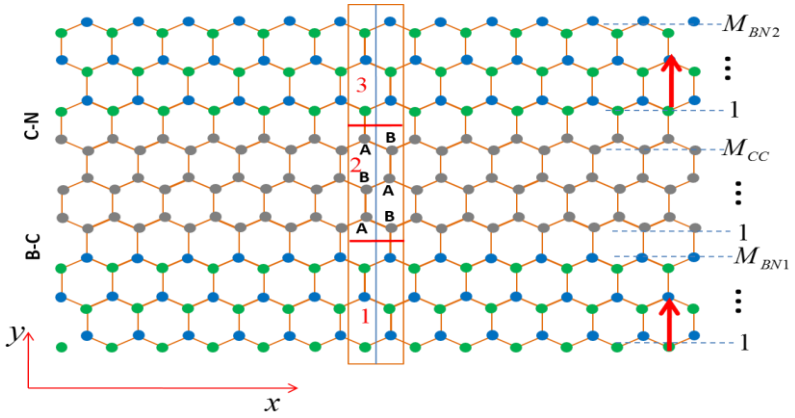

Figure 2-20: The zigzag BN/G/BN has three different configurations of interface connections: (a) B-C--C-B, (b) N-C--C-N, (c) B-C--C-N.

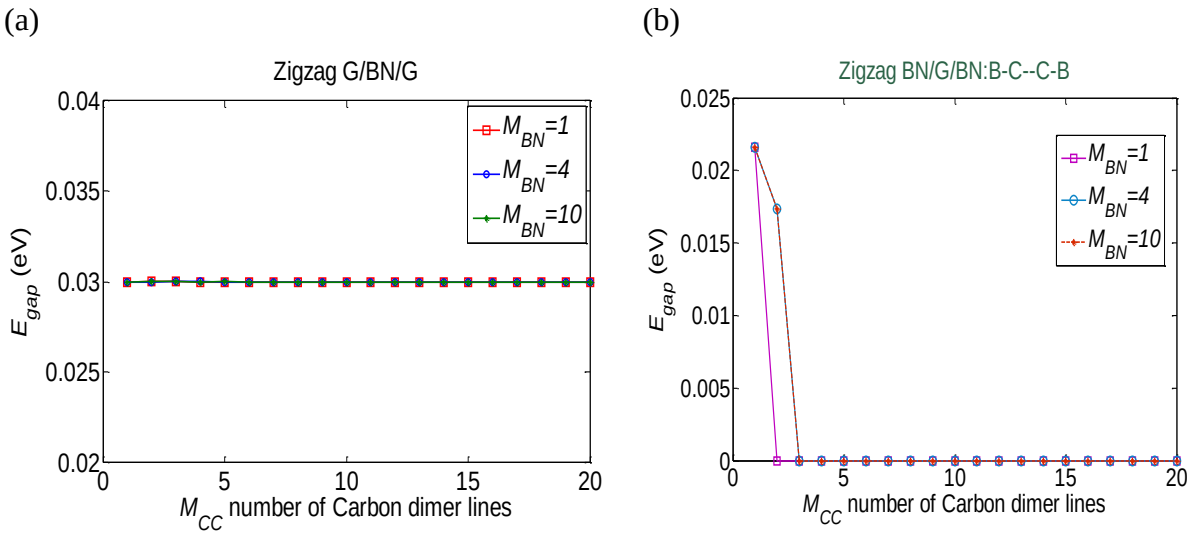

Figure 2-21: Bandgaps in (a) the zigzag G/BN/G and (b) the symmetrical zigzag BN/G/BN with B-C-C-B connections as a function of M_{CC} for several values of M_{BN}.

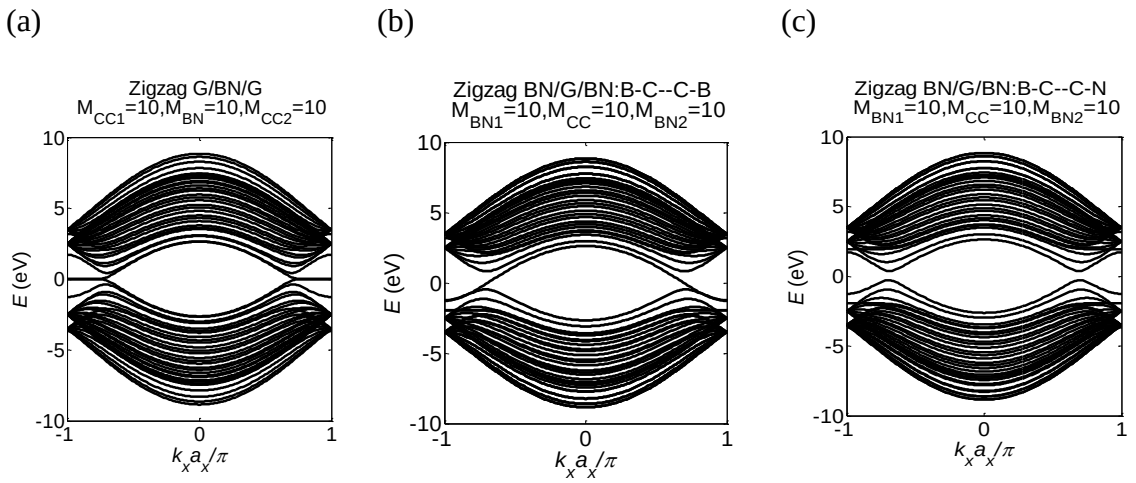

Figure 2-22: Full band structures in (a) zigzag G/BN/G and in BN/G/BN with (b) B-C--C-B and (c) B-C--C-N connections.

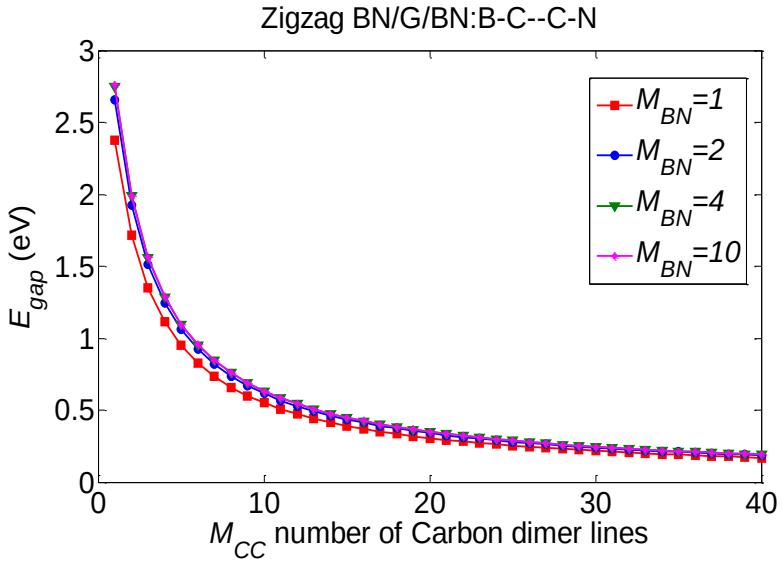

Figure 2-23: Tunable bandgap in the embedded zigzag BN/G/BN with B-C-C-N connections.

2.4 Conclusions

We have investigated the bandgap in a series of in-plane graphene/BN ribbons. By using first nearest neighbor Tight Binding calculations, we have shown that bandgap is open in all armchair structures of Graphene/BN while only two zigzag ribbon structures (B-C and N-C) and the zigzag B-C--C-N have a sizeable gap. In all structures Graphene mainly dominates the bandgap properties of the system while BN has much less influence. For both armchair and zigzag structures, BN shows its strongest influence when it is embedded between two Graphene ribbons. In this case, bandgap depends on BN ribbon width up to M_{BN} = 15. For other cases (including supper lattice), bandgap is stable for M_{BN} (N_{BN}) > 8. Importantly, analysis on group velocity of the super-lattice and G/BN/G structures have shown that electrons in the latter kind of structures have much higher velocity compared to those in the former one. And among three possible configurations of parallel interface structures, it is shown that the structure where a Graphene ribbon is modified at both edges by BN ribbons has the largest gap compared to the others. In particular, for armchair hybrid ribbons, with the opening of bandgap for group $3p + 2$, a new hierarchy is set up with energy gap of the groups in order $3p > 3p + 1 > 3p + 2$ instead of $3p + 1 > 3p > 3p + 2$ as reported for pure armchair graphene.

Chapter 3:

Modulation of bandgap and current in Graphene/BN nanoribbons by tuning the transverse electric field

In this chapter we propose a new approach to designing efficient electronic switches based on Graphene/BN heterostructures. By means of atomistic Tight Binding simulations, we investigate heterostructures made of an armchair BN nanoribbon sided by two armchair graphene ribbons where significant band gaps can be opened. More interestingly, we show that a band gap of about 0.55 eV can be strongly suppressed by applying a relatively weak transverse electric field of 10 mV/Å. Additionally, by using NEGF simulation, we show that this effect can be successfully used to control the current in electron devices even at small biases and small length. An on/off current ratio higher than 10^4 is achieved at room temperature.

3.1 Introduction

Bandgap opening in graphene is a critical issue to make this outstanding material suitable for a wide range of applications. Nanostructuring strategies, as cutting graphene into narrow strips to form graphene nanoribbons (GNRs)[111] or punching a periodic array of nanoholes into a graphene sheet to form a graphene nanomesh (GNM)[112] have been shown to be efficient to generate a bandgap. However, the width of GNRs and neck width of GNMs must be very small, typically smaller than 2-3 nm, for creating a significant bandgap. Such small dimensions are difficult to achieve and give rise to problems of reproducibility and edge disorder control.[113,114] It is also possible to use an external electric field to generate and/or modulate the bandgap in graphene or graphene-like structures. This technique has been first demonstrated in carbon nanotubes (CNTs) by placing a CNT in an electric field perpendicular to the tube axis.[115] In ribbons, a similar effect of transverse electric field applied along the width has been predicted for GNRs,[16,17,116] bi-layer GNRs[117] and BN ribbons,[118] as a consequence of field-induced symmetry breaking. In the case of GNRs, the field may open a small gap in metallic zigzag ribbons. It has a negligible effect on metallic armchair ribbons,[16]while it reduces the gap of semiconducting ones. However, in an armchair GNR

of reasonable width, e.g. with 69 dimer lines, the bandgap reduces only for electric field higher than 4 mV/Å and can be modulated in a limited range of 0.15 eV.[16] In BN ribbons, the significant suppression of the large bandgap requires electric fields of strength higher than hundreds or even thousands of mV/Å.[118]

An external field applied perpendicularly to the sheets can also open and modulate a bandgap, as shown experimentally in bilayer graphene[119] and theoretically in bilayer BN[120] as a consequence of the difference of potential between both layers. However, using this approach, the controllable bandgap is limited to 0.25 eV in bilayer graphene[121] and the modulation of bandgap in BN bilayers is not enough to make this material suitable for carrier transport.

In chapter 2 we have shown the possibility to grow hybrid monolayers consisting of a mixture of BN and carbon nanodomains,[43–45] which suggested new strategies of bandgap engineering and proposal of devices.[45,51] We also demonstrated that bandgap is open in the case of metallic Graphene making all in-plane Graphene/BN ribbons semiconducting and suitable for electronic device applications.

In this chapter we demonstrate that bandgap in graphene/BN structures can be also modulated via an external transverse electric field, making these structures more flexible for a larger range of applications. By using an atomistic Tight Binding approach, we show that an external transverse electric field applied along the width of a hybrid armchair graphene/BN ribbon can modulate the bandgap over a wide range, typically from more than 0.5 eV to less than 0.08 eV. It is worth noting that this effect is obtained for moderate electric fields, smaller than 20 mV/Å. On the basis of this effect, an electronic device where such a ribbon is connected to two graphene leads is proposed. According to our ballistic Green's function-based quantum simulations, an on/off current ratio higher than 10^4 can be achieved due to the field-induced modulation of bandgap.

3.2 Modelling and methodology

In chapter 2 we have demonstrated that all armchair G/BN hybrid ribbons are semiconducting and armchair structures with interfaces parallel to transport direction exhibit better transport properties (higher group velocity) compared to that of superlattice structures. Among several configurations of zigzag Graphene/BN structures, a bandgap appears only in the three structures with B-C, N-C and B-C--C-N interface bonding. These structures with finite

bandgap are thus very promising for switching current in electronic devices. We will see that in some of them it is possible to efficiently modulate the bandgap on a wide range using a reasonably small electric field, i.e. requiring quite small applied voltage. Refs.[16,118,122] showed indeed that the modulation of bandgap can result from the difference of applied voltage between the two edges of the ribbon. Moreover, in chapter 2 we have seen that the bandgap and the low-energy bands in G/BN heterostructures are mainly dominated by Graphene. Thus for a given electric field F_0 and fixing the width of each Graphene sub-ribbon, the effect of the transverse electric field in the armchair G/BN/G structure should be stronger than in armchair G/BN, armchair BN/G/BN, zigzag G/BN (B-C or N-C interface) and zigzag BN/G/BN (with B-C--C-N interfaces) because it contains a wider fraction of Graphene area.

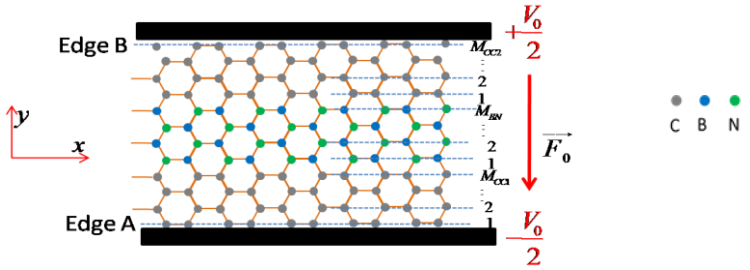

Figure 3-1: Schematic view of the Armchair G/BN/G structure studied in this work with $M_{CC1} = M_{CC2} = 15$, $M_{BN} = 29$. It is placed in between two side gates that generate a transverse electric field.

Based on this analysis, here we focus our study on armchair G/BN/G ribbons under the effect of a transverse electric field. The system is schematized in **Figure 3-1**. Using the same notations as in chapter 2, the width of each sub-ribbon is characterized by the numbers of dimer lines M_{CC1}, M_{CC2}, and M_{BN}. For the band structure analysis, the ribbon is considered to be infinite and periodic along x axis. For $M_{CC1} = M_{CC2} = 15$, $M_{BN} = 29$, i.e. for a total ribbon width W of about 7.1 nm, the calculated bandgap is about 0.55 eV. Two side gates are placed along the edges of the ribbon. At these gates, two potentials V_1 and V_2 equal to $-V_0/2$ and $+V_0/2$, respectively, are applied to generate a transverse electric field F_0 ($F_0=V_0/W$) along the y axis. It should be emphasized here that F_0 is the strength of electric field in free space, before we put the Graphene/BN ribbon inside the region submitted to this electric field. This field is called external field throughout this chapter.

The electronic energy band structure is investigated using a Tight-Binding model for the atomic structures limited to the first nearest neighbor interaction as in equation (2-1) in chapter 2. However, a new term is added due to the contribution from the external electric field,[122] i.e., using the Hamiltonian

$$H = \sum_i \varepsilon_i |i\rangle\langle i| - \sum_{\langle i,j \rangle} t_{ij} |i\rangle\langle j| + \sum_i U_i |i\rangle\langle i| \qquad (3\text{-}1)$$

where the on-site energy ε_i and hoping parameter t_{ij} have been taken from **Table 2-1** in chapter 2. The potential $U_i = -e.V_i$ is the electrostatic potential energy at *i-th* site.

3.3 Results and discussions

3.3.1 Modulation of bandgap under effect of by a transverse electric field: First approach

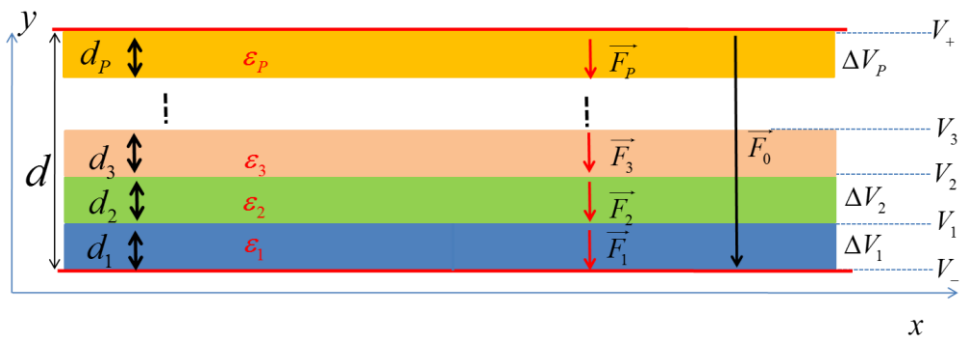

Figure 3-2: *P* parallel regions with different permittivity in an external field generated by two side gates V_- and V_+.

We will first approach the problem of the effect of electric field using a linear potential with the aim of understanding the physics and making a comparison with results previously obtained for pure armchair graphene ribbons. However, unlike the case of pure graphene or BN structures,[16,118,122] in our inhomogeneous heterostructures with different regions made of different materials (graphene, BN), it is necessary to calculate the local electric field in each region. To generalize problem, we assume there are *P* different regions placed in an electric field generated by two side gates V_- and V_+ as shown in **Figure 3-2**. The field F_0 is considered as an average field so that $V_+ - V_- = F_0.d$. The local field in each region can be

found by solving the continuity conditions of dielectric vectors and scalar potentials at the interfaces, i.e. for first condition

$$D_1 = D_2 = ... = D_P \tag{3-2}$$

The second condition is equivalent to the equation

$$V_+ - V_- = \Delta V_1 + \Delta V_2 + ... + \Delta V_P \tag{3-3}$$

where

$$\Delta V_1 = F_1.d_1, \Delta V_2 = F_2.d_2, ..., \Delta V_P = F_P.d_P \tag{3-4}$$

Solving (3-2) and (3-3) by using (3-4) and relations $D_i = \varepsilon_0 \varepsilon_i F_i$ and $V_+ - V_- = F_0.d$ we can get

$$F_i = F_0.\frac{\alpha_i}{\beta} \tag{3-5}$$

With

$$\begin{cases} \alpha_1 = \dfrac{d}{\varepsilon_1}, \alpha_2 = \dfrac{d}{\varepsilon_2}, ..., \alpha_j = \dfrac{d}{\varepsilon_j} \\ \beta_1 = \dfrac{d_1}{\varepsilon_1}, \beta_2 = \dfrac{d_2}{\varepsilon_2}, ..., \beta_j = \dfrac{d_j}{\varepsilon_j} \text{ and } \beta = \sum_{j=1}^{P} \beta_j \end{cases} \tag{3-6}$$

The electrostatic potential in the *i*-th region (*i=1, P*) can be calculated as

$$V(y) = V_{i-1} + F_i.\left[y - \sum_{m=1}^{i-1} d_m \right] \tag{3-7}$$

where

$$V_{i-1} = V_- + \sum_{m=1}^{i-1} F_m.d_m \tag{3-8}$$

is the potential at the end of (*i*-1)-th region.

In the systems consisting of Graphene and BN ribbons, we assume the in-plane relative permittivity to be 1.8 in graphene[123] and 3 in BN[38].

From the electrostatic potential (3-7), the energy potential $U = -eV$ is calculated for each atom position and added into the onsite energy of the atom. It is then added in the Hamiltonian (3-1) and the Eigenvalue problem (2-2) in chapter 2 can be solved to find out the band structure.

In **Figure 3-3**(a) we show the bandgap as a function of the external field F_0 for the armchair G/BN/G hybrid ribbon schematized in **Figure 3-1**. First, we can observe that the bandgap has a sharp fall from about 0.55 eV at F_0 = 0 mV/Å to zero for F_0 > 10 mV/Å. Recently, the effect of electric field on the permittivity in graphene has been reported.[123] It was shown that both in-plane and out-of-plane permittivity may vary significantly under strong field of some hundreds of mV/Å. Moreover, Refs.[124,125] have shown that such strong field could also induce mechanical deformation of the lattice that could dramatically change the electronic structure. Thus the primary result observed in armchair G/BN/G shows that these phenomena can be neglected in the range of field considered here, i.e. smaller than 20 mV/Å. **Figure 3-3**(a) also indicates that effect of an opposite field ($-F_0$) to the bandgap in this structure is the same as that using the $+F_0$ field. This is due to the fact that for $M_{CC1} = M_{CC2}$ the two Graphene ribbons in **Figure 3-1** are symmetrical to the central axis in the middle of BN ribbon. Thus, in an opposite electric field these two Graphene ribbons interchange their roles and the total effect of electric field on the system is unchanged.

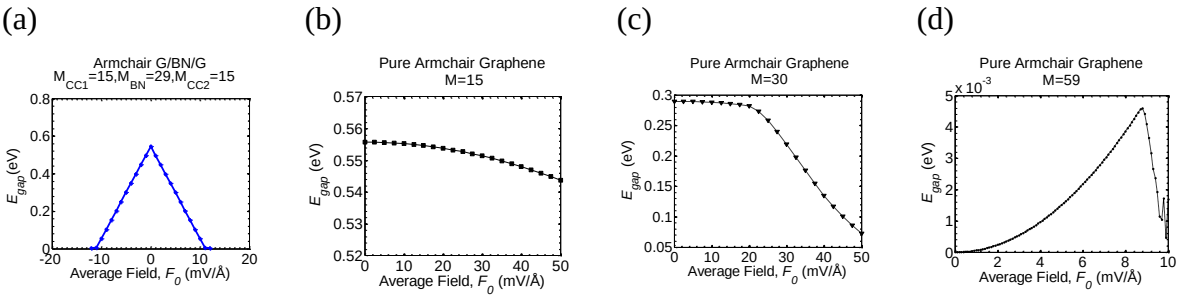

Figure 3-3: The modulation of bandgap is a function of the electric field F_0 for (a) Armchair G/BN/G heterostructure for $M_{CC1} = M_{CC2} = 15$, $M_{BN} = 29$, (b), (c), (d) Pure armchair Graphene for $M = 15$, 30, 59, respectively.

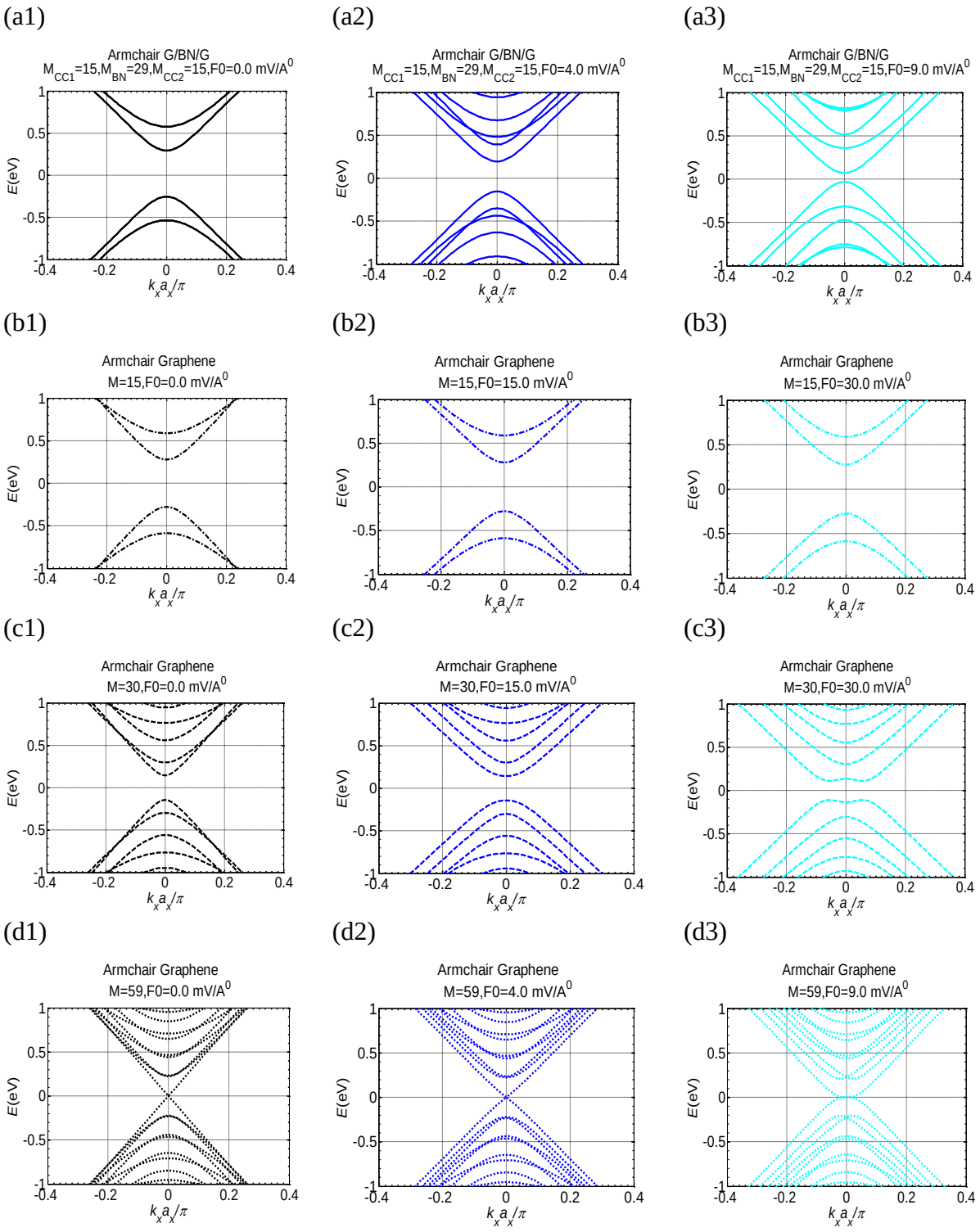

Figure 3-4: Revolution of energy bands in different structures: Figures (a1, a2, a3) with solid lines are band structures of Armchair G/BN/G for $M_{CC1} = M_{CC2} = 15$, $M_{BN} = 29$. Figures b, c, d are band structures of pure armchair Graphene for for $M_{CC} = M = 15, 30, 59$ respectively. The strength of electric field F_0 is indicated in each panel.

To clarify the difference between the armchair G/BN/G heterostructures and pure armchair Graphene ribbons under the effect of a transverse electric field, we also plotted in **Figure 3-3**(b), (c) and (d) the modulation of bandgap in armchair Graphene ribbons of different widths . **Figure 3-3**(b) is for the case of armchair GNR with width of 15 dimer lines that is equal to the width of one of the Graphene ribbon in armchair G/BN/G system. This is the case where the bandgap without electric field is almost the same as in armchair G/BN/G. However, in this structure, even when increasing the electric field up to 50 mV/Å the bandgap is just slightly changed by about 0.01 eV, that is much less efficient than in the armchair G/BN/G system. The second armchair Graphene system with the width equal to the total width of the two Graphene ribbons of G/BN/G structure is shown in **Figure 3-3**(c). In this case we have a smaller bandgap and though the bandgap is suppressed strongly an electric field larger than 50 mV/Å is required to close the gap. In the case of armchair GNR with M = 59 (equal the total width of G/BN/G structure), the bandgap remains almost unchanged with the increase of electric field (see the scale of E_g in **Figure 3-3**(d)).

To understand better the results presented in **Figure 3-3** we plot the energy bands of these four structures for different values of electric field F_0 as indicated in each panel of **Figure 3-4**. In the panels (a1), (a2) and (a3) we can see a clear change in position of energy bands in the armchair G/BN/G structure for (a1) F_0 = 0 mV/Å, (a2) F_0 = 4 mV/Å, (a3) F_0 = 9 mV/Å. Thus the electric field shifts down the lowest conduction bands and shifts up the highest valance bands, which results in a narrower bandgap. In contrast, it is difficult to define a change in bandgap in the panels (b1), (b2) and (b3) of the armchair GNR with M = 15. In the panels (c1), (c2) and (c3) for the case of the armchair GNR with M = 30, there is a small change in bandgap when F_0 increases from 0 to 15 mV/Å, but more important, it tends to reduce the curvature around the band extrema. Physically, this will certainly lead to an increase in effective mass and a reduction of carrier mobility. When F_0 = 30 mV/Å we can even observe a strong distortion of energy bands around Gamma point (k = 0) and the energy gap is no longer direct. For M = 59, without electric field Graphene ribbon is metallic as seen in the panel (d1). With an electric field applied there is a strong distortion in band structure even in high energy bands as seen in the panels (d2) and (d3) but the bandgap remains almost zero and this ribbon remains metallic.

Hence, using G/BN/G heterostructures under transverse electric field seems to be more efficient than using pure Graphene ribbons since we can modulate a wider range of bandgap

by just applying a quite weak electric field. More details on this hybrid structure under the effect of field will be analyzed in the next section using self-consistent simulation.

3.3.2 Modulation of bandgap under effect of by a transverse electric field: Self-consistent study

3.3.2.1 The couple of Schrödinger-Poisson equations

In some previous works[16,116] and in the previous section, the electric field-induced redistribution of charge was neglected and the electrostatic potential in Graphene ribbons was considered as a linear function of atom position along the ribbon width. In fact, this simplification may affect the accuracy of the results because the redistribution of charge inside the ribbon can make the potential profile no longer linear and to reduce the effect of field. In this work, we will perform a self-consistent simulation to compute the potential profile via a coupled Schrödinger-Poisson solver. The hole and electron densities were computed from the wave functions and Eigen-energy values using equations (1-28) and (1-29) in chapter 1, by just replacing E_F by the neutrality point energy E_N to ensure that the total charge of the system is neutral.

To calculate electron and hole distributions, we first have to determine the position of the neutrality point. Using the condition that the number of electrons and holes must be equal at this point, we can define E_N by solving the equation:

$$\sum_{\vec{r}} n_h\left(\vec{r}\right) = \sum_{\vec{r}} n_e\left(\vec{r}\right) \tag{3-9}$$

The results of $n_h\left(\vec{r}\right)$, $n_e\left(\vec{r}\right)$ are very sensitive to the position of E_N. In the case of pure graphene ribbons, the neutral point lays at zero energy. However, in the structure studied here the position is localized somewhere near the zero energy. This is due to the difference of bonding energy between B-C and N-C atoms leading to an asymmetry between conduction and valance bands. The exact position of E_N was numerically determined and is shown in **Table 3-1** as a function of external field F_0.

From the in-plane charge density $\rho = e\left(n_h - n_e\right)$, the 3D charge density $\rho_{3D} = \rho / \Delta z$ [126] to be introduced into Poisson's equation was obtained by assuming the monolayer thickness Δz to

be equal to the distance between two graphene layers in graphite, i.e., $\Delta z = 0.35$ nm.[127] The potential can be found from the Poisson's equation as in equation (1-35) in chapter 1, i.e.:

$$\nabla\left(\varepsilon\nabla V\right) = -\frac{\rho_{3D}}{\varepsilon_0} \tag{3-10}$$

In the self-consistent procedure, the new potential resulting from the Poisson equation is compared to the initial potential by a ratio which is defined by

$$r = \frac{\text{norm}\left(V_{out} - V_{in}\right)}{\text{norm}\left(V_{out}\right) + \text{norm}\left(V_{in}\right)} \tag{3-11}$$

If this number is not small enough, we construct a new potential $V_{in}^{\,i+1} = V_{in}^{\,i} + \delta\left(V_{out}^{\,i} - V_{in}^{\,i}\right)$, where δ is a small number to get convergence. We put this potential in to the Schrödinger's equation and solve again the coupled Schrodinger-Poisson equations (1-35). This procedure is repeated until *r* is as small as we desire. In our simulation, *r* and δ were chosen equal to 10^{-4} and 0.1, respectively.

Table 3-1: Position of E_N for different values of the external field F_0

F_0 (mV/Å)	**0**	**1**	**2**	**3**	**4**	**5**
E_N (eV)	0.01981589	0.01977433	0.01970767	0.01964578	0.01958437	0.01951816
F_0 (mV/Å)	**6**	**7**	**8**	**9**	**10**	**11**
E_N (eV)	0.01944096	0.01934544	0.01922614	0.01908099	0.01891114	0.01871435
F_0 (mV/Å)	**12**	**13**	**14**	**15**	**16**	**17**
E_N (eV)	0.01849003	0.01823574	0.01794853	0.01762447	0.01725922	0.01684806
F_0 (mV/Å)	**18**	**19**	**20**	**21**	**22**	**23**
E_N (eV)	0.01638614	0.01586878	0.01529188	0.01465254	0.01394970	0.01318494
F_0 (mV/Å)	**24**	**25**				
E_N (eV)	0.01236382	0.01149409				

In **Figure 3-5**(a) and (b), the charge distribution and potential are plotted along *y* axis for an external electric field F_0 of 3 and 9 mV/Å, respectively. Interestingly, we found that the charge distribution along the width of the ribbon can be separated in 3 groups as a function of the atom position along the *y* direction. The three groups are composed with atoms which have an index position of the form $3m+1$, $3m+2$ and $3m+3$, respectively, where *m* is a natural number. This classification of charge is similar to the energy rule demonstrated in armchair graphene.[69] We checked that it is the same for all other honeycomb armchair structures such as pure graphene and BN ribbons (no shown). **Figure 3-5**(a) also shows that under the effect of electric field, free positive and negative charges are separated and the local charge neutrality is no longer ensured. Carriers on electron states tend to move close to the high potential gate and carrier on hole states move close to the low potential gate. Additionally, it is not surprising that the charge density is strongly localized in the graphene regions while the central BN region is almost free of charges. The dielectric properties of the involved materials reinforce the weakness of the charge density in BN.

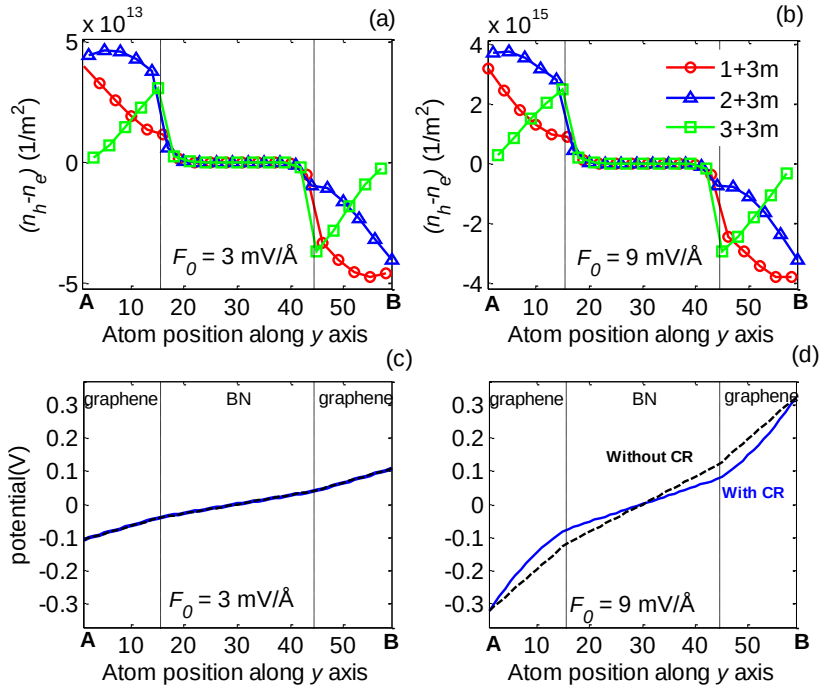

Figure 3-5: (a), (b) Redistribution of charge in the system under effect of the electric field. (c), (d) Potential profile along the width of the ribbon with and without effect of charge redistribution (CR). Here, the external electric field is F_0 = 3 and 9 mV/Å, respectively.

In **Figure 3-5**(c) and (d), the potential profiles obtained by including (solid line) or not (dashed line) the effect of Charge Redistribution (CR) are plotted for $F_0 = 3$ and 9 mV/Å, respectively. Without CR effect the result can be found analytically using the general formula **(3-7)** whereas the calculation with CR effect requires a fully numerical self-consistent procedure. As the two potential profiles are different, **Figure 3-5**(d) clearly illustrates that the CR effect is significant at $F_0 = 9$ mV/Å. However, at smaller electric field the two potential profiles are very similar (**Figure 3-5**(c)). Actually, the CR effect in this structure is negligible for electric fields lower than 6 mV/Å. For larger electric fields, the self-consistent solution is mandatory.

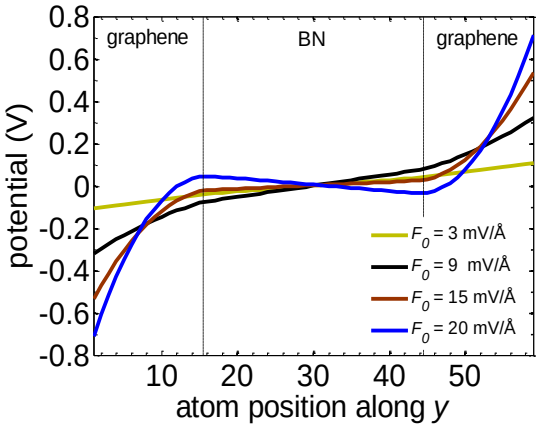

Figure 3-6: Typical potential profiles obtained for different external electric fields F_0 = 3, 9, 15 and 20 mV/Å.

In **Figure 3-6**, the potential profiles (with CR) are plotted for different electric fields F_0 between 3 and 20 mV/Å. At external field high enough to induce significant CR effect, the local electric field in the device is no longer distributed uniformly along the width. While a high field builds up near the ribbon edges where the mobile charges induce a strong screening effect, the field remains relatively small inside the BN sub-ribbon. At external fields F_0 higher than 15 mV/Å, the direction of the local field in the BN region even tends to reverse.

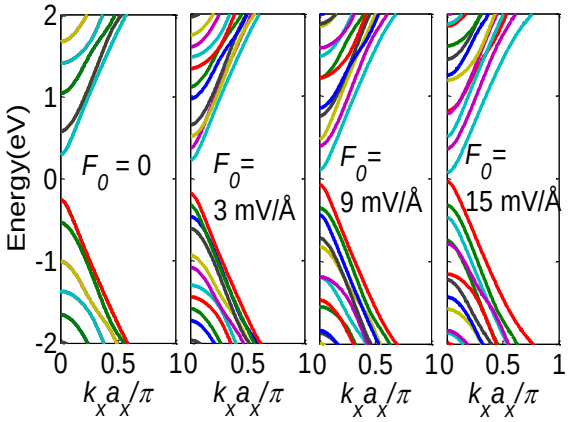

Figure 3-7: Plot of energy bands for four values of the external field F_0 = 0, 3, 9 and 15 mV/Å.

3.3.2.2 The band structure under effect of the external electric field

The band structures of the studied hetero-structure are displayed in **Figure 3-7** for different external fields F_0. The resulting energy gaps are plotted in **Figure 3-8** as a function of the external field. Both figures show clearly the suppression of energy gap when increasing F_0. The physics is thus similar to that observed in **Figure 3-3**(a) and **Figure 3-4** (a1), (a2), (a3) using a simple approach with linear potential in each region. This suppression of bandgap is governed by the effect of the local potential energy $U = -eV$, where V is the local potential which contributes directly to the on-site energy, as expressed in equation (3-1). Thus, at the edge near the gate biased at positive potential, the negative potential energy shifts down the anti-bonding states of the conduction bands, while at the other edge, the positive energy potential shifts up the bonding states of the valence band. This leads to a gradual narrowing of the bandgap when the electric field strength increases. At low external electric field F_0, these complementary phenomena lead to a linear decrease of the band gap when increasing the potential applied between both gates. For this range of electric field the self-consistent result is in agreement with the result in **Figure 3-3**(a) using first approach.

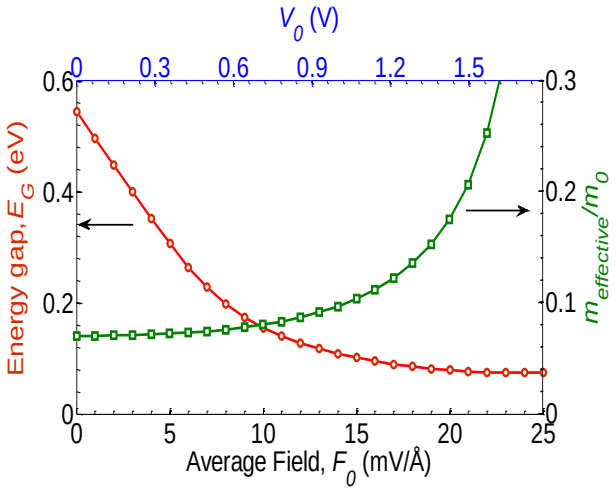

Figure 3-8: Energy bangap of the hybrid ribbon and effective mass in the lowest conduction band as a function of the external field F_0.

A further analysis of **Figure 3-8** shows that for $F_0 > 6$ mV/Å this linear behavior fails and the gap tends to saturate. When the electric field is larger than 20 mV/Å, the gap reaches the nearly constant value of 74 meV. In this structure the gap cannot be fully suppressed by applying an external field, due to the effect of charge redistribution. At high field, the reduction of the gap is not only related to the strength of the external field but depends also on the strength of the local internal electric field limited by the CR effect as seen in **Figure 3-5**(d) and discussed above.

The electron effective mass in the lowest conduction band is also computed using equation (1-33) and plotted in **Figure 3-8** as a function of the external field. At zero field, the calculated effective mass is relatively small and equal to $0.069m_0$ where m_0 is the electron rest mass. This effective mass slightly increases up to $0.077m_0$ at field of 9 mV/Å. At higher field, the effect of charge redistribution not only affects the energy gap but also the shape of the bands. The saturation behavior of the gap is associated with a strong increase of the effective mass that reaches $0.174m_0$ at $F_0 = 20$ mV/Å. The CR effect limits the band mixing between the lowest conduction band and highest valence band. This resistance to the mixing results in the flattening of the bands.

3.3.3 Tuning of current using transverse electric fields

Electrostatic gates are usually used to control the free charge density in the channel by shifting the Fermi level while the energy gap and the shape of the energy bands remain unchanged. Based on the modulation of bandgap under the effect of electric field highlighted previously, we propose a new way to control the electronic current by using two side gates instead of top and/or back gates as sketched in **Figure 3-9**. In an electronic switch based on graphene/BN ribbon with two side gates oppositely biased, the induced transverse electric field modulates the energy gap in the active region. Thus the local ambipolar free carrier density and finally the electronic resistance in the active region are controlled. In this original field-effect mechanism, at weak electric field the gap should remain large enough to cut off the current. At high electric field the gap is close to zero and the current is expected to turn on. Following this idea, the device schematized in **Figure 3-9** has been simulated. The active region is made of a finite portion (10.5 nm) of the hybrid BN/graphene ribbon studied previously, connected to two graphene leads with a width of 59 dimer lines. Two gates are located at each side of the active region to generate the transverse electric field. The graphene contacts are metallic while the active region is semiconducting at zero transverse field. The simulation was performed at room temperature (T = 300 K) and the initial Fermi energy in the contact is E_F = 0.2 eV. The potential profile due to electric field is taken from the self-consistent study in section **3.3.2**.

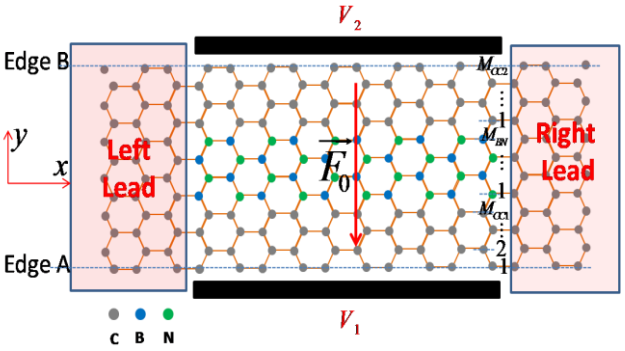

Figure 3-9: Schematic view of the Armchair Graphene/BN/Graphene structure studied in this work with M_{CC1} = M_{CC2} = 15, M_{BN} = 29. It is placed in between two side gates that generate a transverse electric field. For the transport analysis, a portion of this hybrid ribbon is connected to two graphene contacts.

The applied voltages in the two side gates of the device are equal to $V_1 = -E_F$ and $V_2 = V_0 - E_F$, respectively. This bias generates an external field $F_0 = V_0/W$ which is used to modulate the gap in the active region. In the off-regime where F_0 is nearly zero, as the side gate potential is equal to $-E_F$, the Fermi level in the contacts is aligned to the middle of the large gap existing in the active region. Hence, a very low off-current is expected. The increase of the potential V_0, applied on side gate 2, switches on the device. Indeed, the associated increase of F_0 induces a reduction of the band-gap that finally increases the value of the current. Moreover, the increase of the potential V_0 generates a standard field-effect, i.e., it induces an increase of the charge density in the device which reinforces the effect of the gap modulation to switch on the device. Thus, an excellent on-off current ratio is expected in this device.

The simulation of electron transport was performed within the ballistic approximation. The quantum transport was treated by means of the previous tight-binding description coupled to the non-equilibrium Green's function approach[80,82] where the transmission $T(E)$ was computed by equation (1-52) and then the current was computed using the Landauer's formula (1-55).[80]

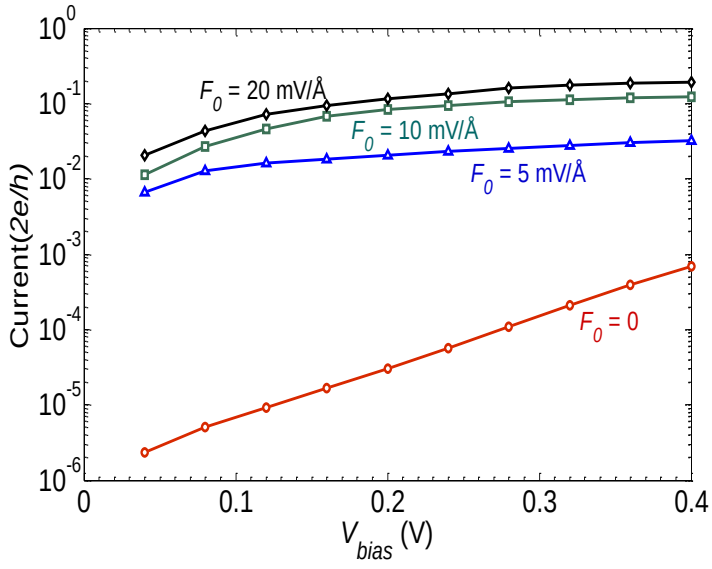

Figure 3-10: Current as a function of bias voltage for transverse electric fields F_0= 0, 5, 10 and 20 mV/Å. The simulation was performed at room temperature T = 300 K, and for E_F = 0.2 eV in the leads. The length of the active region is L_A = 10.5 nm**.**

In **Figure 3-10**, the current is plotted as a function of the bias voltage V_{bias} applied between the graphene leads for transverse electric fields of F_0 = 0, 5, 10 and 20 mV/Å. As the energy bandgap is gradually suppressed, it is remarkable that the current increases strongly. The red curve with circles, which corresponds to F_0 = 0 mV/Å, exhibits very weak current at low bias because the chemical potentials in the leads do not cross available energy states in the active region. Nevertheless, due to the finite and small size of the active region, some evanescent waves can tunnel through the active region. Once the transverse electric field is high enough, the gap is strongly suppressed and the current is widely enhanced due to the increasing contribution of propagating waves. At low F_0, the rapid increase of current when F_0 increases is consistent with the bandgap reduction observed in **Figure 3-8**. For fields higher than about 10-15 mV/Å, the bandgap reduction saturates, which leads to a limited increase of current. Actually, two effects contribute to limit the current at high transverse field: the quasi-saturation of bandgap and the increase of effective mass, as shown in **Figure 3-8**. For this particular ribbon, at V_{bias} = 0.2 V, the on/off current ratio I_{ON}/I_{OFF} defined as the ratio of currents at F_0 = 20 mV/Å and at F_0 = 0 mV/Å reaches the nice value of 3830 and even jumps up to 14200 if the length of the active region increases to 17 nm (see **Figure 3-11**). The rising of ON/OFF current ratio with the increase of the active region length is mainly due to the fact that the OFF-current (the current without electric field and at low bias) is reduced in longer devices as seen in **Figure 3-12**. The reduction of the OFF-current is because the transmission of evanescent waves, which is significant in OFF-state for short lengths of active region, rapidly decays when increasing this length. After decreasing, the OFF-current saturates at long length when the contribution of evanescent states becomes negligible. The ON-current being weakly affected by this length in ballistic regime, the smaller OFF-current results in an increase of the ON/OFF ratio.

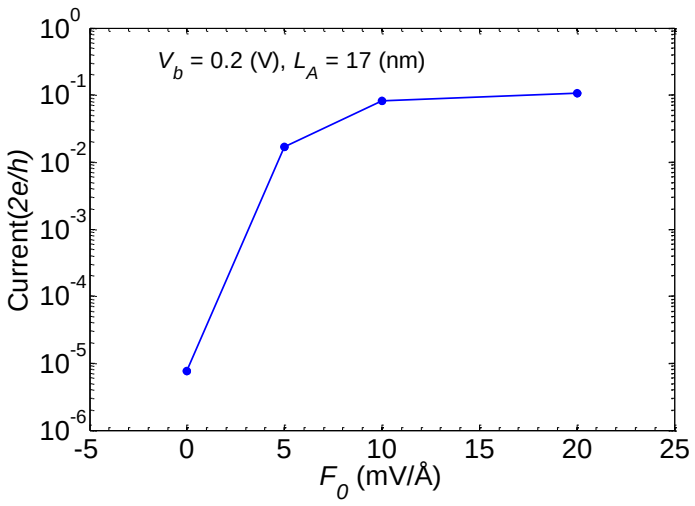

Figure 3-11: The current for the system of 17 nm in length and a bias V_b = 0.2 V is applied. The current without (F_0 = 0 mV/Å) and with electric field (F_0 = 20 mV/Å) are I_{OFF} = 7.54 × 10^{-6} I_0, I_{ON} = 0.107I_0, respectively with I_0 = $2e/h$. This result leads to an on/off current ratio I_{ON}/I_{OFF} ≈ 14200.

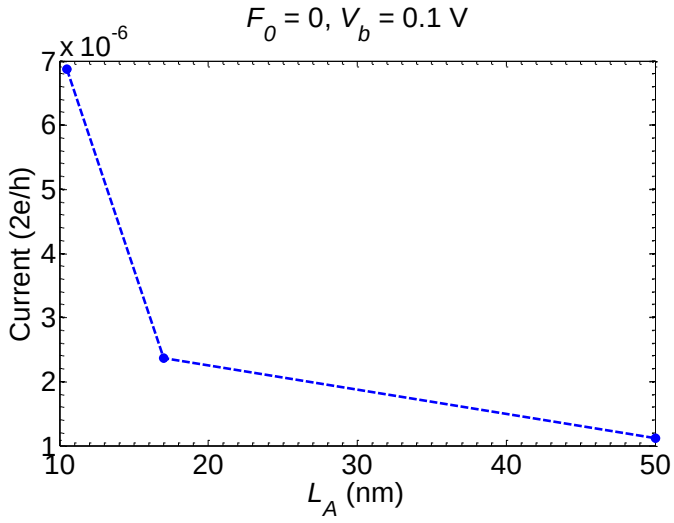

Figure 3-12: The current at a low bias V_b = 0.1 V and no electric field is applied. This current (OFF-current) becomes smaller when increasing the length of the active region.

3.4 Conclusions

In conclusion, we have demonstrated the effect of a moderate transverse electric field on the effective modulation and suppression of the energy bandgap in an armchair Graphene/BN structure, by considering carefully the effect of charge redistribution at high field. We have shown that the gap can be modulated from 0.55 eV down to values lower than 0.1 eV by applying a transverse electric field of about 15 mV/Å. Beyond this value of field, the reduction of bandgap becomes limited as a consequence of the effect of charge redistribution and the effective mass increases strongly, which makes the field range 0-15 mV/Å the most relevant to control the band structure of the ribbon studied here. Taking advantage of this effect, we have proposed an efficient method for controlling the current in devices by using side gates conveniently biased. This could open a new method for controlling electron current in small graphene and graphene-like devices.

Chapter 4:

Dispersive hybrid states and quantum transport in zigzag Graphene/BN heterostructures

In this chapter we are going to evidence the existence and the properties of a special kind of states at zigzag interface of in-plane graphene-BN heterostructures. Using TB calculation up to 2nd neighbor interactions, we analyze a series of structures of in-plane zigzag Graphene/BN ribbons, and we particularly pay attention on edge states in zigzag graphene part. We observe that edge states at the interface Graphene/BN are no longer flat and degenerated but dispersive with very high group velocity up to 4.3×10^5 m/s at the B-C interface and even 7.4×10^5 m/s at the N-C interface. These high speed edge states are similar to those in Topological Insulators, but for a given wave vector the velocities of N-C and B-C hybrid interface states have opposite signs. Additionally, the sophisticated TB calculation also confirms that bandgap is open in the case of asymmetric structure BN/Graphene/BN, reaching about 207 meV for sub-ribbon width of 5 nm. Transport study shows that bandgap and interface states can survive in realistic systems with non-uniform ribbons. A new sight of parity effect is also found with none zero conductance for both even and odd number of chain lines. These specific properties suggest new ways to engineer and control the transport properties of graphene nanostructures with zigzag edges.

4.1 Introduction

Perfect GNRs with edges oriented along the zigzag direction (ZGNRs), have actually zero bandgap regardless of the GNR width.[73,90,110] Additionally, a remarkable feature arises in the band structure. The top of the valence band and the bottom of the conduction band are always degenerate at $k = \pm\pi/a$. Actually these degenerate states correspond to states localized

in the vicinity of the zigzag edges and their probability density decays exponentially into the center of the ribbon, which has been confirmed experimentally.[128] Additionally, it has been suggested that an opposite spin orientation between ferromagnetically ordered edge states on each edge is the ground-state spin configuration in ZGNRs, leading to possible applications for spintronics. [17,110,129] From simple nearest-neighbor tight-binding calculation, these edge states appear in the band structure as flat bands, i.e. with zero group velocity[17,73,90,110] as seen in **Figure 4-1**. Calculations from more sophisticated tight-binding models and ab initio methods have shown that the bands of these states are not perfectly flat but exhibits a very small group velocity compared to the high velocity of bulk states.[57,77] Hence, they cannot reasonably be used for transport applications, though ZGNR-based devices with high negative differential conductance have been proposed [130,131] taking advantage of peculiar symmetry properties as the parity selective rule.[57]

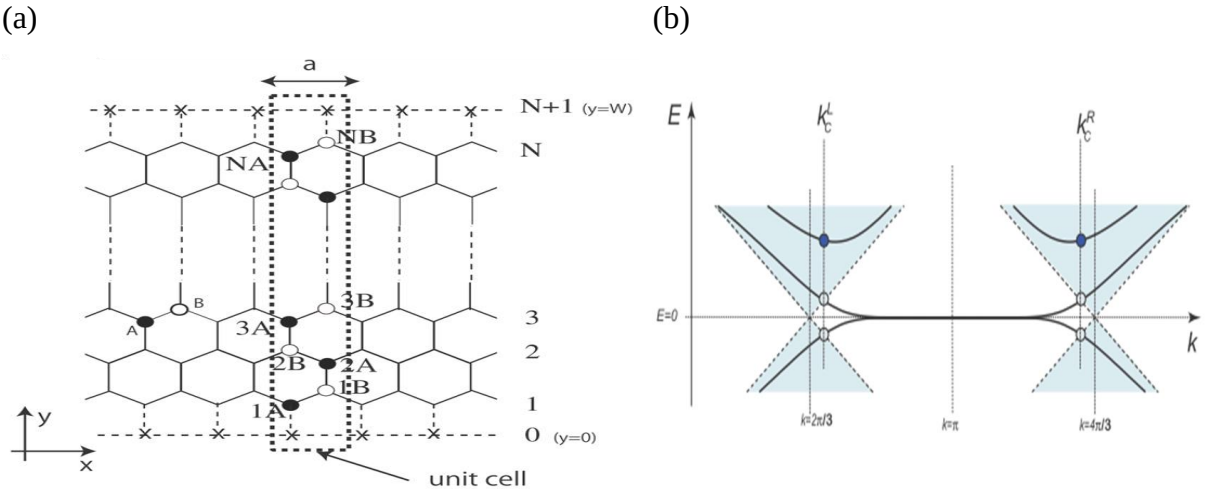

Figure 4-1: A zigzag graphene ribbon (a) with its band structure near zero energy (b). Energy is degenerated at k = ±π and the flat bands are edge states. *Reference: Wakabayashi et al*.[73]

Recently, studies of topological insulators (TI) have revealed the existence of very high group velocity in states localized at the surface or edge of samples (see **Figure 4-2**), while bulk states have the usual properties of states in conventional insulators. This behavior has been first predicted by Kane and Mele in 2005 [20] and then demonstrated in two-dimensional (2D) HgTe/CdTe quantum wells, both theoretically [132,133] and experimentally.[134] TI

states and topological phase transitions have been also evidenced in three-dimensional (3D) materials as $Bi_{1-x}Sb_x$ alloys, Bi_2Se_3 and Bi_2Te_3 .[135–140] Very recently, a new strategy has been proposed to generate a 2D TI state that exhibits a large bulk gap by constructing quantum well structures where a graphene layer is sandwiched between thin slabs of Bi_2Se_3[141] that is shown in **Figure 4-3** (a). The authors have shown that the strong hybridization between graphene and Bi_2Se_3 across the interfaces opens a significant energy gap (30−50 meV) and produces a 2D TI state that is driven by a new mechanism involving an inversion of the graphene Dirac bands and the conduction bands of Bi_2Se_3.

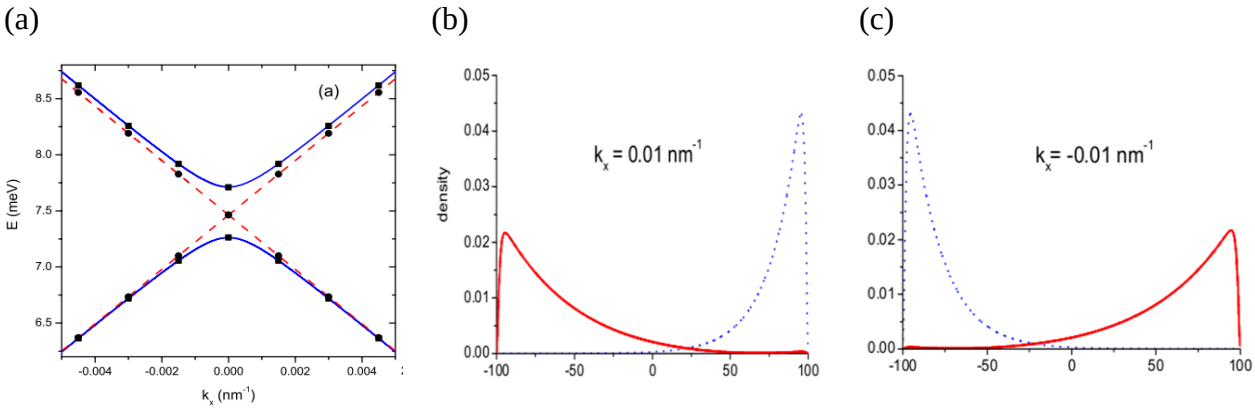

Figure 4-2: Edge states in a quantum Hall bar Topological Insulator HgTe/CdTe: (a) energy bands of edge states in TI HgTe/CdTe with solid lines are for finite width system and the dashed lines are for 2D system. (b) and (c) density distribution of edge states at two opposite momentums k_x and $-k_x$, the solid lines correspond to the upper edge state band and the dot lines correspond to the lower band. *Reference: Zhou et al.* [133]

More recently, the strong similarity of crystallographic structure between graphene and hexagonal Boron-Nitride (h-BN) has led to explore new electronic properties in layered graphene-like materials, either in the form of vertical Van der Waals structures or as in-plane monolayer heterostructures. The electronic properties of the latter type of graphene/BN heterostructures have been explored theoretically [34,35,46,107–109,142–144] and their synthesis has been successfully demonstrated [36,43–45], providing additional flexibility to design new or improved devices.[37,50,51] Most of works were focused on the possibility of tuning the bangap, while just a few of them have paid attention to the specific electronic states at Graphene/BN interfaces.[46,142,145] In Ref. [142] Fan et al. studied the phase transition from semiconducting to half-metal and ferromagnetic metal in Graphene/BN ribbons with

zigzag interface. They found out that the transition takes place when increasing the GNR width and depends strongly on whether the interface type is B-C or N-C. In Ref. [46] Jung et al. have focused on the confinement effect induced when inserting an extremely narrowed graphene ribbon (nanoroad) in a BN sheet. They demonstrated the emergence of valley states in the midgap of BN band structure. However, this effect is strongly dependent on the width of the embedded graphene ribbon, and the physics of structures made of large graphene areas connected to BN regions was still pending. Very recently, Drost et al, [145] demonstrated experimentally and theoretically the existence of interface states in zigzag Graphene/BN heterostructures. However, this work did not investigate the details of the physical properties of these sates.

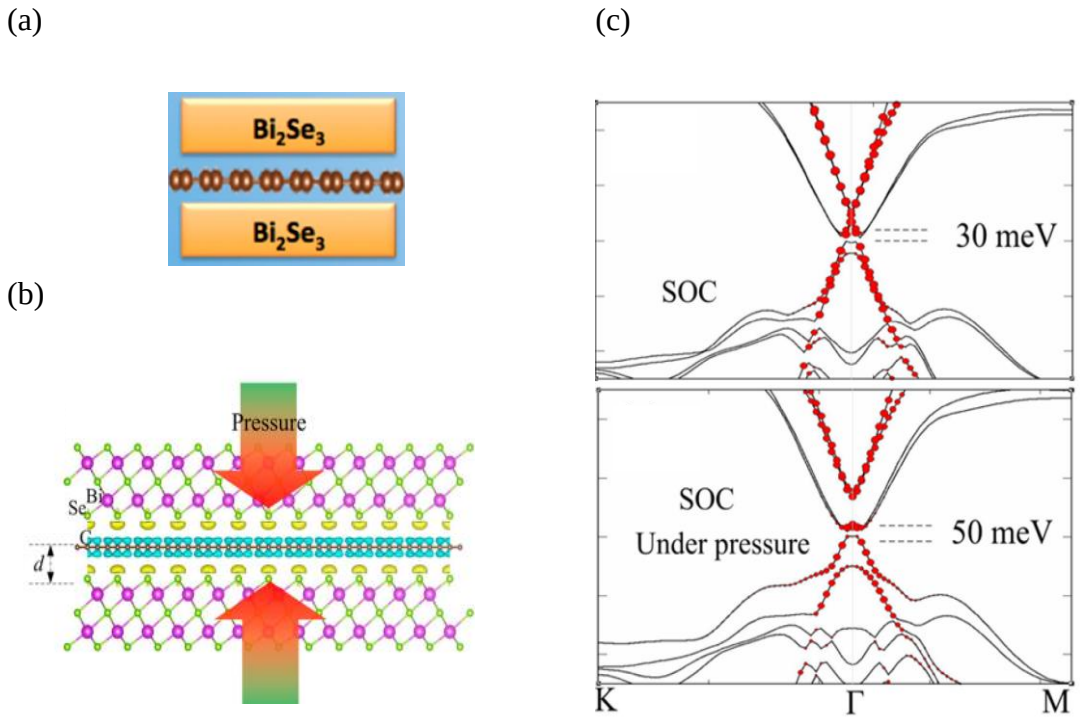

Figure 4-3: (a) A graphene layer is sandwiched between two slabs Bi_2Se_3, (b) illustration of the system under a pressure, (c) band structure without and with pressure. *Reference: Kou et al.* [141]

In this chapter, we investigate the band structure of a series of zigzag graphene/BN (G/BN) heterostructures with each sub-ribbon width larger than 5 nm. On the basis of second nearest-neighbor Tight-Binding calculations we show that a bandgap of 207 meV can be opened in a

zigzag BN/G/BN structure with B-C--C-N type of bonding, even with sub-ribbons as large as 5 nm. More interestingly, we evidence the emergence of interface states that look like edge states in ZGNRs but with high group velocity, as can be observed in TIs. These interface states are localized in the graphene side of G/BN structures. Their group velocity reaches 4.3×10^5 m/s at B-C interfaces and even 7.4×10^5 m/s at N-C interfaces. By using an effective model of single graphene ribbon, we also give a simple interpretation of the role of B(N) atoms on the formation of these interface hybrid states.

4.2 Methodology

To investigate the band structure properties of hybrid G/BN ribbons, second nearest-neighbor (2NN) Tight-Binding (TB) Hamiltonians have been considered, i.e. in the form [35,69]

$$H = \sum_i \varepsilon_i |i\rangle\langle i| - \sum_{\langle i,j\rangle} t_{ij} |i\rangle\langle j| - \sum_{\langle\langle i,j\rangle\rangle} t'_{ij} |i\rangle\langle j| + \sum_i V_i^{dec} |i\rangle\langle i| \quad (4\text{-}1)$$

where ε_i is the on-site energy at site *i*, t_{ij} and t'_{ij} are the hoping-parameters for nearest neighbors and second nearest neighbor interactions between sites *i* and *j*, respectively. The potential $V_i^{dec} = P_{B(N)}\,\varepsilon_{B(N)}\,e^{-d_i/\lambda}$ is the decaying potential from B(N) atoms at site *i* of graphene, where d_i is the distance between B(N) interface atoms and the *i-th* carbon atom, P_B and P_N are the strength of the potential and λ is the characteristic decay length.

Table 4-1: Tight Binding parameters up to 2nd neighbor interactions and decaying potential

E_{C_A} (eV)	E_{C_B} (eV)	E_B (eV)	E_N (eV)	t_{CC} (eV)	t_{BN} (eV)	t_{BC} (eV)	t_{NC} (eV)
0.015	-0.015	1.95	-1.95	2.5	2.9	2.0	2.5
$t_{BC,2}$ (eV)	$t_{CC,2}$ (eV)	t_{BB} (eV)	t_{NN} (eV)	$t_{NC,2}$ (eV)	P_B (eV)	P_N (eV)	λ (Å)
0	0	0	0.15	0.59	0.75	0.68	2.1

Though bandgap of zigzag Graphene/BN ribbons was studied in chapter 2 using first nearest TB calculation, to accurately describe the band structure of BN ribbons within a TB approach, it was proven that the use of a decaying potential is mandatory, in particular to remove the degeneracy at the X point.[94] However, in a pure graphene ribbon, this term is negligible because it is proportional to the onsite-energy of edge atoms, that is zero or very small for carbon atoms of both sub-lattices.[35,94] All TB parameters in (4-1) used in this work were taken from ref [35] where they have been adjusted to provide results fitting very well with ab initio calculations in G/BN ribbons. These TB parameters are given in **Table 4-1**. For infinite ribbons the Schrödinger equation can be computed by considering Bloch wave functions (1-23) in chapter 1 or can be simply written as [79,80]

$$\left|\psi_{\vec{k}}\right\rangle = \sum_{\alpha=1}^{\infty}\sum_{j=1}^{N} c_j \, e^{i\vec{k}.\overrightarrow{R_\alpha}} \left| j_\alpha \right\rangle \tag{4-2}$$

where $\left| j_\alpha \right\rangle$ is the p_z orbital of the j-th atom in the unit cell $\alpha-\text{th}$ and N is the number of atoms in a unit cell. The coefficients c_j are chosen such that the wave function is an eigenstate of the tight-binding Hamiltonian. From one unit cell to another the wave function differs only by a plane wave function. Then, the Schrödinger equation for the whole periodic system can be reduced to the equation of a single unit cell (1-24), i.e. [80,104]

$$h\,\phi = E\,\phi \tag{4-3}$$

with

$$\begin{cases} \phi = \begin{pmatrix} c_1 & c_2 & . & . & . & c_N \end{pmatrix}^T \\ h = H_{n,n-1}\,\mathrm{e}^{-ik_x a_x} + H_{n,n} + H_{n,n+1}\,\mathrm{e}^{ik_x a_x} + V_{n,n} \end{cases} \tag{4-4}$$

where $H_{n,n}$ is the Hamiltonian of the *n-th* unit cell, $H_{n,n\pm1}$ is the coupling term between the *n-th* and *n*±1-*th* unit cells, $V_{n,n}$ is the matrix of the decaying potential in the *n*–th unit cell and $a_x = \sqrt{3}\,a_0$ is the periodic constant along *x* direction, a_0 being the distance between two nearest neighbor atoms.

Once the eigen energies E and the coefficients of the eigen function ϕ are solved for each wave vector k_x, the group velocity can be numerically computed from equation (1-30) in chapter 1.

4.3 Results and discussion

As reported in many previous works on zigzag graphene nanoribbons [73,90,110], nearly flat bands appear in the dispersion relation near the neutrality point. They correspond to edge stages, i.e. states associated to electron densities strongly localized at the edges of the graphene ribbons. In contrast, in perfect armchair GNRs all states are delocalized. Although these localized states in ZGNRs are closed to the neutral point and are thus easily accessible, they do not contribute significantly to charge transport [57] because their group velocity is weak. Hence, they are useless for standard electronic applications.

In this section, we investigate the particular states localized at the interface between graphene and BN zigzag nanoribbons within different kinds of in-plane G/BN heterostructures. As in chapter 2, the notation "B-C" ("N-C") refers to interfaces where only Boron (Nitrogen) atoms are bonded with Carbon atoms. The width of each graphene and BN sub-ribbon is defined by the number of zigzag lines M_{CC} and M_{BN}, respectively. Unless otherwise stated, each of these numbers is 50 atomic lines, corresponding to a width of about 10 nm. Such heterostructures and dimensions are achievable with current technology.[146,147]

4.3.1 Hybrid states in a "one-interface" structure

We first investigate a zigzag hybrid ribbon with just a single Graphene/BN B-C interface, as schematized in **Figure 4-4**(a). For convenience in calculation and analysis of results, each unit cell is divided into two non-equivalent sub-layers L1 and L2, as shown in **Figure 4-4**(a). In **Figure 4-4**(b), we plot the profile of the decaying potential along the width of each of these sub-layers. It is assumed that the decaying potential associated with B or N atoms only affects the sites of carbon atoms within a single slice along the *y* axis and is equal to zero in BN regions.[35,94] The band structure computed for $M_{\mathrm{BN}} = 50$ and $M_{\mathrm{CC}} = 50$ is plotted in **Figure 4-4**(c). The band structure is particularly interesting near the neutrality point, between the lowest conduction band and the highest valence band. In the wave vector ranges $-\pi/a_x \le k_x < -2\pi/3a_x$ and $2\pi/3a_x < k_x \le \pi/a_x$, we observe two relatively flat bands,

while two other bands with finite group velocity extend in the negative energy region (red solid lines).

(a) (b)

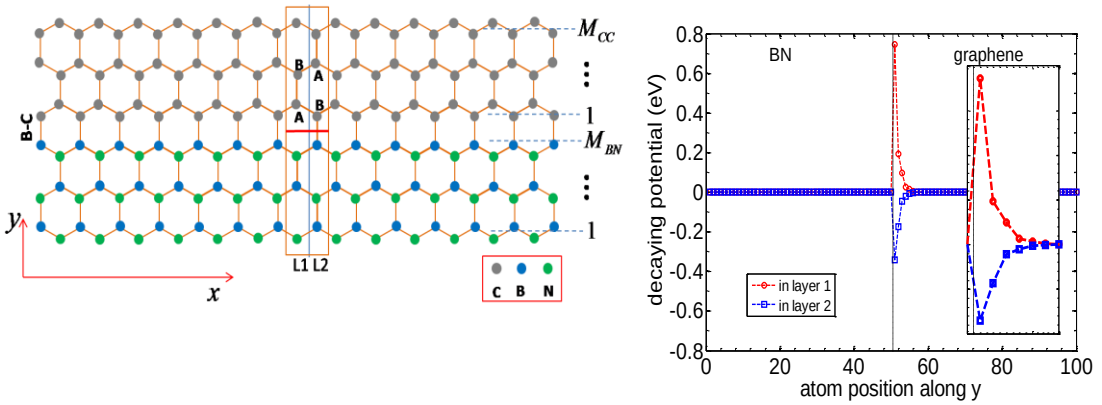

(c) (d)

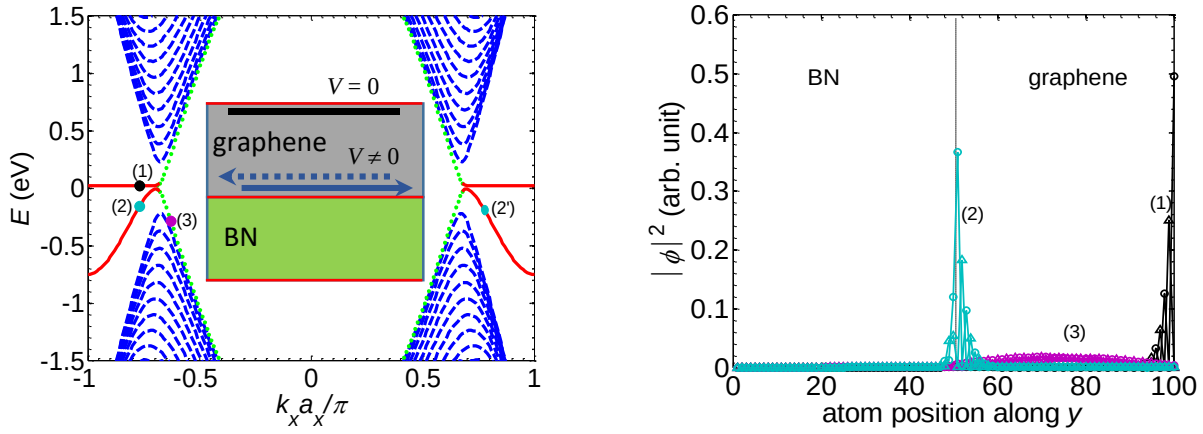

Figure 4-4. (a) Schematic view of zigzag Graphene/BN in-plane heterostructure with B-C bonds. The sub-ribbon widths are defined by the numbers of zigzag lines $M_{CC} = M_{BN} = 50$. (b) Decaying potential V^{dec} related to B and N atoms in the layers L1 and L2 defined in (a), with BN/G boundary indicated by a vertical dashed line. Inset: magnification on the significant range of variation of V^{dec}. (c) Band structure, with hybrid/edge states in solid red lines. Inset: schematic representation of the velocity direction of hybrid/edge states. (d) Profile of the probability density for the three states (1), (2) and (3) defined in (c).

The localization of the wave functions associated with three particular states marked (1), (2) and (3) in **Figure 4-4**(c) is illustrated in **Figure 4-4**(d) where we plot the corresponding

profiles of probability density $|\phi|^2$. On the purple curve, the probability density corresponding to the propagative state (3) of high group velocity, marked with a purple filled circle in **Figure 4-4**(c), is shown to be distributed along the full width of the graphene ribbon. This state is thus a classical "bulk" state. In contrast, the states (2) and (1) marked in **Figure 4-4**(c) with a cyan filled circle and a black filled circle, respectively, correspond to wave functions strongly localized at the edges of the graphene ribbon along the graphene/BN and graphene/vacuum interfaces, respectively. The edge state of type (1) has a nearly zero group velocity and corresponds to the edge state of an isolated zigzag graphene ribbon.[73,90,110] However, the edge state of type (2), though localized at the B-C interface, is strongly dispersive and exhibits a high group velocity. It should be noted that in this case the state (2') belonging to the other dispersive band at opposite wave vector $k_{2'} = -k_2$ is localized at the same interface as the state (2) but with opposite group velocity. It will be further discussed later.

The inset of **Figure 4-4**(c) schematizes the location and the propagation properties of both the zero velocity (top black line) and high velocity (solid arrow for the left band and dashed arrow for the right band) edge states. This peculiar edge state at G/BN interface can significantly contribute to charge transport due to its finite group velocity. It results from the hybridization of carbon and BN states. For the sake of simplicity we call this kind of states "hybrid state". These localized interface states extend from the edges of the Brillouin zone to the points $k_x = \pm 2\pi/3a_x$. This primary conclusion on hybrid states contradicts the discussion in ref [145] wherein the whole highest valence band (or the whole lowest conduction band) was supposed to be formed by localized interface states.

The single-interface structure with N-C bonds has been also investigated and the results are plotted in **Figure 4-5**. With this type of interface, we observe near the neutrality point that two bands extend in the positive energy region (red solid lines) which is thus in contrast with the previous case of the B-C structure where the corresponding bands are in the negative region. These two bands actually correspond to hybrid states localized at the N-C interface as shown from the wave function of state (2) plotted in **Figure 4-5**(d). The other two flat bands remain as edge states at one edge of a pure graphene ribbon.

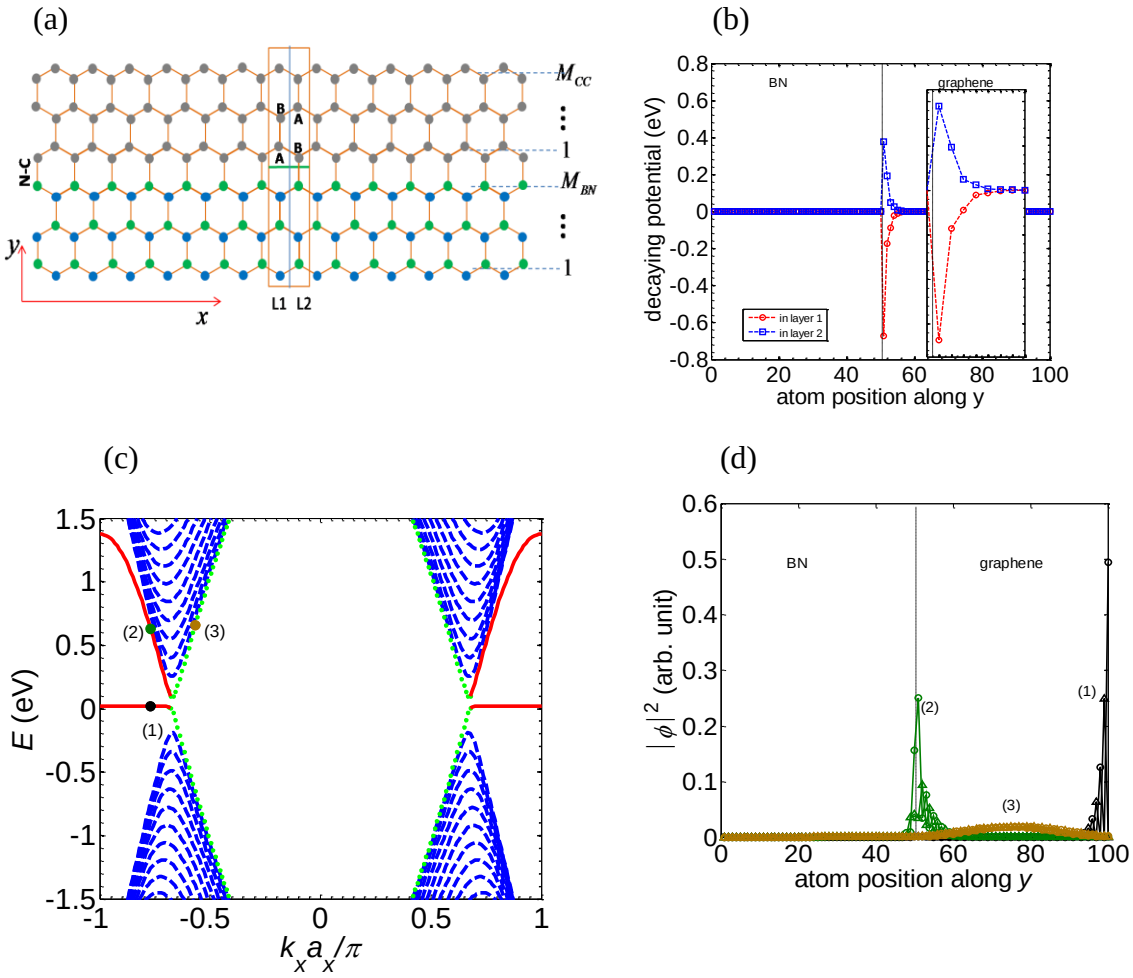

Figure 4-5: (a) Sketch of one interface structure with N-C bonds. (b) Decaying potential V^{dec} in the layers L1 and L2. (c) Band structure, with hybrid/edge states in solid red lines. (d) Profile of the probability density for the three states (1), (2) and (3) defined in (c). Here M_{CC} = M_{BN} = 50.

4.3.2 Hybrid states in a "two-interface" structure

To further analyze the G/BN hybrid states, we now investigate structures with two G/BN interfaces. At the first interface the carbon atoms are bonded with Boron atoms. Two cases are considered for the second interface. In the first case the second interface is similar to the first one, which leads to the symmetric structure referred to as B-C--C-B. In the second case, the second interface is made of C-N bonds. The mirror symmetry is broken and the structure is referred to as B-C--C-N.

4.3.2.1 B-C--C-B structure

The B-C--C-B structure is schematized in **Figure 4-6**(a). Here the GNR is connected with Boron atoms at both interfaces. **Figure 4-6**(b) shows the energy dispersion of this structure. The flat bands previously evidenced in B-C structure (see **Figure 4-4**(c)) are no longer present in this B-C--C-B system. It looks as if the flat band inherent in the C-vacuum interface has been curved downward by B-C bonds, leading to two doubly degenerate dispersive bands with high velocity. As previously observed in the B-C system (sub-section **4.3.1**), these degenerate hybrid states (1) and (2) are localized at the graphene/BN interfaces, as shown in **Figure 4-6**(c). They can contribute symmetrically, i.e. at both interfaces, to charge transport.

4.3.2.2 B-C--C-N structure

In the B-C--C-N structure, schematized in **Figure 4-7**(a), carbon atoms in graphene are now connected to N atoms at the second interface. This change induces new specific features in the band structure plotted in **Figure 4-7**(b). The original flat band in the B-C structure is now curved upward as in the N-C one, and belongs unambiguously to the conduction band. More interestingly, an energy gap is open and separates the first conduction band from the first valence band.

The analysis of the localization of states through the probability densities plotted in **Figure 4-7**(c) clearly demonstrates that the state (1) of the conduction band, i.e. with a dispersive band in the positive energy region, is associated with the C-N interface and thus is a hybrid state resulting from C-N bonds as we observed in **Figure 4-5**(c). Actually, the upward or downward bending of the hybrid bands depends on the on-site energy of the atoms to which edge carbon atoms are attached. When they are attached to Boron atoms of positive on-site energy ($\varepsilon_B = 1.95\,\mathrm{eV}$) the band is bent downward, towards negative energies. In contrast, it is bent upward when Carbon atoms are connected to Nitrogen atoms with negative on-site energy ($\varepsilon_N = -\varepsilon_B = -1.95\,\mathrm{eV}$). These features can be observed separately in B-C, N-C, B-C--C-B and N-C--C-N (not shown) structures or together in the case of the mixed structure B-C--C-N. The asymmetry of the B-C and C-N hybrid states is essentially induced by the difference of the bonding energies between the two types of bond. Since the hopping energy between B

and C atoms (t_{BC} = 2.0 eV) is smaller than between N and C atoms (t_{NC} = 2.5 eV) the curvature is smaller in the former case.

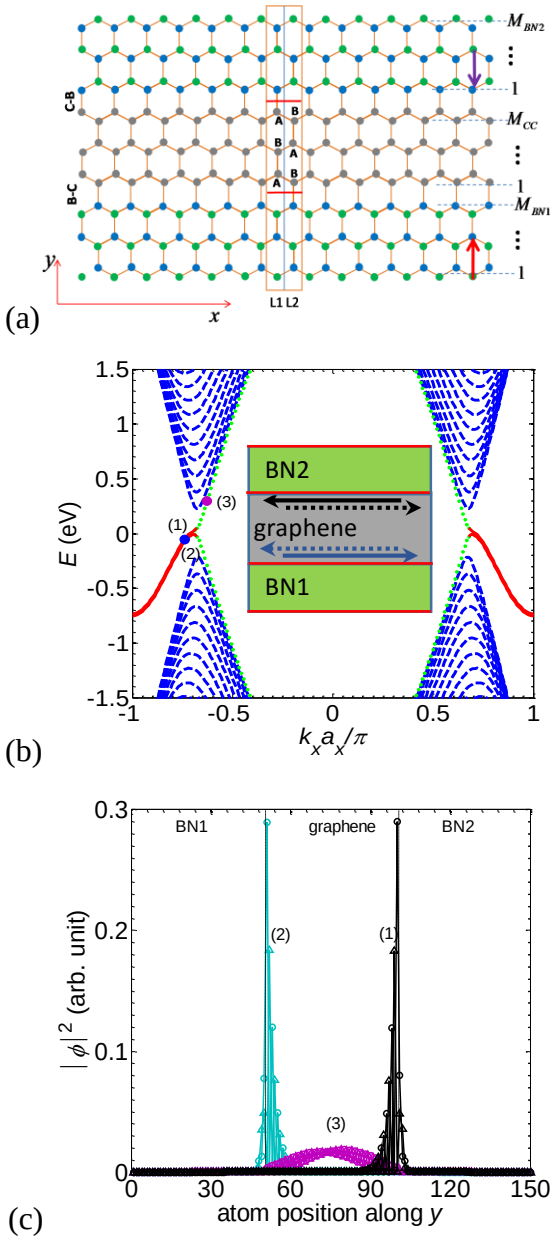

Figure 4-6: (a) Schematic view of a zigzag BN/G/BN structure with two C-B bond interfaces (B-C--C-B). (b) Energy band structure for M_{BN1} = M_{CC} = M_{BN2} = 50. Inset: schematic representation of the velocity direction of hybrid states at both interfaces (c) Profile of the probability density for the three states (1), (2) and (3) indicated in (b).

(a) (b)

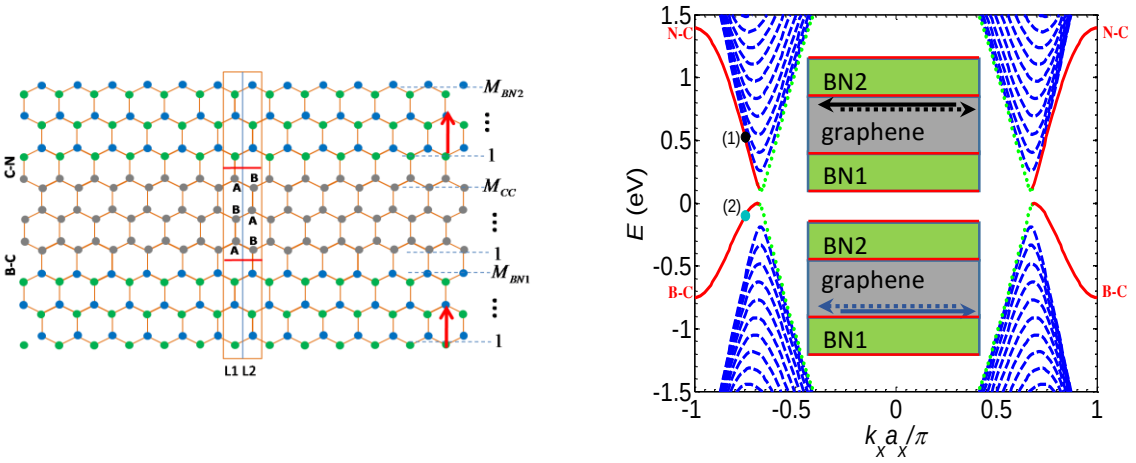

(c) (d)

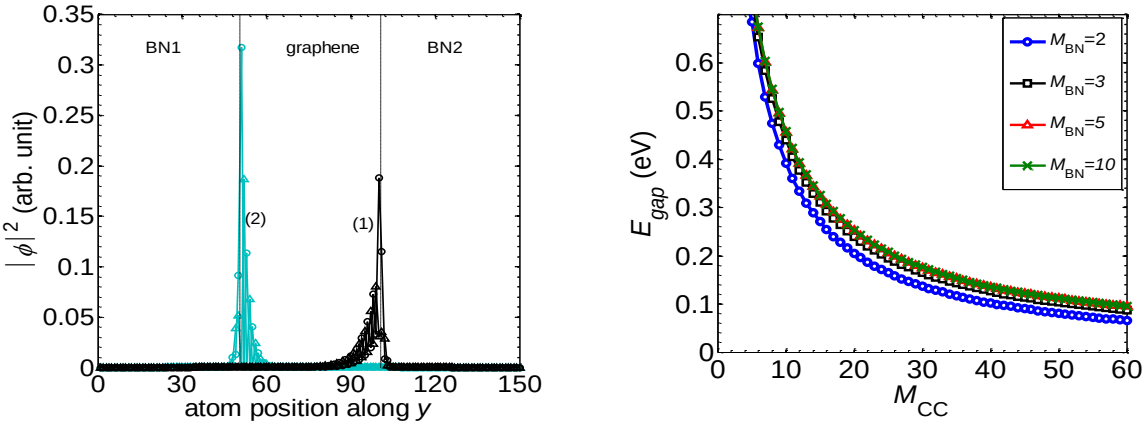

Figure 4-7: (a) Schematic view of a zigzag BN/G/BN with B-C--C-N bond interfaces. (b) Band structure for $M_{BN1} = M_{CC} = M_{BN2} = 50$. (c) Profile of the probability density for the two states (1) and (2) indicated in (b). (d) Bandgap as a function of sub-ribbon width M_{CC} for different values of M_{BN}.

In the case of symmetric systems as B-C--C-B (see **Figure 4-6**(b)), or N-C--C-N the gap is equal to zero, while it is very small in pure ZGNRs (**Figure 4-1**). Our investigations of different structures including B-C, N-C or B-C--C-N structures indicate that the latter gives the largest energy bandgap for a given graphene ribbon width M_{CC}. For example, for $M_{CC} = 25$ (i.e. for a 5 nm width), the structures B-C, N-C and B-C--C-N exhibit a bandgap of 47 meV, 167 meV and 207 meV, respectively. In **Figure 4-7**(d), the energy gap in structure B-C--C-N is plotted as a function of the sub-ribbon width M_{CC} for different BN widths M_{BN}.

Beyond M_{BN} = 2, the gap is very weakly sensitive to the BN width, while bandgaps higher than 0.4 eV are achievable for M_{CC} < 10 thanks to confinement effects.

Thus, the use of zigzag graphene/BN interface not only reveals a new kind of propagative edge states but also opens an energy bandgap. This gives new opportunities for bandgap engineering of graphene and for manipulating the transport properties of graphene nanostructures and devices.

4.3.3 Dispersion of hybrid states: specific properties

As mentioned above, the energy gap depends strongly on the graphene ribbon width M_{CC}. It is thus relevant to analyze in more details the M_{CC}-dependence of the energy dispersion of hybrid states. In **Figure 4-8**(a), the energy dispersions of the lowest conduction band and highest valence band in the B-C-C-N structure is plotted for M_{CC} = 10 and M_{CC} = 50. In each of these bands a specific value of wave vector k_t separates the hybrid states (symbols) from the bulk states (dashed line). In each case the value of k_t has been defined from the plot of the ratio of the probability density at the center of the graphene ribbon to the probability density at the ribbon edge, divided by the width M_{CC} (**Figure 4-8**(b)). This parameter is called here "bulk/edge ratio". As shown in **Figure 4-8**(b), the separation between hybrid states (left side) and bulk states (right side) is characterized by a transition region with a quasi-linear change of the bulk/edge ratio as a function of *k*. Consistently, the value of k_t has been defined in each band as the intersection of the slope of the bulk/edge ratio in the transition region with the wave vector axis. It appears that k_t is dependent on the width M_{CC} and tends to the value $\pm 2\pi/3a_x$ at large width, i.e. to the position of the center of Dirac cones in graphene. It is consistent with the width-dependence of the position k_c of the extrema of conduction and valence bands due to the confinement effects in GNRs,[73] together with the dependence of bandgap. Beyond this behavior of the extrema of the bands, it is remarkable that the main part of the energy dispersion of edge states, i.e. towards the Brillouin zone edge $k = \pm \pi/a_x$, is almost independent on M_{CC}. Thus, the dispersion and the group velocity of hybrid states are stable and insensitive to the graphene ribbon width, except near the neutrality point.

In all these structures, as in topological insulators, to each edge state of positive wave vector $+k_x$ corresponds a symmetric edge state at $-k_x$ of opposite velocity. In TIs these two states are distributed on two different sides of the sample [133] as seen in **Figure 4-2,** while at B-C or N-C interfaces, they are both localized at the same interface. In symmetric B-C--C-B and N-C--C-N structures, the edge states are doubly degenerate and distributed on both interfaces of the graphene sub-ribbon. In the mixed asymmetric structure B-C--C-N, two different dispersive hybrid edge bands are present, one with states localized at the B-C interface, and the other with states localized at the N-C interface, which is a specific property of this system.

To quantify the potential of the hybrid states in terms of transport properties, the group velocities of the upward and downward bands of edge states in structures B-C--C-B and B-C--C-N are plotted in **Figure 4-9**. The edge states in pure zigzag graphene ribbon (circles) have a zero group velocity while the velocity of hybrid states reaches high values at high wave vector. We can observe that the green curve (crosses) related to the lowest band in B-C--C-N is identical to the curve with black squares related to B-C--C-B, because they are associated with the same type of B-C interface. These B-C hybrid states have a maximum group velocity as high as 4.3×10^5 m/s. In the case of N-C hybrid states (red triangles), the maximum velocity even reaches 7.4×10^5 m/s.

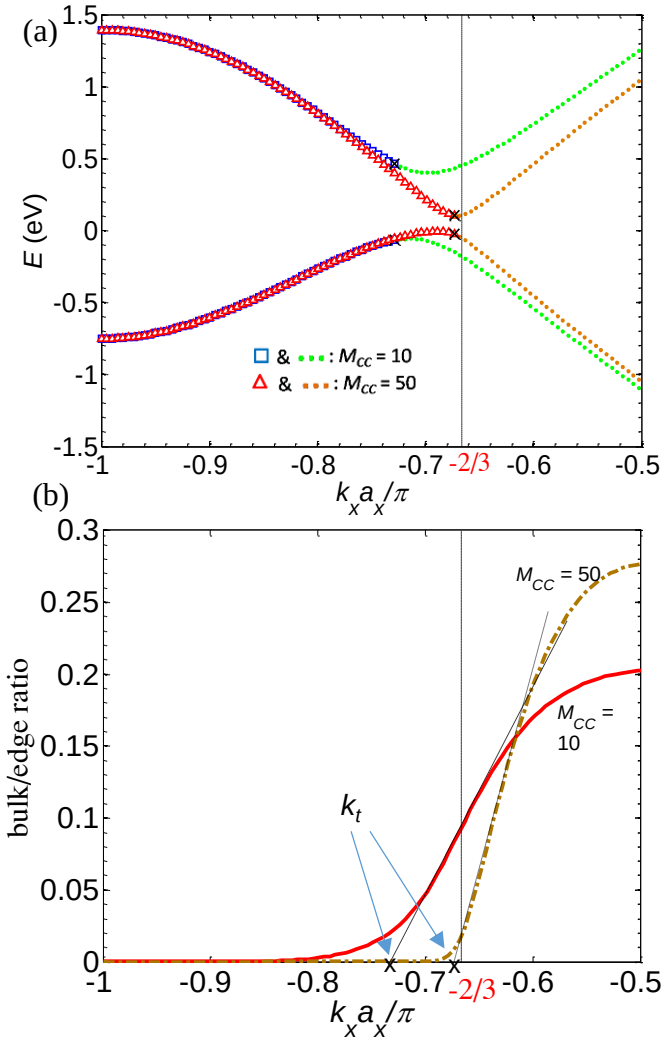

Figure 4-8: (a) Comparison of lowest conduction and highest valence bands in the B-C--C-N structure for different graphene ribbon width M_{CC} = 10 and 50. On each band, hybrid states are marked with symbols and bulk states are in dashed line. (b) bulk/edge ratio (see text) in the highest valence band. The intersection of the slope in dashed line with the abscissa gives the value of k_t separating edge states and bulk states.

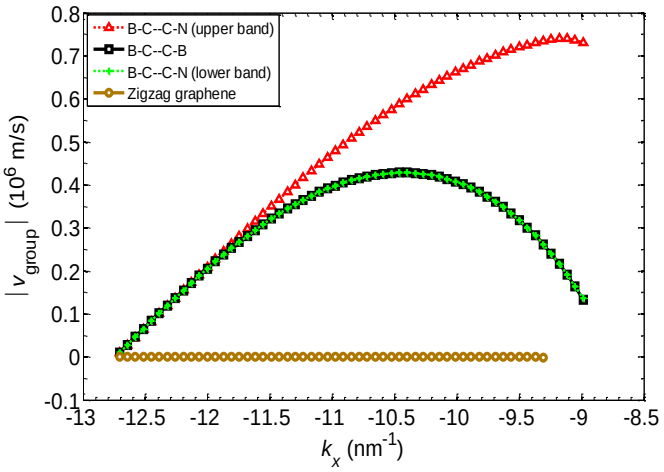

Figure 4-9: Group velocity of hybrid states as a function of the wave vector k_x in different structures.

4.3.4 From the effective model to hybrid states: the role of B (N) atoms

We already mentioned that the behavior of hybrid states is mainly governed by the values of on-site energies for B and N atoms and the hopping energies of B-C and N-C bonds. This can be easily checked by using a simple 1NN TB model without any decaying potential, i.e. considering only interactions with the first nearest neighbors, as widely done in previous works on zigzag graphene ribbons.[90,110] Actually, the results obtained are qualitatively very similar to that obtained with the 2NN model including decaying potential, from both points of view of the energy dispersion and of the localization of states at the interfaces. The resulting effect of these TB parameters applied to the edges of the graphene ribbon is to change the energies of edge states in graphene, leading to the so-called hybrid states. This effect may thus be seen as qualitatively equivalent to the effect of changing the potential on the edge atoms of graphene.

On the basis of this analysis, we propose a simple model that can generate artificially edge states with dispersive energy bands in a ZGNR, and able to mimic the emergence of hybrid states induced by B and N atoms. It consists in applying an effective potential V_{eff} as new on-site energy to the edge atoms of the ribbon, as illustrated in **Figure 4-10**(a). The 1NN approach is used for this simplified approach.

In **Figure 4-10**(b-e), the energy band of a ZGNR is plotted for different values of the effective potential V_{eff} varying from -0.1 to 0.5 eV, applied on a single side of the ribbon. While applying a negative potential leads to the appearance of a dispersive band toward negative energies (see **Figure 4-10**(b)), a positive potential leads to a positive energy band (see **Figure 4-10**(c)). Consistently, the slope of the curve is all the higher if the effective potential is stronger (see **Figure 4-10**(c) to (e)). The probability density associated with one typical state in the dispersive band of **Figure 4-10**(e) is plotted in **Figure 4-10**(f). This state, as all states in the band, is actually localized at one interface. Thus, the first layer of N (with negative onsite energy) atoms at B-C interface or the first layer of B atoms (with positive onsite energy) at N-C interface of G/BN systems plays a role similar to that of edge C atoms with modified on-site energy in a GNR.

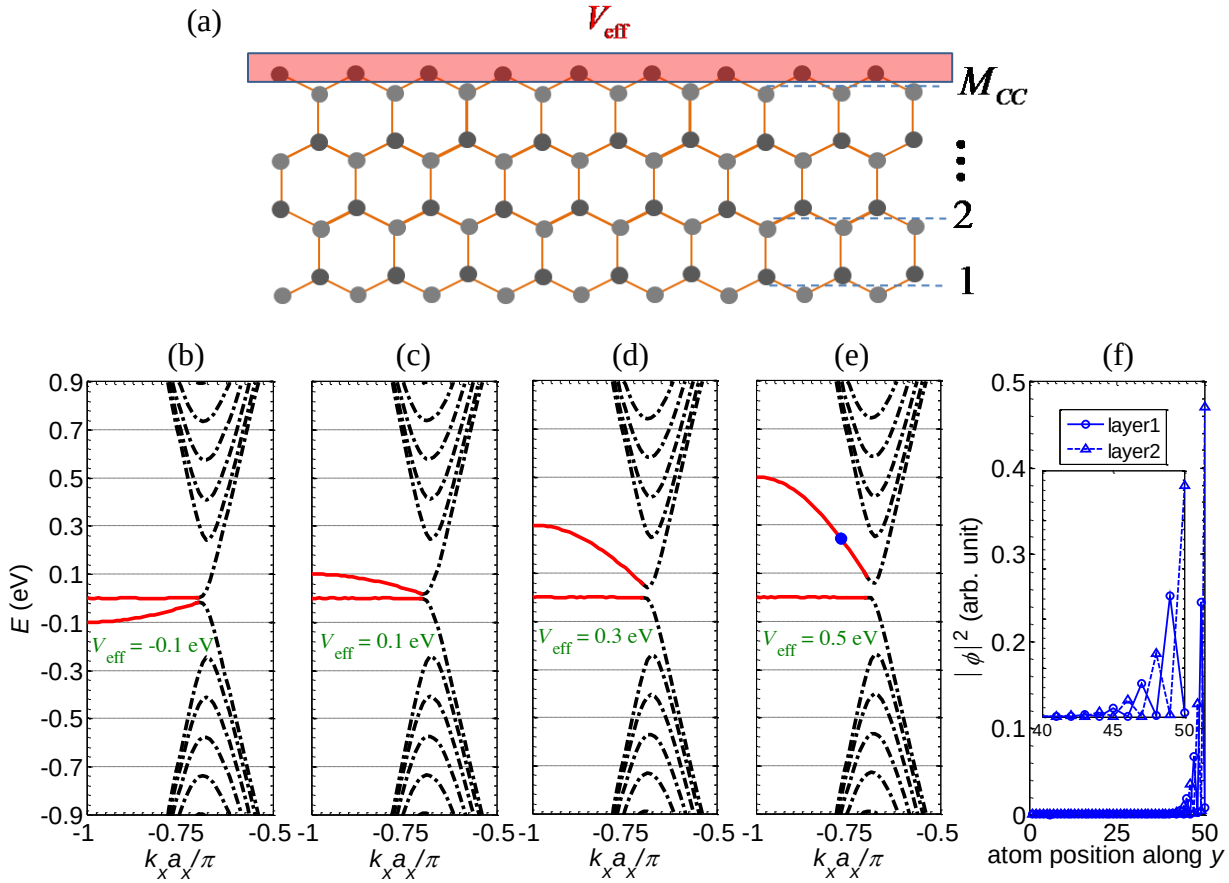

Figure 4-10: (a) Model of effective potential V_{eff} applied on the edge atoms of a zigzag graphene ribbons to mimic the effects of G/BN interface. (b-e) Energy bands for different effective potentials applied. (f) Square wave function corresponding to the state marked with a blue dot in (e). Inset: magnification of the interface region.

It should be noticed that within this simple 1NN model, the highest (or lowest) energy of a dispersive hybrid band (at Brillouin zone edge $k_x = \pm\pi / a_x$) is directly equal to the applied potential V_{eff}. Indeed, by applying on each side two different effective potentials equal to 1.394 eV and -0.75 eV, respectively, i.e. the actual energy values of the hybrid states at the Brillouin zone edge in **Figure 4-7**(b), the energy dispersions plotted in **Figure 4-11** are obtained (symbols solid lines). They are very close to that computed via the complete 2NN approach (including second neighbors and the decaying potential) in the B-C--C-N system. It is thus possible to mimic correctly the hybrid states in in-plane zigzag G/BN heterostructures by using a simple model of ZGNRs with appropriate on-site energies on the edge atoms. However, hybrid states cannot be found in the case of interface with a too high (absolute) onsite energy leading to negligible hybridization, as for instance with Hydrogen atoms.[69,94]

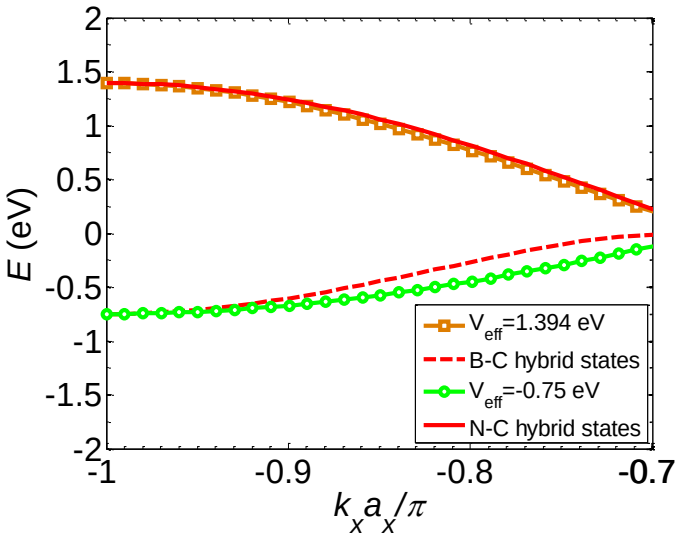

Figure 4-11: The new edge states in the effective potential model (symbols) compared with actual hybrid states (solid and dashed lines) in the B-C--C-N structure.

4.3.5 Enhancement of electron transport from hybrid states

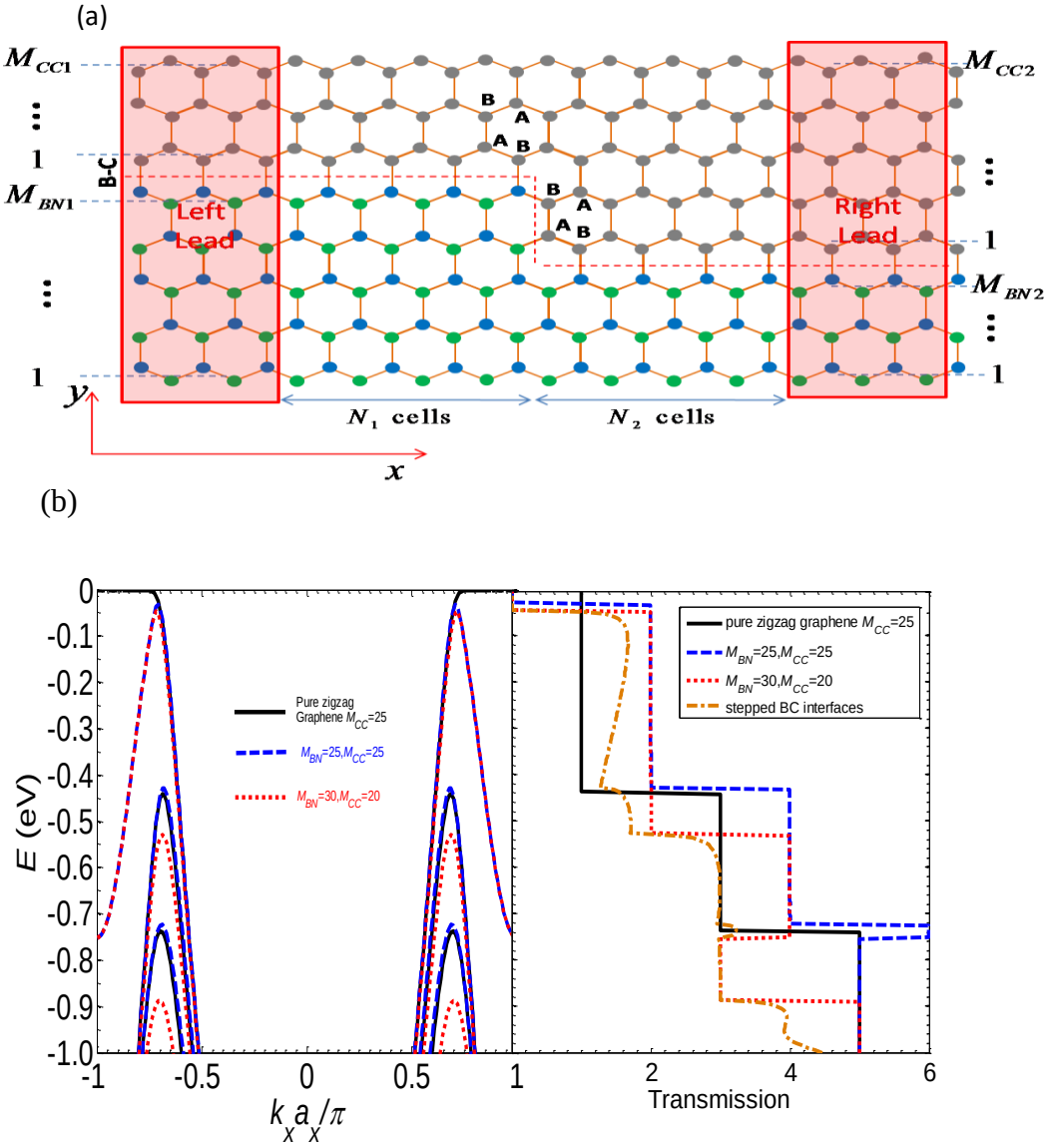

Figure 4-12: (a) Stepped B-C interface structure. (b) Energy bands for a pure zigzag graphene with M_{CC} = 25 (solid black line), straight B-C interface with M_{BN} = 25, M_{CC} = 25 (dashed blue line) and M_{BN} = 30, M_{CC} = 20 (dotted red line). Transmissions are plotted in the right panel for pure zigzag graphene ribbon, straight B-C interface and the stepped B-C interface (dashed-dotted orange line). In the latter case we have M_{BN1} = 30, M_{CC1} = 20, M_{BN2} = 25, M_{CC2} = 25, N_1 = N_2 = 10.

In this section, we intend to check that the emergence of hybrid states at graphene/BN zigzag interface can enhance the electron transport, even in a realistic structure with non-perfectly straight interface.[145] We thus consider the single-step B-C interface structure schematized in **Figure 4-12**(a). In the two parts of this structure the graphene width is either M_{CC1} = 25 or

M_{CC2} = 20. This case can be compared to that of the straight interface with $M_{BN1} = M_{BN2}$ and $M_{CC1} = M_{CC2}$ as schematized in **Figure 4-4**(a). The transmission was investigated using the atomistic non-equilibrium Green's function method. [80,88,148] In **Figure 4-12**(b) we plot the energy bands and transmission spectrum for three cases: pure zigzag graphene (without BN region, solid-black lines), perfectly straight B-C interfaces (dashed-blue or dotted-red lines) and stepped B-C interface (orange dashed-dotted line). It can be seen clearly from the solid-black and dashed-blue lines that the transmission is significantly enhanced in the energy range [- 0.75 eV, 0] due to the presence of hybrid B-C states. Even in the case of the stepped interface we still observe higher transmission in the range [-0.45 eV, -0.05 eV] compared to the case of pure zigzag graphene ribbon. In the stepped interface structure, the bandgap still exists, which is evidenced by the zero transmission in the region of energy close to 0. Thus, hybrid states and bandgap can survive in realistic structures with non-uniform zigzag graphene-BN interfaces.

4.3.6 Experimental evidence of hybrid states

Recently, Drost and his collaborators showed interesting results of interface states in zigzag Graphene/BN heterostructures.[145] Thought the theoretical analysis is limited just to showing energy bands, the experimental results provided a strong evidence of the presence of the interface hybrid states.

First of all, they grew graphene on a (111) iridium (Ir) single crystal using temperature-programmed growth (TPG) process, then BN was deposited. Few layers of gold were also introduced between the sample and the substrate to reduce the reconstruction of graphene and BN (see the left panel of **Figure 4-13**). This technique provided high quality zigzag terminated interface. Later on, the samples were examined by low temperature scanning tunneling microscopy (STM) and spectroscopy (STS). In the right panel of **Figure 4-13** we can observe the spectrum of local density of states from STM images. It can be seen clearly that there is some remarkable signal at the zigzag interface of graphene/BN, while no such kind of peaks appear on interfaces with other terminations. This evidences the existence of interface hybrid states as we demonstrated theoretically above.

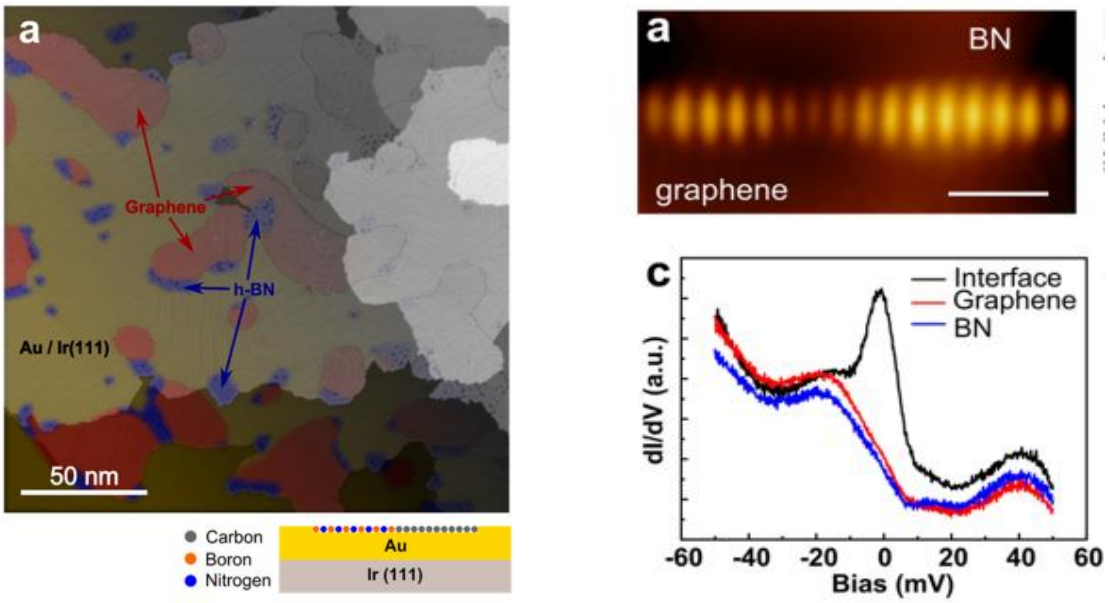

Figure 4-13: Left panel: Graphene/BN heterostructures were grown on a (111) iridium single crystal with gold intercalated under the samples. Right panel: local density of states observed by Scanning Tunneling Spectroscopy (STS) at the interfaces. *Reference: Drost et al*. [145]

4.3.7 The parity of wave functions

In zigzag GNRs, the parity rule is a well-known effect related to the mirror symmetry between A and B carbon sub-lattices with respect to the center axis of the ribbon.[58,59,149] It may have important consequences on the transport properties in zigzag ribbon devices.[59,131,150] The wave function along the width of the ribbon is either even or odd depending on (i) the even/odd number of zigzag chains M_{CC}, (ii) the sub-band number and (iii) the momentum.[150] In this section we are going to check this effect and its consequence on transport in zigzag graphene/BN hetertostructures which were considered above. To check the parity effect in our structures, we will replot energy bands in the range of momentum $0 \leq k_x a_x \leq 2\pi$ (initially we plotted them in the range $-\pi \leq k_x a_x \leq \pi$), to make easier the comparison with results demonstrated for pure zigzag graphene by *Nakabayashi et al.*,[149] *Rainis et al.*.[59]

4.3.7.1 Violation of parity rule in asymmetrical structures

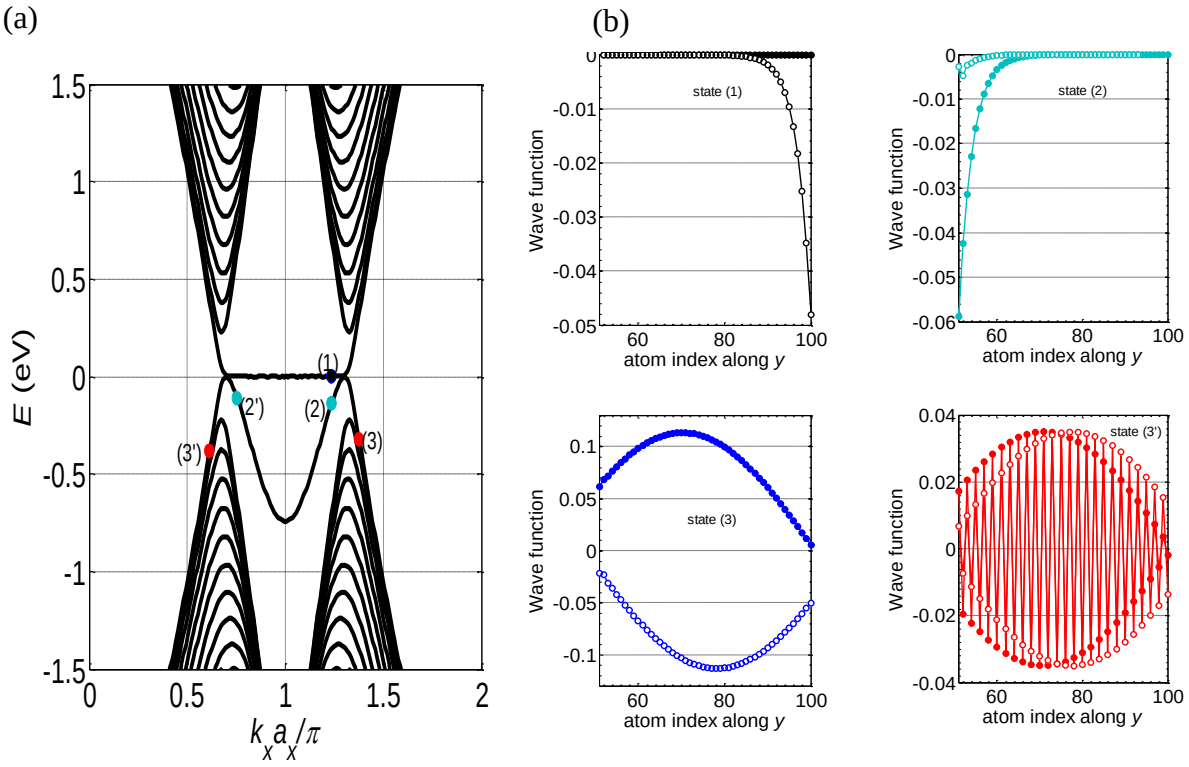

Figure 4-14: (a) The energy band of the B-C structure is plotted in the range of momentum from $0 \leq k_x a_x \leq 2\pi$. (b) Wave functions at states (1), (2), (3), (3') in (a), filled and unfilled circles present the two inequivalent sub-lattices carbon A and B. Here $M_{CC} = M_{BN} = 50$.

In **Figure 4-14**, we show the band structure and wave function (in the graphene section only) at some positions in the energy bands of the structure with single B-C interface. In general, wave functions are complex matrices but here we only plot the real part of wave functions. The imaginary part of wave functions has been checked to have the same parity (or non-parity) as the real part. The wave functions of the states (1), (2), (3) in the valley K and (3') in the valley K' are clearly not even or odd functions of *y*. Thus, the parity is broken in this B-C interface structure. This result can be understood as follows: the parity in zigzag GNRs comes from the mirror symmetry between carbon sub-lattices A and B with respect to the center axis of the ribbon. In single B-C structures, only one edge is modified by bonding with Boron atoms, which leads to a violation of the mirror symmetry between Carbon sub-lattices A and B and breaks the parity. We can thus predict that there is also no parity effect in asymmetrical

structures with N-C and B-C-C-N interfaces. In contrast, the symmetrical structures B-C-C-B and N-C-C-N are highly expected to exhibit a parity effect.

4.3.7.2 Preservation of parity rule in mirror symmetrical structures with non zero conductance.

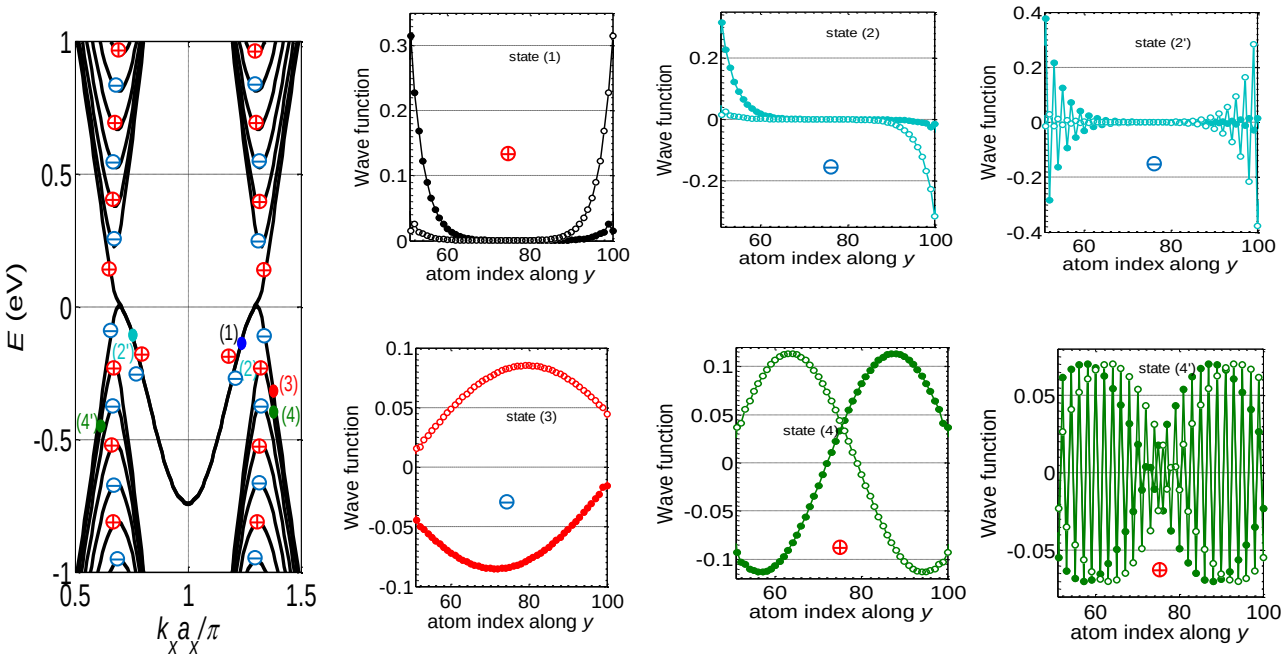

Figure 4-15: Energy bands and wave functions of a B-C-C-B structure with even M_{CC} = 50 (and M_{BN2} = M_{BN2} = 50). Red circle with plus sign '+' and blue circle with minus sign '-' correspond to even/odd states, respectively.

Now we check the parity in the B-C-C-B structure with mirror symmetry with respect to the center of the structure, for both cases of even (**Figure 4-15**) and odd (**Figure 4-16**) number of zigzag chain lines M_{CC}. We denote red circles with plus sign '+' and blue circles with minus sign '-' for even/odd states, respectively. The state (1) comes from the first conduction band, the states (2), (2') and (3) belong to the first valence band, while the states (4) and (4') belong to the second valence band. For the case of even M_{CC} (**Figure 4-15**) the states of the same band but different valleys K and K' have the same parity, while for odd M_{CC} (**Figure 4-16**), these states have opposite parity. It is thus the same as the parity rule which has been found in pure zigzag graphene. [58,59,149]

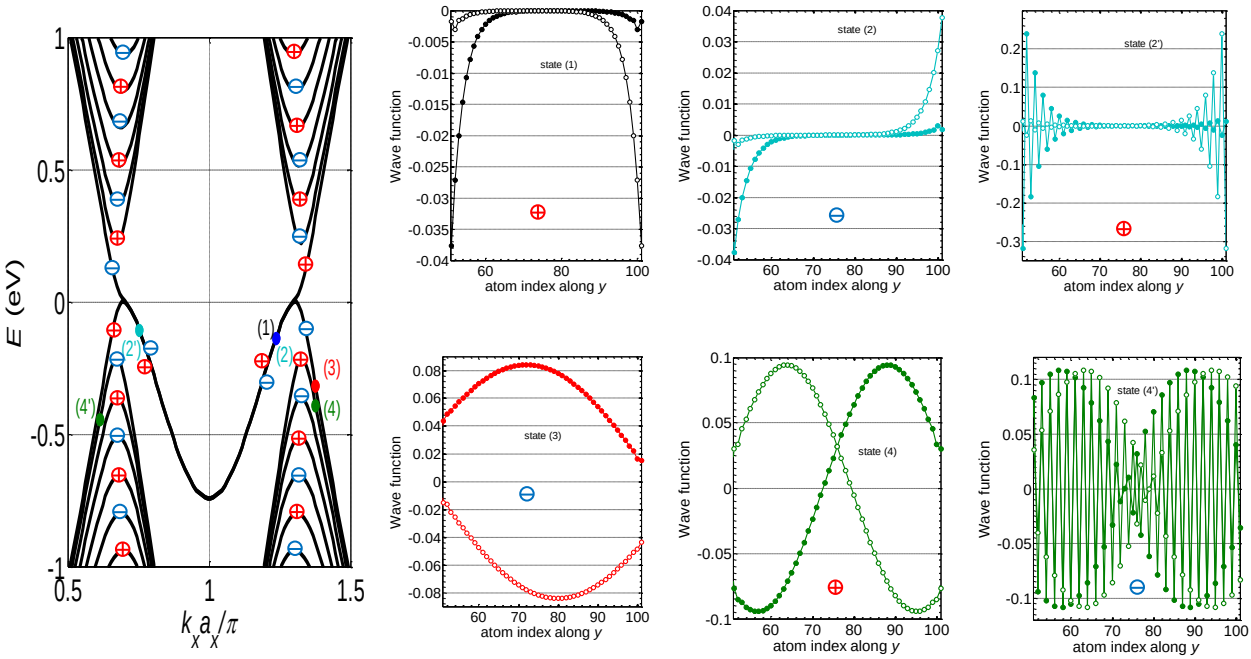

Figure 4-16: Energy bands and wave functions of a B-C-C-B structure with odd M_{CC} = 51. Here, M_{BN2} = M_{BN2} = 50.

Though pure zigzag graphene ribbons are gapless, it was demonstrated that a conduction gap can be observed in a p-n junction system for the case of an even number of chain lines [58] which was later expounded by *Nakabayashi* [149] with a theory of band selective filter. Before studying this transport effect in our zigzag graphene/BN structures, we will first reproduce the effect in zigzag graphene by applying a simple stepped potential model as sketched in **Figure 4-17**(a). Since a potential U is applied to the right region, the band structure of this region shifts up or down a quantity equal to U depending on the sign of the potential. In **Figure 4-17** (b) and (c), Δ is called pseudo-gap [149] which is the energy separation from the Fermi level. U = 0.5Δ was used for both cases of odd and even number of chain lines. As we can observe, the conductance falls to zero in the energy range [0, U] for the case of even M_{CC}, while no such effect can be observed in the case of odd M_{CC}. This effect can only be explained by the parity rule as follows: an electron coming from the left side can only scatter to a state in the right side if this state has the same parity and group velocity direction as the in-coming wave (the same right or left moving waves). In **Figure 4-17**(b) there is always some available states with the same parity and group velocity direction in the range [0, U] in the case of odd M_{CC},

while in **Figure 4-17**(c) we have two opposite parities in the two regions and thus the transmission is blocked, i.e. the conductance drops to zero in this region of energy. In general, zero conductance can be observed for even M_{CC} if $0 \leq U \leq 2\Delta$. The range of zero conductance is $[0, U]$ if $U \leq \Delta$ and $[U-\Delta, \Delta]$ if $\Delta \leq U \leq 2\Delta$.

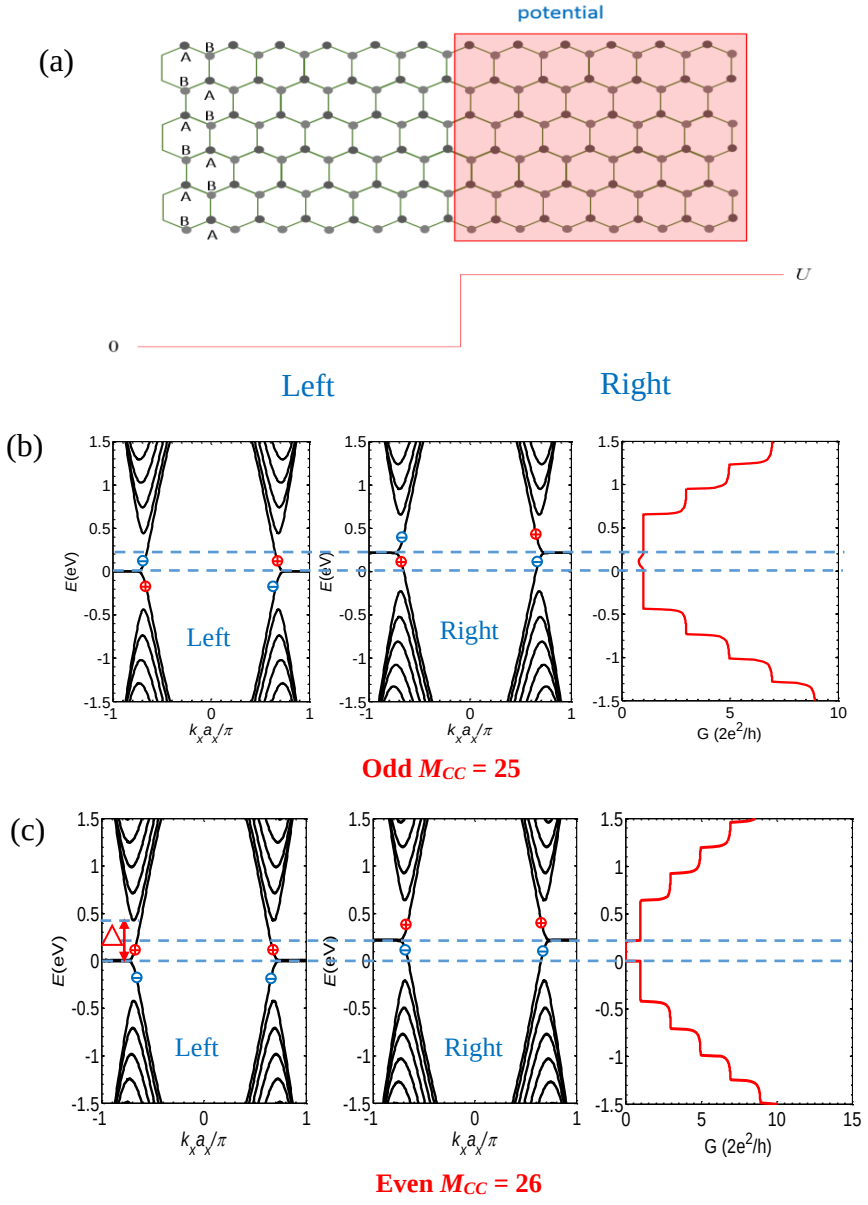

Figure 4-17: (a) An infinite zigzag graphene ribbon with an applied stepped potential. (b) and (c) band structures in each region and conductance for the case of odd and even M_{CC}, respectively. In both cases $U = 0.5\Delta$.

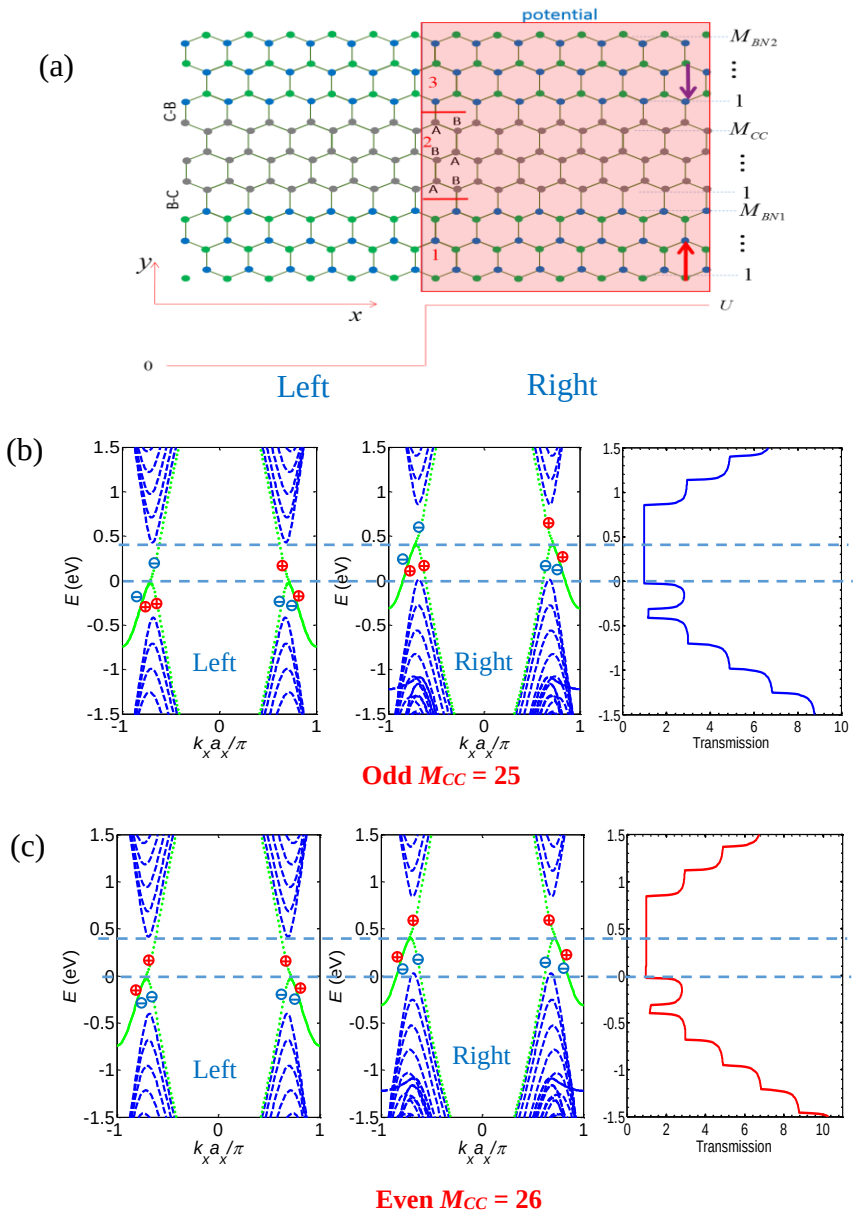

Figure 4-18: (a) A stepped potential based on B-C-C-B structures. (b) and (c) band structures in each region and conductance for the case odd and even M_{CC}. In both cases $M_{BN1} = M_{BN2} = 25$, $U = 1.0\Delta$.

Now we are going to examine this effect in the case of a zigzag graphene/BN structure. As demonstrated above, mirror symmetrical structures such as a zigzag B-C-C-B structure have the same parity as a pure zigzag graphene ribbon, we thus may expect the same transport properties in this hybrid structure. However, it can be seen clearly from **Figure 4-18**(c) that non zero conductance can be observed even for the case of even M_{CC}. In fact, it is due to the emergence of hybrid interface states. Now in the right region and in the range of energy [0, U] we always have some states that contribute from the hybrid states bands which have the same

parity and velocity direction as the in-coming states from the left, and thus the transmission is allowed. Interestingly, the conductance for both cases of odd $M_{CC} = 25$ and even $M_{CC} = 26$ are almost identical. Because non-uniform ribbons are more realistic in devices, this result suggests a new way to standardize transport properties of zigzag structures and to make them less dependent on the preciseness of the atomistic arrangement.

4.4 Conclusions

In this chapter we have demonstrated theoretically the presence of a peculiar kind of hybrid states at the interface between zigzag graphene and BN ribbons. This states are strongly localized close to the interfaces as in pure ZGNRs, but they are able to propagate with a group velocity as high as 7.4×10^5 m/s. Besides, the properties of the hybrid states differ according to the type of bonding atom at the interface. For instance, the group velocity of the hybrid state is higher at the N-C interface than at the B-C one. Moreover, in the case of asymmetric B-C--C-N structure, a relatively wide bandgap of 207 meV can be open for a graphene width of 5 nm, with strong dependence on the graphene width. We have generalized our study to other systems using an effective model and discussed the conditions for the appearance of hybrid state with interesting properties. We have also considered electron transport in a stepped-BC interface system and shown that hybrid states and bandgap can survive in realistic structures with non-uniform ribbons. Finally, we have examined the influence of hybrid states on the parity rule and its effect on transport in our structures. Beyond the experimental evidence of these states by Drost et al,[145] using scanning tunneling microscopy (STM), their dispersive character and the resulting bandgap could be accurately observed by using angle-resolved photoemission spectroscopy (ARPES).[136,151] The synthesis of this type of graphene/BN interface may thus open a new way of modulating and controlling the electronic properties of graphene nanostructures and devices.

Chapter 5:

Enhancement of thermoelectric performance in Graphene/BN heterostructures by interface scattering

In this chapter we investigate the thermoelectric properties of in-plane heterostructures made of Graphene and hexagonal Boron Nitride (BN). The heterostructures consist in armchair graphene nanoribbons to the sides of which BN flakes are periodically attached. This arrangement generates a strong mismatch of phonon modes between the different sections of the ribbons, which leads to a very small phonon conductance, while the electron transmission is weakly affected. In combination with the large Seebeck coefficient resulting from the BN-induced bandgap opening or broadening, it is shown that large thermoelectric figure of merit $ZT > 0.8$ can be reached in perfect structures at relatively low Fermi energy, depending on the graphene nanoribbon width. The high value $ZT = 1.48$ may even be achieved by introducing appropriately vacancies in the channel, as a consequence of further degradation of the phonon conductance.

5.1 Introduction

Due to its exceptional electronic, optical, thermal and mechanical properties, graphene should not only replace conventional materials in some existing applications, but, above all the combination of all these unique properties is expected to inspire fully new applications [5,152] However, one major drawback of graphene for electronic applications, at least for its use as a switching device, is its gapless character [1] that is responsible, e.g., for the low on/off current ratio in graphene transistors.[121,153] It is also an obstacle for thermoelectric applications because it makes difficult to separate the opposite contributions of electron and hole states to the Seebeck coefficient, which is smaller than 100 μV/K in pristine graphene.[14] Additionally, the thermal conductivity in graphene is very high, even higher than 4000 W/mK for a single layer,[3] which is a strong limitation to achieve high thermoelectric figure of merit *ZT*. This quantity is defined by equation (1-60) in terms of electronic and thermal conductance and can be rewritten as

$$ZT = \frac{P}{K}T \tag{5-1}$$

where $P = G_e S^2$ is the power factor, $K = K_e + K_p$ is the total thermal conductance, T is the absolute temperature, while G_e, S, K_e and K_p are the electrical conductance, the Seebeck coefficient, the electron thermal conductance and the phonon thermal conductance, respectively.

Actually, the thermoelectric figure of merit in graphene is limited to $ZT < 0.01$, leading to poor thermoelectric efficiency. However, in spite of these intrinsic obstacles, many suggestions of bandgap nanostructuring have been taken up, at least at the theoretical level, to enhance the thermoelectric performance of graphene and to achieve ZT values higher than 1.[84] Indeed, since the pioneering works of Hicks and Dresselhaus, nanostructuring materials in low-dimensional systems is strongly expected to provide higher ZT and thermoelectric efficiency than bulk materials,[154] thanks to (i) the enhancement of Seebeck coefficient resulting from size quantization and (ii) the reduction of thermal conductance due to interface effects. It has been confirmed experimentally in many systems.[155] In the case of graphene, the primary expectation of nanostructuring is the bandgap opening to enhance the Seebeck coefficient. The reduction of thermal conductance is also expected, if it is not paid by a stronger reduction of electronic conductance, since all parameters entering in the expression of ZT are mutually coupled and difficult to control independently.

As the simplest form of graphene nanostructuring, graphene nanoribbons (GNRs) were first investigated. With finite-bandgap armchair-edges GNRs (AGNRs), significant improvement of thermoelectric properties has been predicted compared to 2D graphene.[31,156] However, in the best case ZT does not exceed 0.35 for the narrowest AGNR with only $M_{CC} = 3$ dimer lines in the width as will be shown later. To enhance further ZT, it is necessary to design more sophisticated ribbons likely to degrade strongly the phonon contribution to the thermal conductance while retaining high electron conduction properties. Several works have suggested to use multi-junction GNRs with alternate sections of different width, different chirality, or different chirality and width.[31,157,158] Values of ZT close to one have been calculated in such structures. Promising results were also obtained in kinked (or chevron-type) GNRs[159] or even by combining chevron-type geometry with isotope cluster engineering.[33] In zigzag-edge GNRs of several micron length, edge disorder and extended

line defects have been shown to enhance *ZT* to values greater than 2 if electron-phonon scattering may remain negligible.[30,160] It has been also predicted that *ZT* can be improved by using graphene nanomesh (GNM), i.e. a graphene layer in which a periodic array of nanopores is perforated[161] or by designing vertical junctions in multilayer graphene.[162]

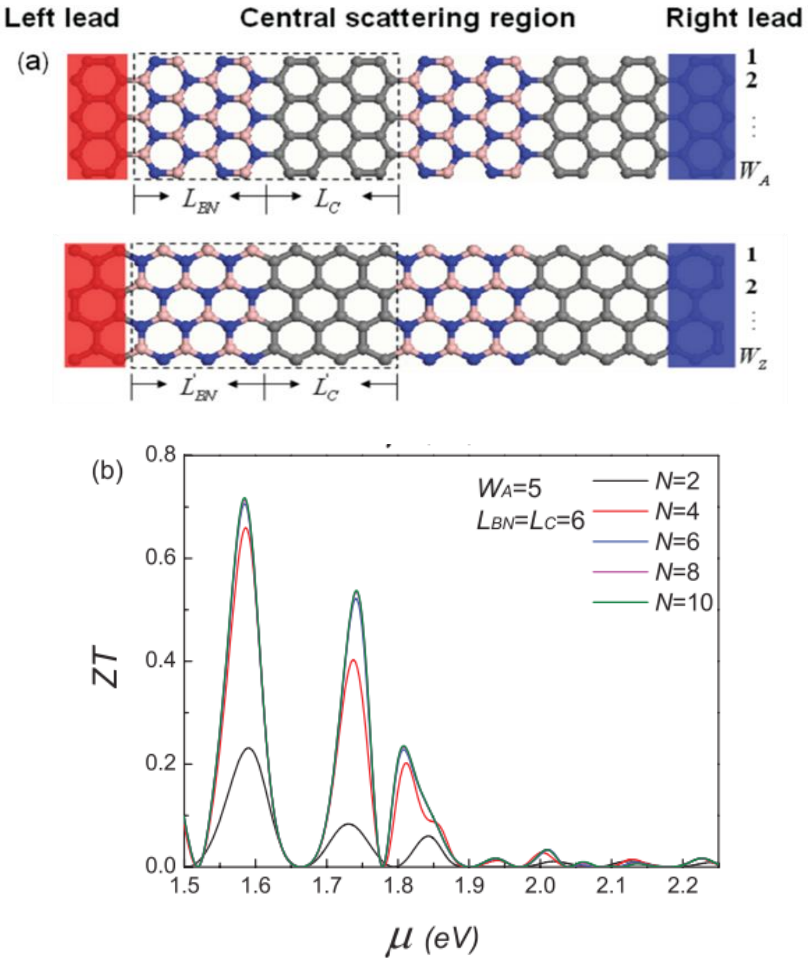

Figure 5-1: (a) The supper cell structures were considered by Yang et al.[163] and (b) the best result of *ZT* is about 0.7 at high chemical energy $\mu \approx 1.58$ eV.

In chapter 2 and also in some theoretical works,[35,46,108,109,142,164] it has demonstrated that Graphene/BN heterostructures made of adjacent armchair ribbons are always semiconducting, while zigzag hybrid ribbons may be either semi-metallict or semiconducting, depending on the type of bonding at graphene/BN interfaces,[61,109,142] which is promising for transistor application with efficient on/off current switching.[37,50] Some works also

considered the thermal transport in these types of heterostructures[165–167] and have shown that they offer the possibility to tune and reduce strongly the phonon thermal conductance. Hence, the large bandgap opening in Graphene/BN hybrid structures should lead to good power factor, and high *ZT*. However, according to our best knowledge only two works have been reported so far on the thermoelectric properties of monolayer graphene/BN structures, by Yang et al. [163] and more recently by Vishkayi et al.[76]. The latter focused on hybrid zigzag ribbons with a graphene/BN junction and two leads made of square lattices (see **Figure 5-2**). Though an enhancement of *ZT* was observed compared to pure zigzag graphene its maximum value was still limited. In the former work,[163] the authors reported a significant improvement of *ZT*, up to 0.7 for some configurations of superlattice armchair ribbons consisting of alternating graphene and BN sections (see **Figure 5-1**). However, the insulating effect of BN sections induces a high electron scattering, which shifts the good *ZT* values to high chemical potentials of about 2 eV, i.e. a range of energy difficult to exploit in practice.

(a) (b)

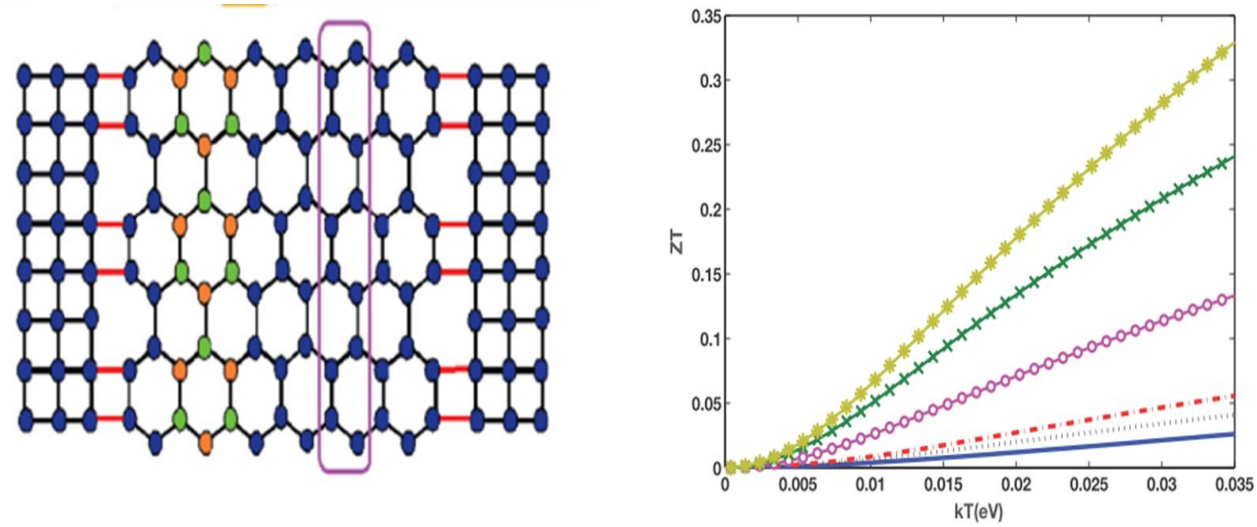

Figure 5-2: A device made of hybrid zigzag ribbons of graphene/BN and two leads made of square lattices. The best *ZT* at room temperature (kT = 0.025 eV) is about 0.23. *Reference: Vishkayi et al.*[76]

In this chapter, by means of atomistic calculation we investigate the thermoelectric performance of GNRs with parallel graphene/BN interfaces appropriately distributed. We demonstrate that by graphene/BN interface engineering it is possible to enhance the phonon scattering in armchair GNRs and thus to reduce strongly the phonon thermal conductance while the electronic conductance is weakly affected. It leads to high values of *ZT* at rather small chemical potential. Additionally, we show that the figure of merit may be enhanced up to 1.48 at room temperature by introducing vacancies in the graphene region.

The chapter is organized as follows. The model and methodology are presented in Sec. 5.2, while the results are discussed in Sec. 5.3, where we analyze dispersions of electrons and phonons (sub-Sec. 5.3.1) and we emphasize the role of interface phonon scattering (sub-Sec. 5.3.2) and that of vacancies (sub-Sec. 5.3.4).

5.2 Studied device and methodology

5.2.1 Device structure

The structure investigated in this work is schematized in **Figure 5-3**. It consists in a graphene ribbon to the sides of which BN flakes are periodically attached. It is thus an alternating arrangement of graphene and BN/graphene/BN (BN/G/BN) sections. Such BN/G/BN ribbons are known to open or broaden the bandgap of free GNRs as we have seen in chapter 2 and also in Refs.[35,164] and they are expected to modify strongly the phonon dispersion, with thus a strong impact on the phonon conductance. In contrast, the electronic conductance in the central graphene ribbon is expected to be weakly affected by the presence of BN flakes. We have focused our study on armchair structures that usually provide higher *ZT* than zigzag edge ribbons.[163]

The width of each sub-region is characterized by the numbers of dimer lines M_{CC} and M_{BN}. Along the transport direction, the structure is characterized by the number n_{BN} of BN/G/BN sections and the numbers of unit cells N_{vc} and N_{BN} in graphene and BN/G/BN sections, respectively. The total number of unit cells in the active region is thus $N_A = (n_{BN}+1)N_{vc} + n_{BN}N_{BN}$. This active region is connected to BN/G/BN leads having a large bandgap.

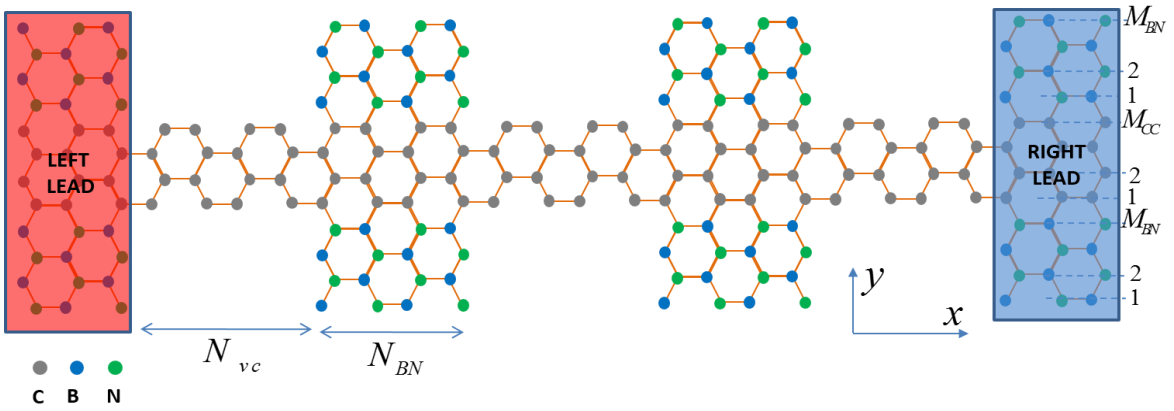

Figure 5-3: Schematic view of studied graphene/BN heterostructure with sub-sections made of BN flakes attached to the main AGNR channel. The two leads are made of BN/G/BN ribbons as the hybrid parts of the active device.

It is assumed that the system can be extended periodically along the *y* direction, which requires $M_{CC} + M_{BN}$ to be an even number.[35]

5.2.2 Methodologies

The electronic properties were investigated using a nearest-neighbor Tight Binding (TB) approach. The corresponding atomistic Hamiltonian takes the general form (2-1) in chapter 2, i.e [69]

$$H_e = \sum_i \varepsilon_i |i\rangle\langle i| - \sum_{\langle i,j \rangle} t_{ij} |i\rangle\langle j| \qquad (5\text{-}2)$$

where ε_i is the on-site energy at site *i* and t_{ij} is the hoping energy between atoms at *i*-th and *j*-th sites. Starting from the second-nearest-neighbor TB model of Ref. [35], we made some small changes to work with a simple nearest-neighbor model, i.e we used t_{NC} = 2.0 eV instead of 2.5 eV as in Ref. [35] and we checked that these parameters reproduces very well the energy band structure of armchair graphene/BN ribbons computed using first principle method.[35] The values of the parameters used are listed in **Table 5-1**.

Table 5-1: Tight Binding parameters for electron study

E_{C_A} (eV)	E_{C_B} (eV)	E_B (eV)	E_N (eV)	t_{CC} (eV)	t_{BN} (eV)	t_{BC} (eV)	t_{NC} (eV)
0.015	-0.015	1.95	-1.95	2.5	2.9	2.0	2.0

The phonon properties were computed using the fourth nearest-neighbor Force Constant (FC) model.[66] The general form of the Hamiltonian for the vibrations of atoms was given in[168] and can be rewritten as

$$H_p = \sum_i \frac{1}{2} M_i \dot{u}_i^{\dagger} \dot{u}_i + \sum_{\langle i,j \rangle} \frac{1}{4} \left(u_i - u_j \right)^{\dagger} K_{ij} \left(u_i - u_j \right) \tag{5-3}$$

where M_i and u_i are the mass and the time-dependent displacement of the *i*-th atom, respectively, and K_{ij} is the 3×3 coupling tensor between the *i*-th and *j*-th atoms. Starting with this equation we can also go to the motion equation (1-7) and then (1-14) in chapter 1. The dynamic matrix *D* in equations (1-14) and (1-15) can be simply described in the form:

$$D = \left[D_{3\times 3}^{ij} \right] = \begin{bmatrix} \begin{cases} -\dfrac{K_{ij}}{\sqrt{M_i M_j}} & \text{for } j \neq i \\ \displaystyle\sum_{n \neq i} \frac{K_{in}}{M_i} & \text{for } j = i \end{cases} \end{bmatrix} \tag{5-4}$$

It should be noted that the term $\sum_{n \neq i} \frac{K_{in}}{M_i}$ is a 3×3 matrix that plays the same role as the on-site energy ε_i in the case of electrons. However, this term is varying for each atom, depending on the number and nature of couplings with other atoms. It is in contrast with the case of electrons wherein the on-site energy depends only on the atom on this site.

The force constant coupling parameters in the radial, in-plane and out-of-plane directions $\Phi_r, \Phi_{t_i}, \text{and} \, \Phi_{t_o}$ in (1-17) depend on the level of neighboring. Within a fourth nearest-

neighbor, we thus need twelve parameters for graphene and fifteen parameters for BN. In this work the parameters were taken from Ref.[54] for graphene and from Ref.[92] for BN. These parameters are given in **Table 5-2** where $\Phi_{CC}^{(n)}$ refers to couplings between a Carbon (C) atom and its *n-th* Carbon neighbors. A similar notation in use for interactions between B-N, B-B and N-N atoms. For the coupling of C atoms with B and N atoms we have taken the average value of the force constant parameters between graphene and h-BN,[163] i.e. $\Phi_{BC}^{(n)} = \left[\Phi_{B(N \text{ or } B)}^{(n)} + \Phi_{CC}^{(n)} \right] / 2$, $\Phi_{NC}^{(n)} = \left[\Phi_{N(B \text{ or } N)}^{(n)} + \Phi_{CC}^{(n)} \right] / 2$ and these parameters are given in **Table 5-3**. The masses of C, B, N atoms were taken to be equal to 1.994×10^{-26}, 1.795×10^{-26} and 2.325×10^{-26} kg, respectively.

Table 5-2: Force constant parameters for interactions between C-C or B-N, B-B, N-N atoms

	$\Phi_{CC}^{(1)}$	$\Phi_{CC}^{(2)}$	$\Phi_{CC}^{(3)}$	$\Phi_{CC}^{(4)}$	$\Phi_{BN}^{(1)}$	$\Phi_{BB}^{(2)}$	$\Phi_{NN}^{(2)}$	$\Phi_{BN}^{(3)}$	$\Phi_{BN}^{(4)}$
r	398.7	72.9	-26.4	1	310	70	80	10	-19
t_i	172.8	-46.1	33.1	7.9	185	-32.3	-7.3	-32.5	12.9
t_o	98.9	-8.2	5.8	-5.2	56	-7	-5.5	6.5	-3

Table 5-3: Force constant parameters for interactions between B-C or N-C atoms

	$\Phi_{BC}^{(1)}$	$\Phi_{BC}^{(2)}$	$\Phi_{BC}^{(3)}$	$\Phi_{BC}^{(4)}$	$\Phi_{NC}^{(1)}$	$\Phi_{NC}^{(2)}$	$\Phi_{NC}^{(3)}$	$\Phi_{NC}^{(4)}$
r	354.35	71.45	–8.2	–9	354.35	76.45	–8.2	–9
t_i	178.9	–39.2	0.3	10.4	178.9	–26.7	0.3	10.4
t_o	77.45	–7.6	6.15	–4.1	77.45	–6.85	6.15	–4.1

In chapter 1, by using matrix representation we went to similar forms for the TB Schrödinger equation for electrons and the FC dynamic equation for phonons, they thus can formally be solved using the same approach. The Green's function method has been used in the ballistic approximation [34]. In the case of electrons the total Hamiltonian can be separated in the

device Hamiltonian H_D of the active region, the Hamiltonian $H_{L(R)}$ of the left (right) lead and the coupling term $\tau_{L(R)}$ between the device and the left (rigt) lead. First, the surface Green's functions $G^0_{L(R)}$ of the uncoupled leads are calculated using the Sancho's iterative scheme.[87] They are used to calculate the self-energies $\Sigma^s_{L(R)} = \tau_{L(R)} G^0_{L(R)} \tau^\dagger_{L(R)}$ (see equation (1-44)) describing the device-lead couplings that take place into the device Green's function $G = \left[E + i\eta - H_D - \Sigma^s_L - \Sigma^s_R \right]^{-1}$. In the case of phonons a similar expression of the Green's function is found by replacing the energy E of electrons with the square of the phonon angular frequency ω^2. A recursive technique is applied to reduce the size of the device Green's function to the size of the Green's function G_{11} of the first layer.[83,88] Then, the electron and phonon transmissions, $T_e(E)$ and $T_p(\omega)$ can be computed efficiently by equation (1-52).

Finally, once the transmission $T_e(E)$ and $T_p(\omega)$ are calculated, the electrical conductance, the Seebeck coefficient, and the electron and phonon contributions to the thermal conductance can be computed by equations (1-59) and (1-63). More practical forms of the intermediate function (1-62) and the phonon conductance (1-59) can be derived as (see Appendix D)

$$\begin{cases} L_n(\mu,T) = \dfrac{1}{h} \displaystyle\int_{-\infty}^{+\infty} dE\, T_e(E) (2k_bT)^{n-1}\, g^e{}_n(E,\mu,T) \\ K_p = \dfrac{k_b}{2\pi} \displaystyle\int_0^{\infty} d\omega\, T_p(\omega)\, g^p(\omega,T) \end{cases} \tag{5-5}$$

Where

$$g^e{}_n(E,\mu,T) = \left(\frac{E-\mu}{2k_bT} \right)^n \Bigg/ \cosh^2\left(\frac{E-\mu}{2k_bT} \right) \tag{5-6}$$

And

$$g^p(\omega,T) = \left(\frac{\hbar\omega}{2k_bT} \right)^2 \Bigg/ \sinh^2\left(\frac{\hbar\omega}{2k_bT} \right) \tag{5-7}$$

Here k_b is the Boltzmann constant. Once G_e, S, K_e and K_p are obtained from equations (1-59) and (1-63), the figure of merit ZT can be computed from equation (5-1).

5.3 Results and discussion

In the following analysis of the thermoelectric performance of the device schematized in **Figure 5-3**, unless otherwise stated we will focus mainly on two cases of graphene ribbon width, i.e. M_{CC} = 5 and M_{CC} = 6, that correspond to a metallic and a semiconducting ribbon, respectively, in the case of pure AGNR. Similarly, the BN width M_{BN} will be chosen equal to 9 and 12 for M_{CC} = 5 and 6, respectively, that correspond to the width beyond which the transport properties are unchanged, as will be discussed later.

5.3.1 Electron and phonon dispersions in infinite structure Graphene or BN/G/BN ribbons

Though the studied device consists of finite Graphene and BN/G sections, transport properties of a device can always be understood from features of material band structures. For instance, in the chapter 4 we have investigated quantum transport in a finite device made of zigzag graphene ribbon. In spite of being gapless, zigzag graphene devices still exhibit a conduction gap in the case of even numbers of chain lines. This so-called parity effect can only be explained by studying in detail the properties of wave functions in an infinite zigzag ribbon. It is thus relevant here to study dispersions of electrons and phonons for infinite structures of graphene and BN/G/BN ribbons which may later help us understanding transport properties of the device.

In the first column of **Figure 5-4** we plot electron dispersion for two cases of graphene ribbons M_{CC} = 5 (upper panel) and M_{CC} = 6 (lower panel). The middle column prersent the dispersion of BN/G/BN ribbons. It can be observed clearly that a band gap is open in BN/G/BN structure for M_{CC} = 5 compared to that of zero gap in the pure graphene counterpart. While the bandgap is enlarged in the case M_{CC} = 6. Seebeck coefficient is thus likely to be enhanced in BN/G/BN structures. The density of state (DOS) of graphene and BN/G/BN ribbons are shown in the third column of **Figure 5-4**. It indicates that the mismatch between two sections is only significant at high energy. Hence, the electron transport should not be strongly affected at low energy.

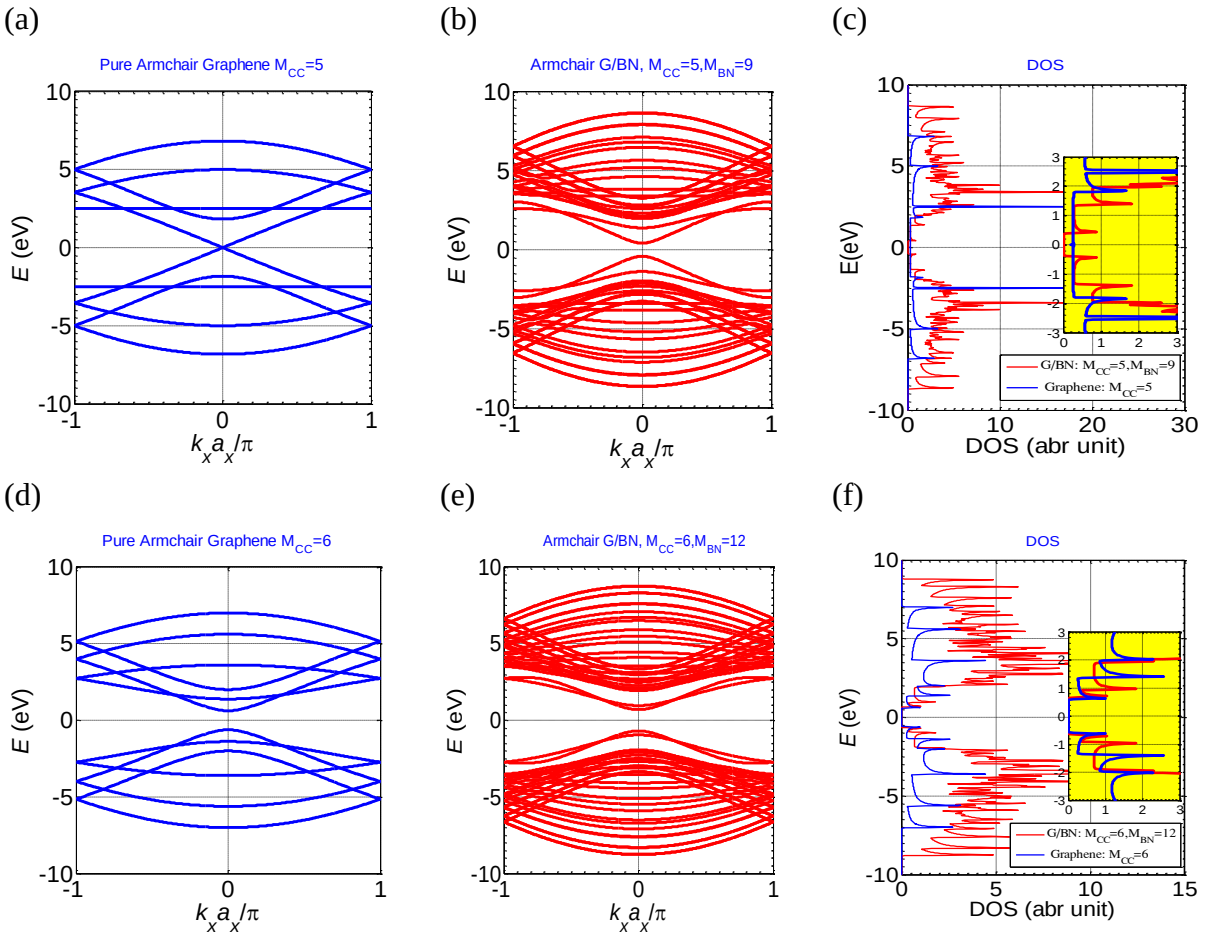

Figure 5-4: Energy bands for two cases: M_{CC} = 5 (metallic graphene) and M_{CC} = 6 (semiconducting graphene). Band structures for armchair BN/G/BN also plotted. DOSs are shown in the third column to illustrate the concentration of states in the two regions.

a) (b) (c)

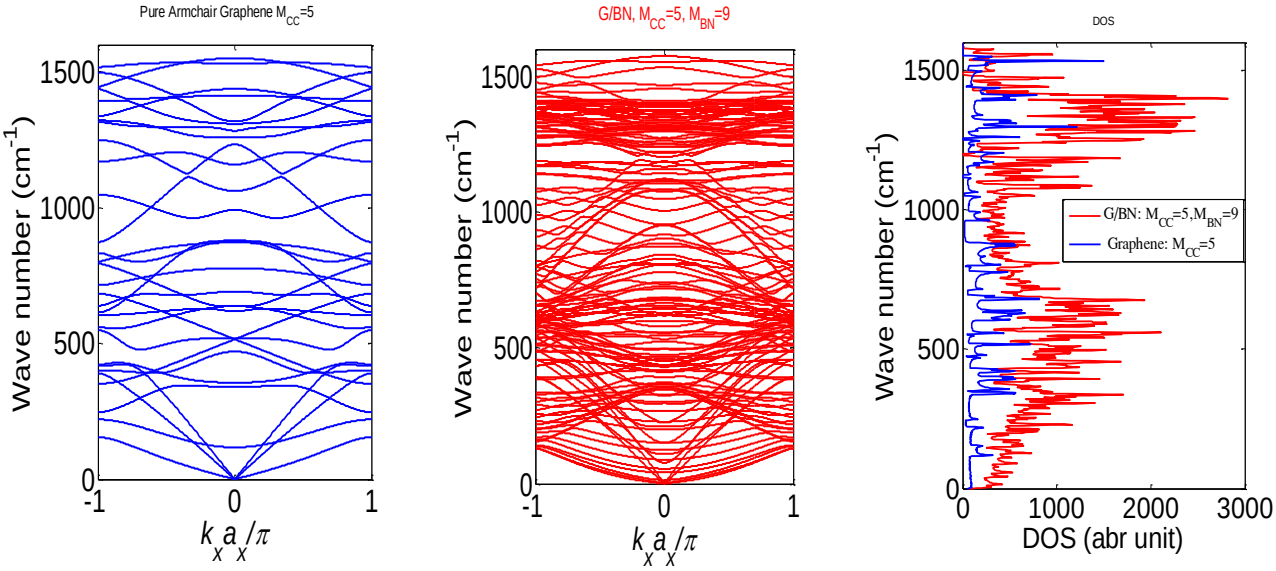

Figure 5-5: Phonon bands for (a) graphene ribbon and (b) BN/G/BN structure with M_{CC} = 5. (c) DOS for phonons are plotted for comparison.

In **Figure 5-5** we show the phonon dispersion and DOSs for both structures, i.e. Graphene and BN/G/BN. The results are shown for M_{CC} = 5 only. Similar physics can be observed for M_{CC} = 6. Unlike the case of electrons as seen in **Figure 5-4**, the phonon modes are strongly modified in BN/G/BN region compared to the case of pure graphene ribbon. As a consequence, higher DOS is obtained in this region, which leads to a remarkable mismatch between sections made of Graphene and BN/G/BN at any range of frequency (**Figure 5-5** (c)). It is thus expected that in this structure phonon scattering is stronger than electron scattering, and it allows us to predict a small phonon conductance in hybrid ribbons while a good electron conductance should be preserved, which is an ideal tendency to get high thermoelectric performance.

5.3.2 Phonon scattering: a key to enhance *ZT*

In this section, transport properties of the device are investigated in detail. The length of active region can be adjusted by changing the number n_{BN} of BN/G/BN sections, which will be used as a parameter in what follows. Indeed, by increasing this number one may expect to reduce the phonon conductance as a consequence of enhanced phonon scattering.

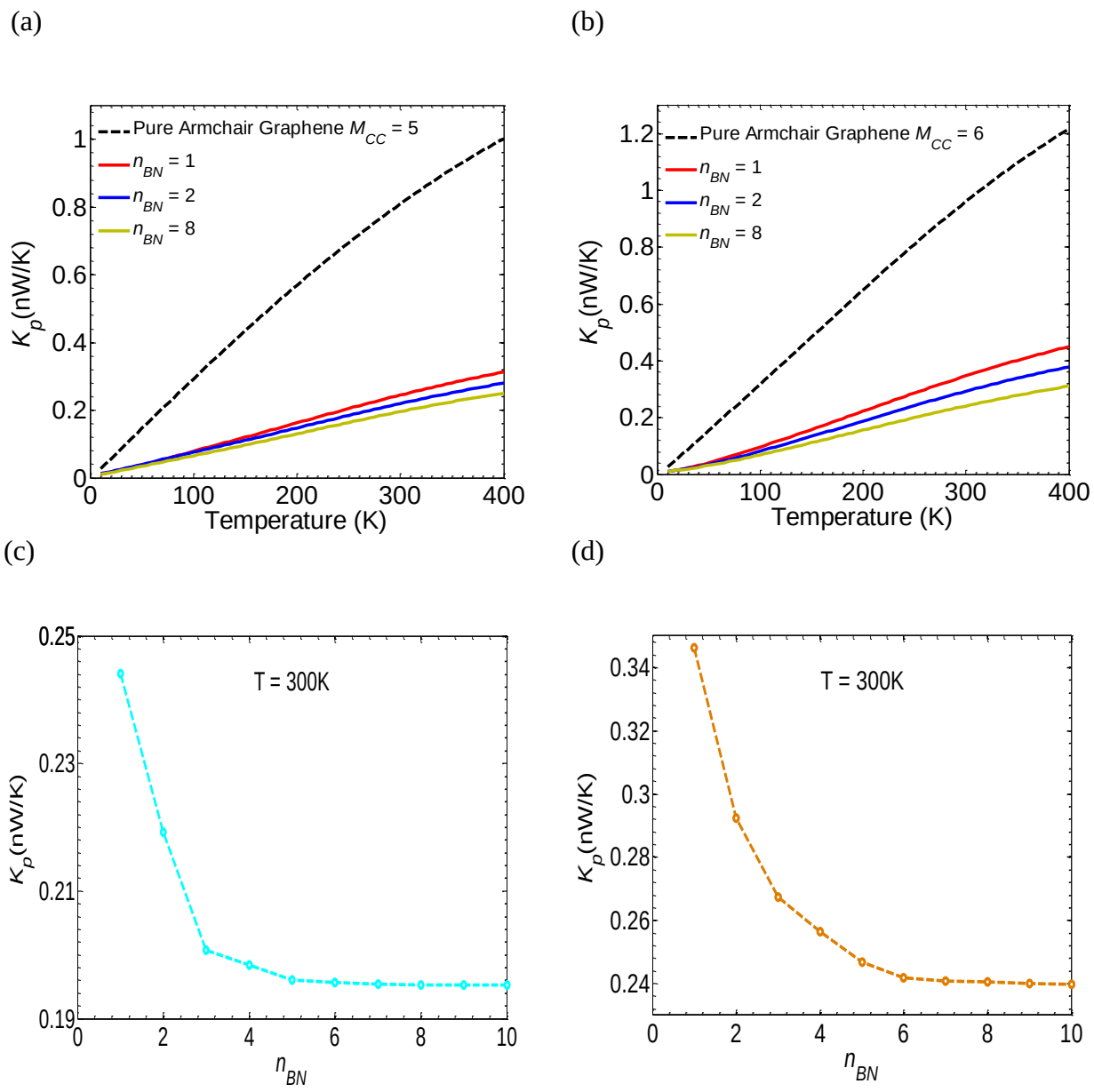

Figure 5-6: Phonon conductance as a function of temperature for M_{CC} = 5 (a), and M_{CC} = 6 (b), for different values of the number n_{BN} of BN/G/BN sections. Phonon conductance at the room temperature for (c) M_{CC} = 5 (cyan circles) and (d) M_{CC} = 6 (brown circles) as a function of n_{BN}.

In **Figure 5-6**(a) and (b) we plot the phonon conductance for M_{CC} = 5 and M_{CC} = 6 as a function of the temperature, for different numbers n_{BN} of BN/G/BN sections in the active

device. We also plot in black lines for comparison the phonon conductance of the corresponding pristine AGNRs. For both widths we obtain a strong reduction of K_p in hybrid structures compared to graphene. Additionally, it can be seen that the phonon conductance decreases further when n_{BN} increases as we observe in **Figure 5-6**(c) and (d). For instance, in the case of M_{CC} = 5 at room temperature (**Figure 5-6**(c)) i.e. phonon conductance drops from 0.244 nW/K for n_{BN} = 1 to 0.196 nW/K for n_{BN} = 5. Then it saturates when the active region is long enough because the system tends to behave as an infinite superlattice system. Finally, for n_{BN} = 10 at room temperature, K_p is about 75% smaller than in the corresponding pristine graphene ribbon.

Similarly, for M_{CC} = 6 (**Figure 5-6**(d)) the phonon conductance falls from 0.96 nW/K (pristine AGNR) to 0.346 nW/K (n_{BN} = 1) and even 0.24 nW/K (n_{BN} = 10). This dramatic reduction of phonon conductance is not only due to phonon scattering at graphene/BN boundaries,[169] but above all to the scattering induced by the mismatch of modes between pristine graphene and BN/G/BN sections as demonstrated in **Figure 5-5**. In terms of transport, the reduction of phonon conductance is understood because of a strong drop of phonon transmission as shown in **Figure 5-7**(a) and (b).

(a) (b)

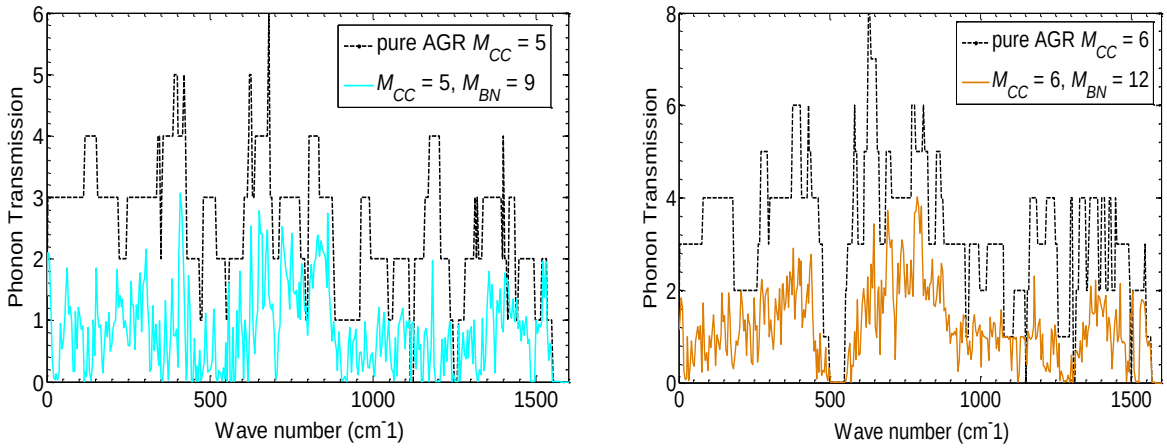

Figure 5-7: (a) & (b) Comparison of phonon transmissions in perfect graphene ribbons (dash lines) and the studied device (cyan and brown lines). For both panels N_{vc} = N_{BN} = 8, n_{BN} = 1.

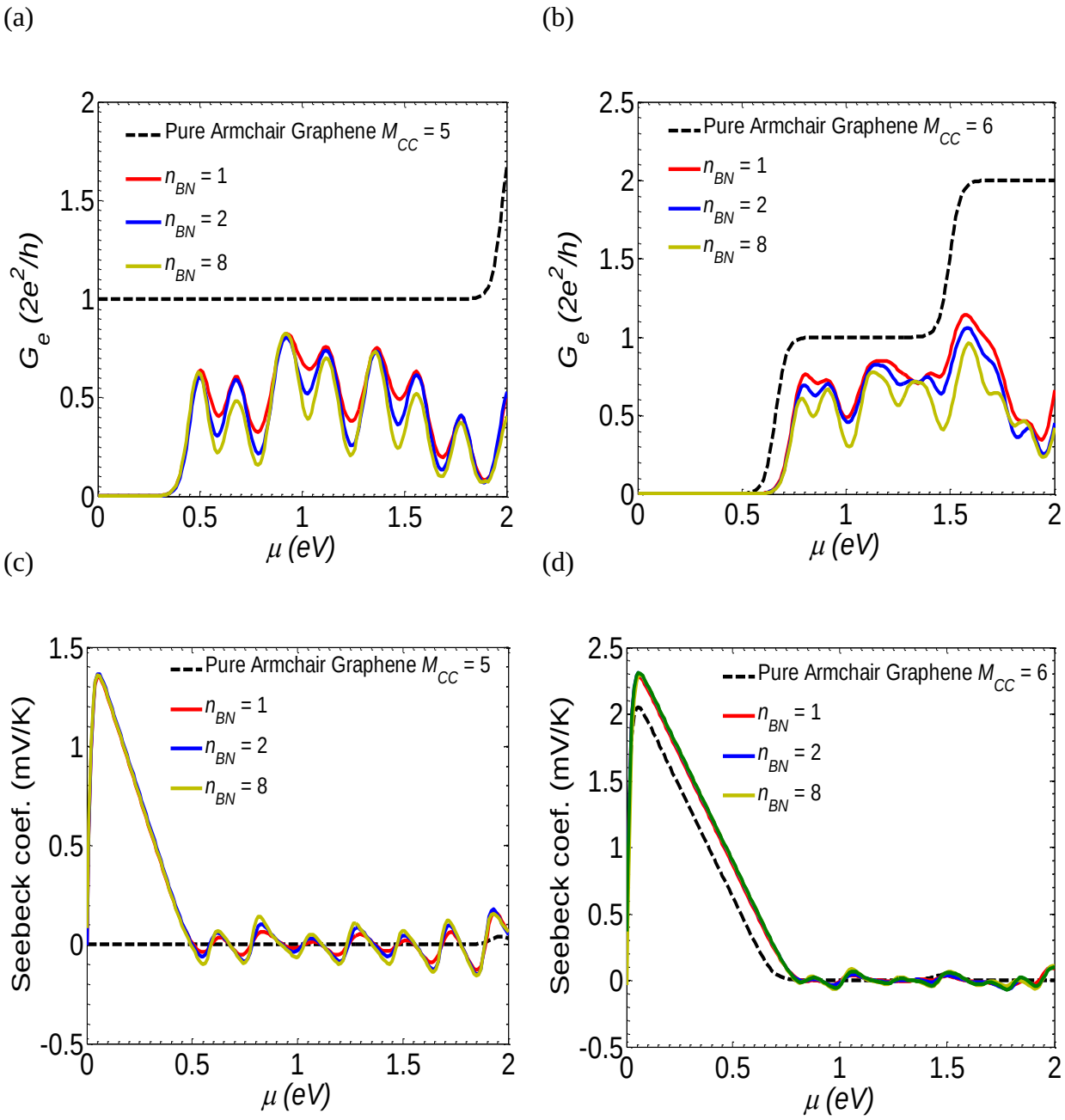

Figure 5-8: (a) (b) Electrical conductance and (c) (d) Seebeck coefficient for the structures with (a) (c) M_{CC} = 5 and (b) (d) M_{CC} = 6 for different numbers n_{BN} of BN/G/BN sections. Other parameters: T = 300K.

The electrical conductance G_e and Seebeck coefficient S are plotted in **Figure 5-8** as a function of chemical energy μ in both cases of M_{CC} = 5 and 6 and, for comparison, in the case of pristine GNR (black dashed lines). In **Figure 5-8**(a) and (c), i.e. for M_{CC} = 5 corresponding

to a metallic AGNR, we can observe the opening of a significant conduction energy gap, which manifests itself not only in the vanishing of G_e at low energy, but also in the strong enhancement of S, compared to its pristine GNR counterpart, whatever the value of n_{BN}. In the case of M_{CC} = 6, for which the pristine GNR is semiconducting, the bandgap is slightly broadened, which yields a small enhancement of the Seebeck coefficient, independently of the number of periods n_{BN} (**Figure 5-8**(b) and (d)).

It is remarkable that in contrast with the phonon conductance, the electronic conductance is not severely degraded with respect to the pristine GNR, whatever the value of n_{BN}, at least at low energy (first step of transmission) at which most of the conduction takes place. Regarding thermoelectric performance, it is definitely a strong advantage of this type of nanostructuring design. It should be noted also that the maximum Seebeck coefficient is higher in the case M_{CC} = 6, corresponding to a larger bandgap. This behavior is consistent to with the bandgap analysis in BN/G/BN regions (section **5.3.1**) and it is also in agreement with the general result which claims that the maximum value of S should be proportional to the bandgap,[170] which has been observed in several other cases.[31,171]

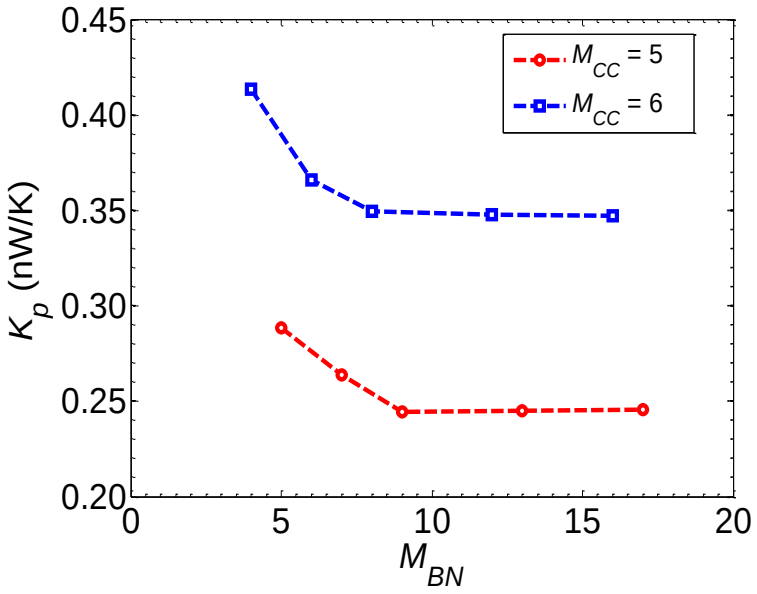

Figure 5-9: Phonon conductance is plotted as a function of the width of BN flakes. Here N_{vc} = N_{BN} = 8 and n_{BN} = 1.

As a consequence of the strong reduction of phonon conductance, together with high power factor $G_e S^2$, good thermoelectric figures of merit are expected in these hybrid structures. Since the phonon conductance appears to be strongly dependent on the alternating arrangement of graphene and BN/G/BN sections in the active region, the results should depend also on the width M_{BN} and the lengths N_{vc} and N_{BN} of these sections. In **Figure 5-9** the phonon conductance is plotted as a function of the width M_{BN} while N_{vc}, N_{BN} and n_{BN} are fixed to be equal to 8, 8, and 1, respectively. It can be seen clearly that a minimum value of about M_{BN} = 10 is required to reach the minimum of phonon conductance. Our investigations of the dependence on N_{vc} and N_{BN} lead us to the conclusion that the maximum value of *ZT* is reached when $N_{vc}/N_{BN} \approx 1$, which is in agreement with the conclusion of Yang et al. [163] in the case of a transverse superlattice of graphene and BN sections. We found also that for M_{CC} = 5 and M_{CC} = 6 the maximum of *ZT* is obtained for N_{vc} = N_{BN} = 8 as seen in **Figure 5-10**. However, for M_{CC} = 3 the best *ZT* is achieved for N_{vc} = 6 and N_{BN} = 4.

In both cases of M_{CC} = 5 and M_{CC} = 6, we plot in **Figure 5-11** the maximum value of *ZT* as a function of the number n_{BN} of BN/G/BN sections in the active region (**Figure 5-11**(a) and **Figure 5-11**(b)), and the evolution of *ZT* as a function of the chemical potential in the leads, for different values of n_{BN} (**Figure 5-11**(c) and **Figure 5-11**(d). In all cases, the case of pristine GNR of same width is shown for comparison. Due to the metallic behavior of AGNRs with $M_{CC} = 3p+2$, the AGNR with $M_{CC} = 5$ exhibits a very small Seebeck coefficient (see **Figure 5-8**(c)) and a *ZT* of about 0.03. Thanks to the bandgap opening and the dramatic reduction of phonon conductance, the figure of merit is strongly enhanced in the hybrid structure (see **Figure 5-11**(a) and **Figure 5-11**(c)), reaching 0.6 for n_{BN} = 1 and 0.81 for longer devices with n_{BN} > 5. More interestingly, it should be remarked that the peak values of *ZT* are observed here for the quite low energy μ = 0.41 eV, which is much smaller and more accessible than in the case of the transverse graphene/BN superlattice shown in **Figure 5-1**.[163]

For M_{CC} = 6, corresponding to a semiconducting AGNR, the peak value of *ZT* reaches 0.65, which is about 3.25 times greater than in the AGNR counterpart (**Figure 5-11(**b)). Due to the larger bandgap, this peak value is obtained for a chemical potential μ = 0.7 eV, i.e. higher than in the case M_{CC} = 5.

(a)

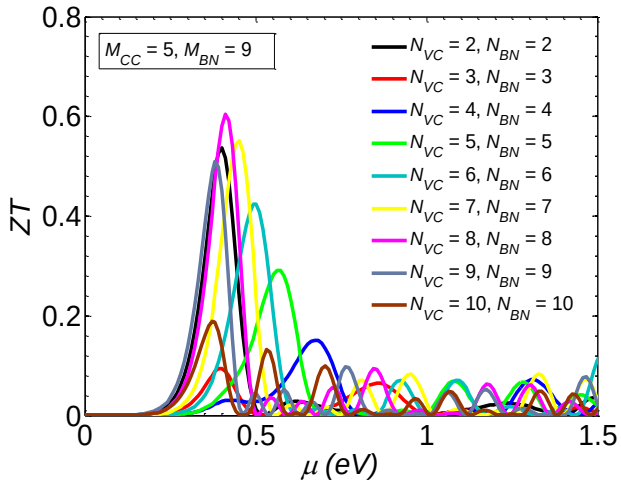

(b)

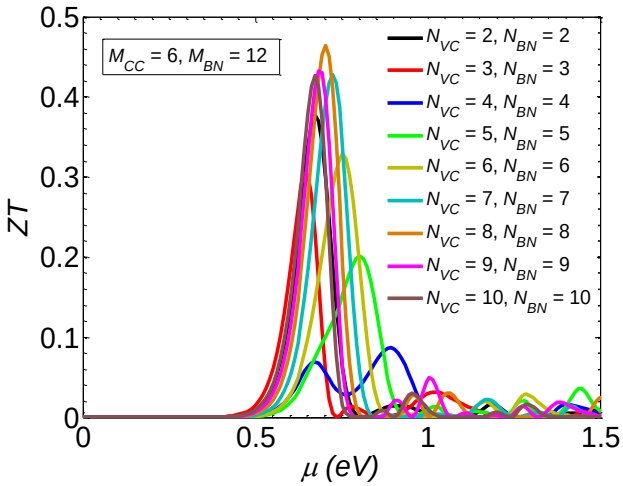

(c)

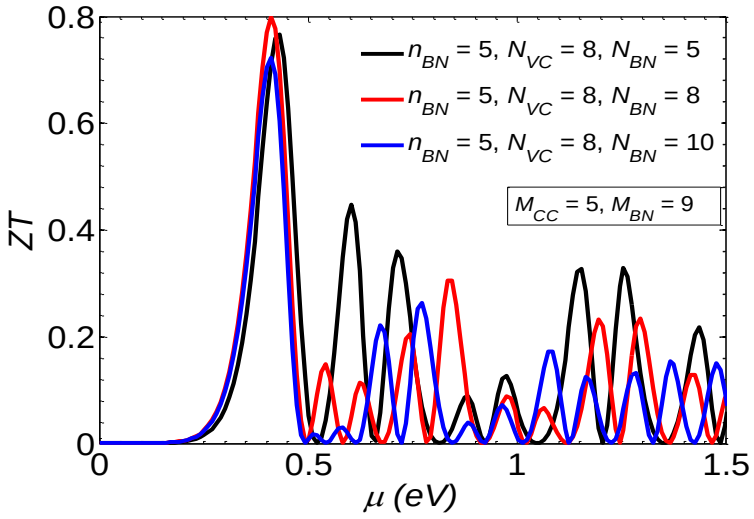

Figure 5-10: Figure of merit was plotted for different length N_{vc} and N_{BN} of graphene and BN/G/BN sections. Fig (a) and (b) were examined with n_{BN} = 1. The results agree that the best ZT for M_{CC} = 5 and M_{CC} = 6 are obtained if N_{vc} = N_{BN} = 8.

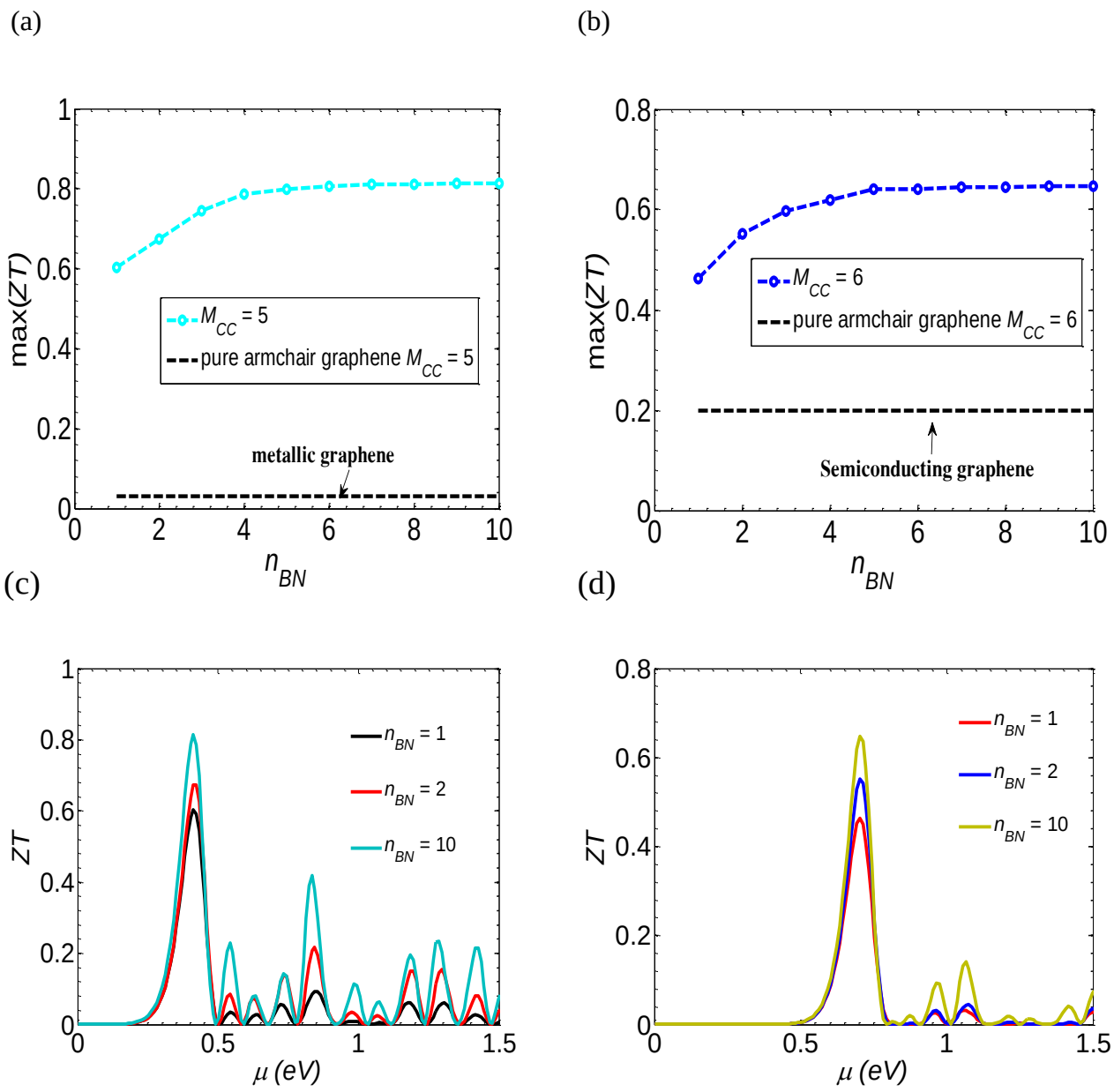

Figure 5-11: (a) (b) Maximum of thermoelectric figure of merit as a function of n_{BN} for (a) M_{CC} = 5 and (b) M_{CC} = 6. Thermoelectric figure of merit ZT as a function of chemical potential μ for (c) M_{CC} = 5 and (d) M_{CC} = 6. T = 300K.

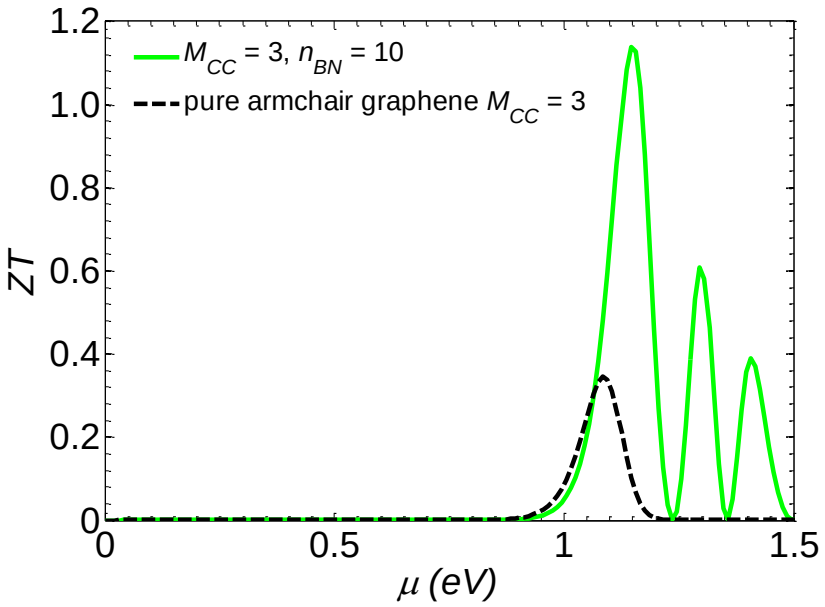

Figure 5-12: *ZT* as a function of chemical potential for the thinnest ribbon M_{CC} = 3 in the cases of pure GNR (dashed line) and hybrid heterostructure with M_{BN} = 11 (solid line), N_{vc} = 6, N_{BN} = 4, n_{BN} = 10, T = 300 K.

In the case of the smallest graphene ribbon M_{CC} = 3 with a large conduction gap, a very high *ZT* can be achieved, as shown in **Figure 5-12**. The maximum value ZT_{max} = 1.14 is reached for n_{BN} = 10 and the chemical potential μ = 1.15 eV. It is again an improvement by a factor of 3.25 compared to the value of 0.35 in the case of pristine AGNR of same width (black dashed line).

Figure 5-13 shows the trend of *ZT* as a function of the width M_{CC} of the main GNR channel. In principle, the maximum of *ZT* reduces when increasing M_{CC} due to the increase of phonon conductance. However, the behavior is not monotonic and the value of *ZT* is smaller for the group of structures with $M_{CC} = 3p + 1$ compared to the groups with $M_{CC} = 3p$ and $M_{CC} = 3p + 2$.

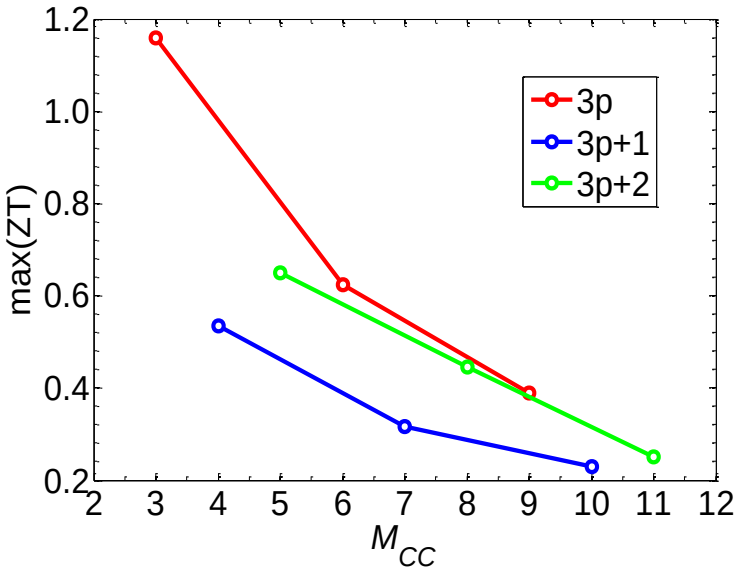

Figure 5-13: Dependence of ZT_{max} on the GNR width M_{CC}, depending on whether M_{CC} can be written in the form $3p$, $3p + 1$ or $3p + 2$, with p is an integer number. M_{BN} = 10, 11 for even, odd M_{CC}, respectively and $N_{vc} = N_{BN} = 5$, $n_{BN} = 10$.

5.3.3 Effect of temperature

In **Figure 5-6** the strong dependence of phonon conductance on temperature was shown. It is thus relevant to consider the effect of temperature on the thermoelectric performance of the structure. In following parts we will focus our investigations on the structure with $M_{CC} = 5$ for which we can observe high ZT at relative low chemical potential.

In **Figure 5-14** we plot ZT as a function of μ for different temperatures ranging from 100 K to 400 K in the case of the structure with $M_{CC} = 5$. Starting from room temperature (orange curve) with $ZT_{max} = 0.81$, when the temperature decreases to 200 K and 100K, the peak value of ZT increases to $ZT_{max} = 0.9$ and $ZT_{max} = 1.01$, respectively. When increasing the temperature to 400 K, the figure of merit reduces to $ZT_{max} = 0.74$. Thus, overall we get higher ZT at lower temperature in this system. Moreover, this reduction of ZT_{max} when the temperature increases is accompanied by a shift of the peak to the left, i.e. to smaller chemical potentials. This is because the functions $g^{e}_{n}(E,\mu,T)$ are broadened at increasing temperature

(**Figure 5-15**(a)), particularly $g^{e}{}_{1}(E,\mu,T)$ which together with T_e directly contributes into $L_1(\mu,T)$ and mainly dominates properties of Seebeck coefficient. As a consequence, the averaged point of Seebeck coefficient shifts to the left (**Figure 5-15** (b)), leading to a shift of the maximum overlap of conductance and square Seebeck coefficient to lower values of μ.

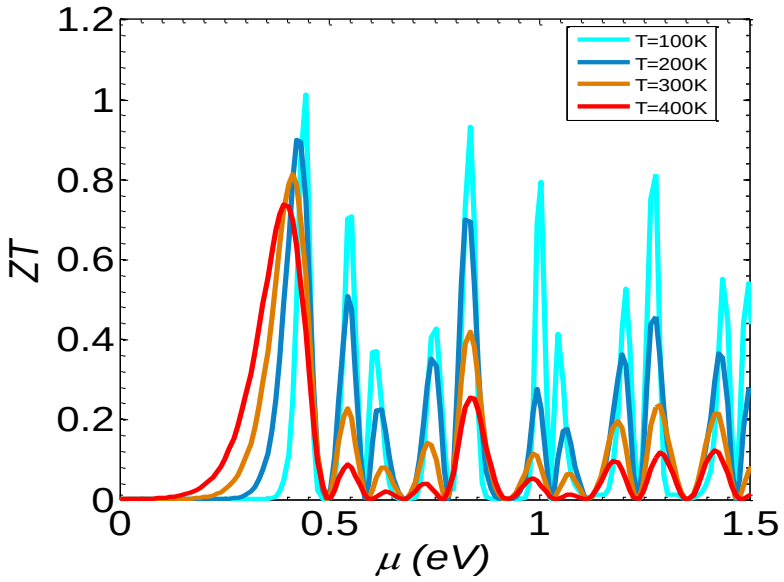

Figure 5-14: *ZT* as a function of chemical potential for different temperatures *T* ranging from 100 K to 400 K for the heterostructure with M_{CC} = 5. Here M_{CC} = 5, M_{BN} = 9, and n_{BN} = 10.

5.3.4 Effect of vacancies: a further improvement

In this section we will discuss the effects of vacancies on the thermoelectric performance of the hybrid structure with M_{CC} = 5.

It has been shown that edge disorder and inner vacancies may have a significant influence on the thermoelectric performance of GNRs.[30,172] In particular, depending on the vacancy position the figure of merit *ZT* can be larger than in a perfect GNR. Most of works on vacancy effects in graphene were focused on either random or periodic arrangement of vacancies. To understand better the influence of vacancies in our hybrid structure, we investigate the effect

of the position of a vacancy. We assume that it may be possible to control experimentally this position by using focused electron beam technique.[173,174]

(a)

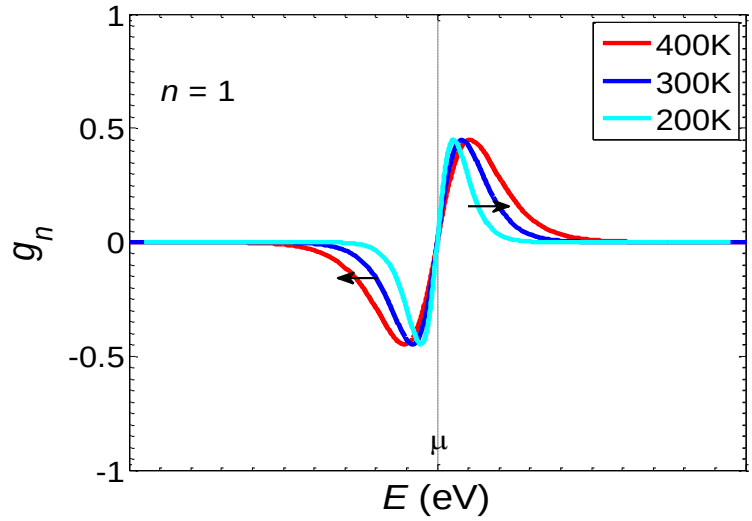

(b)

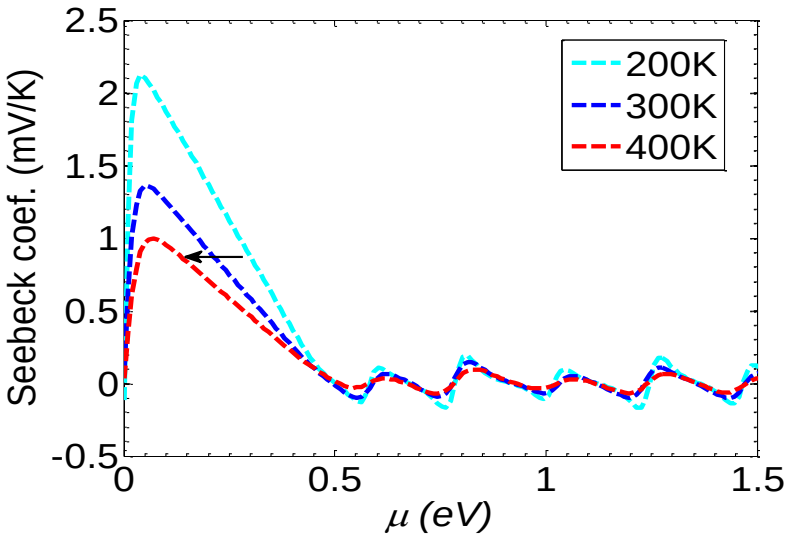

Figure 5-15: (a) The broadening of g_n functions with the increase of temperature. (b) The longest slop of Seebeck coefficient shifts to the left when temperature becomes hotter.

We first consider different configurations of a single vacancy from the middle of channel to the edge and then the effect of a few vacancies is studied. In our structure (**Figure 5-3)**, the position of a vacancy is determined by three indices, i.e. (i) n_{vac} that is the position of the unit cell to which belongs the vacancy, running from 1 to N_A, (ii) L_{id_vac} that is the layer index of a

layer in the cell, equal to 1 or 2, and (iii) m_{vac} that is the position of the vacancy in the layer, ranging from 1 to M, where $M = M_{CC} + 2M_{BN}$ is the total number of dimer lines along the width. For the structure with $M_{CC} = 5$, $M_{BN} = 9$, $N_{vc} = N_{BN} = 8$, $n_{BN} = 10$, we will consider specifically seven different configurations of a single vacancy at $m_{vac} = 12, 13, 14$ (vacancy in graphene) and 15,16,18,23 (vacancy in BN) in layer $L_{id\_vac} = 1$ of the cell $n_{vac} = 25$ which is the first cell of the second BN/G/BN section with respect to the left contact. These positions are sketched in **Figure 5-16**(a).

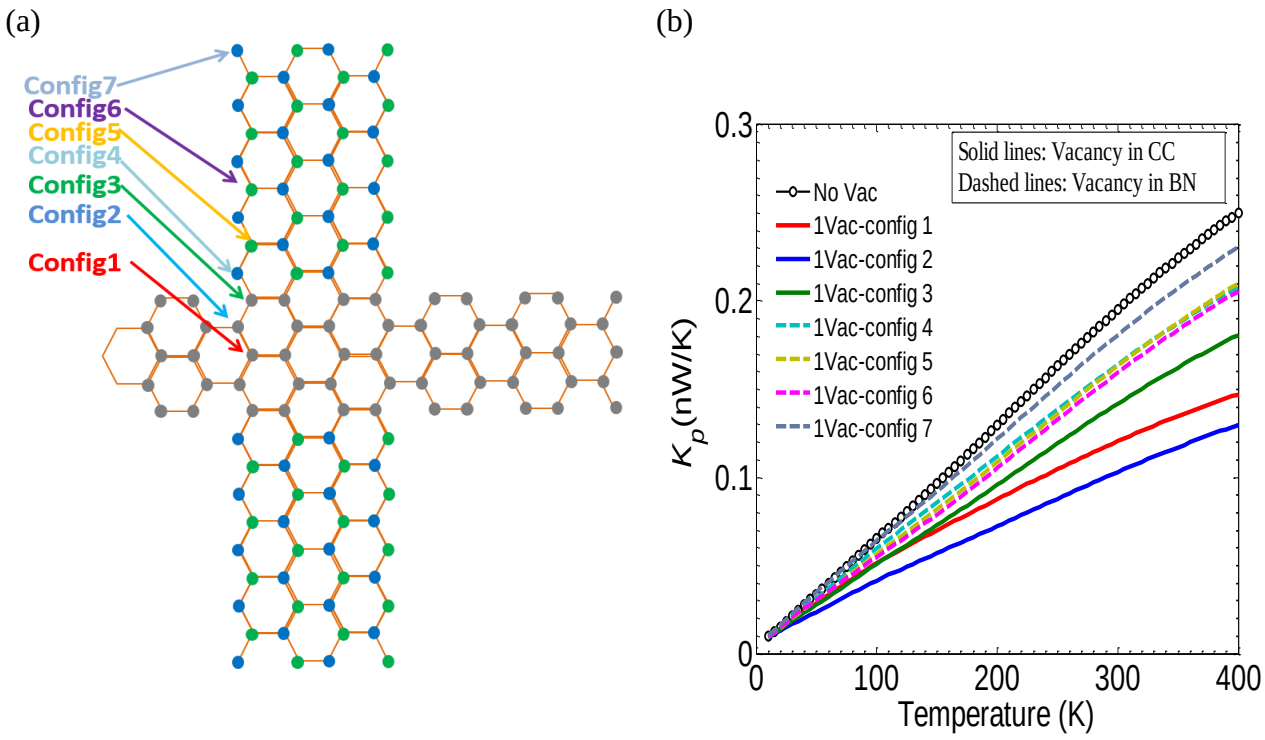

Figure 5-16: Effect of a single vacancy on the thermoelectric properties for the structure with $M_{CC} = 5$. (a) The seven vacancy configurations investigated here. (b) Phonon conductance for the different vacancy configurations.

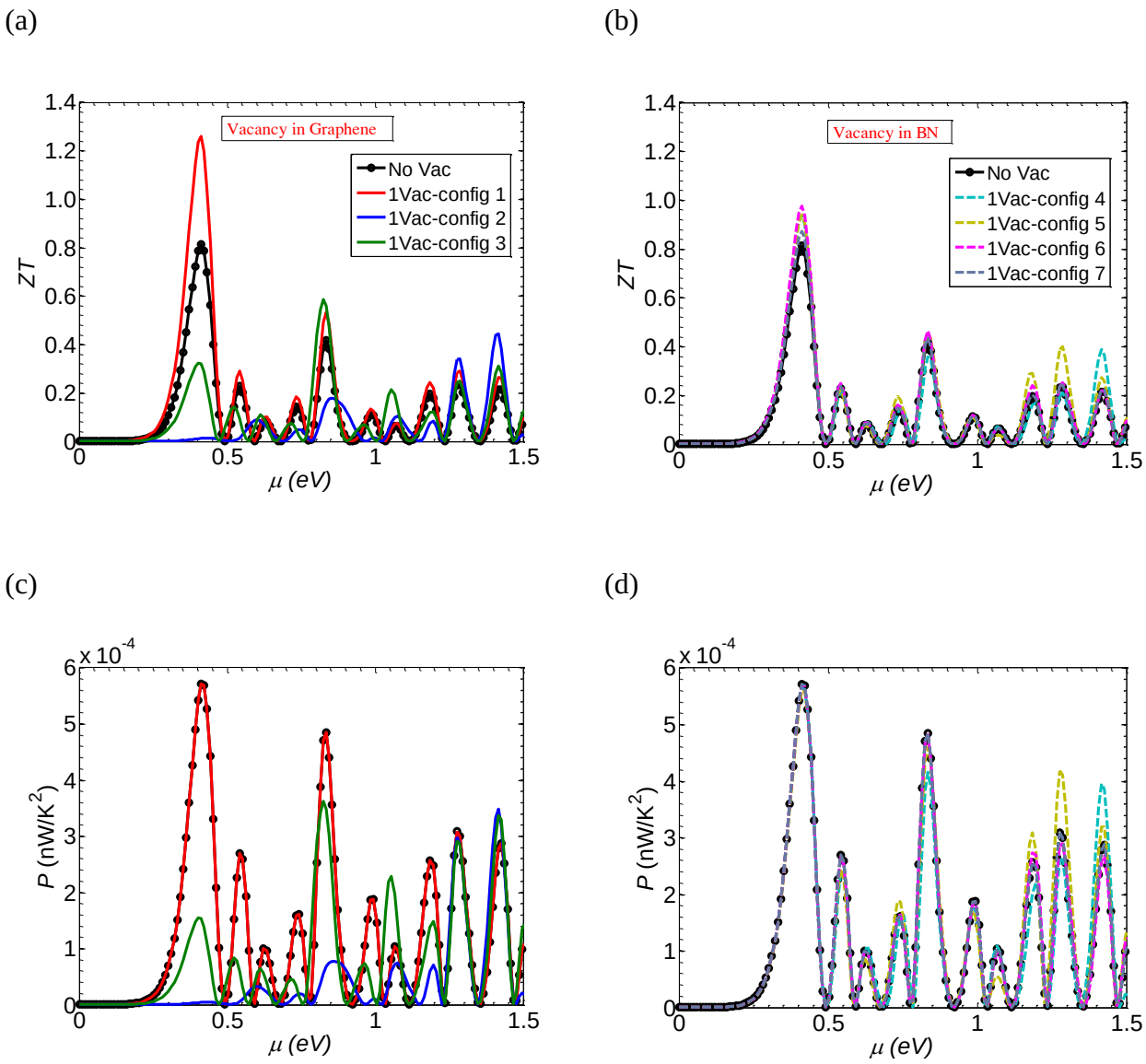

Figure 5-17: Effect of a single vacancy on the thermoelectric properties for the structure with M_{CC} = 5. *ZT* and power factor for the different configurations of vacancy in (a), (c) graphene and (b), (d) BN. Symbols correspond to results without any vacancy. T = 300 K.

The phonon conductance is plotted in **Figure 5-16**(b) for the different positions of the vacancy in graphene (solid lines) or in BN region (dashed lines) and compared with the case of no vacancy (circles). We observe a strong fall of conductance when the vacancy is located in the center of the graphene ribbon (red line, config-1). It is even stronger when the vacancy is on the next lattice site (blue line, config-2), with a reduction by almost a factor of 2 compared to the no-vacancy configuration. When the vacancy is at the edge of the graphene ribbon, the reduction of phonon conductance is smaller (green line, config-3). When the

vacancy is located in the BN region, we still observe a reduction of phonon conductance, but more limited than when it is in graphene and less sensitive to the position of the vacancy.

In **Figure 5-17**(a) and **Figure 5-17**(b) we plot the thermoelectric figure of merit *ZT* as a function of μ for the different configurations of the vacancy in graphene and in BN, respectively. The corresponding power factor *P* is displayed in **Figure 5-17**(c) and (d) In comparison with the case without vacancy, we observe a remarkable enhancement of *ZT* up to 1.26 if the vacancy is in configuration 1, while we see a degradation of *ZT* in the other two cases of vacancy in graphene. Indeed, in spite of the strong reduction of phonon conductance, the configuration 2 surprisingly leads to smaller *ZT*, which is due to a very small power factor, as shown in **Figure 5-17**(c). In contrast, the power factor is not at all affected when the vacancy is in the center of the graphene ribbon, which is also quite surprising. This behavior can be understood from the analysis of the density in the ribbon that is strongly dependent on the lattice site position, as shown in chapter 3 and a previous work by Whilhelm et al..[175] By analyzing the current density in AGNRs Whilhelm et al. shown that as a consequence of quantum confinement in the transverse flow direction, streamlines appear with a threefold periodicity in transverse site position, separated by stripes of almost vanishing flow as seen in **Figure 5-18**.[175] A similar behavior in the graphene part of the structures was observed in chapter 3 with three groups of charged density. This result indicated that starting from an edge of the GNR, i.e. $m = 1$ at the edge, the electron density is minimum for the positions *m* that are multiple of 3. In the particular case of the ribbon of width $M_{CC} = 5$ studied here, the density in the center of the ribbon ($m = 3$) is several order of magnitude smaller than at other positions $m = 1$ (maximum) and $m = 2$ (see **Figure 5-19**). Hence, if there is a vacancy at this position, i.e. in configuration 1, the effect on the density and the conductance of the ribbon is negligible, which explains that the power factor is almost the same as in in the no-vacancy case, leading to an enhancement of *ZT* as a consequence of the reduced phonon conductance. In contrast, if the vacancy is at any other position in the GNR, the electron density and the conductance are strongly affected, which also degrades *ZT* in spite of the reduction of phonon conductance.

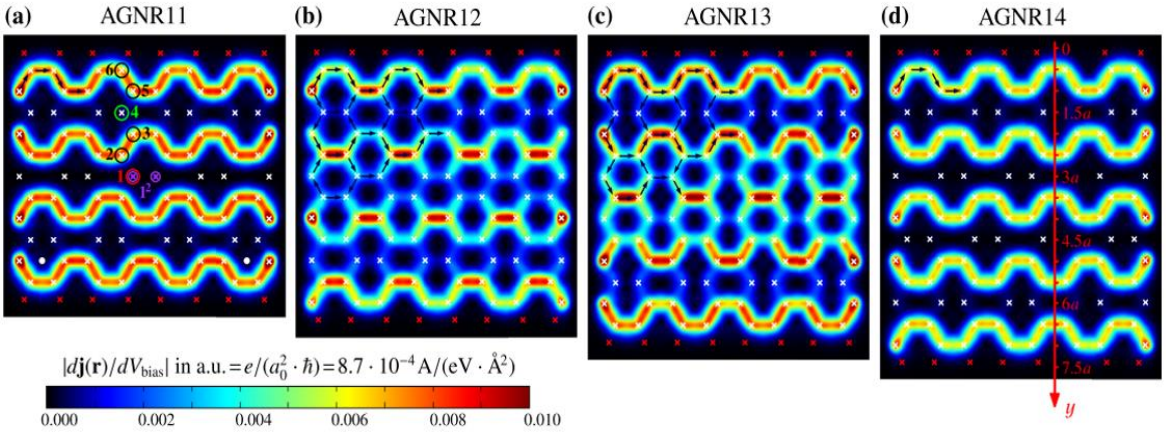

Figure 5-18: Local current in different armchair graphene ribbons. From one edge to the middle of the ribbons, in all cases we can observe that charge distribution is lowest at lattice positions 3*m*. *Reference: Wilhelm et al.* [175]

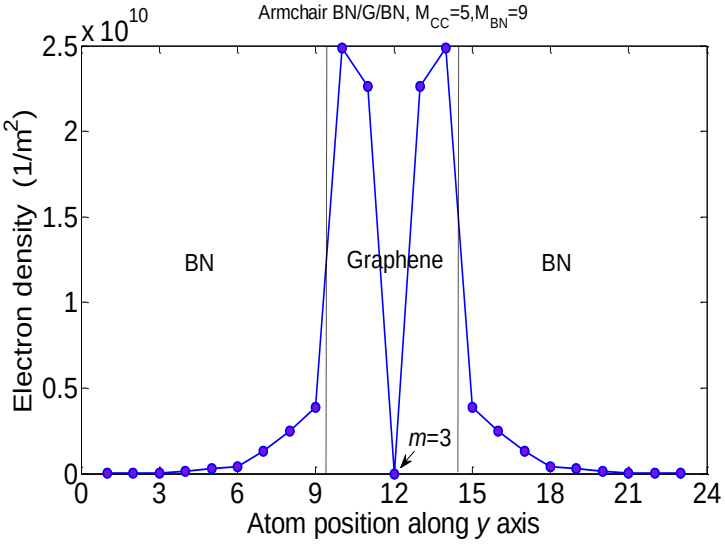

Figure 5-19: Electron density in an infinite structure of armchair BN/G/BN for sub-ribbons width for Graphene and BN are M_{CC} = 5 and M_{BN} = 9, respectively. In the graphene part, the middle point has the lowest charge.

When the vacancy is in the BN region (**Figure 5-17**(b) and (d)) the power factor is almost not influenced at low energy because BN is an insulator, and thus retain good electrical conductance in the channel. This together with the reduction of phonon conductance observed

in **Figure 5-16**(b) results in a small enhancement of *ZT*. In this case, we always observe an enhancement of *ZT* for any vacancy in a BN region. This is an interesting property of G/BN heterostructures compared to pure graphene ribbons in which a vacancy may either degrade or improve *ZT*.

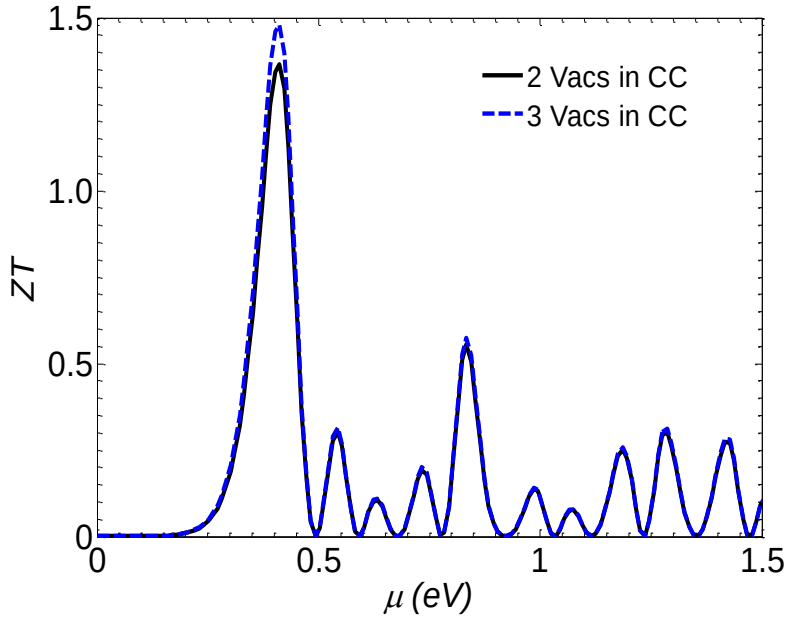

Figure 5-20: Effect of two and three vacancies in the middle of the graphene ribbon on the figure of merit. M_{CC} = 5, T = 300 K.

To fully exploit the influence of vacancies in the center of the graphene ribbon, we have made simulations with two or three vacancies randomly distributed in the center line of the structure with M_{CC} = 5 and n_{BN} = 10. As shown in **Figure 5-20**, *ZT* can be further enhanced and reaches 1.48 in the case of three vacancies, as a consequence of additional degradation of phonon conductance.

5.4 Conclusions

In this chapter we have demonstrated excellent thermoelectric properties of in-plane heterostructures based on armchair GNR with appropriate engineering of graphene/h-BN interfaces. By attaching periodically BN flakes to the GNR, it is indeed possible (i) to reduce

strongly the phonon conductance compared to pure GNR and (ii) to open or broaden the conduction gap which enhances the Seebeck coefficient. And, (iii) the electron conductance is remarkably weakly affected. It finally results in a large enhancement of the thermoelectric figure of merit *ZT*. In the case of perfect ribbons, the maximum value ZT_{max} of 1.14 is reached for the thinnest ribbon with M_{CC} = 3 carbon dimer lines along the width. For larger ribbons with M_{CC} = 5 and M_{CC} = 6 we can obtain ZT_{max} of 0.81 and 0.65, respectively. Interestingly, in the case M_{CC} = 5 the peak of *ZT* is reached at relatively low chemical potential μ = 0.41 eV. When reducing the temperature from 300 K to 100 K, ZT_{max} increases from 0.81 to 1.01. The investigation has also shown that engineering vacancies in graphene or BN regions may allow to further enhance *ZT* thanks to additional reduction of phonon conductance. However, the electron conductance is very sensitive to the vacancy position in graphene. The vacancy position must be chosen carefully at a lattice site where the electron density is small to avoid unacceptable degradation of the power factor. In the case M_{CC} = 5, it is shown that by generating some vacancies in the center of the GNR, i.e. where the charge density is negligible in a perfect ribbon, the power factor is not affected and ZT_{max} reaches up to 1.48 at room temperature.

Summary and possible future works

During the last decade graphene has emerged as an appealing material in several fields of physics due to its outstanding properties which sound promising for many future applications. However, regarding applications in nano-electronics the lack of an energy gap makes it not directly suitable for common devices such as transistors and diodes. Additionally, theory and experiments confirm that in spite of excellent electronic conductance, this gapless character, together with the high thermal conductance, make graphene a poor thermoelectric material. It is thus a major challenge to overcome these limitations and to take fully advantage of its electronic properties, such as exceptionally high intrinsic mobility.

Besides, hexagonal Boron Nitride is known as a quasi-ideal insulating material to be used in heterostructures with graphene because it exhibits the same crystal conformation and almost the same lattice parameter. Taking advantage of the fact that hybrid structures of these two materials can be now synthesized, we proposed efficient designs using in-plane graphene/BN heterostructures to achieve both tunable bandgap and high thermoelectric performance.

The main contributions in my works during the time of PhD project (from December 2012 to November 2015) are summarized as follows:

1. Methodologies. I have developed systematically calculations and numerical simulation codes with a combination of different modellings and methodologies to draw a big physics picture which contains various properties of electrons and phonons in graphene-based nanostructures, heterostructures and devices. Tight Binding model for electrons and Force Constant model for phonons have been formulated in a unique matrix form. This representation coupled with the Green's function formalism is a powerful tool for investigating the energy dispersion and the transport properties. I have also developed a numerical method to solve self-consistently the coupled Schrödinger-Poisson's equations for the case where the effect of charge redistribution is significant

2. Modulation of bandgap and current by side gates-induced electric field. Applying the fundamental idea that an external electric field can modify the energy bands of a structure, I have shown that in armchair graphene/BN structures a band gap can be modulated and even

almost suppressed under the effect of a transverse electric field. This outcome has been successfully applied to control the current in devices made of graphene/BN heterostructures. By turning the gate voltage (i.e. the applied electric field) the current can be efficiently switched off. On/off ratios of about 10^4 have been achieved which is much better than 10, the value typically obtained in transistors made of pure 2D graphene.

3. Robust electron states at zigzag graphene/BN interface. It was previously demonstrated that edge states in zigzag graphene has flat bands and zero group velocity which means that they are useless for charge transport. However, in zigzag graphene/BN heterostructures, I have evidenced that the interface states are localized at the edge of the graphene sub-ribbon like the common edge states but the important property to have a finite and high group velocity. This robust property leads to an improvement of the electron transmission even if the ribbon is not perfectly uniform which should be the case for experimentally fabricated structures.

4. Enhancement of thermoelectric properties. The complementarity of the electronic and phononic properties of graphene and BN has been used to design graphene/BN heterostructures with appealing thermoelectric properties. A strong reduction of phonon conductance can be obtained due to the mismatch of phonon modes between graphene and BN while electron transport is just slightly modified by the presence of BN. I have observed these phenomena in a structure made of an armchair graphene ribbon with BN nanoflakes attached to the edges, leading to thermoelectric figure of merit *ZT* higher than one at room temperature.

Possible future works:

Though this PhD project has reached the end, there are still number of works that can be further performed. Based on the results and physics obtained from the presented works, I propose here some interesting ideas in the view of optimizing electronic and thermoelectric properties:

(i) The effective model in chapter 4 showed that the bonding between Boron (or Nitrogen) and Carbon atoms plays as negative (or positive) potential that acts directly on the Carbon

atoms at the edges. It is thus expected that a tunable gap could be observed in multilayer structures of graphene/BN wherein Boron and Nitrogen atoms should modify differently energy potentials at Carbon sub-lattice A and B resulting in an opening of bandgap.

(ii) The analysis of atom vacancy effect in chapter 5 shows that higher *ZT* is obtained for vacancies at positions 3*m* due to small charge localization at these points compared to the others. This physics can lead to a problem of enhancement of the figure of merit *ZT* in armchair graphene by controlling line of defects. The defect lines at position 3*m* from the edges should not reduce strongly the electrical conductance while they must degrade strongly the phonon conductance. Hence, higher *ZT* could be obtained.

(iii) A combination of graphene and another 2D material such as Silicene which has a shorter vibrational frequency range (graphene:[0,1600 cm^{-1}], Silicene:[0,600 cm^{-1}]) in a heterostructure may lead to a strong reduction of phonon conductance, even more than what we have seen in the heterostructure of graphene/BN in chapter 5. It thus may be possible to achieve higher *ZT* in this kind of heterostructure.

(iv) At high temperatures, many body effects such as phonon-phonon and phonon-electron interactions may become important. It is thus necessary to extend the presented one electron Green's function method to include many body problems.

Appendices

Appendix A: Solving 1D Poisson's equation numerically

In this appendix we present the numerical method developed to solve the 1D Poisson's equation (1-36). The coordinate x is always treated as a discrete quantity as illustrated in **Figure A - 1** with the distance Δx between two adjacent points is small. For x is expanded around an arbitrary point x_n, equation (1-36) can be written as

$$\left.\frac{d\varepsilon}{dx}\right|_{x_n} \cdot \left.\frac{dV}{dx}\right|_{x_n} + \varepsilon_n \cdot \left.\frac{d^2V}{dx^2}\right|_{x_n} = -\frac{\rho_n}{\varepsilon_0} \qquad \text{(A - 1)}$$

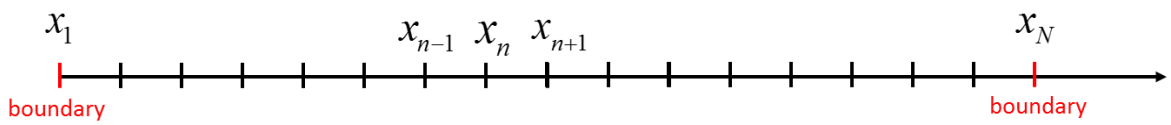

Figure A - 1: The variable x is presented as a series of discrete points x_n.

It is well know that the discrete form of first and second derivative are given by:

$$\begin{cases} \left.\dfrac{df}{dx}\right|_{x=x_n} = \dfrac{f_{n+1} - f_{n-1}}{2.\Delta x} \\ \left.\dfrac{d^2 f}{dx^2}\right|_{x=x_n} = \dfrac{\left.\dfrac{df}{dx}\right|_{x=x_n} - \left.\dfrac{df}{dx}\right|_{x=x_{n-1}}}{\Delta x} = \dfrac{\dfrac{f_{n+1} - f_n}{\Delta x} - \dfrac{f_n - f_{n-1}}{\Delta x}}{\Delta x} = \dfrac{f_{n+1} - 2f_n + f_{n-1}}{(\Delta x)^2} \end{cases} \qquad \text{(A - 2)}$$

Thus the differential terms in (A - 1) can be seen in the relations

$$\begin{cases} \left.\dfrac{d\varepsilon}{dx}\right|_{x=x_n} = \dfrac{\varepsilon_{n+1}-\varepsilon_{n-1}}{2.\Delta x} \\ \left.\dfrac{dV}{dx}\right|_{x=x_n} = \dfrac{V_{n+1}-V_{n-1}}{2.\Delta x} \\ \left.\dfrac{d^2V}{dx^2}\right|_{x=x_n} = \dfrac{V_{n+1}-2V_n+V_{n-1}}{(\Delta x)^2} \end{cases} \qquad \text{(A - 3)}$$

And equation (A - 1) becomes

$$\frac{\varepsilon_{n+1}-\varepsilon_{n-1}}{2.\Delta x}.\frac{V_{n+1}-V_{n-1}}{2.\Delta x}+\varepsilon_n.\frac{V_{n+1}-2V_n+V_{n-1}}{(\Delta x)^2}=-\frac{\rho_n}{\varepsilon_0}$$

Straight forward calculation leads to

$$V_{n-1}\left[\varepsilon_{n-1}+4\varepsilon_n-\varepsilon_{n+1}\right]+V_n.\left(-8\varepsilon_n\right)+V_{n+1}\left[-\varepsilon_{n-1}+4\varepsilon_n+\varepsilon_{n+1}\right]=-4.(\Delta x)^2.\frac{\rho_n}{\varepsilon_0} \qquad \text{(A - 4)}$$

If we set

$$\begin{cases} \gamma_{n,n-1}=\varepsilon_{n-1}+4\varepsilon_n-\varepsilon_{n+1} \\ \gamma_{n,n}=-8\varepsilon_n \\ \gamma_{n,n+1}=-\varepsilon_{n-1}+4\varepsilon_n+\varepsilon_{n+1} \end{cases} \qquad \text{(A - 5)}$$

Equation (A - 4) can be simplified as

$$\gamma_{n,n-1}.V_{n-1}+\gamma_{n,n}.V_n+\gamma_{n,n+1}.V_{n+1}=-4.(\Delta x)^2.\frac{\rho_n}{\varepsilon_0} \qquad \text{(A - 6)}$$

With *N* being the number of *x* points, *n* in (A - 6) can take values from 2 to *N*-1. Thus we have *N*-2 equations from (A - 6), i.e.

$$\begin{cases} \gamma_{21}.V_1 + \gamma_{22}.V_2 + \gamma_{23}.V_3 = -4.(\Delta x)^2.\dfrac{\rho_2}{\varepsilon_0} \\ \gamma_{32}.V_2 + \gamma_{33}.V_3 + \gamma_{34}.V_4 = -4.(\Delta x)^2.\dfrac{\rho_3}{\varepsilon_0} \\ ..... \\ \gamma_{N-1,N-2}.V_{N-2} + \gamma_{N-1,N-1}.V_{N-1} + \gamma_{N-1,N}.V_N = -4.(\Delta x)^2.\dfrac{\rho_{N-1}}{\varepsilon_0} \end{cases}$$

This system of equations is easily transformed into a matrix form as

$$\begin{pmatrix} \gamma_{22} & \gamma_{23} & 0 & . & . \\ \gamma_{32} & \gamma_{33} & \gamma_{34} & 0 & \\ 0 & \gamma_{43} & \gamma_{44} & \gamma_{45} & \\ & 0 & . & . & \gamma_{N-2,N-1} \\ & & & \gamma_{N-1,N-2} & \gamma_{N-1,N-1} \end{pmatrix} \begin{pmatrix} V_2 \\ V_3 \\ . \\ . \\ V_{N-1} \end{pmatrix} + \begin{pmatrix} \gamma_{21}.V_1 \\ 0 \\ . \\ 0 \\ \gamma_{N-1,N}.V_N \end{pmatrix} = -\frac{4.(\Delta x)^2}{\varepsilon_0} \begin{pmatrix} \rho_2 \\ \rho_3 \\ . \\ . \\ \rho_{N-1} \end{pmatrix} \qquad \text{(A - 7)}$$

For convenience, we set

$$U = \begin{pmatrix} \gamma_{22} & \gamma_{23} & 0 & . & . \\ \gamma_{32} & \gamma_{33} & \gamma_{34} & 0 & \\ 0 & \gamma_{43} & \gamma_{44} & \gamma_{45} & \\ & 0 & . & . & \gamma_{N-2,N-1} \\ & & & \gamma_{N-1,N-2} & \gamma_{N-1,N-1} \end{pmatrix} \qquad \text{(A - 8)}$$

Thus equation (A – 7) can be reformulated as

$$\begin{pmatrix} V_2 \\ V_3 \\ . \\ . \\ V_{N-1} \end{pmatrix} = U^{-1}.\begin{pmatrix} \rho_2 \\ \rho_3 \\ . \\ . \\ \rho_{N-1} \end{pmatrix} \left(-\frac{4.(\Delta x)^2}{\varepsilon_0} \right) - U^{-1}.\begin{pmatrix} \gamma_{21}.V_1 \\ 0 \\ . \\ 0 \\ \gamma_{N-1,N}.V_N \end{pmatrix} \qquad \text{(A - 9)}$$

Noting that the relative permittivity $\varepsilon(x)$ of the system is known and ε_n is defined at each node. The matrix U in (A – 8) is also known since $\gamma_{n,n-1}, \gamma_{n,n}$ and $\gamma_{n,n+1}$ are calculated via $\varepsilon_n, \varepsilon_{n\pm1}$ by equation (A – 5). The charge density $\rho(x)$ is given from electron (negative carrier) and hole (positive carrier) density which are calculated by (1-28), (1-29). The potentials V_1

and V_N are determined at the two boundaries. Thus equation (A - 9) is sufficient for solving potential matrix $\begin{pmatrix} V_2 & V_3 & . & . & . & V_{N-1} \end{pmatrix}^T$, and the full potential profile is $V = \begin{pmatrix} V_1 & V_2 & V_3 & . & . & . & V_{N-1} & V_N \end{pmatrix}^T$.

This method can also be extended to 2D and 3D Poisson's equation.

Appendix B: Green's function of an open system and Dyson's equation

In general, the Hamiltonian of a system (X+A) in **Figure (1-5)** can be written as

$$H = \begin{pmatrix} H_A & \tau_{AX} \\ \tau_{XA} & H_X \end{pmatrix} \tag{B - 1}$$

Where $H_{X(A)}$ is the isolated Hamiltonian of X (A) and τ_{XA} and τ_{AX} are the matrix coupling between X and A.

The Schrödinger's equation for the whole system is

$$\begin{pmatrix} H_A & \tau_{AX} \\ \tau_{XA} & H_X \end{pmatrix} \begin{pmatrix} \phi_A \\ \phi_X \end{pmatrix} = E \begin{pmatrix} \phi_A \\ \phi_X \end{pmatrix} \tag{B - 2}$$

Here ϕ_A and ϕ_X are the wave functions in part A and X, respectively (they are not the same as the wave functions in the isolated state of A and X).

Expanding equation (B – 2) we have

$$\begin{cases} H_A\phi_A + \tau_{AX}\phi_X = E\phi_A \\ \tau_{XA}\phi_A + H_X\phi_X = E\phi_X \end{cases}$$

By gathering homogeneous terms we can get

$$\begin{cases} \left(E - H_A\right)^{-1}\tau_{AX}\phi_X = \phi_A \\ \tau_{XA}\phi_A = \left(E - H_X\right)\phi_X \end{cases}$$

By noting that $g_A = \left(E - H_A\right)^{-1}$, $g_X = \left(E - H_X\right)^{-1}$ are the Green's functions of the isolated systems A and X, respectively. The first equation can be written as

$$\phi_A = g_A\tau_{AX}\phi_X \tag{B - 3}$$

While the second one remains as

$$\left(E-H_X\right)\phi_X=\tau_{XA}\phi_A \tag{B - 4}$$

If we plug (B - 3) in to (B - 4) we have

$$\left(E-H_X\right)\phi_X=\tau_{XA}g_A\tau_{AX}\phi_X \quad \text{Or} \quad \left(E-H_X-\tau_{XA}g_A\tau_{AX}\right)\phi_X=0$$

Comparing it to the definition of Green's function from (1-40) and (1-41), we thus have

$$G_X=\left(E-H_X-\tau_{XA}g_A\tau_{AX}\right)^{-1}=\left(E-H_X-\Sigma_A\right)^{-1} \tag{B - 5}$$

that is the Green's function of X in the system (X+A).

Equation (B – 5) or (1-42) is general for any open system X. If we compare the Green' functions before and after attaching A to X: $g_X=\left(E-H_X\right)^{-1}$ and $G_X=\left(E-H_X-\Sigma_A\right)^{-1}$ we see that it is equivalent to that where the system X has a new Hamiltonian $H_X{}'=H_X+\Sigma_A$ and thus Σ_A plays as a perturbation potential V in this system. By this notice we can derive another important equation from (B - 5) as follows: $g=\left(E-H\right)^{-1}$ and $G=\left(E-H-V\right)^{-1}$ are the isolated and new Green's functions of a certain system, V is the perturbation potential. Thus

$$G=\left(g^{-1}-V\right)^{-1} \tag{B - 6}$$

Taking inversion of this equation we have $G^{-1}=g^{-1}-V$ and then by multiplying by G on both sides of the new equation we have $I=g^{-1}G-VG$. In the next step, we multiply by g on both sides of this equation and simply get $g=G-gVG$ or

$$G=g+gVG \tag{B - 7}$$

Equation (B – 7) is the famous Dyson's equation which describes the change in a system under a perturbation.

Appendix C: Transmission with single layer matrix size calculation

Though (1-50) is the standard formula to calculate the transmission via a Green's function, it is actually not a good form in practice because the matrix size of device Green's function is very large for big systems. This limitation can be overcome using formula (1-52) which only contains small size matrices of single layers in the device and thus making calculation (simulation) possible. The derivation of (1-52) from (1-50) is presented in this appendix.

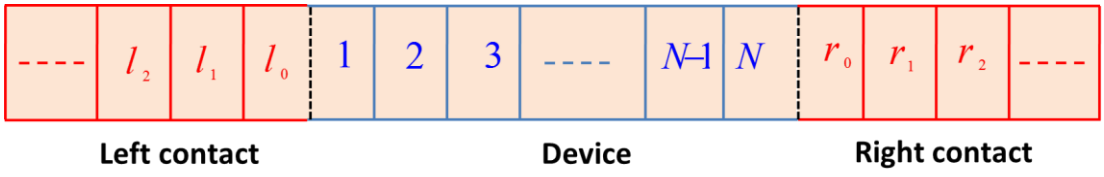

Figure C- 1: An open system (device) is connected to two infinite contacts. The device and the contacts are decomposed into different layers so that one layer only interacts with its nearest neighbor layers.

As mentioned in section **1.6** in chapter 1, if we can divide a system into layers so that one layer only couples with its nearest neighbor layers. The Hamiltonian of the system can be written as a tri-diagonal matrix of block of layers. In this way, only the first layer (l_0 or r_0) of each contact connects to the first (end) layer of the device (see Figure C- 1). This leads to the self-energy (1-44) of left (right) contact which is equal to zero except for the term (block) of the surface layer l_0 (or r_0) $\Sigma^s_{L(R)} = \tau_{DL(R)} G^0{}_{L(R)} \tau_{L(R)D}$ where G^0 is the surface Green's function of contacts and can be computed using the iterative Sancho's technique.

Thus the left (right) injection rate (1-51) only has one block (due to surface layer) that is non zero, i.e.

$$\Gamma_L = \begin{pmatrix} \Gamma^s{}_L & 0 & . & . & . \\ 0 & 0 & & & \\ . & & . & & \\ . & & & . & \\ . & & & & . \end{pmatrix}, \ \Gamma_R = \begin{pmatrix} . & . & . & . & . \\ . & . & & & . \\ . & & . & & . \\ . & & & 0 & 0 \\ . & . & . & 0 & \Gamma^s{}_R \end{pmatrix} \qquad \text{(C - 1)}$$

Where $\Gamma^s_{L(R)} = i\left(\Sigma^s_{L(R)} - \Sigma^s_{L(R)}{}^\dagger\right)$.

The full size of device Green's function (simply noted as *G*)

$$G = \begin{pmatrix} G_{11} & G_{12} & G_{13} & . & G_{1N} \\ G_{21} & G_{22} & G_{23} & . & G_{2N} \\ G_{31} & G_{32} & G_{33} & . & G_{3N} \\ . & & & & \\ G_{N1} & G_{N2} & G_{N3} & . & G_{NN} \end{pmatrix} \qquad \text{(C - 2)}$$

With G_{ii} is the Green function of layer *i*-th. It is thus

$$\Gamma_L G \Gamma_R G^\dagger = \begin{pmatrix} \Gamma^s{}_L & 0 & . & . & . \\ 0 & 0 & & & \\ . & & . & & \\ . & & & . & \\ . & & & & . \end{pmatrix} \begin{pmatrix} G_{11} & G_{12} & G_{13} & . & G_{1N} \\ G_{21} & G_{22} & G_{23} & . & G_{2N} \\ G_{31} & G_{32} & G_{33} & . & G_{3N} \\ . & & & & \\ G_{N1} & G_{N2} & G_{N3} & . & G_{NN} \end{pmatrix} \begin{pmatrix} . & . & . & . & . \\ . & . & & & . \\ . & & . & & . \\ . & & & 0 & 0 \\ . & . & . & 0 & \Gamma_R \end{pmatrix} \begin{pmatrix} G_{11}{}^\dagger & G_{21}{}^\dagger & G_{31}{}^\dagger & . & G_{N1}{}^\dagger \\ G_{12}{}^\dagger & G_{22}{}^\dagger & G_{32}{}^\dagger & . & G_{N2}{}^\dagger \\ G_{13}{}^\dagger & G_{23}{}^\dagger & G_{33}{}^\dagger & . & G_{3N} \\ . & & & & \\ G_{1N}{}^\dagger & G_{2N}{}^\dagger & G_{3N}{}^\dagger & . & G_{NN}{}^\dagger \end{pmatrix}$$

This equation finally contains only one non zero row

$$\Gamma_L G \Gamma_R G^\dagger = \begin{pmatrix} \Gamma^s{}_L G_{1N} \Gamma^s{}_R G_{1N}{}^\dagger & \Gamma^s{}_L G_{1N} \Gamma^s{}_R G_{2N}{}^\dagger & \Gamma^s{}_L G_{1N} \Gamma^s{}_R G_{3N}{}^\dagger & . & \Gamma^s{}_L G_{1N} \Gamma^s{}_R G_{NN}{}^\dagger \\ 0 & 0 & 0 & . & 0 \\ . & & . & & \\ . & & & . & \\ . & & & & . \end{pmatrix}$$

This equation suggests that the trace of the full size matrix $\left(\Gamma_L G \Gamma_R G^\dagger\right)$ is actually equal to the trace of the small block $\left(\Gamma^s{}_L G_{1N} \Gamma^s{}_R G_{1N}{}^\dagger\right)$ and the transmission (1-50) is simplified as

$$T = trace\left\{\Gamma^{s}{}_{L} G_{1N} \Gamma^{s}{}_{R} G_{1N}{}^{\dagger}\right\} \qquad \text{(C - 3)}$$

Equation (C – 3) is already good compared to equation (1-50) because the matrix size of $\Gamma^{s}{}_{L}$, $\Gamma^{s}{}_{R}$ and G_{1N} are just equal to the matrix size of one layer and much smaller than the matrix size of Green's function (or Hamiltonians) of the whole system. For equation (C – 3) we need to determine three block matrices $\Gamma^{s}{}_{L}$, $\Gamma^{s}{}_{R}$ and G_{1N} (by recursive techniques). For computational efficiency we even can go to another equation (equation (1-52)) that is more efficient with only two block matrices required for the calculation of transmission. To obtain this equation, we need a few more steps of derivation.

Now we use the spectral function which is defined by (as presented in equation (1-48))

$$A = i\left(G - G^{\dagger}\right) \qquad \text{(C - 4)}$$

And noting that the full size device Green's function is $G = \left[E^{+} - H_{D} - \Sigma_{L} - \Sigma_{R}\right]^{-1}$, we have

$$\left(G^{+}\right)^{-1} - G^{-1} = \left(\Sigma_{L} - \Sigma_{L}{}^{\dagger}\right) + \left(\Sigma_{R} - \Sigma_{R}{}^{\dagger}\right) = -i\left(\Gamma_{L} + \Gamma_{R}\right) = -i\Gamma$$

Or in an equivalent form $1 - G^{-1}G^{+} = -i\Gamma G^{+} \Leftrightarrow G - G^{+} = -iG\Gamma G^{+}$. Comparing with (C - 4) we have

$$A = i\left(G - G^{\dagger}\right) = G\Gamma G^{+} \qquad \text{(C - 5)}$$

First, the right hand side of (C - 5) can be treated as

$$G\Gamma G^{+} = G\left(\Gamma_L + \Gamma_R\right)G^{+}$$

$$= \begin{pmatrix} G_{11} & G_{12} & G_{13} & . & G_{1N} \\ G_{21} & G_{22} & G_{23} & . & G_{2N} \\ G_{31} & G_{32} & G_{33} & . & G_{3N} \\ . & & & & \\ G_{N1} & G_{N2} & G_{N_3} & . & G_{NN} \end{pmatrix} \left\{ \begin{pmatrix} \Gamma^s{}_L & 0 & . & . & . \\ 0 & 0 & & & \\ . & & . & & \\ . & & & . & \\ . & & & & . \end{pmatrix} + \begin{pmatrix} . & . & . & . & . \\ . & . & & & . \\ . & & . & & . \\ . & & & 0 & 0 \\ . & . & . & 0 & \Gamma^s{}_R \end{pmatrix} \right\} \begin{pmatrix} G_{11}{}^{\dagger} & G_{21}{}^{\dagger} & G_{31}{}^{\dagger} & . & G_{N1}{}^{\dagger} \\ G_{12}{}^{\dagger} & G_{22}{}^{\dagger} & G_{32}{}^{\dagger} & . & G_{N2^{\dagger}} \\ G_{13}{}^{\dagger} & G_{23}{}^{\dagger} & G_{33}{}^{\dagger} & . & G_{3N} \\ . & & & & \\ G_{1N}{}^{\dagger} & G_{2N}{}^{\dagger} & G_{3N}{}^{\dagger} & . & G_{NN}{}^{\dagger} \end{pmatrix}$$

The matrix calculation leads to

$$G\Gamma G^{+} = \begin{pmatrix} G_{11}\Gamma^s{}_L G_{11}{}^{\dagger} + G_{1N}\Gamma^s{}_R G_{1N}{}^{\dagger} & . & . & . & . \\ . & & . & . & . \\ . & & . & . & . \\ . & & . & . & . \\ . & & . & . & G_{N1}\Gamma^s{}_L G_{N1}{}^{\dagger} + G_{NN}\Gamma^s{}_R G_{NN}{}^{\dagger} \end{pmatrix} \qquad \text{(C - 6)}$$

We just want to see the relationship with interface blocks G_{11} and G_{NN} so others are not necessary to be shown here.

In the other hand, the left hand side $i\left(G - G^{\dagger}\right)$ in (C - 5) can be calculated by using the form of Green's function (C - 2)

$$i\left(G - G^{\dagger}\right) = \begin{pmatrix} i\left(G_{11} - G_{11}{}^{\dagger}\right) & . & . & . & . \\ . & & . & . & . \\ . & & . & . & . \\ . & & . & . & . \\ . & & . & . & i\left(G_{NN} - G_{NN}{}^{\dagger}\right) \end{pmatrix} \qquad \text{(C - 7)}$$

Comparing (C - 6) and (C - 7) with notice to (C - 5) we have

$$i\left(G_{11} - G_{11}{}^{\dagger}\right) = G_{11}\Gamma^s{}_L G_{11}{}^{\dagger} + G_{1N}\Gamma^s{}_R G_{1N}{}^{\dagger} \qquad \text{(C - 8)}$$

And

$$i\left(G_{NN}-G_{NN}^{\dagger}\right)=G_{N1}\Gamma^{s}{}_{L}G_{N1}^{\dagger}+G_{NN}\Gamma^{s}{}_{R}G_{NN}^{\dagger} \qquad \text{(C - 9)}$$

From (C - 8) it is easy to obtain $G_{1N}\Gamma^{s}{}_{R}G_{1N}^{\dagger}=i\left(G_{11}-G_{11}^{\dagger}\right)-G_{11}\Gamma^{s}{}_{L}G_{11}^{\dagger}$. Thus the transmission calculated by (C - 3) is now

$$T=Trace\left\{\Gamma^{s}{}_{L}\left[i\left(G_{11}-G_{11}^{\dagger}\right)-G_{11}\Gamma^{s}{}_{L}G_{11}^{\dagger}\right]\right\} \qquad \text{(C - 10)}$$

If (C - 10) using surface blocks $\Gamma^{s}{}_{L}$, G_{11} at the junction with left contacts for calculating transmission, a similar expression can be formulated with surface blocks at the right junction using relation (C - 9) with a little effort is required in derivation

$$T=Trace\left\{\left[i\left(G_{NN}-G_{NN}^{\dagger}\right)-G_{NN}^{\dagger}\Gamma^{s}{}_{R}G_{NN}\right]\Gamma^{s}{}_{R}\right\} \qquad \text{(C - 11)}$$

Appendix D: Intermediate functions and Phonon conductance

In this part we present practical forms of equation (1-59) and (1-62) for calculation of Phonon conductance K_p and intermediate function $\mathrm{L}_n(\mu,T)$.

(1) Intermediate functions

The partial derivative of Fermi function with respect to Energy can be calculated as

$$\frac{\partial f_e(E,\mu,T)}{\partial E}=\frac{-\frac{1}{K_bT}.e^{\frac{E-\mu}{K_bT}}}{\left(1+e^{\frac{E-\mu}{K_bT}}\right)^2}=\frac{-\frac{1}{K_bT}}{\left(e^{-\frac{E-\mu}{2K_bT}}+e^{\frac{E-\mu}{2K_bT}}\right)^2}=\frac{-\frac{1}{4K_bT}}{\cosh^2\left(\frac{E-\mu}{2K_bT}\right)} \qquad \text{(D - 1)}$$

Plugging (D - 1) in to equation (1-62) we get

$$\mathrm{L}_n(\mu,T)=\frac{2}{h}\int_{-\infty}^{+\infty}dE.T_e(E).\left(\frac{-\frac{1}{2}.\frac{(E-\mu)^n}{2K_bT}}{\cosh^2\left(\frac{E-\mu}{2K_bT}\right)}\right)=\frac{1}{h}\int_{-\infty}^{+\infty}dE.T_e(E).(2K_bT)^{n-1}.\frac{\left(\frac{E-\mu}{2K_bT}\right)^n}{\cosh^2\left(\frac{E-\mu}{2K_bT}\right)}$$

By setting

$$g^e{}_n(E,\mu,T)=\left(\frac{E-\mu}{2k_bT}\right)^n\Big/\cosh^2\left(\frac{E-\mu}{2k_bT}\right) \qquad \text{(D - 2)}$$

The formula to calculate the intermediate functions is now as simple as

$$L_n(\mu,T)=\frac{1}{h}\int_{-\infty}^{+\infty}dE\;T_e(E)(2k_bT)^{n-1}\;g^e{}_n(E,\mu,T) \qquad \text{(D - 3)}$$

(2) Phonon conductance

For the Bose-Einstein‘s distribution function $n=1/\left(e^{\hbar\omega/K_bT}-1\right)$, we have

$$\frac{\partial n}{\partial T}=\frac{\frac{\hbar\omega}{K_bT^2}.e^{\hbar\omega/K_bT}}{\left(e^{\hbar\omega/K_bT}-1\right)^2} \qquad \text{(D - 4)}$$

And (1-59) can be converted to

$$K_{ph}=\int_0^\infty \frac{d\omega}{2\pi}.\hbar\omega.\mathrm{T}_{\mathrm{ph}}(\omega).\frac{\frac{\hbar\omega}{K_bT^2}.e^{\hbar\omega/K_bT}}{\left(e^{\hbar\omega/K_bT}-1\right)^2}=\int_0^\infty \frac{d\omega}{2\pi}.\mathrm{T}_{\mathrm{ph}}(\omega).K_b.\frac{\left(\frac{\hbar\omega}{K_bT}\right)^2.e^{\hbar\omega/K_bT}}{\left(e^{\hbar\omega/K_bT}-1\right)^2}$$

$$=\int_0^\infty \frac{d\omega}{2\pi}.\mathrm{T}_{\mathrm{ph}}(\omega).K_b.\frac{\left(\frac{\hbar\omega}{K_bT}\right)^2}{\left(e^{\frac{\hbar\omega}{2K_bT}}-e^{-\frac{\hbar\omega}{2K_bT}}\right)^2}=\frac{K_b}{2\pi}\int_0^\infty d\omega.\mathrm{T}_{\mathrm{ph}}(\omega).\frac{\left(\frac{\hbar\omega}{2K_bT}\right)^2}{\sinh^2\left(\frac{\hbar\omega}{2K_bT}\right)}$$

So if we set

$$g^p(\omega,T)=\left(\frac{\hbar\omega}{2k_bT}\right)^2\Big/\sinh^2\left(\frac{\hbar\omega}{2k_bT}\right) \qquad \text{(D - 5)}$$

The phonon conductance then is calculated by formula

$$K_p=\frac{k_b}{2\pi}\int_0^\infty d\omega\, T_p(\omega)\, g^p(\omega,T) \qquad \text{(D - 6)}$$

The advantage of (D - 3) and (D - 6) compared to (1-62) and (1-59) is that they contain the function $g^e{}_n(E,\mu,T)$ and $g^p(\omega,T)$ which are exponential functions and decaying very fast with the increase of Energy E or frequency ω. Thanks to this property, the range of integrals (D - 3) and (D - 6) can be limited by examining these functions.

Bibliography

[1] Castro Neto a. H, Guinea F, Peres N M R, Novoselov K S and Geim a. K 2009 The electronic properties of graphene *Rev. Mod. Phys.* **81** 109–62

[2] Bolotin K I, Sikes K J, Jiang Z, Klima M, Fudenberg G, Hone J, Kim P and Stormer H L 2008 Ultrahigh electron mobility in suspended graphene *Solid State Commun.* **146** 351–5

[3] Balandin A a., Ghosh S, Bao W, Calizo I, Teweldebrhan D, Miao F and Lau C N 2008 Superior thermal conductivity of single-layer graphene *Nano Lett.* **8** 902–7

[4] Sharma B K and Ahn J-H 2013 Graphene based field effect transistors: Efforts made towards flexible electronics *Solid. State. Electron.* **89** 177–88

[5] Ferrari A C, Bonaccorso F, Fal'ko V, Novoselov K S, Roche S, Boggild P, Borini S, Koppens F H L, Palermo V, Pugno N, Garrido J A, Sordan R, Bianco A, Ballerini L, Prato M, Lidorikis E, Kivioja J, Marinelli C, Ryhanen T, Morpurgo A, Coleman J N, Nicolosi V, Colombo L, Fert A, Garcia-Hernandez M, Bachtold A, Schneider G F, Guinea F, Dekker C, Barbone M, Sun Z, Galiotis C, Grigorenko A N, Konstantatos G, Kis A, Katsnelson M, Vandersypen L, Loiseau A, Morandi V, Neumaier D, Treossi E, Pellegrini V, Polini M, Tredicucci A, Williams G M, Hee Hong B, Ahn J-H, Min Kim J, Zirath H, van Wees B J, van der Zant H, Occhipinti L, Di Matteo A, Kinloch I A, Seyller T, Quesnel E, Feng X, Teo K, Rupesinghe N, Hakonen P, Neil S R T, Tannock Q, Lofwander T and Kinaret J 2015 Science and technology roadmap for graphene, related two-dimensional crystals, and hybrid systems *Nanoscale* **7** 4598–810

[6] Wallace P R 1947 The Band Theory of Graphite *Phys. Rev.* **71** 622–34

[7] Novoselov K S 2004 Electric Field Effect in Atomically Thin Carbon Films *Science (80-.).* **306** 666–9

[8] Ishigami M, Chen J H, Cullen W G, Fuhrer M S and Williams E D 2007 Atomic structure of graphene on SiO2. *Nano Lett.* **7** 1643–8

[9] Fratini S and Guinea F 2008 Substrate-limited electron dynamics in graphene *Phys. Rev. B* **77** 195415

[10] Chen S C, Lin C Y and Lin M F 2008 Electronic properties of nanographite ribbons in a spatially modulated electric field *Diam. Relat. Mater.* **17** 1545–9

[11] Konschuh S, Gmitra M and Fabian J 2010 Tight-binding theory of the spin-orbit coupling in graphene *Phys. Rev. B - Condens. Matter Mater. Phys.* **82** 1–11

[12] Dutta S and Wakabayashi K 2012 Tuning charge and spin excitations in zigzag edge nanographene ribbons. *Sci. Rep.* **2** 519

[13] Cao C 2012 Electronic Transport of Zigzag Graphene Nanoribbons with Edge Hydrogenation and Oxidation *Open Chem. Phys. J.* **4** 1–7

[14] Zuev Y M, Chang W and Kim P 2009 Thermoelectric and magnetothermoelectric transport measurements of graphene *Phys. Rev. Lett.* **102** 096807

[15] Chang C P, Lu C L, Shyu F L, Chen R B, Huang Y C and Lin M F 2005 Magnetoelectronic properties of nanographite ribbons *Phys. E Low-dimensional Syst. Nanostructures* **27** 82–97

[16] Chang C P P, Huang Y C C, Lu C L L, Ho J H H, Li T S S and Lin M F F 2006 Electronic and optical properties of a nanographite ribbon in an electric field *Carbon N. Y.* **44** 508–15

[17] Son Y-W, Cohen M L and Louie S G 2006 Half-metallic graphene nanoribbons *Nature* **444** 347–9

[18] Son Y W, Cohen M L and Louie S G 2006 Energy gaps in graphene nanoribbons *Phys. Rev. Lett.* **97** 216803

[19] Abergel D S L, Apalkov V, Berashevich J, Ziegler K and Chakraborty T 2010 Properties of graphene: a theoretical perspective *Adv. Phys.* **59** 261–482

[20] Kane C L and Mele E J 2005 Z2 topological order and the quantum spin hall effect *Phys. Rev. Lett.* **95** 146802

[21] Nam Do V, Nguyen V H, Dollfus P and Bournel a. 2008 Electronic transport and spin-polarization effects of relativisticlike particles in mesoscopic graphene structures *J. Appl. Phys.* **104** 063708

[22] Pedersen T G, Flindt C, Pedersen J, Mortensen N A, Jauho A-P and Pedersen K 2008 Erratum: Graphene Antidot Lattices: Designed Defects and Spin Qubits [Phys. Rev. Lett. **100** , 136804 (2008)] *Phys. Rev. Lett.* **100** 189905

[23] Joucken F, Tison Y, Lagoute J, Dumont J, Cabosart D, Zheng B, Repain V, Chacon C, Girard Y, Botello-Méndez A R, Rousset S, Sporken R, Charlier J-C and Henrard L 2012 Localized state and charge transfer in nitrogen-doped graphene *Phys. Rev. B* **85** 161408

[24] Bai J, Zhong X, Jiang S, Huang Y and Duan X 2010 Graphene nanomesh. *Nat. Nanotechnol.* **5** 190–4

[25] Li D, Xu Y, Chen X, Li B and Duan W 2014 Tunable anisotropic thermal conduction in graphane nanoribbons *Appl. Phys. Lett.* **104** 143108

[26] Kharche N and Nayak S K 2011 Quasiparticle band gap engineering of graphene and graphone on hexagonal boron nitride substrate *Nano Lett.* **11** 5274–8

[27] Su L, Zhao W, Zhang Y, Querlioz D, Zhang Y, Klein J-O, Dollfus P and Bournel A 2015 Proposal for a graphene-based all-spin logic gate *Appl. Phys. Lett.* **106** 072407

[28] Lin C-C, Gao Y, Penumatcha A V, Diep V Q, Appenzeller J and Chen Z 2014 Improvement of Spin Transfer Torque in Asymmetric Graphene Devices *ACS Nano* **8** 3807–12

[29] Zhang D-B, Seifert G and Chang K 2014 Strain-Induced Pseudomagnetic Fields in Twisted Graphene Nanoribbons *Phys. Rev. Lett.* **112** 096805

[30] Sevincli H and Cuniberti G 2009 Enhanced thermoelectric figure of merit in edge disordered zigzag graphene nanoribbons *Phys. Rev. B* **81** 4

[31] Mazzamuto F, Hung Nguyen V, Apertet Y, Caër C, Chassat C, Saint-Martin J and Dollfus P 2011 Enhanced thermoelectric properties in graphene nanoribbons by resonant tunneling of electrons *Phys. Rev. B* **83** 235426

[32] Yan Y, Liang Q F, Zhao H, Wu C Q and Li B 2012 Thermoelectric properties of one-dimensional graphene antidot arrays *Phys. Lett. Sect. A Gen. At. Solid State Phys.* **376** 2425–9

[33] Sevinçli H, Sevik C, Caın T and Cuniberti G 2013 A bottom-up route to enhance thermoelectric figures of merit in graphene nanoribbons. *Sci. Rep.* **3** 1228

[34] Liu Y, Wu X, Zhao Y, Zeng X C and Yang J 2011 Half-metallicity in hybrid graphene/boron nitride nanoribbons with dihydrogenated edges *J. Phys. Chem. C* **115** 9442–50

[35] Seol G and Guo J 2011 Bandgap opening in boron nitride confined armchair graphene nanoribbon *Appl. Phys. Lett.* **98** 143107

[36] Gao Y, Zhang Y, Chen P, Li Y, Liu M, Gao T, Ma D, Chen Y, Cheng Z, Qiu X, Duan W and Liu Z 2013 Toward single-layer uniform hexagonal boron nitride-graphene patchworks with zigzag linking edges *Nano Lett.* **13** 3439–43

[37] Tran V-T, Saint-Martin J and Dollfus P 2014 Large on/off current ratio in hybrid graphene/BN nanoribbons by transverse electric field-induced control of bandgap *Appl. Phys. Lett.* **105** 073114

[38] Dean C R, Young a F, Meric I, Lee C, Wang L, Sorgenfrei S, Watanabe K, Taniguchi T, Kim P, Shepard K L and Hone J 2010 Boron nitride substrates for high-quality graphene electronics. *Nat. Nanotechnol.* **5** 722–6

[39] Fiori G, Bonaccorso F, Iannaccone G, Palacios T, Neumaier D, Seabaugh A, Banerjee S K and Colombo L 2014 Electronics based on two-dimensional materials *Nat. Nanotechnol.* **9** 768–79

[40] Zhang S, Zhou J, Wang Q, Chen X, Kawazoe Y and Jena P 2015 Penta-graphene: A new carbon allotrope *Proc. Natl. Acad. Sci.* **112** 2372–7

[41] Sevinçli H and Sevik C 2014 Electronic, phononic, and thermoelectric properties of graphyne sheets *Appl. Phys. Lett.* **105** 223108

[42] Kang J, Wu F and Li J 2012 Modulating the bandgaps of graphdiyne nanoribbons by transverse electric fields. *J. Phys. Condens. Matter* **24** 165301

[43] Ci L, Song L, Jin C, Jariwala D, Wu D, Li Y, Srivastava A, Wang Z F, Storr K, Balicas L, Liu F and Ajayan P M 2010 Atomic layers of hybridized boron nitride and graphene domains. *Nat. Mater.* **9** 430–5

[44] Sutter P, Cortes R, Lahiri J and Sutter E 2012 Interface formation in monolayer graphene-boron nitride heterostructures *Nano Lett.* **12** 4869–74

[45] Liu Z, Ma L, Shi G, Zhou W, Gong Y, Lei S, Yang X, Zhang J, Yu J, Hackenberg K P, Babakhani A, Idrobo J-C, Vajtai R, Lou J and Ajayan P M 2013 In-plane heterostructures of graphene and hexagonal boron nitride with controlled domain sizes *Nat. Nanotechnol.* **8** 119–24

[46] Jung J, Qiao Z, Niu Q and MacDonald A H 2012 Transport properties of graphene nanoroads in boron nitride sheets *Nano Lett.* **12** 2936–40

[47] Tang C, Kou L and Chen C 2012 Tunable band gap and magnetism in C2x-(BN)y sheets and ribbons *Chem. Phys. Lett.* **523** 98–103

[48] Modarresi M, Roknabadi M R and Shahtahmasbi N 2011 Transport properties of an armchair boron-nitride nanoribbon embedded between two graphene electrodes *Phys. E Low-dimensional Syst. Nanostructures* **43** 1751–4

[49] Yu Z, Hu M L, Zhang C X, He C Y, Sun L Z and Zhong J 2011 Transport Properties of Hybrid Zigzag Graphene and Boron Nitride Nanoribbons *J. Phys. Chem. C* **115** 10836–41

[50] Fiori G, Betti A, Bruzzone S and Iannaccone G 2012 Lateral graphene-hBCN heterostructures as a platform for fully two-dimensional transistors *ACS Nano* **6** 2642–

8

[51] Nguyen V H, Mazzamuto F, Bournel a and Dollfus P 2012 Resonant tunnelling diodes based on graphene/h-BN heterostructure *J. Phys. D. Appl. Phys.* **45** 325104

[52] Kogan E, Nazarov V U, Silkin V M and Kaveh M 2014 Energy bands in graphene: Comparison between the tight-binding model and *ab initio* calculations *Phys. Rev. B* **89** 165430

[53] Son Y-W, Cohen M L and Louie S G 2006 Energy Gaps in Graphene Nanoribbons *Phys. Rev. Lett.* **97** 216803

[54] Wirtz L and Rubio A 2004 The phonon dispersion of graphite revisited *Solid State Commun.* **131** 141–52

[55] Reich S, Maultzsch J, Thomsen C and Ordejón P 2002 Tight-binding description of graphene *Phys. Rev. B* **66** 035412

[56] Bruzzone S, Iannaccone G, Marzari N and Fiori G 2014 An Open-Source Multiscale Framework for the Simulation of Nanoscale Devices *IEEE Trans. Electron Devices* **61** 48–53

[57] Cresti A, Grosso G and Parravicini G P 2008 Electronic states and magnetotransport in unipolar and bipolar graphene ribbons *Phys. Rev. B - Condens. Matter Mater. Phys.* **77** 115408

[58] Cresti A, Grosso G and Parravicini G P 2008 Valley-valve effect and even-odd chain parity in p-n graphene junctions *Phys. Rev. B - Condens. Matter Mater. Phys.* **77** 233402

[59] Rainis D, Taddei F, Dolcini F, Polini M and Fazio R 2009 Andreev reflection in graphene nanoribbons *Phys. Rev. B* **79** 115131

[60] Grassi R, Poli S, Gnani E, Gnudi A, Reggiani S and Baccarani G 2009 Tight-binding and effective mass modeling of armchair graphene nanoribbon FETs *Solid. State. Electron.* **53** 462–7

[61] Tran V-T, Saint-Martin J and Dollfus P 2015 Dispersive hybrid states and bandgap in zigzag graphene/BN heterostructures *Semicond. Sci. Technol.* **30** 105002

[62] Slater J C and Koster G F 1954 Simplified LCAO Method for the Periodic Potential Problem *Phys. Rev.* **94** 1498–524

[63] Born M, Huang K and Huang K 1956 *Dynamical theory of crystal lattices* (Clarendon Press)

[64] Kaplan H 1962 Remarks on Force-Constant Models for Lattice Dynamics *Phys. Rev.* **125** 1905–10

[65] Lombardo M and Askes H 2010 Elastic wave dispersion in microstructured membranes *Proc. R. Soc. London A Math. Phys. Eng. Sci.*

[66] Saito R, Dresselhaus G and Dresselhaus M S 1998 *Physical Properties of Carbon Nanotubes* (Imperial College Press)

[67] Chow T L 2000 *Mathematical Methods for Physicists: A Concise Introduction* (Cambridge University Press)

[68] Dirac P A M 1939 A new notation for quantum mechanics *Math. Proc. Cambridge Philos. Soc.* **35** 416–8

[69] Zheng H, Wang Z, Luo T, Shi Q and Chen J 2007 Analytical study of electronic

structure in armchair graphene nanoribbons *Phys. Rev. B* **75** 165414

[70] Nakabayashi J, Yamamoto D and Kurihara S 2009 Band-Selective Filter in a Zigzag Graphene Nanoribbon *Phys. Rev. Lett.* **102** 066803

[71] Mochizuki Y and Yoshioka H 2009 Theoretical Study on Transport Properties of Normal Metal–Zigzag Graphene Nanoribbon–Normal Metal Junctions *J. Phys. Soc. Japan* **78** 123701

[72] Ma M M, Ding J W and Xu N 2009 Odd-even width effect on persistent current in zigzag hexagonal graphene rings. *Nanoscale* **1** 387–90

[73] Wakabayashi K, Sasaki K, Nakanishi T and Enoki T 2010 Electronic states of graphene nanoribbons and analytical solutions *Sci. Technol. Adv. Mater.* **11** 054504

[74] Jungthawan S, Limpijumnong S and Kuo J L 2011 Electronic structures of graphene/boron nitride sheet superlattices *Phys. Rev. B - Condens. Matter Mater. Phys.* **84** 1–9

[75] Modarresi M, Roknabadi M R R and Shahtahmasbi N 2011 Transport properties of an armchair boron-nitride nanoribbon embedded between two graphene electrodes *Phys. E Low-dimensional Syst. Nanostructures* **43** 1751–4

[76] Vishkayi S I, Tagani M B and Soleimani H R 2015 Enhancement of thermoelectric efficiency by embedding hexagonal boron-nitride cells in zigzag graphene nanoribbons *J. Phys. D. Appl. Phys.* **48** 235304

[77] Cresti A, Nemec N, Biel B, Niebler G, Triozon F, Cuniberti G and Roche S 2008 Charge transport in disordered graphene-based low dimensional materials *Nano Res.* **1** 361–94

[78] Chung H-C, Lee M-H, Chang C-P, Huang Y-C and Lin M-F 2011 Effects of Transverse Electric Fields on Quasi-Landau Levels in Zigzag Graphene Nanoribbons *J. Phys. Soc. Japan* **80** 44602

[79] Bena C and Montambaux G 2009 Remarks on the tight-binding model of graphene *New J. Phys.* **11** 095003

[80] Datta S 2005 *Quantum Transport : Atom to Transistor* (Cambridge: Cambridge University Press)

[81] Meir Y and Wingreen N S 1992 Landauer formula for the current through an interacting electron region *Phys. Rev. Lett.* **68** 2512–5

[82] Lewenkopf C H and Mucciolo E R 2013 The recursive Green's function method for graphene *J. Comput. Electron.* **12** 203–31

[83] Lewenkopf C H and Mucciolo E R 2013 The recursive Green's function method for graphene *J. Comput. Electron.* **12** 203–31

[84] Dollfus P, Nguyen V H and Saint-Martin J 2015 Thermoelectric effects in graphene nanostructures *J. Phys. Condens. Matter* **27** 133204

[85] Chung D Y, Hogan T, Schindler J, Iordarridis L, Brazis P, Kannewurf C R, Chen B, Uher C and Kanatzidis M G 1997 Complex bismuth chalcogenides as thermoelectrics *Thermoelectrics, 1997. Proceedings ICT '97. XVI International Conference on* pp 459–62

[86] D'Agosta R 2013 Towards a dynamical approach to the calculation of the figure of merit of thermoelectric nanoscale devices *Phys. Chem. Chem. Phys.* **15** 1758–65

[87] Sancho M P L, Sancho J M L and Rubio J 2000 Quick iterative scheme for the

calculation of transfer matrices: application to Mo (100) *J. Phys. F Met. Phys.* **14** 1205–15

[88] Li T C and Lu S P 2008 Quantum conductance of graphene nanoribbons with edge defects *Phys. Rev. B - Condens. Matter Mater. Phys.* **77** 085408

[89] Carpio A, Bonilla L L, de Juan F and Vozmediano M A H 2008 Dislocations in graphene *New J. Phys.* **10** 53021

[90] Nakada K, Fujita M, Dresselhaus G and Dresselhaus M 1996 Edge state in graphene ribbons: Nanometer size effect and edge shape dependence. *Phys. Rev. B. Condens. Matter* **54** 17954–61

[91] Zhao K, Zhao M, Wang Z and Fan Y 2010 Tight-binding model for the electronic structures of SiC and BN nanoribbons *Phys. E Low-dimensional Syst. Nanostructures* **43** 440–5

[92] Xiao Y, Yan X H, Cao J X, Ding J W, Mao Y L and Xiang J 2004 Specific heat and quantized thermal conductance of single-walled boron nitride nanotubes *Phys. Rev. B - Condens. Matter Mater. Phys.* **69** 205415

[93] Ouyang T, Chen Y, Xie Y, Yang K, Bao Z and Zhong J 2010 Thermal transport in hexagonal boron nitride nanoribbons. *Nanotechnology* **21** 245701

[94] Zheng F, Sasaki K, Saito R, Duan W and Gu B-L 2009 Edge States of Zigzag Boron Nitride Nanoribbons *J. Phys. Soc. Japan* **78** 074713

[95] Ribeiro R M and Peres N M R 2011 Stability of boron nitride bilayers: Ground-state energies, interlayer distances, and tight-binding description *Phys. Rev. B* **83** 235312

[96] Panchakarla L S, Subrahmanyam K S, Saha S K, Govindaraj A, Krishnamurthy H R, Waghmare U V. and Rao C N R 2009 Synthesis, Structure, and Properties of Boron- and Nitrogen-Doped Graphene *Adv. Mater.* NA – NA

[97] Lu J, Gomes L C, Nunes R W, Castro Neto a H and Loh K P 2014 Lattice relaxation at the interface of two-dimensional crystals: graphene and hexagonal boron-nitride. *Nano Lett.* **14** 5133–9

[98] Giovannetti G, Khomyakov P, Brocks G, Kelly P and van den Brink J 2007 Substrate-induced band gap in graphene on hexagonal boron nitride: Ab initio density functional calculations *Phys. Rev. B* **76** 073103

[99] Sławińska J, Zasada I and Klusek Z 2010 Energy gap tuning in graphene on hexagonal boron nitride bilayer system *Phys. Rev. B* **81** 155433

[100] Ramasubramaniam A, Naveh D and Towe E 2011 Tunable band gaps in bilayer graphene-BN heterostructures *Nano Lett.* **11** 1070–5

[101] Sakai Y and Saito S 2012 Electronic properties of graphene/h-BN bilayer superlattices *J. Phys. Soc. Japan* **81** 1–4

[102] Lambin P, Amara H, Ducastelle F and Henrard L 2012 Long-range interactions between substitutional nitrogen dopants in graphene: Electronic properties calculations *Phys. Rev. B* **86** 045448

[103] Gebhardt J, Koch R J, Zhao W, Höfert O, Gotterbarm K, Mammadov S, Papp C, Görling a., Steinrück H-P and Seyller T 2013 Growth and electronic structure of boron-doped graphene *Phys. Rev. B* **87** 155437

[104] Noei M, Fathipour M and Pourfath M 2012 A computational study on the electronic properties of armchair graphene nanoribbons confined by boron nitride *Jpn. J. Appl.*

Phys. **51** 035101

[105] He J, Chen K-Q, Fan Z-Q, Tang L-M and Hu W P 2010 Transition from insulator to metal induced by hybridized connection of graphene and boron nitride nanoribbons *Appl. Phys. Lett.* **97** 193305

[106] Chanana A, Sengupta A and Mahapatra S 2014 Performance analysis of boron nitride embedded armchair graphene nanoribbon metal–oxide–semiconductor field effect transistor with Stone Wales defects *J. Appl. Phys.* **115** 034501

[107] Bhowmick S, Singh A K and Yakobson B I 2011 Quantum dots and nanoroads of graphene embedded in hexagonal boron nitride *J. Phys. Chem. C* **115** 9889–93

[108] Ding Y, Wang Y and Ni J 2009 Electronic properties of graphene nanoribbons embedded in boron nitride sheets *Appl. Phys. Lett.* **95** 95–8

[109] Li S, Ren Z, Zheng J, Zhou Y, Wan Y and Hao L 2013 Band gap engineering of graphene/h-BN hybrid superlattices nanoribbons *J. Appl. Phys.* **113** 033703

[110] Fujita M, Wakabayashi K, Nakada K and Kusakabe K 1996 Peculiar Localized State at Zigzag Graphite Edge *J. Phys. Soc. Japan* **65** 1920–3

[111] Han M Y, Özyilmaz B, Zhang Y and Kim P 2007 Energy band-gap engineering of graphene nanoribbons *Phys. Rev. Lett.* **98** 206805

[112] Bai J, Zhong X, Jiang S, Huang Y and Duan X 2010 Graphene nanomesh. *Nat. Nanotechnol.* **5** 190–4

[113] Hung Nguyen V, Chung Nguyen M, Nguyen H-V and Dollfus P 2013 Disorder effects on electronic bandgap and transport in graphene-nanomesh-based structures *J. Appl. Phys.* **113** 013702

[114] Querlioz D, Apertet Y, Valentin a., Huet K, Bournel a., Galdin-Retailleau S and Dollfus P 2008 Suppression of the orientation effects on bandgap in graphene nanoribbons in the presence of edge disorder *Appl. Phys. Lett.* **92** 042108

[115] O'Keeffe J, Wei C and Cho K 2002 Bandstructure modulation for carbon nanotubes in a uniform electric field *Appl. Phys. Lett.* **80** 676

[116] Chung H, Lee M, Chang C, Huang Y and Lin M 2011 Effects of transverse electric fields on quasi-landau levels in zigzag graphene nanoribbons *J. Phys. Soc. Jpn* **80** 1–6

[117] Chung H-C, Yang P-H, Li T-S and Lin M-F 2014 Effects of transverse electric fields on Landau subbands in bilayer zigzag graphene nanoribbons *Philos. Mag.* **94** 1859–72

[118] Zhang Z and Guo W 2008 Energy-gap modulation of BN ribbons by transverse electric fields: First-principles calculations *Phys. Rev. B* **77** 075403

[119] Oostinga J B, Heersche H B, Liu X, Morpurgo A F and Vandersypen L M K 2008 Gate-induced insulating state in bilayer graphene devices. *Nat. Mater.* **7** 151–7

[120] Yang Z and Ni J 2010 Modulation of electronic properties of hexagonal boron nitride bilayers by an electric field: A first principles study *J. Appl. Phys.* **107** 104301

[121] Xia F, Farmer D B, Lin Y M and Avouris P 2010 Graphene field-effect transistors with high on/off current ratio and large transport band gap at room temperature *Nano Lett.* **10** 715–8

[122] Ritter C, Makler S S and Latgé A 2008 Energy-gap modulations of graphene ribbons under external fields: A theoretical study *Phys. Rev. B* **77** 195443

[123] Santos E J G and Kaxiras E 2013 Electric-field dependence of the effective dielectric

constant in graphene. *Nano Lett.* **13** 898–902

[124] Guo W and Guo Y 2003 Giant Axial Electrostrictive Deformation in Carbon Nanotubes *Phys. Rev. Lett.* **91** 115501

[125] Tang C, Guo W and Guo Y 2006 Electrostrictive effect on electronic structures of carbon nanotubes *Appl. Phys. Lett.* **88** 243112

[126] Andrijauskas T 2012 Thomas–Fermi and Poisson modeling of gate electrostatics in graphene nanoribbon *Lith. J. Phys.* **52** 63–9

[127] Hashimoto A, Suenaga K, Urita K, Shimada T, Sugai T, Bandow S, Shinohara H and Iijima S 2005 Atomic Correlation Between Adjacent Graphene Layers in Double-Wall Carbon Nanotubes *Phys. Rev. Lett.* **94** 045504

[128] Tao C, Jiao L, Yazyev O V., Chen Y-C, Feng J, Zhang X, Capaz R B, Tour J M, Zettl A, Louie S G, Dai H and Crommie M F 2011 Spatially resolving edge states of chiral graphene nanoribbons *Nat. Phys.* **7** 616–20

[129] Wolf S a, Awschalom D D, Buhrman R a, Daughton J M, von Molnár S, Roukes M L, Chtchelkanova a Y and Treger D M 2001 Spintronics: a spin-based electronics vision for the future. *Science* **294** 1488–95

[130] Wang Z F, Li Q, Shi Q W, Wang X, Yang J, Hou J G and Chen J 2008 Chiral selective tunneling induced negative differential resistance in zigzag graphene nanoribbon: A theoretical study *Appl. Phys. Lett.* **92** 133114

[131] Nam Do V and Dollfus P 2010 Negative differential resistance in zigzag-edge graphene nanoribbon junctions *J. Appl. Phys.* **107** 063705

[132] Bernevig B A, Hughes T L and Zhang S-C 2006 Quantum spin Hall effect and topological phase transition in HgTe quantum wells. *Science* **314** 1757–61

[133] Zhou B, Lu H-Z, Chu R-L, Shen S-Q and Niu Q 2008 Finite size effects on helical edge states in a quantum spin-Hall system. *Phys. Rev. Lett.* **101** 246807

[134] König M, Wiedmann S, Brüne C, Roth A, Buhmann H, Molenkamp L W, Qi X-L and Zhang S-C 2007 Quantum spin hall insulator state in HgTe quantum wells. *Science* **318** 766–70

[135] Fu L, Kane C L and Mele E J 2007 Topological insulators in three dimensions *Phys. Rev. Lett.* **98** 106803

[136] Hsieh D, Qian D, Wray L, Xia Y, Hor Y S, Cava R J and Hasan M Z 2008 A topological Dirac insulator in a quantum spin Hall phase. *Nature* **452** 970–4

[137] Roy R 2006 Three dimensional topological invariants for time reversal invariant Hamiltonians and the three dimensional quantum spin Hall effect *Phys. Rev. B* **79** 195322

[138] Xia Y, Qian D, Hsieh D, Wray L, Pal a., Lin H, Bansil a., Grauer D, Hor Y S, Cava R J and Hasan M Z 2009 Observation of a large-gap topological-insulator class with a single Dirac cone on the surface *Nat. Phys.* **5** 398–402

[139] Zhang H, Liu C-X, Qi X-L, Dai X, Fang Z and Zhang S-C 2009 Topological insulators in Bi2Se3, Bi2Te3 and Sb2Te3 with a single Dirac cone on the surface *Nat. Phys.* **5** 438–42

[140] Yan B and Zhang S-C 2012 Topological materials *Reports Prog. Phys.* **75** 096501

[141] Kou L, Yan B, Hu F, Wu S C, Wehling T O, Felser C, Chen C and Frauenheim T 2013 Graphene-based topological insulator with an intrinsic bulk band gap above room

temperature *Nano Lett.* **13** 6251–5

[142] Fan Y, Zhao M, Zhang X, Wang Z, He T, Xia H and Liu X 2011 Manifold electronic structure transition of BNC biribbons *J. Appl. Phys.* **110** 034314

[143] Lam K-T, Lu Y, Feng Y P and Liang G 2011 Stability and electronic structure of two dimensional C[sub x](BN)[sub y] compound *Appl. Phys. Lett.* **98** 022101

[144] Shinde P P and Kumar V 2011 Direct band gap opening in graphene by BN doping: Ab initio calculations *Phys. Rev. B - Condens. Matter Mater. Phys.* **84** 125401

[145] Drost R, Uppstu A, Schulz F, Hämäläinen S K, Ervasti M, Harju A and Liljeroth P 2014 Electronic States at the Graphene–Hexagonal Boron Nitride Zigzag Interface *Nano Lett.* **14** 5128–32

[146] Li X, Wang X, Zhang L, Lee S and Dai H 2008 Chemically derived, ultrasmooth graphene nanoribbon semiconductors. *Science* **319** 1229–32

[147] Rousseau J, Morel R, Vila L, Brenac a., Marty a., Notin L and Beigné C 2014 Sub-10 nm nano-gap device for single-cluster transport measurements *Appl. Phys. Lett.* **104** 073103

[148] Hung Nguyen V, Mazzamuto F, Saint-Martin J, Bournel a. and Dollfus P 2011 Giant effect of negative differential conductance in graphene nanoribbon p-n hetero-junctions *Appl. Phys. Lett.* **99** 042105

[149] Nakabayashi J, Yamamoto D and Kurihara S 2009 Band-Selective Filter in a Zigzag Graphene Nanoribbon *Phys. Rev. Lett.* **102** 66803

[150] Wang J, Zhang L and Chan K S 2011 Tunneling conductance of a magnetized zigzag graphene nanoribbon/ superconductor junction *Phys. Rev. B - Condens. Matter Mater. Phys.* **83** 125425

[151] Sugawara K, Sato T, Souma S, Takahashi T and Suematsu H 2006 Fermi surface and edge-localized states in graphite studied by high-resolution angle-resolved photoemission spectroscopy *Phys. Rev. B - Condens. Matter Mater. Phys.* **73** 045124

[152] Novoselov K S, Fal′ko V I, Colombo L, Gellert P R, Schwab M G and Kim K 2012 A roadmap for graphene *Nature* **490** 192–200

[153] Alarcon A, Nguyen V H, Berrada S, Querlioz D, Saint-Martin J, Bournel A and Dollfus P 2013 Pseudosaturation and negative differential conductance in graphene field-effect transistors *IEEE Trans. Electron Devices* **60** 985–91

[154] Hicks L D and Dresselhaus M S 1993 Effect of quantum-well structures on the thermoelectric figure of merit *Phys. Rev. B* **47** 12727–31

[155] Vineis C J, Shakouri A, Majumdar A and Kanatzidis M G 2010 Nanostructured thermoelectrics: Big efficiency gains from small features *Adv. Mater.* **22** 3970–80

[156] Ouyang Y and Guo J 2009 A theoretical study on thermoelectric properties of graphene nanoribbons *Appl. Phys. Lett.* **94** 263107

[157] Li K M, Xie Z X, Su K L, Luo W H and Zhang Y 2014 Ballistic thermoelectric properties in double-bend graphene nanoribbons *Phys. Lett. Sect. A Gen. At. Solid State Phys.* **378** 1383–7

[158] Xie Z X, Tang L M, Pan C N, Li K M, Chen K Q and Duan W 2012 Enhancement of thermoelectric properties in graphene nanoribbons modulated with stub structures *Appl. Phys. Lett.* **100** 10–4

[159] Liang L and Meunier V 2013 Electronic and thermoelectric properties of assembled

graphene nanoribbons with elastic strain and structural dislocation *Appl. Phys. Lett.* **102** 143101

[160] Karamitaheri H, Neophytou N, Pourfath M, Faez R and Kosina H 2012 Engineering enhanced thermoelectric properties in zigzag graphene nanoribbons *J. Appl. Phys.* **111** 054501

[161] Chang P H and Nikolic B K 2012 Edge currents and nanopore arrays in zigzag and chiral graphene nanoribbons as a route toward high-ZT thermoelectrics *Phys. Rev. B - Condens. Matter Mater. Phys.* **86** 41406

[162] Hung Nguyen V, Nguyen M C, Nguyen H-V, Saint-Martin J and Dollfus P 2014 Enhanced thermoelectric figure of merit in vertical graphene junctions *Appl. Phys. Lett.* **105** 133105

[163] Yang K, Chen Y, D'Agosta R, Xie Y, Zhong J and Rubio A 2012 Enhanced thermoelectric properties in hybrid graphene/boron nitride nanoribbons *Phys. Rev. B - Condens. Matter Mater. Phys.* **86** 1–8

[164] Tang C, Kou L and Chen C 2012 Tunable band gap and magnetism in C 2x-(BN) y sheets and ribbons *Chem. Phys. Lett.* **523** 98–103

[165] Jiang J W, Wang J S and Wang B S 2011 Minimum thermal conductance in graphene and boron nitride superlattice *Appl. Phys. Lett.* **99** 2011–3

[166] Yokomizo Y and Nakamura J 2013 Giant Seebeck coefficient of the graphene/h-BN superlattices *Appl. Phys. Lett.* **103** 12–5

[167] Zhu T and Ertekin E 2014 Phonon transport on two-dimensional graphene/boron nitride superlattices *Phys. Rev. B* **90** 195209

[168] Yamamoto T and Watanabe K 2006 Nonequilibrium green's function approach to phonon transport in defective carbon nanotubes *Phys. Rev. Lett.* **96** 255503

[169] KInacI A, Haskins J B, Sevik C and ÇağIn T 2012 Thermal conductivity of BN-C nanostructures *Phys. Rev. B* **86** 1–8

[170] Goldsmid H J and Sharp J W 1999 Estimation of the thermal band gap of a semiconductor from seebeck measurements *J. Electron. Mater.* **28** 869–72

[171] Nguyen M C, Nguyen V H, Nguyen H-V, Saint-Martin J and Dollfus P 2015 Enhanced Seebeck effect in graphene devices by strain and doping engineering *Phys. E Low-dimensional Syst. Nanostructures* **73** 207–12

[172] Mazzamuto F, Saint-Martin J, Nguyen V H, Chassat C and Dollfus P 2012 Thermoelectric performance of disordered and nanostructured graphene ribbons using Green's function method *J. Comput. Electron.* **11** 67–77

[173] Rodriguez-Manzo J A and Banhart F 2009 Creation of individual vacancies in carbon nanotubes by using an electron beam of 1 \AA diameter. *Nano Lett.* **9** 2285–9

[174] Robertson A W, Allen C S, Wu Y a., He K, Olivier J, Neethling J, Kirkland A I and Warner J H 2012 Spatial control of defect creation in graphene at the nanoscale *Nat. Commun.* **3** 1144

[175] Wilhelm J, Walz M and Evers F 2014 *Ab initio* quantum transport through armchair graphene nanoribbons: Streamlines in the current density *Phys. Rev. B* **89** 195406

List of publications and conferences

Publications

3. Van-Truong Tran, Jérôme Saint-Martin and Philippe Dollfus, "High thermoelectric performance in graphene nanoribbons by graphene/BN interface engineering". arXiv:1508.01837, *Nanotechnology* **26**, 495202 (2015). http://dx.doi.org/10.1088/0957-4484/26/49/495202

2. Van-Truong Tran, Jérôme Saint-Martin and Philippe Dollfus , **"**Dispersive hybrid states and bandgap in zigzag Graphene/BN heterostructures**"**, arXiv:1412.6798 , *Semiconductor Science and Technology* **30,** 105002 (2015). http://dx.doi.org/10.1088/0268-1242/30/10/105002

1. Van-Truong Tran, Jérôme Saint-Martin and Philippe Dollfus , **"**Large on/off current ratio in hybrid graphene/BN nanoribbons by transverse electric field-induced control of bandgap**"**, *Applied Physics Letters* **105**, 073114 (2014). http://dx.doi.org/10.1063/1.4893697

Conferences

5. **Van-Truong Tran**, Saint-Martin Jérôme, Dollfus Philippe, *Enhancement of thermoelectric properties in in-plane Graphene/BN structures*, Trends in Nanotechnology International Conference (TNT2015), 7-11 September 2015, Toulouse, France**.**

4. **Van-Truong Tran**, Saint-Martin Jérôme, Dollfus Philippe**,** *Hybrid states and bandgap in zigzag Graphene/BN heterostructures*, International Workshop on Computational Electronics (IWCE 2015), 02-04 September 2015, West Lafayette, Indiana USA.

DOI: 10.1109/IWCE.2015.7301953

3. **Van-Truong Tran**, Saint-Martin Jérôme, Dollfus Philippe, *Hybrid states at interfaces of zigzag Graphene/BN heterostructures*, Graphene 2015, 10-13 March 2015, Bilbao, Spain.

2. **Van-Truong Tran**, Saint-Martin Jérôme, Dollfus Philippe, *Modulation of bandgap and current inGraphene/BN heterostructures by tuning the transverse electric field*, 17th International Workshop on Computational Electronics, (IWCE 2014), 201410603 – 20140606, Paris, France.

DOI: 10.1109/IWCE.2014.6865869

1. **Tran Van Truong**, Saint-Martin Jérôme, Dollfus Philippe, *Modulation of bandgap and current inGraphene/BN heterostructures by tuning the transverse electric field*, NanoSaclay Nanoelectronics Workshop, 20131210 – 20131213, Paris, France.

Other conferences:

2. Dollfus Philippe, Nguyen Viet-Hung, Berrada Salim, **Tran Van-Truong**, Nguyen Mai-Chung, Bournel Arnaud, Saint-Martin Jérôme, Strategies to control the current in graphene transistors, *CMOS Emerging Technologies Research Symposium*, 20140706 – 20140708, Grenoble, France.

1. Dollfus Philippe, Nguyen Viet-Hung, Berrada Salim, **Tran Van-Truong**, Nguyen Mai-Chung, Bournel Arnaud, Saint-Martin Jérôme, Strategies to improve the control of current in graphene transistors, *18th European Conference on Mathematics for Industry (ECMI 2014)*, 20140609 – 20140613, Taormina, Italia.

université PARIS-SACLAY

ÉCOLE DOCTORALE
Physique et ingénierie : électrons, photons, sciences du vivant (EOBE)

Titre : Propriétés électroniques et thermoélectriques des hétérostructures planaires de graphène et de nitrure de bore

Mots clés : graphène, nitrure de bore, simulation atomistique, électronique / thermoélectricité, transport quantique, Fonctions de Green

Résumé : Les excellentes propriétés électroniques, thermiques et mécaniques du graphène confère à ce matériau planaire (bi-dimensionnel) un énorme potentiel applicatif, notamment en électronique. Néanmoins, ce matériau présente de sérieux inconvénients qui pourraient limiter son champ d'applications. Par exemple, sa structure de bandes électronique sans bande interdite rend difficile le blocage du courant dans un dispositif. De plus, pour les applications thermoélectriques, sa forte conductance thermique est aussi une forte limitation. Il y a donc beaucoup de défis à relever pour rendre ce matériau vraiment utile pour des applications.
Cette thèse porte sur l'étude des propriétés électroniques et thermoélectriques dans les hétérostructures planaires constituées de graphène et de nitrure de bore hexagonal (BN). Différentes configuration de ce nouveau matériau hybride permettent de moduler la bande interdite, la conductance thermique et le coefficient Seebeck. Cette étude a été menée au moyen de calculs atomistiques basés sur les approches des liaisons fortes (TB) et du modèle à constantes de force (FC). Le transport d'électrons et de phonons a été simulé dans le formalisme des fonctions de Green hors équilibre.
Les résultats montrent que, grâce à la modulation de la bande interdite, des transistors à base d'hétérostructures de BN et de graphène peuvent présenter un très bon rapport courant passant/bloqué d'environ 10^4 à 10^5. En outre, nous montrons l'existence d'états quantiques hybrides à l'interface zigzag entre le graphène et le BN donnant lieu à des propriétés de transport électronique très intéressantes. Enfin, ce travail montre qu'en agençant correctement des nano-flocons de BN sur les côtés d'un nanoruban de graphène, la conductance des phonons peut être fortement réduite alors que l'ouverture de bande interdite conduit à un accroissement important du coefficient Seebeck. Il en résulte qu'un facteur de mérite thermoélectrique *ZT* plus grand que l'unité peut être réalisé à température ambiante.

Title: Electronic and thermoelectric properties of graphene/boron nitride in-plane heterostructures

Keywords: graphene, boron nitride, atomistic simulation, electronics / thermoelectrics, quantum transport, Green's functions

Abstract: Graphene is a fascinating 2-dimensional material exhibiting outstanding electronic, thermal and mechanical properties which confer to this planar (bi-dimensional) material a huge application potential, notably in electronics. However, this material presents serious drawbacks which could limit its field of applications. For example, its electronic band structure without band gap makes difficult the blocking of current in a device. Moreover, for thermoelectric applications, its high thermal conductance is also a strong limitation. There is thus many challenges to overcome to make this material really useful for applications.
This thesis deals with the study of electronic and thermoelectric properties in graphene/boron nitride hexagonal (BN) in-plane heterostructures. Different configuration of this novel hybrid material allow to modulate the band gap, the thermal conductance and the Seebeck coefficient. The work is performed using atomistic simulations based on tight binding (TB), force constant (FC) models for electrons

Université Paris-Saclay
Espace Technologique / Immeuble Discovery
Route de l'Orme aux Merisiers RD 128 / 91190 Saint-Aubin, France

mechanical properties. Is this expected to have a huge potential for a wide range of applications, in particular in electronics. However, this material also suffers from a strong drawback for most electronic devices due to the gapless character of its band structure, which makes it difficult to switch off the current. For thermoelectric applications, the high thermal conductance of this material is also a strong limitation. Hence, many challenges have to be taken up to make it useful for actual applications.

This thesis work focuses on the theoretical investigation of a new strategy to modulate and control the properties of graphene that consists in assembling in-plane heterostructures of graphene and Boron Nitride (BN). It allows us to tune on a wide range the bandgap, the thermal conductance and the Seebeck coefficient of the resulting hybrid nanomaterial.

and phonons, respectively, coupled with the Green's function formalism for transport calculation.

The results show that thanks to the tunable bandgap, it is possible to design graphene/BN based transistors exhibiting high on/off current ratio in the range 10^4-10^5. We also predict the existence hybrid quantum states at the zigzag interface between graphene and BN with appealing electron transport. Finally this work shows that by designing properly a graphene ribbon decorated with BN nanoflakes, the phonon conductance is strongly reduced while the bandgap opening leads to significant enhancement of Seebeck coefficient. It results in a thermoelectric figure of merit *ZT* larger than one at room temperature.